Self-standing Fe-N-C cathodes prepared by electrospinning for fuel cells

Svitlana Yarova

THÈSE POUR OBTENIR LE GRADE DE DOCTEUR DE L'UNIVERSITÉ DE MONTPELLIER

En Chimie et Physico-Chimie des Matériaux

École doctorale Sciences Chimiques Balard – ED 459

Unité de recherche Institut Charles Gerhard de Montpellier – UMR 5253

Préparation de cathodes FeNC autosupportées par filage électrostatique pour piles à combustible

Présentée par Svitlana YAROVA
Le 30 Juin 2020

Sous la direction de Frédéric JAOUEN
et Sara CAVALIERE

Devant le jury composé de

Deborah JONES, Directeur de Recherche, ICG Montpellier	Président du jury
Patricia HORCAJADA, Directeur de Recherche, IMDEA Espagne	Rapporteur
Michele PIANA, Directeur de Recherche, TUM Allemagne	Rapporteur
Elsje Alessandra QUADRELLI, Directeur de Recherche, CNRS CPE Lyon, France	Examinateur
Frédéric JAOUEN, Chargé de Recherche, ICG Montpellier	Directeur de thèse
Sara CAVALIERE, Maitre de Conférences, ICG Montpellier	Co-directeur de thèse

UNIVERSITÉ DE MONTPELLIER

Table of Contents

List of figures:

List of tables:

Acknowledgments

This journey of three years was undoubtedly full of adventures. First of all, I would like to thank Dr. Frédéric Jaouen and Dr. Sara Cavaliere for the opportunity to work on this project, for their very valuable supervision, their endless support, trust and patience. They offered me plenty of valuable advices, help and critical comments on the experimental aspects of my research and on the thesis manuscript. I also would like to acknowledge the members of my PhD thesis committee, in particular the reviewers of my thesis: Dr. Patricia Horcajada and Dr. Michele Piana, and the examiners, Dr. Alessandra Quadrelli and Dr. Deborah Jones, for their valuable time, important comments and scientific discussion.

A large part of the experimental work could not have been carried out without the precious help of engineers and technicians of the équipe AIME. I wish to thank Dr. Marc Dupont, Dr. Nicolas Donzel, Dr. Bernard Fraisse, Julien Fullenwarth and Léa Daenens of the équipe AIME for all the practical help and discussions during my PhD thesis.

I would like to acknowledge the project CAT²CAT (From catalysts to cathodes: a controlled-architecture approach for PEMFC electrodes catalyzed by Earth-abundant metals), funded by Agence Nationale de la Recherche (ANR-16-CE05-0007) that financed my PhD project. Also I wish to thank project collaborators, laboratories LEPMI and IRCELYON for precious help and discussions during the project meetings and a special thanks to Dr. Katia Barbera and Dr. Kavita Kumar for sharing results and ideas.

I wish to express my gratitude also to Alexandre Heitz, who spent 6 months of his Master internship in the laboratory and helped me with synthesis, characterizations and many discussions during our numerous meetings. Thank you for your brilliant ideas and endless enthusiasm! And of course I am grateful to my other colleagues, who helped me went through my PhD path. I want to thank and acknowledge every PhD student and postdoc for sharing fruitful discussions during our time spent together in the lab, or during coffee breaks. Without the support of the team, who bothered me while drinking coffee, I do not think I could have finished this project. Thank you all.

Lastly, I wish to thank my friends, who supported me and will still support me in the future, no mater what. I am infinitely grateful to them for staying by my side during my hardships and sharing my moment of joy. I am not me without you. Спасибо. And the last last acknowledgment goes to my family, who always had a trust in me and encouraged me to never give up in my dreams and supported me unconditionally. I cannot imagine how my life would be without you

I promise that one day, everything is going to be better for you.

Introduction

General introduction

Currently, most of the world's energy supply comes from fossil sources (coal, fuel oil and natural gas) or from nuclear reserves (radioactive materials)[1]. With high consumption of those non-renewable sources of energy and the growing awareness about the negative effect of emission of greenhouse gases, the demand for sustainable energy conversion and storage devices such as fuel cells, supercapacitors (SCs), batteries and solar cells has rapidly increased[2]. Among all energy carriers, hydrogen is considered as one of the most promising and clean, offering the prospect of large energy storage capacities [3]. Europe identified it as one of the pillars of the transition to a decarbonised energy system to limit global warming[4]. Today, 98 % of hydrogen is however produced by steam reforming of natural gas, emitting megatons of CO_2 every year. Water electrolysis, eventually coupled with renewable but intermittent energy sources (solar and wind power), is a clean and sustainable technology allowing energy storage *via* the production of highly pure hydrogen. [5,6]

1. Hydrogen as a fuel for energy conversion systems. Fuel cells

The interest of using hydrogen in energy conversion and storage systems as the replacement of fossil fuel resources is growing, and one of the most promising energy conversion devices are fuel cells using this gas as a fuel. A fuel cell is an electrochemical device that directly converts chemical energy into electricity. Firstly introduced in 1839 by Sir William Robert Grove, fuel cells have been used for years mostly as backup power in remote or inaccessible areas, military applications, and space applications, such as the NASA space programs[7]. Starting from the 1960's, fuel cells started to receive renewed attention and were developed as a promising energy conversion device for the transportation and stationary applications[8].

Due to targets of low or zero CO_2 emissions in the near future, the automobile industry has demonstrated rapidly growing interest in the last years in fuel cells (Toyota, Honda, Hyundai) and as well for heavy-duty vehicles (buses, trucks or trains)[3].

Figure 1 depicts the increase in the megawatts of rated electric power cumulated for all types of fuel cells produced over the last years, and also by fuel cell type. So far, leading countries in fuel cell market development are South Korea, China, The United States and The European Union[9]. Fuel cell electric

vehicles are produced in small series since 2017 (*e.g.* Toyota Mirai) [10]. However their cost is still high, mostly due to the use of platinum group metal (PGM) catalysts, a rare and expensive metal.

Over the past decades, different types of fuel cells have been developed, each of them suitable for different domains and applications, although they all operate under the same principle, with fuel electro-oxidation on the anode, O_2 electro-reduction on the cathode, and an ion-conducting (but not electron-conductive) electrolyte separating the two electrodes. As a function of the nature of the ions conducted and the nature of the electrolyte (aqueous electrolyte, functionalized polymer, an oxide or a molten carbonate), the operating temperature of a fuel cell can range from sub-zero to 1000°C (Figure 2).

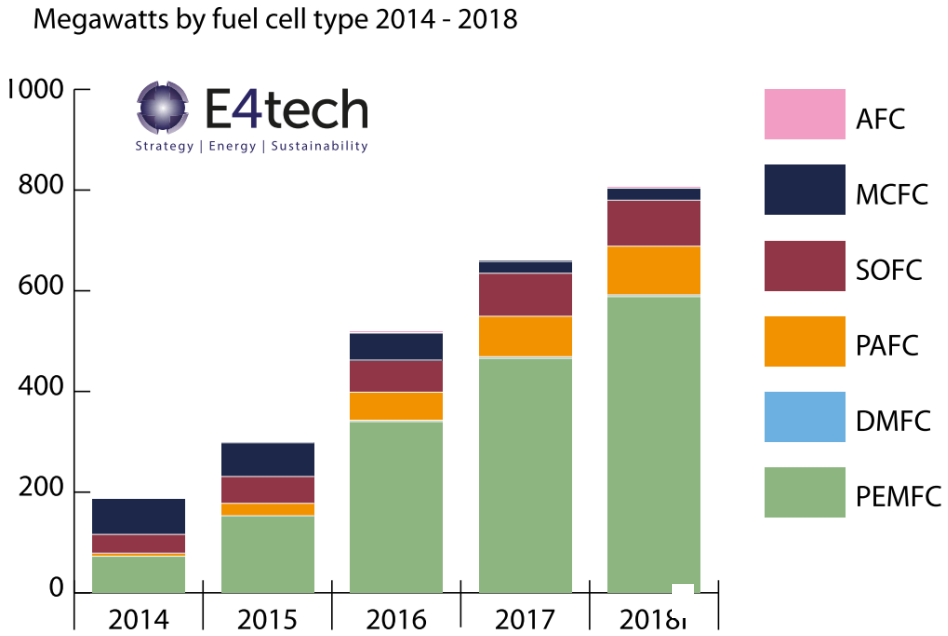

Figure 1: Cumulative electric power for all types of fuel cells produced per year, and by fuel-cell type, in 2014-2018 (reprinted from Ref. [3])

Among the different types of fuel cells, one can mention alkaline fuel cells (AFC), phosphoric acid (PAFC), solid oxide (SOFC), molten carbonate (MCFC), biofuel cells, direct methanol (DMFC), proton ceramic (PCFC) and proton exchange membrane fuel cells (PEMFC). So far, the most developed one is perhaps the PEMFC, due to its high energy efficiency, fast startup and shutdown and low maintenance cost [11]. This PhD thesis work will be focused on the low-temperature PEMFC and the following paragraphs are briefly presenting the principle of this electrochemical device and its main components.

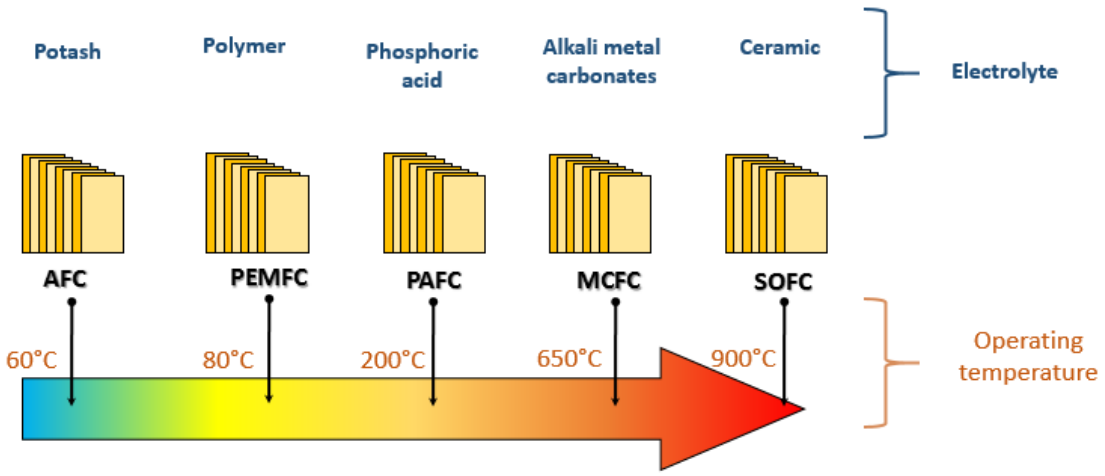

Figure 2: Electrolytes and operating temperatures for different types of fuel cells (reprinted from website https://www.h2sys.fr)

2. The proton exchange membrane fuel cell

A PEMFC directly generates electrical energy through electrochemical processes with a constant fuel feeding. The overall chemical reaction taking place in a PEMFC is the conversion of hydrogen and oxygen gas into water, heat and electricity. A PEMFC operates at low temperature (typically 80 °C) with a cationic exchange membrane (in proton form) as electrolyte[12]. The structure of the PEMFC core, the membrane-electrode-assembly (MEA), is shown in Figure 3. It is composed of a proton exchange membrane (PEM) placed between two electrodes, the whole sandwich structure defining the so-called MEA. The role of the membrane is to electrically separate the electrodes and to transport the protons generated at the anode by hydrogen oxidation reaction (HOR, 1) to the cathode, where the oxygen reduction reaction (ORR, 2) takes place, reducing oxygen and forming water as a final product of the reaction[13]. Electrons, produced after (1) flow through the outer circuit from the anode to the cathode, resulting in an electric current and electric power that can be used to power any device. Heat is also produced due to Ohmic losses and overpotential losses of the electrochemical reactions.

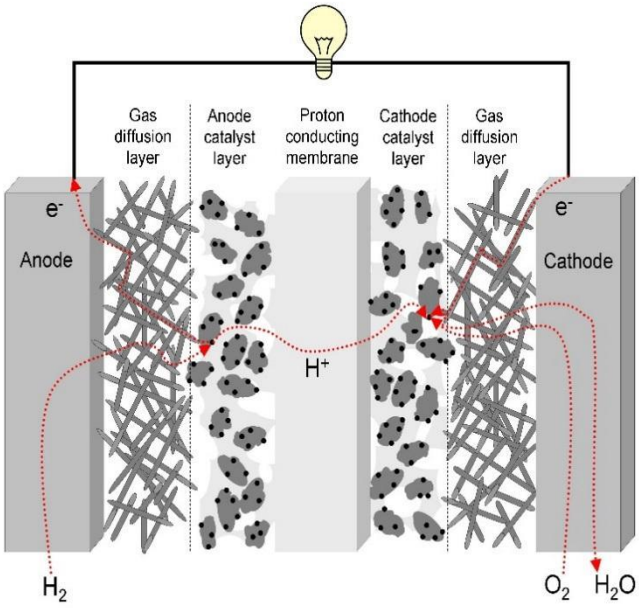

Figure 3: Schematic representation of an MEA and the operation principle of a PEMFC, reprinted from ref[14]

The reactions in an operating PEMFC are the following:

Anode (HOR):	$H_2 \rightarrow 2H^+ + 2e^-$	($E^0 = 0$ V vs. RHE)	(1)
Cathode (ORR):	$O_2 + 4H^+ + 4e^- \rightarrow 2H_2O$	($E^0 = 1.23$ V vs. RHE)	(2)
Total:	$H_2 + ½O_2 \rightarrow H_2O$	($\Delta E = 1.23$ V)	(3)

The membrane placed between the electrodes is composed of a proton conducting polymer. The material conventionally used nowadays is a perfluorosulfonic acid (PFSA) polymer, usually a commercial membrane called Nafion®, developed in the 1960's by Dupont de Nemours. The chemical structure of a repeating unit of Nafion® is depicted in Figure 4:

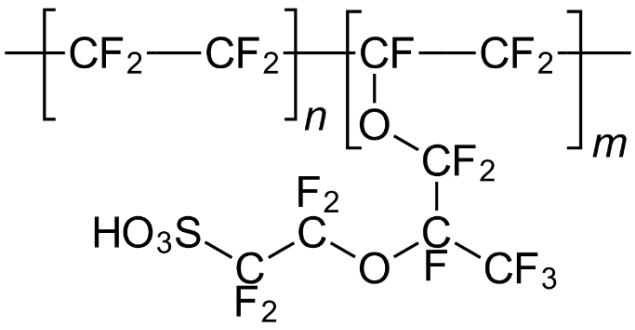

Figure 4: Nafion® chemical structure.

Nafion® is a long-side-chain PFSA, where side groups terminate in hydrophilic sulfonic acid groups (SO_3H) providing the protons responsible for the membrane's proton conductivity, while the hydrophobic polytetrafluoroethylene backbone determines the mechanical stability and impermeability to gases[15].

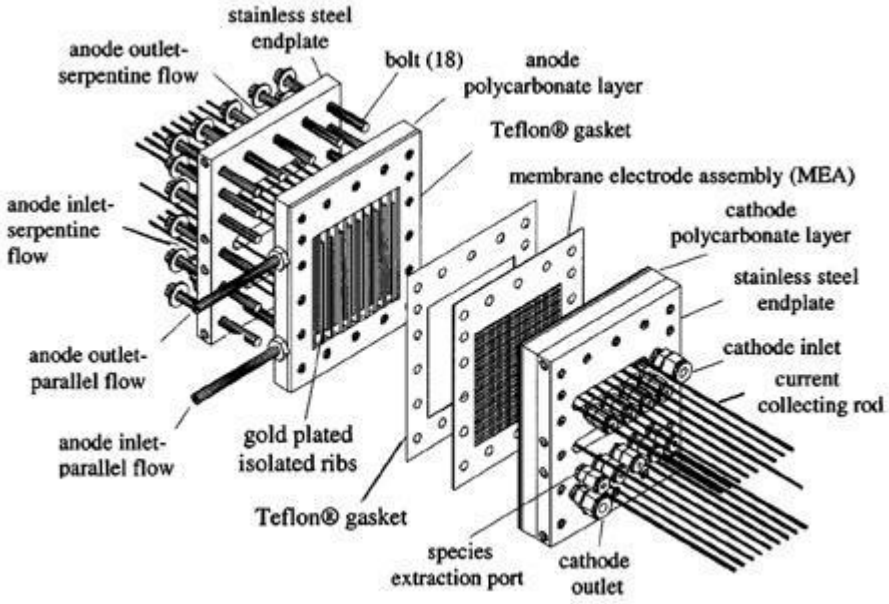

Figure 5: Schematic representation of a PEMFC stack. Reproduced from www.sensorprod.com

The two electrodes include each a gas diffusion layer (GDL) and a catalyst layer. The role of the GDL is to let the gas diffuse to the catalytic layer, to provide the mechanical support and also the electrical connection between the catalytic layer and the current collector (end-plates). Usually, GDLs are made of carbon fibers.[16] The catalytic layer can be deposited on the GDL, forming a gas diffusion electrode (GDE) or directly applied to the membrane (catalyst-coated membrane, CCM). The anode, membrane and

cathode are then usually hot pressed to develop a suitable interface between the catalyst layer and the proton-conducting membrane.

While the development of PEM is at the root of the PEMFC development, almost no electric power can be produced by PEMFCs without catalysts, due to the low operating temperature. In particular, the ORR is five orders of magnitude slower than the HOR, in acidic medium and on the state-of-art catalytic surface known to date, platinum. Therefore the electrochemical reaction taking place on the cathode (ORR) needs a special attention for the catalysis [16]. The catalyst layer is the electroactive part of the fuel cell, where electrochemical reactions take place. It is today based on platinum (or platinum alloy) particles supported on highly porous carbon blacks, ensuring good dispersion of the Pt electrocatalyst particles and of the ionomer, that is needed in order to conduct through the active layer the protons coming from the anode side. The protons are essential, since they are reactants of the electrocatalytic reactions. HOR and ORR reactions occur at confined spatial sites, the so-called “triple phase boundary” (TPB) where protons from the PEM, electrons from the electrically connected catalyst regions and gas molecules can be in contact[17]. The presence of Nafion® improves the number of TPB sites where the catalytically active electrode particles, electrolyte phase and gas pores intersect. The ORR reaction in the cathode active layer and the cathode TPB are depicted in Figure 6.

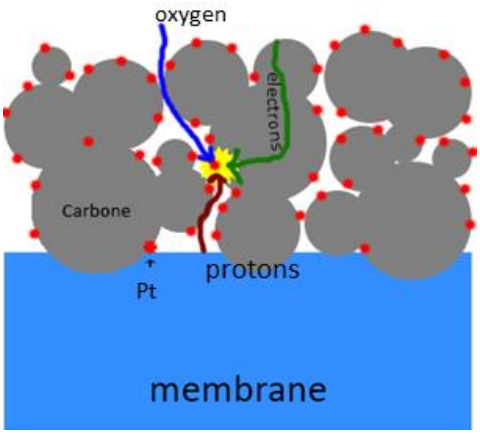

Figure 6: Graphical representation of the ORR and the triple phase boundary

The key to maximize the utilisation of the catalytic particles at the cathode, and therefore to maximize the PEMFC power performance, is to provide the maximum accessibility of all the catalytic particles in the active layer by electrons, protons and O_2 molecules.

The key advantages of PEMFC over other fuel cell types are high efficiency, simple structure and as a consequence low maintenance cost, and low pollution emissions since the only chemical product of PEMFC

is water[11]. Despite these factors, the limited commercial success and deployment of PEMFCs till now is related to the high cost of the device, mainly relied to platinum-based catalysts and the membrane cost[18]. While the cost of the latter is expected to decrease with scaled-up production through economies of scale, the price of platinum is in contrast expected to increase with increased production of PEMFCs, due the low of demand/supply. Therefore, the platinum content in a PEMFC stack of a given rated electric power output should be either decreased by optimizing Pt-based catalysts, or ideally completely removed by developing new catalysts based on non-critical materials. One of possible alternative to replace Pt nanoparticle catalysts are catalysts based on Earth-abundant metals, in particular the family of FeNC catalysts in which the Fe-based active sites have a molecular-like FeN_4 structure [19].

3. Electrocatalysts for the oxygen reduction reaction

3.1 Platinum catalysts

As mentioned above, the ORR plays a key role in the performance of PEMFCs, and the major challenge in its development is the improvement of the cathode electrocatalytic activity while reducing the loading of noble metals. As the state-of-the-art, platinum is the best electrocatalyst for the ORR, with sufficiently high activity and durability in acid media[20]. Nonetheless, the cathode still remains the major source of losses in efficiency, due to sluggish ORR and due to poor mass-transport properties when the cathode is fed with air, while pure H_2 is used on the anode side[2].

The utilization of Pt is limited by its high cost, but also by the limited resources of Pt in the world. Therefore, according to the US Department of Energy (DOE), the target of total Pt loading (both cathode and anode) is required to be below 0.125 mg per cm^2 of geometric area of the MEA, in 2020 [21]. Reducing the Pt loading and keeping similar performance is a great challenge for all scientists around the globe.

Three possible ways to introduce platinum in the electrocatalyst are:

1) Pure platinum electrocatalysts (Pt particles, nanorods, nanowires, thin films, etc)[22]
2) Core-shell metal-platinum (de-alloyed, monolayer, hollow particles, etc)[23,24]
3) Platinum alloyed with a non-precious metal (with Ni, Co, Cu)[25–27]

Pure platinum catalysts can give the best structure control and stability in acidic media. Another axis of research involves the formation of extended Pt thin film areas (2D) on different supports, to benefit from the much higher intrinsic activity of extended 2D area of Pt while still having a nanometric Pt film thickness and unsupported Pt foams.[28,29]

Platinum alloyed with one or several non-precious metals [30] can show improved ORR catalytic activity per mass of platinum. However, the acid-stability of these systems under operating conditions is still a challenge. Core-shell platinum catalysts have demonstrated high potential as ORR catalysts with high ORR activity per mass of Pt and are relatively stable in acidic media, which can be a good compromise between performance and durability.

While all these approaches can significantly reduce the amount of Pt per kW of rated electric power of a PEMFC in the near future, it is still desirable to fully replace Pt-based electrocatalysts by earth-abundant elements. Even with *ca* 20 times less Pt in the catalytic converter of an internal combustion engine today than in a SoA PEMFC automotive stack, the Pt worldwide production (mostly, South Africa) just meets the demand for Pt from the automobile, catalysis and jewellery industries[31–33].

3.2 Catalysts free of platinum-group-metals

At present time, platinum-based catalysts are the only commercially available option for PEMFCs. The replacement of platinum-group metals (PGM, comprising the elements Pt, Ir, Rh, Ru, Os, Pd) by Earth-abundant elements has been a long-standing quest.[34] The highly acidic medium of PEMFCs however restricts the library of substitution materials. Major progress has recently been reported with catalysts synthesized *via* the pyrolysis of transition metal (Fe, Co), nitrogen and carbon precursors. This class of catalysts was discovered firstly in 1965 by R. Jasinski [35]. Jasinski used an unpyrolyzed cobalt phthalocyanine as a potential cathode catalyst in alkaline electrolyte. This work was followed by that of Janke et al., who made a revision and proposed a heat-treatment of N_4-metal chelates in order to achieve better electrical connection with the carbon support, and also better stability in alkaline media[36]. Since then, a major progress was made by developing synthesis resorting to the pyrolysis of separate sources of the transition metal (Fe and Co), nitrogen and carbon sources, and high electrochemical activity was achieved with pyrolyzed FeNC catalysts in 2009[37]. It was also identified that the microporous surface and/or volume in FeNC catalyst is positively correlated with their activity [19,39–42].

The nature of the active sites formed during pyrolysis has been a topic of intense debate since the pyrolysis approach started. However, with some synthetic approaches, the complete conversion of the Fe precursor into atomically-dispersed FeN_x active sites has been achieved, with no formation of Fe aggregates (metallic, carbide, oxide), that are not or much less ORR active in acidic medium.[38] The spectroscopic investigation of such model catalysts has allowed unambiguously demonstrating that atomically-dispersed FeN_x sites are formed during pyrolysis of separate Fe, N and C precursors, leading to

a Fe coordination very similar to those existing in Fe phthalocyanine and porphyrin [38,39]. Figure 7 shows for example the identification of the structure of active sites in FeNC catalyst pyrolysed in argon, by comparison of calculated XANES spectra of different hypothetical site structures and the experimental XANES spectrum of a model FeNC catalysts comprising only FeN_x sites.

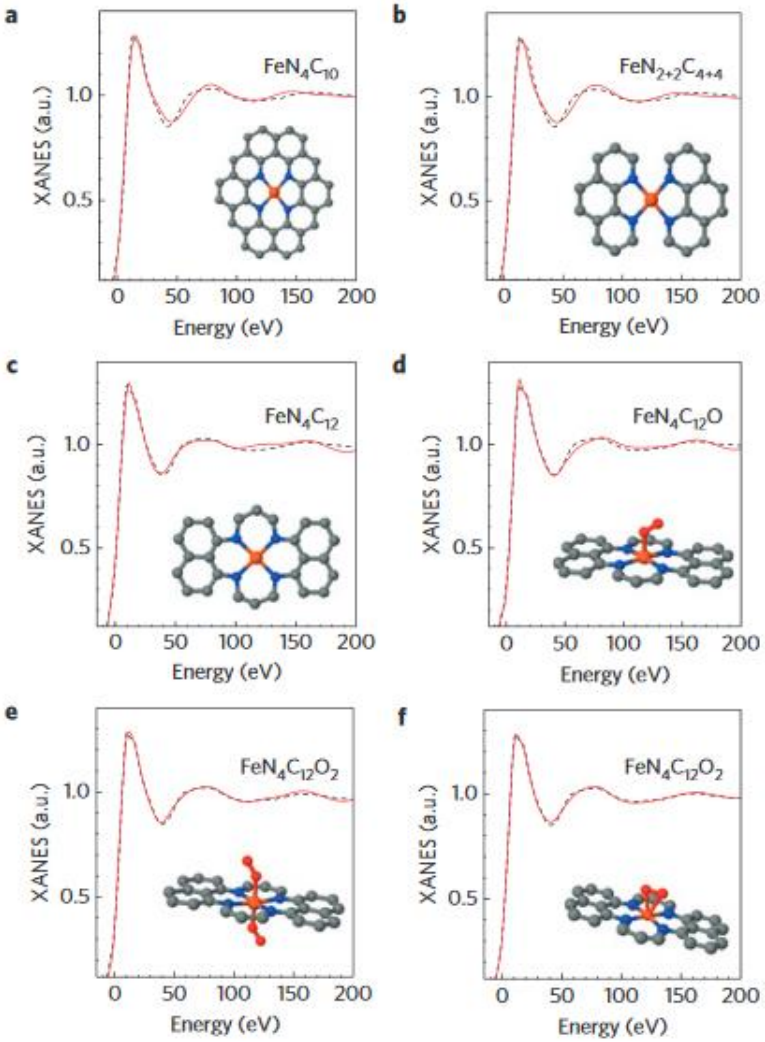

Figure 7: Comparison between the K-edge XANES experimental spectrum of $Fe_{0.5}NC$ (black dashed curves) and the theoretical spectrum calculated with the depicted structures (solid red curves). a, FeN_4C_{10} moiety. b, $FeN_{2+2}C_{4+4}$ moiety. c, FeN_4C_{12} moiety. d, FeN_4C_{12} moiety with one O_2 molecule adsorbed in end-on mode. e, FeN_4C_{12} moiety with two O_2 molecules adsorbed in end-on mode. f, FeN_4C_{12} moiety with one O_2 molecule adsorbed in side-on mode. The brown sphere represents an iron atom, whereas blue, grey and red spheres identify nitrogen, carbon and oxygen atoms, respectively (reprinted from ref [38])

Due to the low-cost of 3d transition metals compared to Pt, this type of catalyst is very promising to use in PEMFC. However, in order to successfully replace Pt with non-noble catalysts, the latter should fulfil several requirements:

- Provide a power density equivalent to Pt-based catalysts in an operating fuel cell
- Demonstrate a sufficient stability in an operating fuel cell.

The laboratory at which this PhD thesis has been carried out, ICGM, team Aggregates Interfaces and Materials for Energy (AIME), has played a key role in advancing such materials.[37,40,43–45]

Due to the low cost of Fe & Co vs. Pt, the key figure for Metal-N-C catalysts is the activity normalized by the overall mass of catalyst. The latter is proportional to the thickness of the cathode active layer, dictating in turn the accessibility of active sites by the reactants. Since Metal-N-C catalysts typically comprise 95 % C and N, their mass activity is a measure of the packing of metal-based ORR active sites in a N-doped carbon matrix. At high metal content however, the parallel formation of ORR-inactive or less active metal-based particles along with the most active sites (MN_xC_y moieties, M = Fe, or Co) restricts the density of such active sites. A key figure for Metal-N-C catalysts is their mass activity, or volumetric activity, at 0.8 V vs. RHE[34]. The conversion from mass to volumetric activity is carried out with the apparent density of Me-N-C catalysts in a cathode layer, *ca* 0.4 g cm^{-3} (25 µm thick electrode for 1 mg cm^{-2})[34]. The current target for the volumetric activity of non-PGM catalysts adopted by the USDOE is 60 A cm^{-3} measured at 0.8 V in H_2/O_2 PEMFC conditions, or 165 A cm^{-3} at 0.8 V from the extrapolation of the Tafel kinetic regime observed at higher potential[46]. With a catalyst having a volumetric activity of 60 A cm^{-3}, a 100 µm-thick cathode is expected to produce 0.6 A cm^{-2} at 0.8 V, if the cathode is not limited by O_2 diffusion or conduction of protons/electrons. While volumetric activities (extrapolated from the Tafel slope observed at higher potential) of 99 and 230 A cm^{-3} have been reported[37,40], the highest current densities measured at 0.8 V in H_2/O_2 PEMFC have been *ca* 0.2 A cm^{-2}[40]. Even stronger deviation between the performance expected from the high ORR activity and measured performance has been observed for air operation, with maximum current densities at 0.4-0.5 V in the range of 0.35-0.45 A cm^{-2} only[41,47]. This impedes a practical replacement of Pt by of non-PGM catalysts in PEMFC, due to increased cost of other components, and increased stack volume for a given PEMFC electric power output.

4. Positioning of the PhD thesis work

Research on Metal-N-C catalysts is intense since 2009 due to the breakthroughs reported in their ORR activity and initial PEMFC performance.[37,40,48,49] While many groups have hitherto focused on

improving their ORR activity and rationalizing the factors that control it, few efforts have focused on improving the mass transport properties of their catalytic layers. Resorting to thicker layers for MNC catalysts ensues from their lower volumetric activity versus Pt/C catalysts.[34]

The use of metal organic frameworks (MOFs) as a sacrificial source of N and C for preparing MNC catalysts was firstly reported in 2011 [40,50]. The approach of Liu's group leaned on the transformation of a microporous cobalt-based zeolitic imidazolate framework (ZIF), namely ZIF-67, into a CoNC catalyst via pyrolysis [50]. For preparing FeNC catalysts from MOF, a Zn-based ZIF (ZIF-8) was used for the first time in 2011 by Dodelet's group[40]. ZIF-8 was mixed with Fe(II) acetate and 1,10-phenanthroline and pyrolyzed, resulting in a highly active FeNC material with dramatically increased PEMFC performance at 0.6 V (*circa* x 2, [40]). A modified synthesis of FeNC from ZIF-8, Fe(II) acetate and 1,10-phenanthroline was established in 2015, leading to a model catalyst comprising only atomically-dispersed iron sites[38,51]. This model catalyst is used in this PhD thesis work as a reference, and labeled reference $Fe_{0.5}NC$. The XANES spectrum of that reference is shown in Figure 7.

The high surface area of the starting ZIF-8 porous material and of the N-doped carbon matrix derived from the pyrolysis of ZIF-8 are important factors for its successful use as a sacrificial MOF for preparing FeNC, while the Zn cations present in the ZIF-8 structure can be conveniently removed to a very large extent during pyrolysis, due to the low boiling point of zinc (907°C). The highly active FeNC catalyst derived from ZIF-8 and reported in Ref. [40] is however still strongly limited by mass-transport at high current density, as seem from the deviation from the Tafel law at the volumetric current of 10 A cm^{-3}*, i.e.* at the current density normalized per geometric area of cathode of *circa* 0.1 A cm^{-2}. The laboratory in which this PhD thesis was performed, ICGM-AIME, showed before the start of this PhD work that nano-sized MOFs are templated during pyrolysis in Ar into nano-sized FeNC catalytic particles, with improved local mass-transport properties.[51] Recent data from ICGM demonstrate that poor utilization of the active sites in thick FeNC layers is not intrinsic to this class of catalysts, but also applies to thick layers comprising ultralow contents of platinum nanoparticles. Unpublished results shown in Figure 8 demonstrate that Pt-based catalysts suffer from the same mass-transport limitations when Pt nanoparticles are deposited in low amounts (few wt %) on carbon black, simulating the low density of Fe-based active sites in FeNC materials. Comparing curves 1 and 2 in Figure 8, similar ORR activity at 0.85 V is observed due to identical Pt loadings (40 μg_{Pt} cm^{-2}) but the spatial dilution of Pt in the electrode corresponding to curve 2 (1% Pt/C) leads to a five-fold increase in electrode thickness and a dramatic decrease of current density at 0.5 V from 2.7 to 0.9 A cm^{-2}. Moreover, the polarization curve for our reference FeNC catalyst (Fe(II) acetate, phenanthroline

and ZIF-8, pyrolyzed in Ar at 1050°C) at a total loading of 4 mg cm^{-2} (curve 3) is similar to curve 2. In conclusion, Pt- and Fe-based sites lead to similar mass-transport limitation at high current if the volumetric ORR activity and thickness are similar for both electrodes.

Radically improving the electrode architecture with current FeNC materials to result in a dramatically enhanced power performance with 50-100 µm-thick electrodes was the starting point of the ANR project CAT^2CAT (From catalysts to cathodes: a controlled-architecture approach for PEMFC electrodes catalyzed by Earth-abundant metals) and for this PhD thesis. Dramatic improvement in performance at high current density might thus be reached with current FeNC materials if O_2 diffusion though the layer and also inside the individual catalytic particles is improved, while retaining high proton and electron conduction through the cathode active layer.

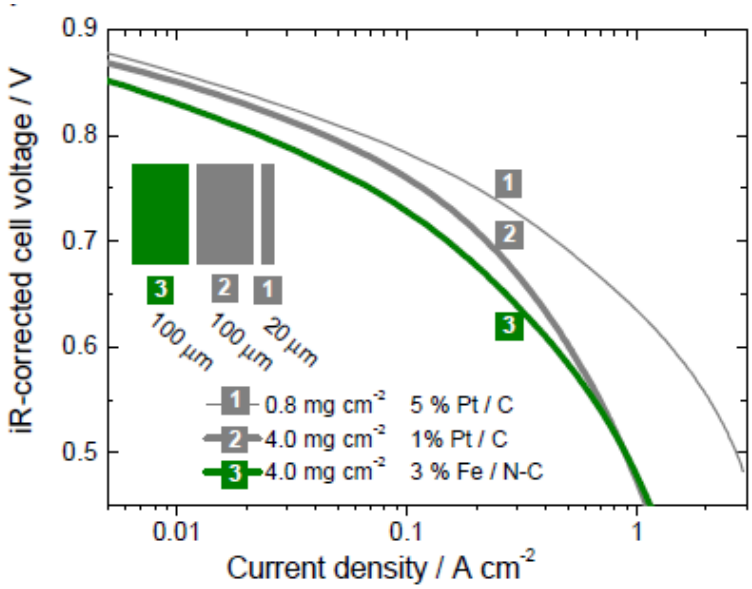

Figure 8. Experimental demonstration of mass-transport limitations; Curve 1: 5 wt % Pt on carbon black at total loading 0.8 mg_{Pt+C} cm^{-2} (40 μg_{Pt} cm^{-2}), Curve 2: 1 wt % Pt on carbon black at total loading 4.0 mg_{Pt+C} cm^{-2} (40 μg_{Pt} cm^{-2}), Curve 3: FeNC with 3 wt % Fe at total loading 4.0 mg_{Fe+N+C} cm^{-2}. Measured at 80°C, 1 bar gauge pressure, 100% RH, O_2 & H_2, 0.5 mg_{Pt} cm^{-2} at anode.

Previous approaches for controlling the architecture of PEMFC cathodes have involved for example 2D arrays of vertically-aligned multiwall carbon nanotubes (MWCNT), with active sites being either Pt particles,[52–54] nitrogen or FeN_x functional groups, [55,56]. Improved mass-transport of Pt-decorated

vertically-aligned MWCNT over classical ink derived cathodes was demonstrated, with increased current from 1.1 to 1.4 A cm^{-2} at 0.4 V in air. [53] Transfer of 2D arrays of aligned CNTs onto a membrane is however a risky step during MEA fabrication. Not only may the tube alignment and structure porosity be broken during the process, but protrusion of tubes into the thin membrane is a danger. This is especially true for the cathode thickness targeted for non-PGM catalysts (50-100 µm), thicker than the PEM membrane (20-25 µm).

Thus, while some works have demonstrated the correct operation in PEMFC of such 3D structures for Pt-based electrocatalysis, there is to date no convincing demonstration for non-PGM electrocatalysis of ordered cathode structures in PEMFC. The concept of ordered non-PGM cathode has till now been demonstrated only in liquid electrolyte and at very low current density,[55–57] which cannot show the benefit expected for a PEMFC where the diffusion of O_2 occurs via the gas phase.

The recent work by Liu's group on co-electrospun polymer and ZIF-8 has led to high power performance in O_2 but regular performance in air (2 bars O_2 or air, 80°C, 100% RH), 1.8 and 0.3 A cm^{-2} at 0.5 V, respectively.[58] The collapse of the structure after pyrolysis and non-self-standing nature of the electrode probably explains the poor air-performance. That work highlights however the great potential of this fabrication method but also the need for in-depth optimization and characterization, as proposed in this thesis project. Other recent works that resorted to electrospinning for synthesizing FeNC materials have led to catalytic powders. While some of the catalysts made by electrospinning have shown decent ORR activity in rotating-disk electrode at pH 1 or 13,[48,59–61] no other work has implemented such catalysts or structures in PEMFC, where mass-transport issues are critical in order to reach high power performance.

5. Application of electrospinning for the preparation of electrodes

The performance of electrodes in PEMFC depends on two main factors:

a) the density of active sites (sites per cm^3 of electrode), or active area (cm^2 per cm^3) where the electrochemical reaction occurs

b) the mass- and charge-transport of gas to and from the active sites across the porous electrode[62,63].

The design of porous and hollow nanostructures is important to obtain high surface areas, or micro or macroporous level and a high density of electrochemically-accessible active sites. Particularly, carbon is

exceedingly used as a support for fuel cells or active material due to its high electrical conductivity combined with low cost and sufficient stability in specific electrochemical potentials.

Carbon nanofibers (CNFs) are very promising materials for the fabrication of electrodes for fuel cells due to their high aspect ratio and the possibility to assemble CNFs in unique 3D web structures with high macropore volume between the fibers. In order to avoid slow Knudsen diffusion regime in gas-diffusion electrodes for fuel cells, high porosity within electrodes is critical.

A very efficient and upscalable approach to prepare a CNF network is via the electrospinning and carbonization of a polymer solution [64,65]. The electrospinning process can lead to mechanically stable fibrous electrodes and through-plane electric conductivity materials that can be used as free-standing electrodes, that was already proved by studies on supercapacitors [66–68], batteries[69,70], vanadium redox-flow [71], Li-O_2 batteries [72] and fuel cells [73–75].

This approach can maximize the macropore volume of the electrodes and also simplify the fabrication process. A standard electrospinning system is shown on Figure 9. During the process, the viscous polymer (e.g. polyacrylonitrile (PAN)) solution passes through the needle as a jet, resulting from the high voltage applied between the needle and the drum collector. When this high voltage is initially applied, the intensity of electric field increases and a droplet of polymer solution elongates under those forces to form a conical shaped, referred commonly as Taylor cone. After reaching a critical value, the cone emits a solution jet. Solvent evaporates during the flight of jet to the collector, and as result an ultra-thin polymer fiber is formed on the collector. By rotating the cylindrical drum collector and by horizontally moving the needle, a self-standing mat of polymer fibers can be obtained.

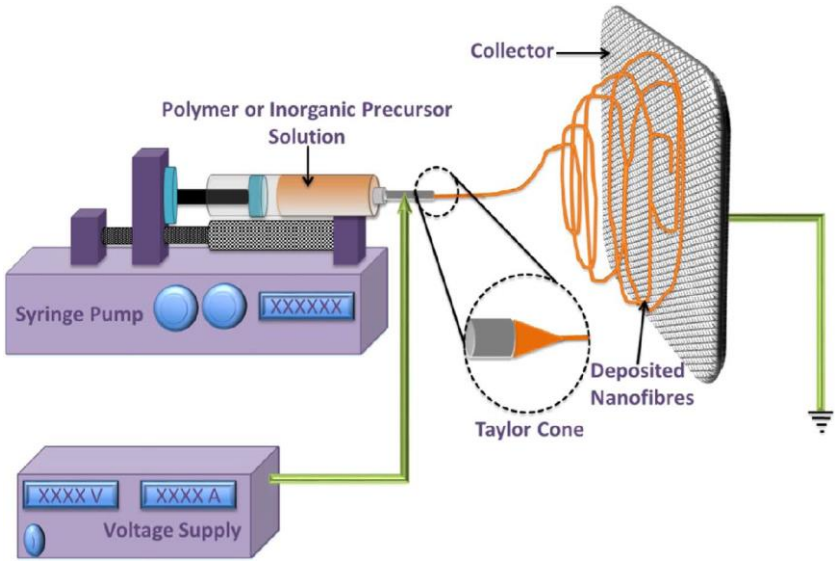

Figure 9: Graphical representation of the electrospinning process (reprinted from ref [76]).

The resulting fiber mat is subjected to at least one thermal treatment in order to be converted into a conductive CNF mat [77].

Different factors can influence the mechanical, electric and morphological properties of the CNF webs: the nature and molecular weight of the polymer precursor, the concentration of the latter in the electrospun solution, the nature of the solvent, environmental factors (humidity and temperature), process parameters (applied voltage, needle diameter, tip-target distance, pump rate etc) and the thermal treatment conditions applied to the polymer fiber mat.

In this work, the electrospinning technique has been used to prepare Fe- and N-doped carbon nanofibers derived from polymer fibrous precursor to be used as PEMFC non-platinum self-standing cathodes. The subsection below is a literature review of the application of the electrospinning to prepare CNFs as support of Pt nanoparticles for PEMFC application.

5.1 CNF supports for electrocatalysts derived from electrospun polymer fibers

PAN was used first to prepare CNFs via electrospinning in the 1990's. At present time, many other polymers have been used to prepare CNFs, such as polyvinylalcohol (PVA), polybenzimidazole (PBI), polyvinylidene fluoride (PVDF), polyacrylic acid (PAA), polyvinylpyrrolidone (PVP) and polyimide(PI)[78–82]. Although numerous research work has been done, PAN is still the most used polymer for

electrospinning because of the high carbon yield and high mechanical rigidity of CNFs obtained after the thermal treatment of PAN.

As mentioned above, every electrospun polymer nanofibers needs at least one thermal treatment (called carbonization) to obtain a conductive carbon fibrous structure. PAN needs an additional step in the process, usually called stabilization and which consists in a first step in air at a temperature of 150-280 °C, allowing a cyclisation of the initially non-aromatic polymeric structure (Figure 10). After this step, the stabilized PAN fibers undergo a thermal treatment at high temperature (> 900°C) in inert atmosphere in order to obtain partially planar sp^2 structure of carbon. The graphitization extent can be controlled by the temperature of pyrolysis, but usually the carbon is quite amorphous (similar to carbon black) up to temperatures of 1200°C.

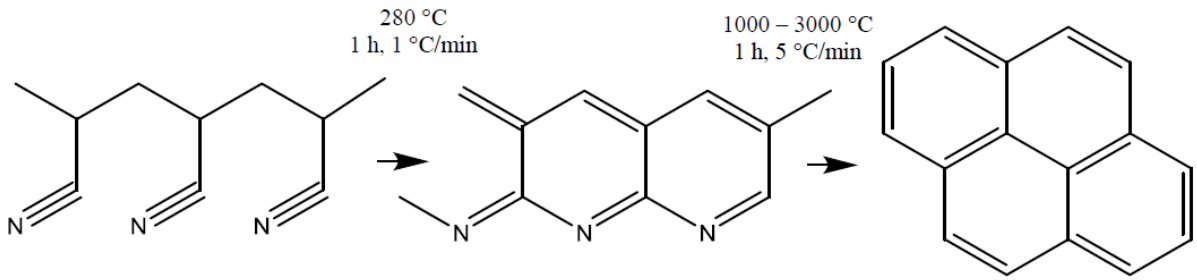

Figure 10: Polyacrylonitrile stabilization and carbonization process (reprinted from[83])

This intermediate stabilization step is not needed for other polymer precursor mats, however, this can affect the rigidity of the resulting CNF fibers and as consequence, their use as self-standing mats.

Another polymer precursor-derived CNFs that will be used in this work is cross-linked PBI. The chemical-cross-linking is widely used for example in the preparation of PBI-based polymer electrolyte membranes, in order to increase the mechanical strength and dimensional stability of PEMs. The use of a cross-linking agent is beneficial, as the resulting polymer precursor mat becomes more rigid and also insoluble in the majority of solvents. The cross-linking reaction can be triggered via the introduction of molecular cross-linkers in the polymers fibrous mat and the application of light, heat or pressure. [84] The cross-linking molecule can be introduced in the polymer solution before electrospinning [85–87] or used after the electrospinning via impregnation in liquid or vapor solution [88,89]. In this work, PBI was doped by α,α'-dichloro-p-xylene (DCX) in the electrospun solution and then cross-linked under 150° C in air , a methodology developed in the ICGM-AIME laboratory previously [90]. The cross-linking reaction is illustrated in Figure 11. Such reinforcement leads to resulting polymer mat being insoluble in DMAc and

DMF that can be beneficial for the further immersion in these solvents in order to prepare self-standing electrodes for the PEMFC.

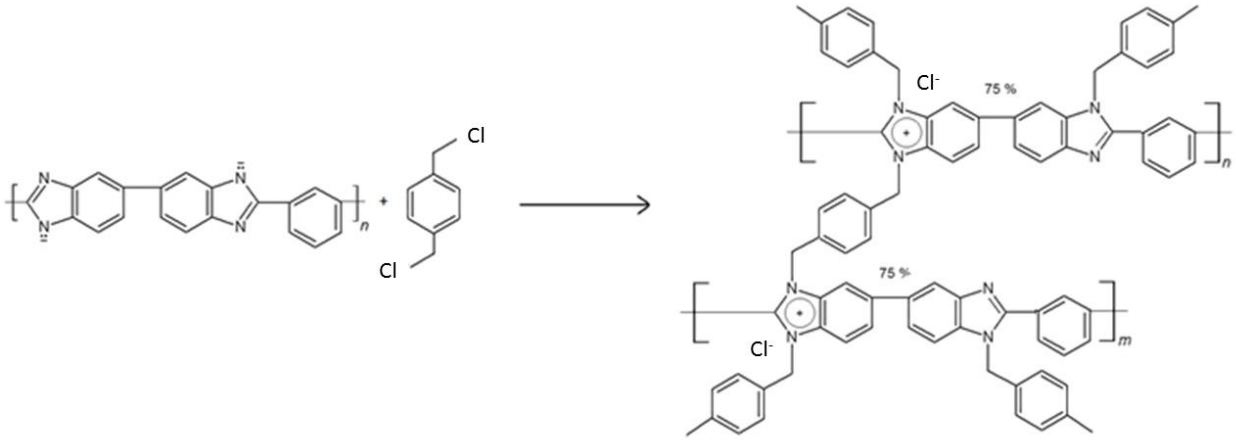

Figure 11: Graphical representation of the cross-linking of PBI by α,α'-dichloro-p-xylene agent (reprinted from [91])

The Pt-based catalytic sites can be introduced on CNFs with different methods. For example, pre-existing Pt/C catalyst powders were introduced in the electrospun solution, containing also a carrier polymer, leading to highly active nanofiber electrodes for fuel cells[92,93]. The main reason for using CNFs as support for electrocatalysts for fuel cell and other energy storage devices is increased macroporosity of the active layer, resulting from the highly anisotropic shape of CNFs. A secondary reason is the alleged improved corrosion resistance of CNFs over the regular carbon black supports. Some of previous works used CNFs as an alternative support for platinum nanoparticles [94,95].

5.2 Self-standing carbon nanofiber mats as electrocatalyst supports

Hitherto, the vast majority of the studies have not used the self-standing CNF mat derived from the electrospinning and pyrolysis process itself as an electrode support for Pt nanoparticles (or other active nanoparticles), but have first broken the self-standing mat by separating the CNFs. Self-standing electrospun CNF webs were however recently investigated in other energy storage devices than PEMFCs, such as supercapacitors and batteries[78,96,97]. A first step towards the preparation of self-standing electrodes for PEMFC was reported by our group in 2017[73]. In that work, ORR-active platinum particles were electrodeposited on CNF webs, in order to obtain active electrodes with tunable morphology. The

research was followed by Chan et al in 2018. That group deposited Pt nanoparticles on a PAN-derived self-standing CNF electrode structure, and reported interesting MEA performance in PEMFC [75,98].

One drawback of CNFs as a support for Pt nanoparticles but even more so for the integration of a high number of FeN_x sites (with the most active sites in FeNC catalysts being located in the micropores of the N-doped carbon support) is their usually low BET area, due to the lack of porosity inside the CNFs derived from a polymer fiber comprising a single polymer precursor. This internal porosity is important to increase the number of FeN_x active sites, but also to increase the reactant mass transfer from outside the CNFs to the sites located inside the micropores. In a nutshell, it is important to control both the macroporosity of the 3D electrode, but also the microporosity inside the CNFs. Microporosity might be introduced by the addition of organic or inorganic porogens inside the polymer fibers during the electrospinning process itself [65,72,99–102]. Typical porogens that have been used to prepare CNFs with high BET area are PMMA, PVP and Nafion itself (Figure 12). The use of such porogens with PAN has been reinvestigated in this PhD thesis (chapter 1). Alternatively, a 3D electrode structure with both macro- and microporosity can be prepared by using polymer fibers and MOF nanocrystals. It is known that the latter are transformed into highly microporous carbon domains during pyrolysis. Different approaches for the combination of polymer fibers and MOF nanocrystals were investigated in this PhD thesis (chapters 2 to 4).

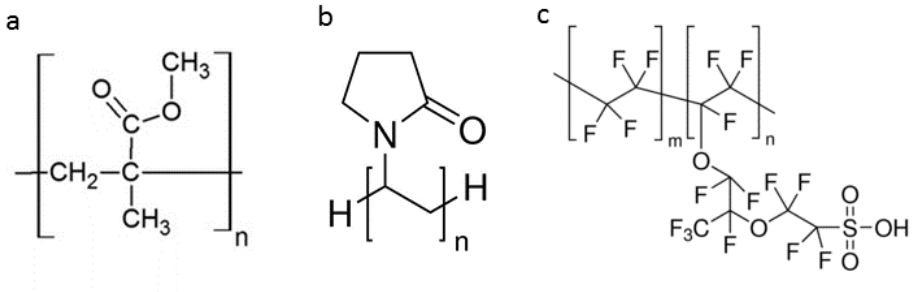

Figure 12: Possible organic porogens investigated in the literature in combination with PAN to prepare CNFs with internal porosity inside CNFs: a) PMMA, b) PVP and c) Nafion.

6 Objectives of the PhD thesis

The starting idea of the present PhD thesis work is that the fabrication of 50-100 µm thick cathodes with improved mass-transport properties and combined with reasonably high volumetric activities for a FeNC catalyst have the potential to significantly improve the power performance of FeNC cathodes under air operation, compared to the state-of-art. The PhD thesis project therefore leans on a paradigm shift

where it is realized that we do not necessarily need higher ORR activity (measured at 0.8-0.9 V vs. RHE, a region of potential at which the current density produced is only controlled by electrochemical kinetics) for FeNC catalysts but improved accessibility of their active sites, in order to increase the current density produced at operating fuel cell voltages of 0.5-0.6 V. Improved accessibility might be achieved with improved electrode structures.

Attempts to improve the architecture with high macroporosity and percolating paths for electrons and protons has therefore been studied in this PhD thesis work, resorting to the electrospinning technique to prepare self-standing FeNC electrodes. While the laboratory at which the PhD thesis has been carried out had already a long experience in the application of electrospinning for the preparation of proton exchange membranes, conductive metal-oxide fibers as durable supports for Pt particles [103,104] and PAN-derived CNF webs[105], however, the application of electrospinning for the preparation of self-standing FeNC electrodes (or even of FeNC powder catalysts) had not been studied at the laboratory before the start of this PhD thesis.

It is recognized that an ideal FeNC cathode should have a bimodal structure with micropores hosting active sites[19] and macropores allowing Fickian diffusion of O_2.[106] Combining these properties is difficult with the conventional approach for MEA fabrication, involving the preparation of catalytic ink from powder FeNC catalyst and a Nafion solution, then sprayed or deposited on a Nafion membrane or Gas diffusion layer (GDL). The objective was thus to develop an integrated approach of cathode fabrication that will move from the synthesis of FeNC catalyst powders based on metal-organic-frameworks (MOFs, ZIF-8 in particular) to the preparation of self-standing FeNC cathodes.

The main approaches involving electrospinning that have been studied in this PhD thesis to prepare self-standing FeNC cathodes are illustrated in Figure 13. Figure 13a depicts the one-pot approach whereby an Fe salt precursor was introduced in the polymer solution, electrospun and then pyrolyzed, leading to a self-standing CNF web with Fe-based active sites. Figure 13b shows a second approach, where a synthesis of Fe-doped MOFs was first developed, resorting to the encapsulation of ferrocene inside the cavities of zeolitic imidazolate frameworks during their formation. These ferrocene-doped ZIFs (ZIF-8 and SIM-1) were first studied separately from any electrospinning process, in order to optimize the ORR activity of FeNC powder catalysts derived from them by pyrolysis. Then, the optimized ferrocene-doped ZIFs were used in the context of the electrospinning process. Figure 13c and 13d illustrate how the ferrocene-doped ZIF nanocrystals were grown on electrospun polymer fiber webs. The latter were prepared from different

polymers (PAN and PBI) and functionalized or not with zinc, as seeds for the crystalline growth of the Zn-based ZIFs investigated in this work (ZIF-8 and SIM-1). Figure 13c shows the concept of growing ferrocene-doped nanocrystals on zinc-functionalized polymer fibers, while Figure 13d shows the concept of growing ferrocene-doped ZIFs on raw polymer fibers. The seeding of ferrocene-doped nano-MOFs on a preexisting 3D architecture of polymer fibers is a key step toward the preparation of self-standing FeNC cathodes. The pyrolysis of such an "electrode precursor" resulted into a FeNC cathode, that then further needs to be functionalized by a proton-conducting ionomer before testing in PEMFC.

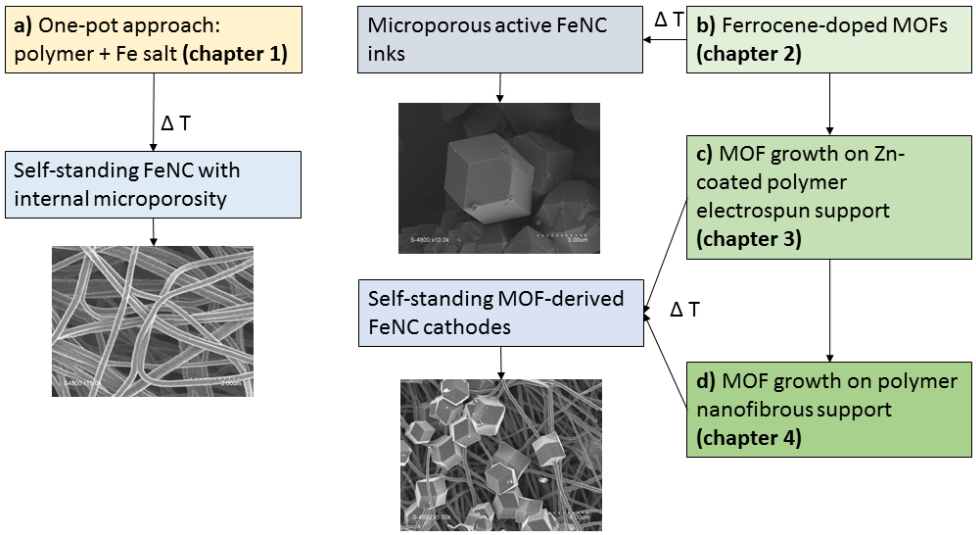

Figure 13: Scheme of the main approaches investigated in this PhD thesis for preparing self-standing FeNC cathodes: a) one-pot co-electrospinning of an Fe-salt precursor, a polymer and an additional porogen leading to self-standing FeNC electrodes with intra-fiber porosity after pyrolysis, b) intermediate study on the optimized encapsulation of ferrocene in the MOF cavities during ZIF crystallization, leading to ORR-active FeNC powder catalysts after pyrolysis, c) application of approach b) to prepare self-standing FeNC cathodes by the growth of ferrocene-doped ZIFs on a zinc-functionalized polymer fibrous web (PAN), leading to self-standing FeNC electrodes after pyrolysis, d) application of approach b) to prepare self-standing FeNC cathodes by the growth of ferrocene-doped ZIFs on raw polymer fibrous web (PAN or cross-linked PBI), leading to self-standing FeNC electrodes after pyrolysis.

During the PhD thesis, performed in the frame of the ANR project CAT^{2}CAT, the synthesis of ZIFs with controlled size & shape grown on various surfaces was studied by IRCELYON (specialist in MOF synthesis on various substrates, including carbon) while the preparation of self-standing 3D FeNC electrodes and their testing in RDE and PEMFC were developed at ICGM-AIME.

The first approach described in chapter 1 was dedicated to the preparation of CNFs with internal microporosity, obtained by co-electrospinning of PAN with a porogen agent (organic or inorganic). The fibers were pyrolyzed in argon at 1000 °C and then subjected to ammonia activation at 900 °C. The resulting fibers with highest internal microporosity were down-selected for the preparation of FeNC electrodes. The latter were prepared via electrospinning PAN, two down-selected porogens and three different Fe salts, and pyrolyzed in argon at 1000 °C and ammonia activated at 900 °C. Those electrodes were electrochemically characterized in RDE.

Chapter 2 was a first step toward the goal of the second approach of the thesis work and was done in collaboration with IRCELYON and LEPMI. The MOFs was firstly synthesized by IRCELYON, and then pyrolyzed and characterized at ICGM-AIME. The electrochemical activity in ORR of resulting catalysts was also verified by LEPMI laboratory in Grenoble, the third partner of the CAT^{2}CAT project.

Chapter 3 was also a result of collaboration between IRCELYON and ICGM-AIME. The self-standing electrodes were prepared via the growth of ferrocene-doped SIM-1 on different polymer mats. Also the effect of Zn-coating for MOF growth was investigated in this chapter.

The last chapter was dedicated to the design and optimization of self-standing FeNC electrodes prepared by the growth of ferrocene-doped SIM-1 and ZIF-8 on different polymer mats, prepared by electrospinning and this work was fully done by ICGM-AIME laboratory with a collaboration with master 2 student Alexandre Heitz.

1. IEA, “Fuel shares in OECD total primary energy supply, 2018”, IEA, P. https://www. iea. org/data-and-statistics/charts/fuel-shares-in-oecd-total-primary-energy-suppl.-2018 No Title.

2. Debe, M.K. Electrocatalyst approaches and challenges for automotive fuel cells. *Nature* **2012**, *486*, 43–51.

3. Carter, D.; Wing, J. The Fuel Cell Industry Review 2018. **2018**, 1–50.

4. Fuel Cells and Hydrogen 2 Joint Undertaking *Hydrogen Roadmap Europe - A Sustainable Pathway for the European Energy Transition*; 2019;

5. Carmo, M.; Fritz, D.L.; Mergel, J.; Stolten, D. A comprehensive review on PEM water electrolysis. *Int. J. Hydrogen Energy* **2013**, *38*, 4901–4934.

6. Feng, Q.; Yuan, X.Z.; Liu, G.; Wei, B.; Zhang, Z.; Li, H.; Wang, H. A review of proton exchange membrane water electrolysis on degradation mechanisms and mitigation strategies. *J. Power Sources* **2017**, *366*, 33–55.

7. Andújar, J.M.; Segura, F. Fuel cells: History and updating. A walk along two centuries. *Renew. Sustain. Energy Rev.* **2009**, *13*, 2309–2322.

8. Carrette, L.; Friedrich, K.A.; Stimming, U. Fuel Cells: Principles, Types, Fuels, and Applications. *ChemPhysChem* **2000**, *1*, 162–193.

9. David Hart, Franz Lehner, Stuart Jones, Jonathan Lewis, M.K. The Fuel Cell Industry Review 2017. *E4tech* **2017**, 49.

10. Https://global.toyota/en/newsroom/corporate/22647198.html No Title. **2018**.

11. Wang, G.; Yu, Y.; Liu, H.; Gong, C.; Wen, S.; Wang, X.; Tu, Z. Progress on design and development of polymer electrolyte membrane fuel cell systems for vehicle applications: A review. *Fuel Process. Technol.* **2018**, *179*, 203–228.

12. Wilkinson, D.; Zhang, J.; Hui, R.; Fergus, J.; Li, X. Proton exchange membrane fuel cells: materials properties and performance. **2009**.

13. Generation, E. Engineered Nanomaterials for Energy Applications. *Handb. Nanomater. Ind. Appl.* **2018**, 751–767.

14. Pfrang, A. No Title. *GIT Lab. J. Eur.* **2009**, *13*, 42–44.

15. Ito, H.; Maeda, T.; Nakano, A.; Takenaka, H. Properties of Nafion membranes under PEM water electrolysis conditions. *Int. J. Hydrogen Energy* **2011**, *36*, 10527–10540.

16. Barbir, F. *Fuel Cell Electrochemistry*; 2013; ISBN 9780123877109.

17. O'Hayre, R.; Barnett, D.; Prinz, F. The triple phase boundary a mathematical model and experimental investigations for fuel cells. *J. Electrochem. …* **2005**, *152*, A439–A444.

18. Mathias, M.F.; Makharia, R.; Gasteiger, H.A.; Conley, J.J.; Fuller, T.J.; Gittleman, C.J.; Kocha, S.S.; Miller, D.P.; Mittelsteadt, C.K.; Xie, T.; et al. Two fuel cell cars in every garage? *Electrochem. Soc. Interface* **2005**, *14*, 24–35.

19. Lefèvre, M.; Proietti, E.; Jaouen, F.; Dodelet, J.P. Iron-Based catalysts with improved oxygen reduction activity in polymer electrolyte fuel cells. *Science (80-.).* **2009**, *324*, 71–74.

20. Nørskov, J.K.; Rossmeisl, J.; Logadottir, A.; Lindqvist, L.; Kitchin, J.R.; Bligaard, T.; Jónsson, H. Origin of the overpotential for oxygen reduction at a fuel-cell cathode. *J. Phys. Chem. B* **2004**, *108*, 17886–17892.

21. Https://www.energy.gov/eere/fuelcells/doe-technical-targets-polymer-electrolyte-membrane-fuel-cell-components DOE Technical Targets for Polymer Electrolyte Membrane Fuel Cell Components.

22. Adzic, R.R.; Zhang, J.; Sasaki, K.; Vukmirovic, M.B.; Shao, M.; Wang, J.X.; Nilekar, A.U.; Mavrikakis, M.; Valerio, J.A.; Uribe, F. Platinum monolayer fuel cell electrocatalysts. *Top. Catal.* **2007**, *46*, 249–262.

23. Shao, M.; Chang, Q.; Dodelet, J.P.; Chenitz, R. Recent Advances in Electrocatalysts for Oxygen Reduction Reaction. *Chem. Rev.* **2016**, *116*, 3594–3657.

24. Stamenkovic, V.R.; Fowler, B.; Mun, B.S.; Wang, G.; Ross, P.N.; Lucas, C.A.; Markovic, N.M. Improved oxygen reduction activity on Pt3Ni(111) via increased surface site availability. *Science (80-.).* **2007**, *315*, 493–497.

25. Stamenkovic, V.R.; Mun, B.S.; Arenz, M.; Mayrhofer, K.J.J.; Lucas, C.A.; Wang, G.; Ross, P.N.; Markovic, N.M. Trends in electrocatalysis on extended and nanoscale Pt-bimetallic alloy surfaces. *Nat. Mater.* **2007**, *6*, 241–247.

26. Wang, J.; Li, B.; Yersak, T.; Yang, D.; Xiao, Q.; Zhang, J.; Zhang, C. Recent advances in Pt-based

octahedral nanocrystals as high performance fuel cell catalysts. *J. Mater. Chem. A* **2016**, *4*, 11559–11581.

27. Escudero-Escribano, M.; Malacrida, P.; Hansen, H.M.; Vej-Hansen, U.; Velazquez-Palenzuela, A.; Tripkovic, V.; Schiøtz, J.; Rossmeisl, J.; Stephens, I.E.L.; Chorkendorff, I. Tuning the activity of Pt alloy electrocatalysts by means of the lanthanide contraction. *Science (80-.).* **2016**, *352*, 73–76.

28. Brouzgou, A.; Song, S.Q.; Tsiakaras, P. Low and non-platinum electrocatalysts for PEMFCs: Current status, challenges and prospects. *Appl. Catal. B Environ.* **2012**, *127*, 371–388.

29. Kongkanand, A.; Gu, W.; Mathias, M.F. Fuel Cells and Hydrogen Production. *Fuel Cells Hydrog. Prod.* **2019**.

30. Sui, S.; Wang, X.; Zhou, X.; Su, Y.; Riffat, S.; Liu, C. jun A comprehensive review of Pt electrocatalysts for the oxygen reduction reaction: Nanostructure, activity, mechanism and carbon support in PEM fuel cells. *J. Mater. Chem. A* **2017**, *5*, 1808–1825.

31. Cawthorn, R.G. The platinum group element deposits of the bushveld complex in South Africa. *Platin. Met. Rev.* **2010**, *54*, 205–215.

32. Gordon, R.B.; Bertram, M.; Graedel, T.E. Metal stocks and sustainability. *Proc. Natl. Acad. Sci.* **2006**, *103*, 1209–1214.

33. Armaroli, N.; Balzani, V. The future of energy supply: Challenges and opportunities. *Angew. Chemie - Int. Ed.* **2007**, *46*, 52–66.

34. Gasteiger, H.A.; Kocha, S.S.; Sompalli, B.; Wagner, F.T. Activity benchmarks and requirements for Pt, Pt-alloy, and non-Pt oxygen reduction catalysts for PEMFCs. *Appl. Catal. B Environ.* **2005**, *56*, 9–35.

35. Jasinski, R. Cobalt Phthalocyanine as a Fuel Cell Cathode. *J. Electrochem. Soc.* **1965**, *112*, 526–528.

36. Jahnke, H.; Schönborn, M.; Zimmermann, G. Organic dyestuffs as catalysts for fuel cells. *Top. Curr. Chem.* **1976**, *61*, 133–181.

37. Lefèvre, M.; Proietti, E.; Jaouen, F.; Dodelet, J.P. Iron-Based catalysts with improved oxygen reduction activity in polymer electrolyte fuel cells. *Science (80-.).* **2009**, *324*, 71–74.

38. Zitolo, A.; Goellner, V.; Armel, V.; Sougrati, M.-T.; Mineva, T.; Stievano, L.; Fonda, E.; Jaouen, F.

Identification of catalytic sites for oxygen reduction in iron- and nitrogen-doped graphene materials. *Nat. Mater.* **2015**, *14*, 937–942.

39. Jaouen, F.; Proietti, E.; Lefèvre, M.; Chenitz, R.; Dodelet, J.P.; Wu, G.; Chung, H.T.; Johnston, C.M.; Zelenay, P. Recent advances in non-precious metal catalysis for oxygen-reduction reaction in polymer electrolyte fuel cells. *Energy Environ. Sci.* **2011**, *4*, 114–130.

40. Proietti, E.; Jaouen, F.; Lefèvre, M.; Larouche, N.; Tian, J.; Herranz, J.; Dodelet, J.P. Iron-based cathode catalyst with enhanced power density in polymer electrolyte membrane fuel cells. *Nat. Commun.* **2011**, *2*.

41. Wu, G.; More, K.L.; Johnston, C.M.; Zelenay, P. High-performance electrocatalysts for oxygen reduction derived from polyaniline, iron, and cobalt. *Science (80-.).* **2011**, *332*, 443–447.

42. Chen, Z.; Higgins, D.; Yu, A.; Zhang, L.; Zhang, J. A review on non-precious metal electrocatalysts for PEM fuel cells. *Energy Environ. Sci.* **2011**, *4*, 3167–3192.

43. Jaouen, F.; Lefèvre, M.; Dodelet, J.P.; Cai, M. Heat-treated Fe/N/C catalysts for O2 electroreduction: Are active sites hosted in micropores? *J. Phys. Chem. B* **2006**, *110*, 5553–5558.

44. Jaouen, F.; Charreteur, F.; Dodelet, J.P. Fe-based catalysts for oxygen reduction in PEMFCs. *J. Electrochem. Soc.* **2006**, *153*.

45. Tian, J.; Morozan, A.; Sougrati, M.T.; Lefèvre, M.; Chenitz, R.; Dodelet, J.P.; Jones, D.; Jaouen, F. Optimized synthesis of Fe/N/C cathode catalysts for PEM fuel cells: A mater of iron-ligand coordination strength. *Angew. Chemie - Int. Ed.* **2013**, *52*, 6867–6870.

46. http://energy.gov/eere/fuelcells/downloads/fuel-cell-technologies-officemulti- year-research-development-and-22.

47. Larouche, N.; Chenitz, R.; Lefèvre, M.; Proietti, E.; Dodelet, J.P. Activity and stability in proton exchange membrane fuel cells of iron-based cathode catalysts synthesized with addition of carbon fibers. *Electrochim. Acta* **2014**, *115*, 170–182.

48. Wu, N.; Wang, Y.; Lei, Y.; Wang, B.; Han, C.; Gou, Y.; Shi, Q.; Fang, D. Electrospun interconnected Fe-N/C nanofiber networks as efficient electrocatalysts for oxygen reduction reaction in acidic media. *Sci. Rep.* **2015**, *5*, 1–9.

49. Choi, J.Y.; Higgins, D.; Chen, Z. Highly durable graphene nanosheet supported iron catalyst for

oxygen reduction reaction in PEM fuel cells. *J. Electrochem. Soc.* **2012**, *159*, 2012–2015.

50. Ma, S.; Goenaga, G.A.; Call, A. V.; Liu, D.J. Cobalt imidazolate framework as precursor for oxygen reduction reaction electrocatalysts. *Chem. - A Eur. J.* **2011**, *17*, 2063–2067.

51. Armel, V.; Hannauer, J.; Jaouen, F. Effect of ZIF-8 crystal size on the O<inf>2</inf> electro-reduction performance of pyrolyzed Fe–N–C catalysts. *Catalysts* **2015**, *5*, 1333–1351.

52. Yuan, Y.; Smith, J.A.; Goenaga, G.; Liu, D.J.; Luo, Z.; Liu, J. Platinum decorated aligned carbon nanotubes: Electrocatalyst for improved performance of proton exchange membrane fuel cells. *J. Power Sources* **2011**, *196*, 6160–6167.

53. Liu, D.J.; Yang, J.; Kariuki, N.; Goenaga, G.; Call, A.; Myers, D. Performance improvement in PEMFC using aligned carbon nanotubes as electrode catalyst SUPPORT. *ECS Trans.* **2008**, *16*, 1123–1129.

54. Ruvinskiy, P.S.; Bonnefont, A.; Houllé, M.; Pham-Huu, C.; Savinova, E.R. Preparation, testing and modeling of three-dimensionally ordered catalytic layers for electrocatalysis of fuel cell reactions. *Electrochim. Acta* **2010**, *55*, 3245–3256.

55. Yang, J.; Liu, D.J.; Kariuki, N.N.; Chen, L.X. Aligned carbon nanotubes with built-in FeN4 active sites for electrocatalytic reduction of oxygen. *Chem. Commun.* **2008**, *3*, 329–331.

56. Mo, Z.; Liao, S.; Zheng, Y.; Fu, Z. Preparation of nitrogen-doped carbon nanotube arrays and their catalysis towards cathodic oxygen reduction in acidic and alkaline media. *Carbon N. Y.* **2012**, *50*, 2620–2627.

57. Gong, K.; Du, F.; Xia, Z.; Durstock, M.; Dai, L. Nitrogen-doped carbon nanotube arrays with high electrocatalytic activity for oxygen reduction. *Science (80-.).* **2009**, *323*, 760–764.

58. Shui, J.; Chen, C.; Grabstanowicz, L.; Zhao, D.; Liu, D.J. Highly efficient nonprecious metal catalyst prepared with metal-organic framework in a continuous carbon nanofibrous network. *Proc. Natl. Acad. Sci. U. S. A.* **2015**, *112*, 10629–10634.

59. Shin, D.; Jeong, B.; Mun, B.S.; Jeon, H.; Shin, H.J.; Baik, J.; Lee, J. On the origin of electrocatalytic oxygen reduction reaction on electrospun nitrogen-carbon species. *J. Phys. Chem. C* **2013**, *117*, 11619–11624.

60. Yan, X.; Gan, L.; Lin, Y.C.; Bai, L.; Wang, T.; Wang, X.; Luo, J.; Zhu, J. Controllable synthesis and enhanced electrocatalysis of iron-based catalysts derived from electrospun nanofibers. *Small*

2014, *10*, 4072–4079.

61. Qiu, Y.; Yu, J.; Wu, W.; Yin, J.; Bai, X. Fe-N/C nanofiber electrocatalysts with improved activity and stability for oxygen reduction in alkaline and acid solutions. *J. Solid State Electrochem.* **2013**, *17*, 565–573.

62. Aricò, A.S.; Bruce, P.; Scrosati, B.; Tarascon, J.-M.; van Schalkwijk, W. Nanostructured materials for advanced energy conversion and storage devices. *Nat. Mater.* **2005**, *4*, 366–77.

63. Du, L.; Shao, Y.; Sun, J.; Yin, G.; Liu, J.; Wang, Y. Advanced catalyst supports for PEM fuel cell cathodes. *Nano Energy* **2016**, *29*, 314–322.

64. Cavaliere, S.; Subianto, S.; Savych, I.; Jones, D.J.; Rozière, J. Electrospinning: designed architectures for energy conversion and storage devices. *Energy Environ. Sci.* **2011**, *4*, 4761.

65. Peng, S.; Li, L.; Kong Yoong, J.L.; Tian, L.; Srinivasan, M.; Adams, S.; Ramakrishna, S. Electrospun carbon nanofibers and their hybrid composites as advanced materials for energy conversion and storage. *Nano Energy* **2016**.

66. Li, X.; Zhao, Y.; Bai, Y.; Zhao, X.; Wang, R.; Huang, Y.; Liang, Q.; Huang, Z. A Non-Woven Network of Porous Nitrogen-doping Carbon Nanofibers as a Binder-free Electrode for Supercapacitors. *Electrochim. Acta* **2017**, *230*, 445–453.

67. Gopalakrishnan, A.; Sahatiya, P.; Badhulika, S. Template-Assisted Electrospinning of Bubbled Carbon Nanofibers as Binder-Free Electrodes for High-Performance Supercapacitors. *ChemElectroChem* **2018**, *5*, 531–539.

68. Liu, D.; Zhang, X.; Sun, Z.; You, T. Free-standing nitrogen-doped carbon nanofiber films as highly efficient electrocatalysts for oxygen reduction. *Nanoscale* **2013**, *5*, 9528–31.

69. Liu, Y.; Fan, L.Z.; Jiao, L. Graphene highly scattered in porous carbon nanofibers: A binder-free and high-performance anode for sodium-ion batteries. *J. Mater. Chem. A* **2017**, *5*, 1698–1705.

70. Peng, Y.; Lo, C. Electrospun porous carbon nanofibers as lithium ion battery anodes. *J. Solid State Electrochem.* **2015**, *19*, 3401–3410.

71. Sun, J.; Zeng, L.; Jiang, H.R.; Chao, C.Y.H.; Zhao, T.S. Formation of electrodes by self-assembling porous carbon fibers into bundles for vanadium redox flow batteries. *J. Power Sources* **2018**, *405*, 106–113.

72. Cao, Y.; Lu, H.; Hong, Q.; Bai, J.; Wang, J.; Li, X. Co decorated N-doped porous carbon nanofibers as a free-standing cathode for Li-O2 battery: Emphasis on seamlessly continuously hierarchical 3D nano-architecture networks. *J. Power Sources* **2017**, *368*, 78–87.

73. Ercolano, G.; Farina, F.; Cavaliere, S.; Jones, D.J.; Rozière, J. Towards ultrathin Pt films on nanofibres by surface-limited electrodeposition for electrocatalytic applications. *J. Mater. Chem. A* **2017**, *5*, 3974–3980.

74. Kayarkatte, M.K.; Delikaya, Ö.; Roth, C. Freestanding Catalyst Layers: A Novel Electrode Fabrication Technique for PEM Fuel Cells via Electrospinning. *ChemElectroChem* **2017**, *4*, 404–411.

75. Chan, S.; Jankovic, J.; Susac, D.; Saha, M.S.; Tam, M.; Yang, H.; Ko, F. Electrospun carbon nanofiber catalyst layers for polymer electrolyte membrane fuel cells: Structure and performance. *J. Power Sources* **2018**, *392*, 239–250.

76. Sood, R.; Cavaliere, S.; Jones, D.J.; Rozière, J. Electrospun nanofibre composite polymer electrolyte fuel cell and electrolysis membranes. *Nano Energy* **2016**, *26*, 729–745.

77. Liu, C.-K.; Lai, K.; Liu, W.; Yao, M.; Sun, R.-J. Preparation of carbon nanofibres through electrospinning and thermal treatment. *Polym. Int.* **2009**, *58*, 1341–1349.

78. Inagaki, M.; Yang, Y.; Kang, F. Carbon Nanofibers Prepared via Electrospinning. *Adv. Mater.* **2012**, *24*, 2547–2566.

79. Zou, L.; Gan, L.; Lv, R.; Wang, M.; Huang, Z.H.; Kang, F.; Shen, W. A film of porous carbon nanofibers that contain Sn/SnOx nanoparticles in the pores and its electrochemical performance as an anode material for lithium ion batteries. *Carbon N. Y.* **2011**, *49*, 89–95.

80. Kim, B.-H.; Wazir, A.H.; Yang, K.-S.; Bang, Y.-H.; Kim, S.-R. Molecular structure effects of the pitches on preparation of activated carbon fibers from electrospinning. *Carbon Lett.* **2011**, *12*, 70–80.

81. Kim, C.; Choi, Y.O.; Lee, W.J.; Yang, K.S. Supercapacitor performances of activated carbon fiber webs prepared by electrospinning of PMDA-ODA poly(amic acid) solutions. *Electrochim. Acta* **2004**, *50*, 883–887.

82. Chung, G.S.; Jo, S.M.; Kim, B.C. Properties of carbon nanofibers prepared from electrospun polyimide. *J. Appl. Polym. Sci.* **2005**, *97*, 165–170.

83. Kulesza, M.P.; Recherche, D. De; Knauth, M.P. Délivré par l ' Université Montpellier 2 Sciences et Techniques du Languedoc Préparée au sein de l ' école doctorale Sciences Chimiques Balard Et de l ' unité de recherche UMR5253 Spécialité : Chimie et Physicochimie des Matériaux Présentée par Iuliia SAVYCH MACIEJASZ SYNTHESE ET CARACTERISATION DE NANOCOMPOSITES PLATINE / NANOFIBRES POUR ELECTRODES DE PILES A COMBUSTIBLE. **2014**.

84. Subianto, S.; Pica, M.; Casciola, M.; Cojocaru, P.; Merlo, L.; Hards, G.; Jones, D.J. Physical and chemical modification routes leading to improved mechanical properties of perfluorosulfonic acid membranes for PEM fuel cells. *J. Power Sources* **2013**, *233*, 216–230.

85. Mollá, S.; Compañ, V. Performance of composite Nafion/PVA membranes for direct methanol fuel cells. *J. Power Sources* **2011**, *196*, 2699–2708.

86. Lin, H.-L.; Wang, S.-H. Nafion/poly(vinyl alcohol) nano-fiber composite and Nafion/poly(vinyl alcohol) blend membranes for direct methanol fuel cells. *J. Memb. Sci.* **2014**, *452*, 253–262.

87. Mollá, S.; Compañ, V. Nanocomposite SPEEK-based membranes for Direct Methanol Fuel Cells at intermediate temperatures. *J. Memb. Sci.* **2015**, *492*, 123–136.

88. Quartarone, E.; Mustarelli, P. Polymer fuel cells based on polybenzimidazole/H3PO4. *Energy Environ. Sci.* **2012**, *5*, 6436.

89. Mollà, S.; Compan, V. Polyvinyl alcohol nanofiber reinforced Nafion membranes for fuel cell applications. *J. Memb. Sci.* **2011**, *372*, 191–200.

90. Li, H.-Y.; Liu, Y.-L. Polyelectrolyte composite membranes of polybenzimidazole and crosslinked polybenzimidazole-polybenzoxazine electrospun nanofibers for proton exchange membrane fuel cells. *J. Mater. Chem. A* **2013**, *1*, 1171–1178.

91. Kreisz, A. PhD thesis, University of Montpellier II, 2016.

92. Zhang, W.; Pintauro, P.N. High-performance nanofiber fuel cell electrodes. *ChemSusChem* **2011**, *4*, 1753–1757.

93. Waldrop, K.; Slack, J.; Gumeci, C.; Dale, N.; Reeves, K.S.; Cullen, D.A.; More, K.L.; Pintauro, P.N. Electrospun Particle/Polymer Fiber Electrodes with a Neat Nafion Binder for Hydrogen/Air Fuel Cells. *ECS Trans.* **2019**, *92*, 595–602.

94. Park, J.H.; Ju, Y.W.; Park, S.H.; Jung, H.R.; Yang, K.S.; Lee, W.J. Effects of electrospun

polyacrylonitrile-based carbon nanofibers as catalyst support in PEMFC. *J. Appl. Electrochem.* **2009**, *39*, 1229–1236.

95. Wang, Y.; Jin, J.; Yang, S.; Li, G.; Qiao, J. Highly active and stable platinum catalyst supported on porous carbon nanofibers for improved performance of PEMFC. *Electrochim. Acta* **2015**, *177*, 181–189.

96. Lu, X.; Wang, C.; Favier, F.; Pinna, N. Electrospun Nanomaterials for Supercapacitor Electrodes: Designed Architectures and Electrochemical Performance. *Adv. Energy Mater.* **2017**, *7*, 1–43.

97. Subianto, S.; Cornu, D.; Cavaliere, S. Fundamentals of Electrospinning. In *Electrospinning for Advanced Energy and Environmental Applications*; Cavaliere, S., Ed.; Boca Raton, 2015; pp. 1–27 ISBN 978-1-4822-1767-4.

98. Chan, S., Jankovic, J., Susac, D. et al. Electrospun carbon nanofiber catalyst layers for polymer electrolyte membrane fuel cells: fabrication and optimization. *J Mater Sci* **2018**, *53*, 11633–11647.

99. An, G.-H.; Koo, B.-R.; Ahn, H.-J. Activated mesoporous carbon nanofibers fabricated using water etching-assisted templating for high-performance electrochemical capacitors. *Phys. Chem. Chem. Phys.* **2016**, *18*, 6587–6594.

100. He, T.; Fu, Y.; Meng, X.; Yu, X.; Wang, X. A novel strategy for the high performance supercapacitor based on polyacrylonitrile-derived porous nanofibers as electrode and separator in ionic liquid electrolyte. *Electrochim. Acta* **2018**, *282*, 97–104.

101. Tran, C.; Kalra, V. Fabrication of porous carbon nanofibers with adjustable pore sizes as electrodes for supercapacitors. *J. Power Sources* **2013**, *235*, 289–296.

102. Liu, J.; Xiong, Z.; Wang, S.; Cai, W.; Yang, J.; Zhang, H. Structure and electrochemistry comparison of electrospun porous carbon nanofibers for capacitive deionization. *Electrochim. Acta* **2016**, *210*, 171–180.

103. Savych, I.; Bernard D'Arbigny, J.; Subianto, S.; Cavaliere, S.; Jones, D.J.; Rozière, J. On the effect of non-carbon nanostructured supports on the stability of Pt nanoparticles during voltage cycling: A study of TiO2 nanofibres. *J. Power Sources* **2014**, *257*, 147–155.

104. Savych, I.; Subianto, S.; Nabil, Y.; Cavaliere, S.; Jones, D.; Rozière, J. Negligible degradation upon in situ voltage cycling of a PEMFC using an electrospun niobium-doped tin oxide supported Pt

cathode. *Phys. Chem. Chem. Phys.* **2015**, *17*, 16970–16976.

105. Ercolano, G.; Farina, F.; Cavaliere, S.; Jones, D.J.; Rozière, J. Nickel based electrospun materials with tuned morphology and composition. *Nanomaterials* **2016**, *6*, 1–12.

106. Chen, L.; Wu, G.; Holby, E.F.; Zelenay, P.; Tao, W.Q.; Kang, Q. Lattice boltzmann pore-scale investigation of coupled physical-electrochemical processes in C/PT and non-precious metal cathode catalyst layers in proton exchange membrane fuel cells. *Electrochim. Acta* **2015**, *158*, 175–186.

Chapter 1: Self-standing electrodes prepared by “one-pot” approach

Table of content

1.1 Introduction

In this chapter, the first objective was the formation of self-standing CNF webs with intra-fiber porosity. Intra-fiber porosity is necessary to form a high number of Fe-based ORR active sites when a Fe precursor is added. The addition of Fe salt to the electrospinning solution was studied in a second step, only after the identification of synthetic approaches leading to porous CNFs. The CNFs were derived from electrospun PAN, resorting either to pre-synthetic and/or post-synthetic approaches in order to create porosity inside the fibers. PAN was selected for its relatively high melting point, high carbon yield and facility to be electrospun [1]. For the pre-synthetic approach, various hard ($ZnCl_2$) and soft templating agents (PMMA, PVP, Nafion®) were co-electrospun with PAN. For the post-synthetic approach, NH_3 pyrolysis was applied to CNF webs derived from electrospun porogen-PAN solutions. The resulting CNF webs were characterized for their properties relevant for electrochemical applications, including not only mass-specific surface area and porosity but also morphology, structure, composition, and electrical conductivity.

Then, the most interesting approaches leading to CNF webs with intra-fiber porosity were applied to prepare self-standing FeNC cathodes via one-pot approach, simply by incorporating an optimized amount of Fe salt in addition to the other precursors in the electrospinning solution. The resulting self-standing electrodes were electrochemically characterized in a RDE setup.

Two main strategies have been investigated previously to prepare porous carbon fibers by electrospinning, one in which a porogen is introduced in the electrospinning solution and which results in biphasic polymer-porogen fibers, and another in which the plain CNFs are subjected after their synthesis to a reactive chemical (gas or solid). In the former case (labelled pre-synthesis), the carbonization of the biphasic polymer fibers leads to the selective removal of the porogen during the temperature ramp-up, resulting in CNFs having either a closed or open porosity. In the second case (labelled post-synthesis), the selective etching of less-organized carbon domains in the CNFs by the reactive chemical may result in the formation of open pores from the outer surface of CNFs and inwards. However, if the carbon structure of the CNF is homogeneous, the reactive etching may simply result in a thinning of the CNF, without the creation of internal porosity.

For the pre-synthetic approach, the electrospinning technique allows introducing various porogens in the polymer precursor solution, whereby the porogen acts as a hard or soft template during the

subsequent carbonization step. Most studied hard templates for preparing CNFs are preformed nanoparticles or nanostructures (silica [2,3], nano-$CaCO_3$ [4]) that generate porosity upon their removal with chemical or/and thermal treatment. The hard template approach allows control of the size and morphology of the pores while minimizing undesired chemical reactions between the template and the carbon structure [5]. Hard templates can also form during the carbonization treatment itself, as is the case when introducing metal salts (e.g. $Co(NO_3)_2$ $6H_2O$, $(Ni(CH_3COO)_2$, $ZnCl_2$) in the electrospun polymer solution. The transition metal salt form metallic or metal oxide particles (e.g. Co, Ni, ZnO), which then serve as porogen, and in some cases, as a catalyst for enhanced graphitization of the CNF formed from the polymer precursor carbonization [6–10]. Other templates including Prussian blue analogues [11] and metal organic frameworks [12–14] have been used in conjunction with polymer precursors, conferring both porosity and heteroatom doping to CNFs obtained by electrospinning and carbonization. Sacrificial polymers or organic molecules such as polymethyl methacrylate (PMMA) [15–19], polyvinylpyrrolidone (PVP) [20,21], poly(ethylene oxide) [22], Nafion® [23], polysulfone [24], polystyrene [25], poly-L-lactic acid [26] and beta-cyclodextrin [27] can also be spun together with the main carbon precursor (any polymer forming conductive carbon with high yield during pyrolysis), allowing the formation of porous CNFs upon their removal by solvent or thermal treatment. Different kinds of templates can further be combined to produce hierarchical porosity, which is crucial for the transport of different species (ions, gases, liquids) in the electrodes of various electrochemical devices. For instance, the combination of PVP with Mg salts [9][28] gave rise to hierarchical meso- and microporosity inside CNFs prepared by electrospinning. For the post-synthetic approach, various chemical activations have been investigated to create porosity in preformed CNFs. Immersion of CNFs in concentrated KOH solutions followed by a treatment at high temperature is a recognized approach. [29,30] Other more direct approaches consist in re-pyrolyzing the CNFs but in a reactive atmosphere, such as steam [30,31] or ammonia [32].

While a number of studies on CNFs prepared by resorting to either a pre-synthetic approach involving a given porogen and given carbon precursor or a post-synthetic approach, few studies have compared the figure of merits of different porogens in otherwise identical preparation conditions for CNFs, and even less studies have reported on the combination of i) porogen-PAN electrospun solution and ii) a post-synthetic treatment to further increase intra-fiber porosity.

1.2 Preparation of CNFs from PAN and a porogen

To prepare reference CNFs, PAN (M_w=150,000 g mol^{-1}, Sigma-Aldrich) was first dissolved in N,N-dimethylformamide (DMF, pure, Carlo Erba) for 12 hours at 50 °C (10 wt% PAN concentration), then the solution was cooled to room temperature. The polymer fibers were then electrospun at 20 °C and collected on a drum rotating at 100 rpm (Spraybase®). The distance between the tip of the needle (22 gauge) and the collector was 10 cm, and the voltage of 13 kV (Auto-Reversing High Voltage Power Supply Spellman CZE1000R, West Sussex, United Kingdom) was applied to obtain a stable Taylor cone. The flow rate was kept as a constant 1 mL h^{-1} (syringe pump KDS 100 Legacy Syringe Pump, KD Scientific)

The obtained PAN-based fibers were submitted to stabilization and carbonization to give rise to carbon materials [33,34]. In particular, the electrospun PAN fibers were treated in air at 150 °C for 2 hours with heating rate 2.5 °C min^{-1}, and then at 250 °C for 3 hours with heating rate 2.5 °C min^{-1}. The stabilized nanofibers were finally carbonized at 1000 °C (ramp rate 5 °C min^{-1}) for 2 h under flowing argon atmosphere. After 2 h at 1000 °C, the heating was stopped and the sample cooled down naturally to room temperature under flowing Ar. The obtained CNFs are labelled PAN_{10}-CNF, the scalar 10 standing for the wt% PAN in DMF solution.

To prepare biphasic polymer fibers comprising PAN, the porogen was solubilized or dissolved in a PAN/DMF solution. The investigated porogens are PMMA (Sigma-Aldrich,M_w = 15,000 or 120,000 g mol^{-1}), PVP (Sigma-Aldrich, Mw ~ 1,300,000 g mol^{-1}), Nafion® (NR50, Sigma-Aldrich) and zinc chloride ($ZnCl_2$ anhydrous, >98 % purchased from Alfa Aesar). For PMMA and $ZnCl_2$, the PAN and/or porogen concentration in DMF was varied, since the introduction of the porogen had an obvious influence on rheological properties of the solution and morphology of the electrospun polymer fiber web. Table 1 details the investigated compositions of the electrospun solutions. Such biphasic polymer fibers were stabilized in air and carbonized in flowing Ar in the exact same conditions as described above for pure-PAN based fibers. For the preparation of FeNC electrodes in this chapter, a given amount of Fe salt was added in the PAN/porogen/salt polymeric solution, as noted in Table 2. The same procedure was then applied for the stabilization step in air and pyrolysis in argon as described above for preparing the Fe-free CNFs.

Chemical activation of selected CNFs was performed by applying a flash pyrolysis in flowing pure ammonia gas at 900 °C. Unless otherwise indicated, the pyrolysis duration in ammonia was 15 minutes. The resulting materials are identified by their label ending with ACNF (activated CNF), instead of CNF for non-activated material.

The morphology of the polymer fibers and/or CNFs was investigated by field emission-scanning electron microscopy (FE-SEM) using a Hitachi S-4800 microscope. Data analysis and fiber diameter distribution were performed using an image processing software Image J 1.48 v (U. S. National Institutes of Health). CNFs were analyzed by transmission electron microscopy (TEM) using a JEOL 2200FS (Source: FEG) microscope operating at 200 kV equipped with a CCD camera Gatan USC (16 MP). For TEM cross-sectional analysis, a microtome was used on resin-encapsulated sample and slices were deposited on carbon-coated copper grids (Agar Scientific).

Surface area and porosimetry of the samples was analyzed with N_2 physisorption with a Tristar II Micromeritics instrument at 77 K. Prior to analysis, all samples were outgassed overnight at 120 °C under vacuum. The resulting isotherms being of type I according to the IUPAC classification, BET plots were drawn below the relative pressure of 0.1 from the adsorption branches and employed to evaluate the BET specific surface (S_{BET}). The alpha-plot method was utilized to determine the mesoporous (V_{meso}) and microporous volumes (V_{micro}) as well as average pore diameter (d_{pore}). C, H, N, O elemental analysis was performed with a Vario MICRO Element Analyzer. Raman spectra were recorded on a LabRAM Aramis IR2 Horiba Jobin Yvon spectrometer equipped with a He/Ne laser (λ = 633 nm) and a long work distance objective x 50. The spectra were fitted with five bands using Origin software (OriginLab Corporation). The in-plane electrical conductivity of self-standing CNF webs was measured using a 2400 Keithley in a 4-electrode configuration on a 5 x 40 x 0.05 mm carbon electrode strip in a Fumatech MK3-L cell operated in the current range 0–100 mA.

The in-plane electronic conductivity was measured using a 4 probe cell (Fumatech) with 4 electrodes. The CNFs were cut into pieces of 4 x 1 cm and attached to electric tape. The measurement was carried out using Keithley's Series 2400 Source Measure Unit at room temperature.

The electrochemical activity towards ORR was determined in RDE setup. For RDE measurements on the fibrous free-standing electrodes (FSE), the latter were cut out with a punch as circles of 0.196 cm^2, matching the size of the glassy carbon (GC) tip used for the RDE setup, with diameter of 5 mm. The FSE was then attached on GC by placing it onto the GC and adding a drop of Nafion perfluorinated resin solution (5 wt% in lower aliphatic alcohols and water, Sigma-Aldrich) on top of the FSE. The typical weight of FSE electrodes for electrodes resulted in a different catalyst loading, described in section 1.5. The RDE experiment was performed in 0.1 M aqueous solution of H_2SO_4. The working electrode was glassy carbon electrode (Pine research), rotating speed was 1600 rpm and all RDE data was measured with a BioLogic Potentiostat SP-300. In order to remove air from the large pore volume of FSE the preliminary

chronoamperometry at 0.2 V/RHE was applied with rotating speed of 1600 rpm in same solution). Cyclic voltammetry scans were acquired between 0 and 1 V/RHE (v = 5 mV s^{-1} for nitrogen-saturated solutions and v = 2 mV s^{-1} for oxygen-saturated solutions). All solutions were nitrogenated or oxygenated for 15 minutes each.

For RDE measurements on the grinded FSE, 10 mg of grinded FSE was added to 108.5 µL of Nafion perfluorinated resin solution (5 wt% in lower aliphatic alcohols and water, Sigma-Aldrich), 300 µL of ethanol (absolute, Sigma-Aldrich) and 36.5 µL ultrapure water 18 MΩ. The prepared ink was ultra-sonicated for 1 h at 25 °C and 8.8 µL were then deposited on the GC tip and dried in air, resulting in a catalyst loading of 1.0 mg/cm^2.

1.3 Characterization of porogen-PAN fibrous webs after carbonization in argon

The characterized materials are labelled as $Porogen_x$-PAN_y-CNF, with x standing for the wt% of porogen in the electrospun solution, y the wt% of PAN in the electrospun solution, and CNF indicating the pyrolysis was performed in argon (see labels in Table 1).

Table 1. Composition of the PAN/Porogen electrospun solutions and labels of the resulting CNFs and ACNFs. The DMF amount in the electrospun solutions was (100 - porogen wt% - PAN wt%).

Porogen (M_w)	Porogen wt%	PAN wt%	CNF label (after carbonization in Ar)	CNF label (after carbonization in Ar and NH_3 activation)
none	0	10	PAN_{10}-CNF	PAN_{10}-ACNF
PMMA (15,000)	2	8	15k$PMMA_2$-PAN_8-CNF	15k$PMMA_2$-PAN_8-ACNF
PMMA (120,000)	4	6	120k$PMMA_4$-PAN_6-CNF	-
PMMA (15,000)	2	8	15k$PMMA_2$-PAN_8-CNF	-
PMMA (120,000)	4	6	120k$PMMA_4$-PAN_6-CNF	-
PVP	5	10	PVP_5-PAN_{10}-CNF	PVP_5-PAN_{10}-ACNF
Nafion®	2	8	$Nafion_2$-PAN_8-CNF	$Nafion_2$-PAN_8-ACNF
$ZnCl_2$	1	10	Zn_1-PAN_{10}-CNF	-
$ZnCl_2$	3	10	Zn_3-PAN_{10}-CNF	-
$ZnCl_2$	5	10	Zn_5-PAN_{10}-CNF	-
$ZnCl_2$	7	10	Zn_7-PAN_{10}-CNF	Zn_7-PAN_{10}-ACNF

Table 2. Composition of the FeNC from PAN/Porogen/Salt ACNFs. The DMF amount in the electrospun solution was (100 - porogen wt% - Fe salt wt% - PAN wt%)

Porogen	Porogen wt%	Fe salt	Fe salt wt%	CNF label (after carbonization in Ar and then NH_3 activation)
$ZnCl_2$	7	FeAc	0.5	Zn_7-$FeAc_{0.5}$-PAN_{10}-ACNF
	7	FeAcAc	0.5	Zn_7-$FeAcAc_{0.5}$-PAN_{10}-ACNF
	7	$FeCl_3$	0.5	Zn_7-$FeCl_{3\text{-}0.5}$-PAN_{10}-ACNF
	7	FeAc	1	Zn_7-$FeAc_1$-PAN_{10}-ACNF
	7	FeAcAc	1	Zn_7-$FeAcAc_1$-PAN_{10}-ACNF
	7	$FeCl_3$	1	Zn_7-$FeCl_{3\text{-}1}$-PAN_{10}-ACNF
	7	FeAc	2	Zn_7-$FeAc_2$-PAN_{10}-ACNF
	7	FeAcAc	2	Zn_7-$FeAcAc_2$-PAN_{10}-ACNF
	7	$FeCl_3$	2	Zn_7-$FeCl_{3\text{-}2}$-PAN_{10}-ACNF
PVP	5	FeAc	1	PVP_5-$FeAc_1$-PAN_{10}-ACNF
	5	FeAcAc	1	PVP_5-$FeAcAc_1$-PAN_{10}-ACNF
	5	$FeCl_3$	1	PVP_5-$FeCl_{3\text{-}1}$-PAN_{10}-ACNF

As a reference, the CNF web prepared only from PAN was characterized (labelled PAN_{10}-CNF). The resulting CNF web was self-standing and flexible, as already reported by us [35]. The morphology of PAN_{10}-CNF was investigated by SEM and TEM. The material is randomly oriented cylindrical fibers (Figure 14a) with an average diameter of 200 nm (Figure 15a). Such fibers are smooth and dense, as demonstrated by the TEM cross-section in Figure 16a. According to the latter image and to previous reports [36], the porosity and specific surface area developed by such fibers is very low (*ca* 20 $m^2\ g^{-1}$), mainly attributed to the outer surface area of the fibers, with no internal porosity. The nearly flat N_2 adsorption isotherm demonstrates the lack of porosity inside the fibers (Figure 18).

In order to create internal porosity within fibers, a range of porogens were added to the precursor PAN solution prior to electrospinning, as described in the experimental methods. The investigated polymer templates (PMMA, PVP, Nafion®) were selected for their relative stability and rigidity. They are known to be stable up to 250 °C in air, conditions used during the stabilization step. When heated to much higher

temperature in inert gas, they decompose and form mainly volatile products, thereby acting as porogens, while PAN decomposes also but is converted to carbon in high yield.

The results obtained with PMMA are discussed first. PMMA of two different molecular weights (15,000 and 120,000 g mol^{-1}) and in different ratio to PAN (2:8 and 4:6) was added in the electrospun DMF-based solution. Those ratios were selected on the basis of a previous study on PMMA-PAN composite fibers [36]. In all the cases, the addition of PMMA resulted in CNFs with slightly smaller average diameter (compare Figure 14b and 14a) than for the reference PAN_{10}-CNF web (average diameter of 175 nm, see Figure 15b), but with otherwise practically identical features and properties (Figure 17). Figure 14b depicts the sample 15k$PMMA_2$-PAN_8-CNF as an example. The decrease in fiber diameter is most probably due to the lower concentration of PAN in the electrospun solution relative to the reference PAN_{10}-CNF (8 vs 10 %), and was also expected due to the change in precursor viscosity already observed upon addition of this polymer [37]. The developed porosity is clearly visible on the cross-sectional TEM micrograph (Figure 16b), where pores of 10 nm of average diameter appeared within the fibers. The modification of the preparation parameters (higher molecular weight for PMMA, or different PMMA:PAN ratio) did not have significant effects on the obtained morphology and porosity (Figure 17). The question whether the formed porosity is open or closed is discussed later.

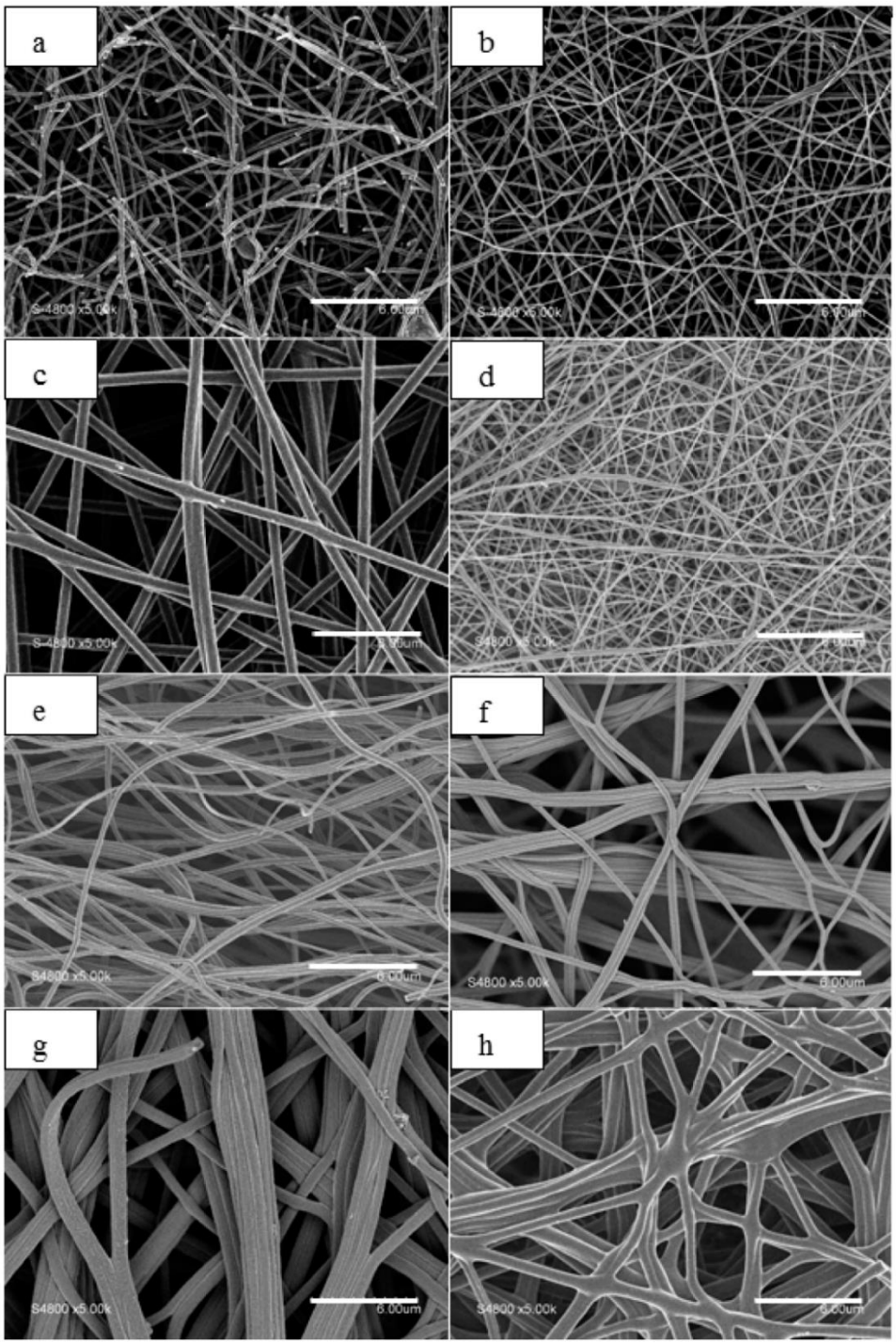

Figure 14. FE-SEM micrographs of: (a) PAN_{10}-CNF; (b) 15k$PMMA_2$-PAN_8-CNF; (c) PVP_5-PAN_{10}-CNF; (d) $Nafion_2$-PAN_8-CNF; (e) Zn_1-PAN_{10}-CNF; (f) Zn_3-PAN_{10}-CNF; (g) Zn_5-PAN_{10}-CNF; (h) Zn_7-PAN_{10}-CNF; Scale bar corresponds to 6 μm.

The results obtained with PVP porogen are now discussed. A PVP:PAN ratio of 5:10 was employed (sample labelled PVP_5-PAN_{10}-CNF). In these conditions, carbon fibers with considerably greater diameter compared to the reference PAN_{10}-CNF (average diameter of 750 nm) (Figure 14c, 15c) were obtained. This can be attributed to a modification of the viscosity of the electrospun solution, affected by the presence of PVP aggregates and consequent decrease in chain entanglement. The pores generated inside the CNFs presented an average size around 3 nm (Figure 16c).

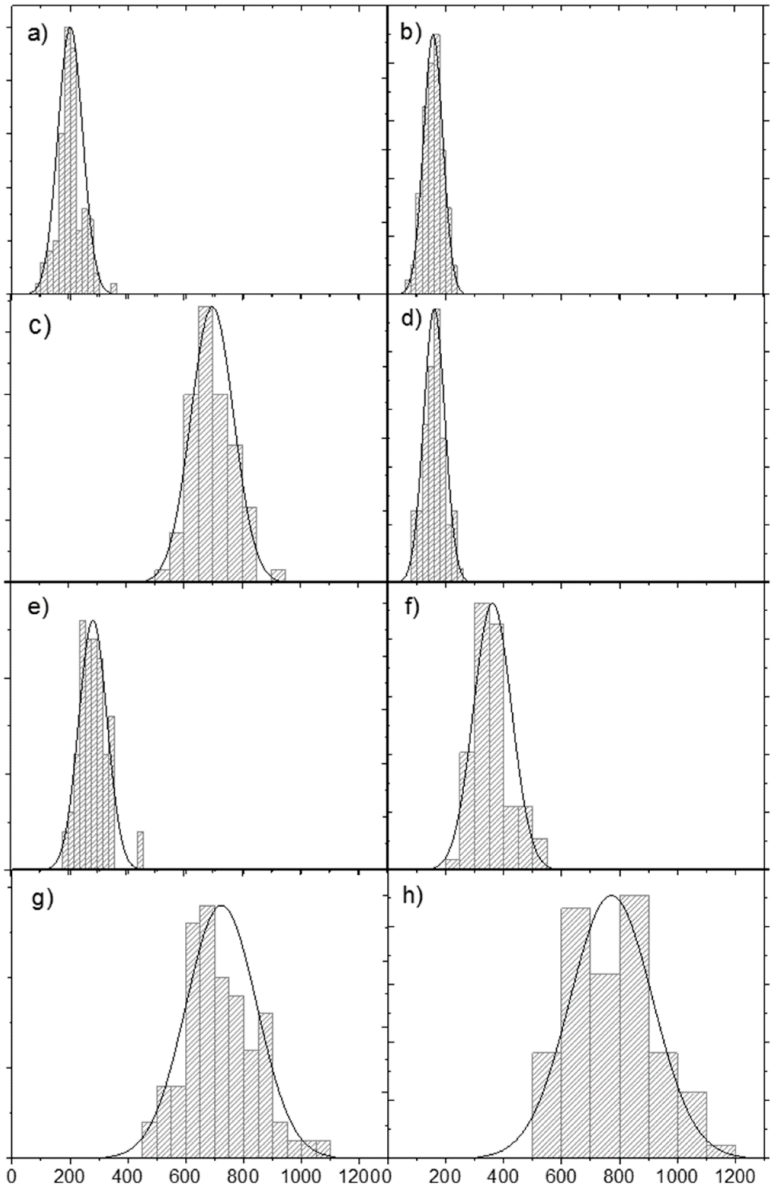

Figure 15. Histograms of the fiber diameter distribution for: (a) PAN_{10}-CNF; (b) 15k$PMMA_2$-PAN_8-CNF; (c) PVP_5-PAN_{10}-CNF; (d) $Nafion_2$-PAN_8-CNF; (e) Zn_1-PAN_{10}-CNF; (f) Zn_3-PAN_{10}-CNF; (g) Zn_5-PAN_{10}-CNF; (h) Zn_7-PAN_{10}-CNF.

The third polymer template investigated was Nafion® perfluorosulfonic acid. It has been previously demonstrated to be effective in creating nanoscale porous domains inside carbon nanofibers [34]. In this work, its addition to PAN (sample labelled $Nafion_2$-PAN_8-CNF) resulted in the formation of thin carbon fibers (average fiber diameter is 180 nm) (Figure 14d, 15d). The CNF webs has also obviously a higher density of fibers (compare Figure 14d and 14a), which is beneficial for improved conductivity and mechanical stability. The fibers have a well-developed internal porosity, as shown by TEM analysis of the cross-sections, Figure 16d. A homogeneous distribution of pores with 4 nm size can be observed within the CNF structure.

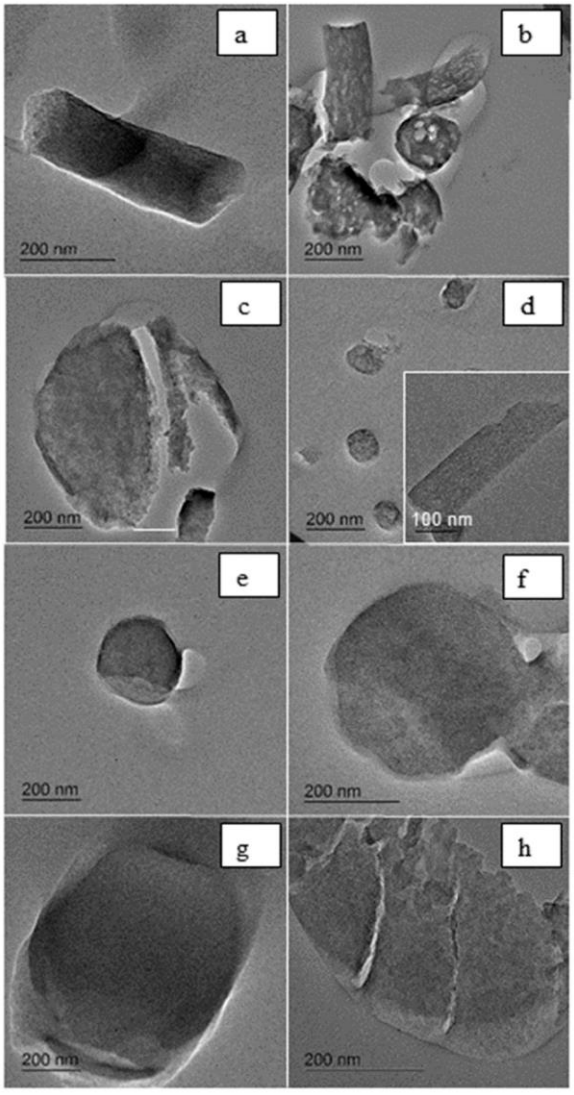

Figure 16. TEM micrographs of: (a) PAN_{10}-CNFs; (b) $15kPMMA_2$-PAN_8-CNF; (c) PVP_5-PAN_{10}-CNF; (d) $Nafion_2$-PAN_8-CNF; (e) Zn_1-PAN_{10}-CNF; (f) Zn_3-PAN_{10}-CNF; (g) Zn_5-PAN_{10}-CNF; (h) Zn_7-PAN_{10}-CNF.

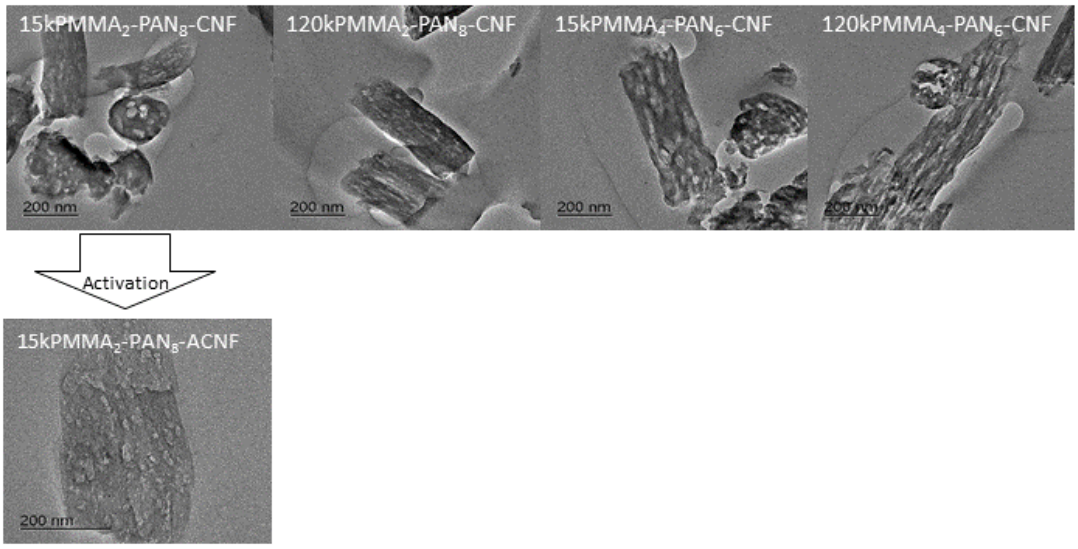

Figure 17. TEM micrographs of PAN CNFs prepared from PAN and PMMA by carbonization in argon and, for a selected CNF, after an additional activation step in ammonia (labelled ACNF).

Finally, the inorganic template precursor $ZnCl_2$ was investigated. The presence of $ZnCl_2$ may allow the formation of pores during the ensuing stabilization and carbonization steps in air and in argon, respectively, with the following mechanism: during the stabilization step, hydrated chloride hydrolyzes and forms an oxychloride, from which zinc oxide forms creating microporosity by etching carbon atoms [10]. FE-SEM characterization of Figure 14e-h showed that increasing the $ZnCl_2$ concentration in the electrospun solution from 1 to 7 wt% (samples Zn_1-PAN_{10}-CNF, Zn_3-PAN_{10}-CNF, Zn_5-PAN_{10}-CNF, Zn_7-PAN_{10}-CNF) the diameter of the carbon fibers increased tremendously from 300 to 700 nm (Figure 15-h). It is known that solution conductivity affects fiber uniformity. The high conductivity of the PAN/$ZnCl_2$ (13:0.25) solution was reported to lead to instability in the electrospinning process with the formation of large fibers and bundles as a cotton-like 3D deposit [38]. However, the reverse has also been observed: increasing the conductivity through the addition of salt may produce finer, more uniform fibers, resulting in an increased elongational force exerted on the fiber jet [39]. Indeed, other reports on the electrospinning of $ZnCl_2$/PAN solutions showed that the average diameters of the obtained CNFs gradually decrease from 350 to 200 nm with increasing zinc chloride content from 1 to 5 wt% [10].

Another particular feature of CNFs derived from electrospun $ZnCl_2$/PAN solutions is the formation of progressively larger fiber bundles with increased Zn salt concentration (see Figure 14g-h in particular). This phenomenon was already observed for PAN/polystyrene mixtures, where the template not only acted as

sacrificial decomposable phase, but also controlled the formation of these architectures [40]. In the TEM micrographs of the cross-sections of Zn_1-PAN_{10}-CNF, Zn_3-PAN_{10}-CNF, Zn_5-PAN_{10}-CNF, Zn_7-PAN_{10}-CNF samples (Figure 16e-h), no pores are visible inside the fibers.

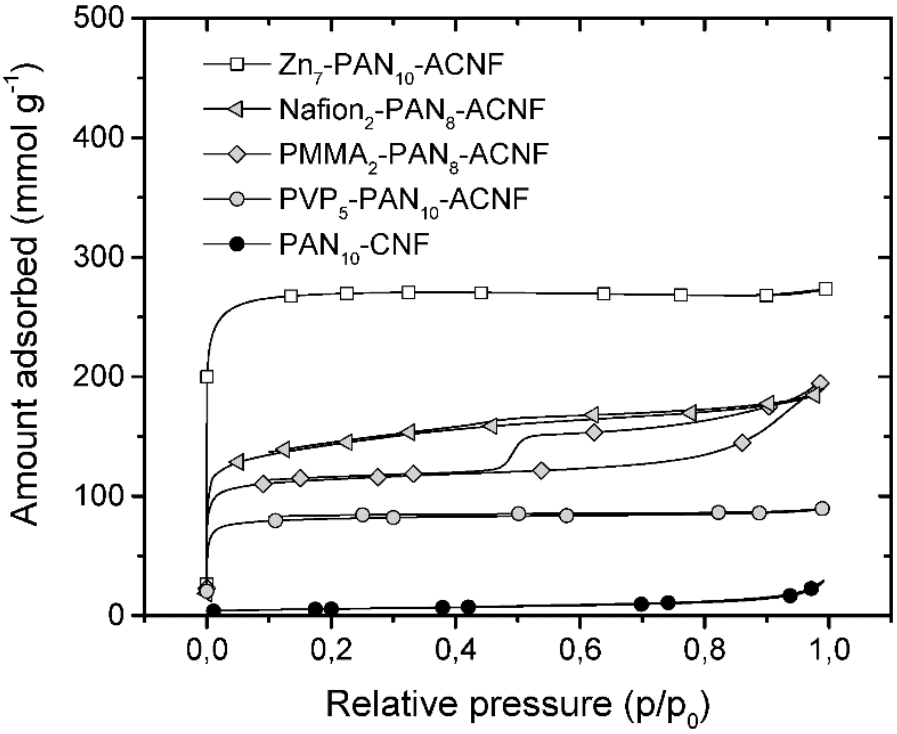

Figure 18. Selected N_2 adsorption-desorption isotherms of carbonized and NH_3-activated CNF webs (ACNF). The carbonized web obtained from PAN-only is also shown as a reference (PAN_{10}-CNF).

Except for the latter Zn-PAN-CNF samples, all other CNFs derived from polymer/PAN solutions containing the sacrificial polymers presented pores visible by TEM in the mesoscopic range, in agreement with previous works.[15,16,18,23,41] The nitrogen adsorption/desorption isotherms of all the investigated CNFs showed however very low S_{BET} values (below 20 m^2 g^{-1}, see * in column 2 of Table 3), almost unchanged compared to the reference PAN-CNFs (Table 3).

Table 3. Textural properties of carbonized (CNFs) and ammonia-activated (ACNFs) polymer fibers.

Fiber precursor	CNFs	ACNFs				
	S_{BET}, m^2 g^{-1}	S_{BET}, m^2 g^{-1}	C_{BET}	V_{meso}, cm^3 g^{-1}	V_{micro}, cm^3 g^{-1}	d_{pore}, nm
PAN_{10}	20	n/a*	-	-	-	
$15kPMMA_2$-PAN_8	35	450	3034	0.0599	0.1243	2.9
$120kPMMA_2$-PAN_8	n/a*	645	2410	0.0877	0.1669	1.9
$15kPMMA_4$-PAN_6	n/a*	360	2927	-	0.1006	0.5
$120kPMMA_4$-PAN_6	n/a*	410	3324	0.0083	0.1177	0.8
PVP_5-PAN_{10}	3	325	2012	-	0.0941	1.8
$Nafion_2$-PAN_8	n/a*	535	1993	0.1166	0.1327	2.4
Zn_1-PAN_{10}	n/a*	680	1986	0.0791	0.1814	1.6
Zn_3-PAN_{10}	n/a*	570	1707	0.0721	0.1614	2.5
Zn_5-PAN_{10}	n/a*	865	1791	-	0.1982	1.5
Zn_7-PAN_{10}	n/a*	1083	3558	0.0980	0.3098	1.4

* $S_{BET} < 3$ m^2 g^{-1}

This result, apparently in contrast with the micrographs of Figure 16 showing pores of different size in the prepared CNFs and in contrast with previous reports using the same templates and similar synthesis conditions [15–19,23], demonstrates that the obtained porosity is closed, and not accessible from outside the CNFs. This observation may be due to the partial collapse of the percolating porous network formed during the thermal removal of the template or porogen.[23] As a result, free-standing porous fiber webs are obtained, with closed porosity and low surface area. The latter is assigned only to the outer surface area of plain and smooth CNFs with diameters in the range 150-700 nm, depending on the porogen used. The appealing approach of using a soft or hard template added during the preparation step of electrospinning seems therefore ineffective in creating open porosity. The conditions necessary to reach an open porosity are shown later in this study.

Relevant properties for electrochemical applications are the graphitic character and the related electrical conductivity of the carbon based electrode materials. To investigate them, Raman spectroscopy and four-electrode method were used to characterize the carbon nanofiber networks prepared in this work. In particular, the modification of this properties upon the different steps of preparation was studied. The Raman spectra of all CNFs prepared with different porogens (Figure 19) present two intense and broad bands, the so-called D band at 1357 cm^{-1} ascribed to defects and disorder in the graphitic structure and the so-called G band at 1560 cm^{-1} corresponding to the in-plane vibration of sp^2-bonded carbon in graphite. The spectra were fitted with more contributions, namely the D4 band, ascribed to sp^3-carbon (1180 cm^{-1}), the D3 band (1500 cm^{-1}) associated with an amorphous sp^2 carbon bonded in the graphitic phase and the D2 band (1580 cm^{-1}) corresponding to graphitic lattices in the structure (Figure 20)[42].

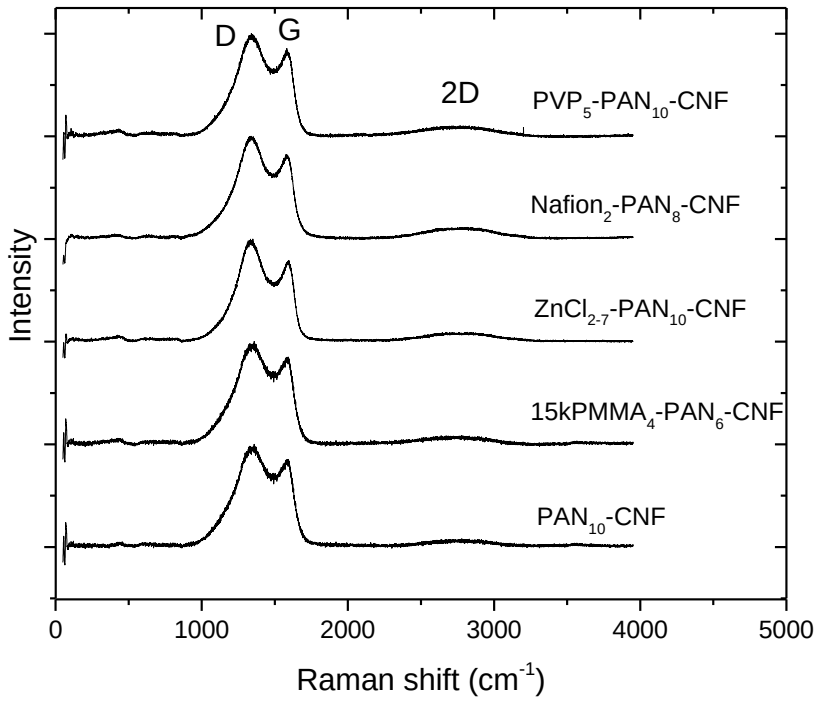

Figure 19. Raman spectra of CNFs (after carbonization).

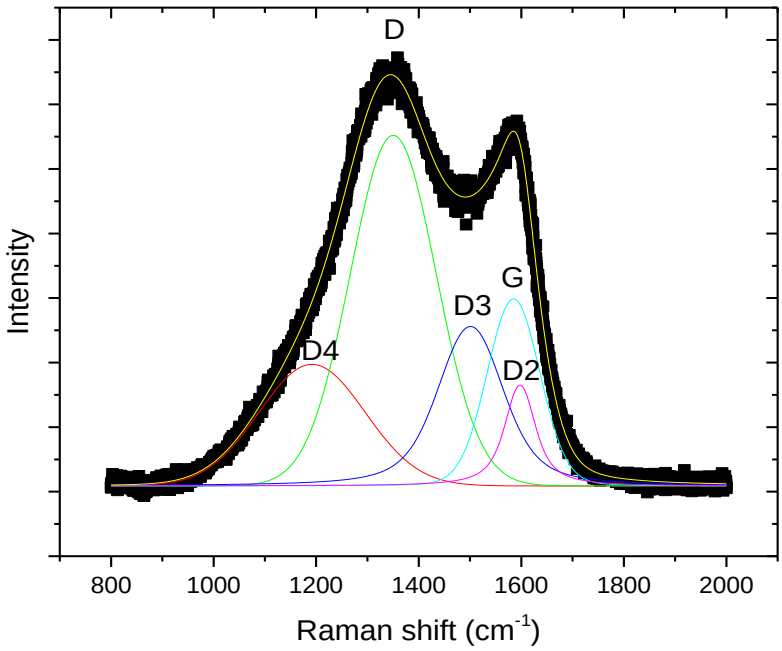

Figure 20. Example of deconvolution of a Raman spectrum of CNFs (PAN_{10}-CNF) by using Gaussian and Lorentzian curves (Voigt).

The relative intensities of the D and G bands (I_D/I_G) as well as the relative areas (A_D/A_G) are often used to estimate the degree of graphitization of carbon materials [28,43]. The lower the I_D/I_G ratio, the higher is the level of crystalline sp^2-carbon [44,45]. The I_D/I_G and A_D/A_G values obtained after deconvolution of the spectra of all CNFs derived from the carbonization of porogen/PAN solutions are summarized in Table 4. It is evident that the addition of polymer or inorganic salt porogen did not significantly influence the graphitization of the carbon fibers. Similar I_D/I_G ratios were obtained for reference PAN_{10}-CNFs and the other CNF webs. Their values between 1.8 and 2.7 demonstrate that the fibers are composed by disordered carbon (due to the relatively low carbonization temperature of 1000 °C) with local graphite inclusions (turbostratic domains) already evidenced for electrospun CNFs [11,28,36,46].

Table 4. Relative areas and intensities of D and G bands (I_D/I_G, A_D/A_G) in the Raman spectra after carbonization in Ar (CNF) and after a subsequent activation in ammonia (ACNF).

Fiber precursor	CNF		ACNF	
	$A_{D/G}$	$I_{D/G}$	$A_{D/G}$	$I_{D/G}$
PAN_{10}	3.01	1.83	2.95	1.86
$15kPMMA_2$-PAN_8	4.73	2.45	3.06	1.88
$120kPMMA_2$-PAN_8	4.59	2.02	5.00	2.39
$15kPMMA_4$-PAN_6	3.24	2.20	3.78	2.08
$120kPMMA_4$-PAN_4	3.14	1.86	3.76	2.02
PVP_5-PAN_{10}	4.69	2.09	3.21	2.28
$Nafion_2$-PAN_8	5.34	2.77	2.52	2.33
Zn_1-PAN_{10}	4.40	2.43	4.65	2.49
Zn_3-PAN_{10}	6.34	2.40	9.61	2.56
Zn_5-PAN_{10}	4.24	2.57	2.30	1.88
Zn_7-PAN_{10}	6.54	2.39	3.06	1.89

The electrical conductivity of the CNFs prepared by electrospinning, determined directly on the self-standing CNF webs, are consistent with the partial graphitic character evidenced by Raman spectroscopy. Except for the fibers prepared using zinc chloride as porogen precursor, which show significantly lower conductivity, all CNF networks present similar conductivity values around 6-9 S cm^{-1} (Table 5), which is in agreement with previous results obtained on PAN based electrospun materials [35,36,47]

Table 5. In-plane electrical conductivity and elemental content of all CNF webs and selected ACNF webs.

Fiber precursor	CNF				ACNF			
	Conductivity S cm^{-1}	C wt%	N wt%	O wt%	Conductivity S cm^{-1}	C wt%	N wt%	O wt%
PAN_{10}	6.6	66.8	5.6	17.5	3.8	78.4	7.0	7.8
15k$PMMA_2$-PAN_8	8.8	75.8	5.5	11.1	1.9	77.8	5.8	6.7
PVP_5-PAN_{10}	9.7	76.2	2.2	10.9	4.8	78.8	7.0	8.2
$Nafion_2$-PAN_8	7.0	74.3	5.5	16.0	2.4	70.3	5.5	9.6
Zn_1-PAN_{10}	1.1	70.3	5.2	14.6	-	-	-	-
Zn_3-PAN_{10}	0.8	71.5	4.6	17.1	-	-	-	-
Zn_5-PAN_{10}	3.3	61.2	6.8	20.9	-	-	-	-
Zn_7-PAN_{10}	0.8	68.1	2.5	19.2	0.3	71.3	6.1	11.3

The carbon fibers prepared from $ZnCl_2$-PAN_{10} fibers demonstrated very low conductivity, between 3.3 and 0.8 S cm^{-1}. The graphitic structure being the same for all the samples as indicated by the Raman study, this decrease in conductivity from the pristine CNFs may be ascribed to the microstructure of the $ZnCl_2$-PAN-CNFs in which, due to $ZnCl_2$ removal, electron paths are likely disrupted. Furthermore, its particular morphology with fibers forming large bundles can affect the inter-fiber/inter-bundle connection (decreased number of connection points) and thus the electron transport.

1.4 Characterization of porogen-PAN fibrous webs after carbonization and NH_3 activation

The post-treatment with ammonia at high temperature is a conventional approach to create porosity in carbon-based materials by etching, which can also introduce nitrogen functionalities on the surface [56]. The mechanism for the formation of both pores and nitrogen groups is based on the reaction of ammonia with carbon. This gasification reaction continuously occurs during NH_3 pyrolysis and react with surface

carbon atoms forming volatile compounds such as HCN [48][49]. When the reaction between ammonia and carbon occurs at different rates on the surface (due to carbon structure heterogeneity), increased porosity is obtained. When the ammonia pyrolysis is stopped, nitrogen atoms that were reacting with carbon surface atoms at that moment remain on the surface, with different environments including amino, cyanide, pyrrolic, pyridinic and quaternary nitrogen groups [50,51].

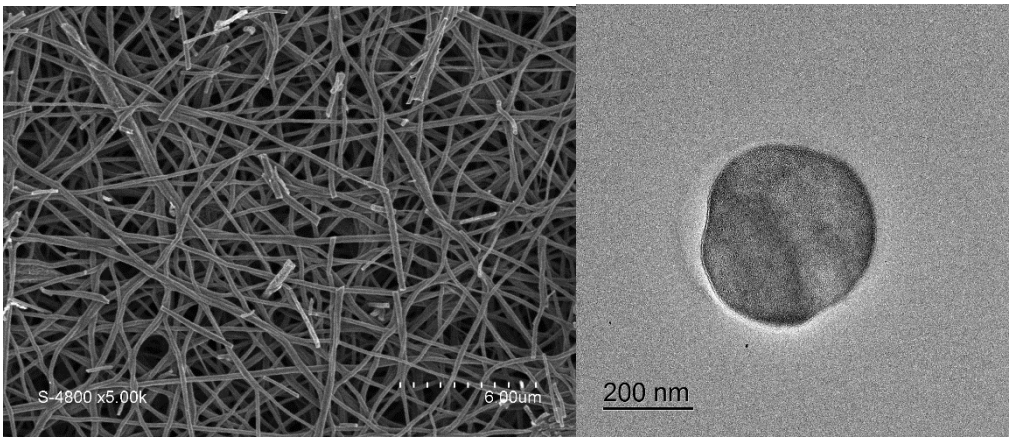

Figure 21. FE-SEM (left side) and cross-section TEM (right side) micrographs of PAN_{10}-ACNF fibers.

We first subjected the reference electrospun carbon nanofibers PAN_{10}-CNF web to treatment under pure flowing ammonia at 900 °C [52]. The resulting activated nanofibers (ACNFs), labelled PAN_{10}-ACNFs, did not present significant modification of their average diameter (200 nm) nor of their porosity, which was non-existent as shown by TEM cross-section (Figure 21). As a consequence, specific surface area determined from nitrogen adsorption/desorption isotherms remained low (Table 3)

Due to the low surface area obtained with the porogen/PAN template method after carbonization in Ar, as described previously, and the low surface area obtained with ammonia activation on pure PAN-derived CNFs, the combination of the two approaches was then investigated as a last attempt to develop high specific area. All CNF webs that had been prepared by porogen/PAN templating and carbonized in Ar (labelled CNF) were then further activated in flowing ammonia gas in the same conditions as for PAN_{10}-ACNF.

N_2 adsorption-desorption measurements were performed to characterize their porosity and specific surface area (Table 3 and Figure 18). Figure 18 clearly shows that ACNF webs adsorbed a significant amount of N_2, the three polymer porogens resulting in intermediate adsorbed volumes and the $ZnCl_2$ porogen resulting in the highest adsorbed volumes. The isotherms of the different ACNF webs are of type I and/or type II according to IUPAC classification, which indicates that fibers presented an overall microporous

structure, as well as mesopores. With Nafion® as a porogen, significant hysteresis of type H4 is observed during desorption, closing at $P/P_0 = 0.45$. This is assigned to mesopores with bottleneck shape, which may be related to the existence of Nafion® polymer aggregates in the electrospinning solution [53,54], while other polymers were fully dissolved. In the case of microporous structures, the BET energetic constant (C_{BET}, related to the energy of adsorption of the first layer of N_2 adsorbate on the carbon surface) is expected to be higher than the usual value expected for mesoporous carbon structure as seen in Table 3[55]. The values of the specific surface area, meso and micropore volume as well as average pore diameter of all ACNF webs are summarized in Table 3.

The specific surface area of all ACNF webs ranges from 325 to 1083 $m^2 g^{-1}$, the maximum value corresponding to $ZnCl_7$-PAN_{10}-ACNF, while the average pore size was comprised between 0.5 and 2.9 nm.

The carbon fibers derived from PMMA-PAN solutions presented surface areas between 360 and 645 $m^2 g^{-1}$. The specific area increased by increasing the molecular weight of the sacrificial polymer from 15,000 to 120,000 g mol^{-1} and by decreasing the PMMA:PAN ratio from 4:6 to 2:8. The carbon fibers derived from the PVP-PAN solution with PVP:PAN ratio of 5:10 presented a surface area of 325 $m^2 g^{-1}$. This is comparable to the BET value obtained with PMMA in high ratio to PAN (4:6), and may also be increased if the PVP:PAN ratio had been further optimized (lowered). The carbon fibers derived from Nafion®-PAN solution with Nafion®:PAN ratio of 2:8 presented a surface area of 535 $m^2 g^{-1}$, also comparable to the SBET value obtained with PMMA:PAN ratio of 2:8 (450 and 645 $m^2 g^{-1}$, depending on PMMA molecular weight). The carbon fibers obtained from $ZnCl_2$-PAN solutions showed a S_{BET} value of 680 $m^2 g^{-1}$ already at a low $ZnCl_2$:PAN ratio of 1:10, further increasing with increasing amounts of $ZnCl_2$:PAN ratio from 3:10 to 7:10. Due to the high value of 1083 $m^2 g^{-1}$ measured for the carbon fibers obtained using a $ZnCl_2$:PAN ratio of 7:10 and for the regular ammonia activation duration of 15 min at 900 °C, the effect of the duration of activation was performed for this sample, at the same temperature of 900 °C. It is noted that the ammonia pyrolysis was performed in flash mode [56], (sample heated from room temperature to 900 °C in *circa* 1-1.5 minute), which allows very precise control of the pyrolysis duration down to 5 min. To stop the pyrolysis, the quartz tube was immediately removed from the split hinge oven. The results are depicted in Figure 22. The specific area was already high only after 5 minutes of ammonia activation, with a slightly increased value for increased duration up to 20 minutes. The optimal duration was considered at 15 minutes, corresponding to a best compromise between highly developed area and retained sufficient mechanical resistance. A longer treatment of 20 minutes led to an increased fragility of the carbon web, limiting its utilization as a self-standing electrode.

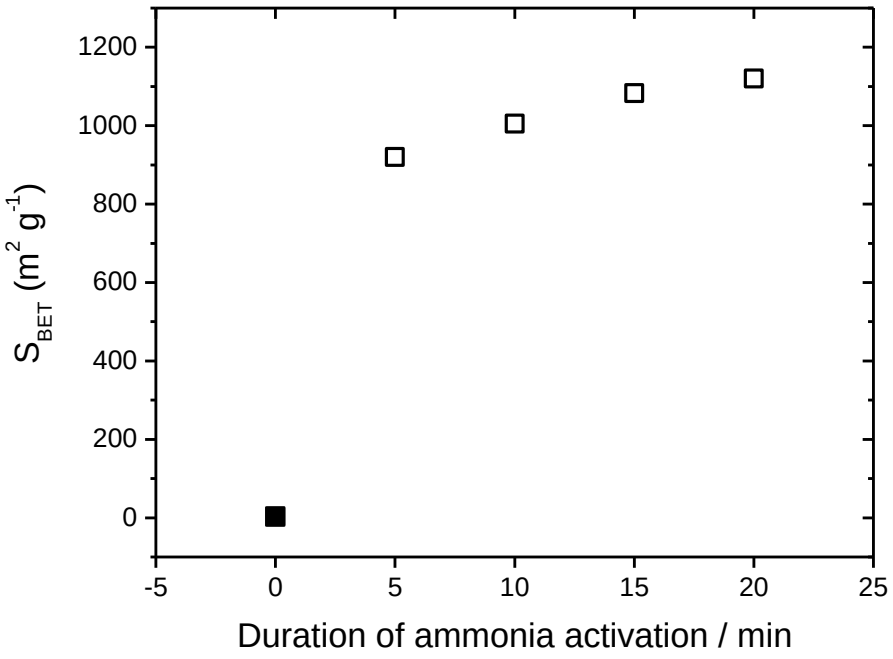

Figure 22. Effect of the duration of ammonia activation at 900 °C on the mass-specific surface area (S_{BET}) of Zn_7-PAN_{10}-CNF.

Raman spectra recorded on activated fibrous webs were very similar to those obtained with carbonized samples (Figure 23). The calculated I_D/I_G ratio (Table 4) were practically unchanged upon activation in ammonia, demonstrating that the degree of graphitization was not significantly impacted by the ammonia treatment.

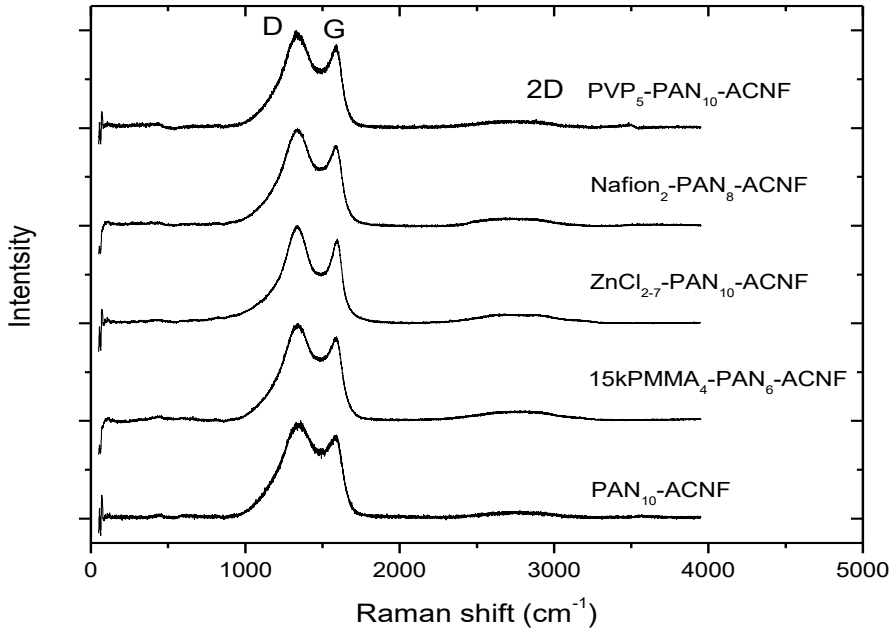

Figure 23. Raman spectra of porous CNFs after ammonia activation.

As already mentioned, ammonia activation usually leads to additional nitrogen doping of the carbon [50,57]. In order to evaluate the introduction of nitrogen sites in the prepared ACNF webs, elemental analysis was performed before and after the NH_3 treatment, for selected CNF webs (Table 5). The nitrogen amount in the CNF derived from PAN only is around 5.6 wt% after carbonization (PAN_{10} row in Table 5, CNF column), in agreement with previous reports and with the carbonization temperature of 900 °C. It is known that the higher the pyrolysis temperature, the lower is the nitrogen content [1]. For the reference PAN_{10}-CNF, the nitrogen amount slightly increased to 7.0 % after ammonia activation, while a decrease in oxygen content is observed. The latter effect is explained by selective etching of oxygen-containing surface groups by ammonia. For PVP_5-PAN_{10} and Zn_7-PAN_{10}, a *circa* 3-fold increase in nitrogen amount was observed from CNF to ACNF webs, accompanied by a reduction in oxygen content [50]. All ACNF webs had however comparable nitrogen amount, in the range 6.1 to 7.0 wt%.

While nitrogen doping, in particular via pyrolysis under ammonia (leading to highly basic nitrogen groups), is interesting for some electrochemical applications such as supercapacitors or as oxygen-reducing sites (in alkaline electrolyte in particular), the etching of some carbon mass during ammonia activation results in carbon fibers with increased internal porosity and also possibly weakened inter-fiber

connections, which may impact the mechanical stability of self-standing fiber webs and also their electrical conductivity. The electrical conductivity of selected carbon fiber webs (one selected for each type of porogen) was halved after the ammonia activation (Table 5). For example, it dropped from 6.6 to 3.8 S cm^{-1} for the reference web derived from PAN only, and from 9.7 to 4.8 S cm^{-1} for PVP_5-PAN_{10}-CNF and PVP_5-PAN_{10}-ACNF, respectively. Interestingly, the fact that the conductivity decreased significantly even for PAN_{10}-ACNF while such fibers have no open porosity, indicates that the decreased in-plane conductivity cannot be assigned to the formation of open pores in the fibers. The decreased conductivity of carbon fiber webs after ammonia activation may be due to the nitrogen doping itself (decreasing the intrinsic conductivity of carbon) or weakened electrical contact at the nodes of the fibrous web (possibly due to etching of carbon at the nodes). As already mentioned earlier for the series of Zn_7-PAN_{10}-CNF fibers subjected to various duration of activation in ammonia, activation longer than 20 minutes still resulted in a self-standing web but with much increased fragility, which is directly related to the quality of the nodes of the webs.

All these results lead to the conclusion that the open porosity in the PAN-derived CNFs resulted from a two-step approach involving the combination of a template route with a chemical activation step. The porogens incorporated in the electrospun PAN solution led first to carbon fibers with closed pores after the carbonization in Ar. The closed pores could be opened and interconnected within the fiber upon a post-treatment in ammonia atmosphere at high temperature. Other examples of etching in combination with the use of porogens have been reported (e.g. water etching-assisted templating).[20]

The purpose of this work was the rationalization of an effective strategy to obtain CNF webs with high porosity between fibers but also high specific area by introducing porosity inside the fibers for application in electrochemical energy conversion and storage devices. While having this objective in mind, it is also important to maintain the electrical conductivity of the self-standing CNF webs to sufficiently high values. Typically, to be not limited by the conduction of electrons across an electrode, the electric conductivity must be *circa* 100 times higher than the electrolyte conductivity. The results indicate that the approach combining the introduction of templates and chemical activation led to open micro and mesoporosity inside the fibers, while the electric conductivity was circa halved during the ammonia activation step. This decrease in conductivity may be due to the removal of a fraction of the carbon from the bulk of the CNFs during ammonia activation and/or the embrittlement of the interfibrous connection. In addition, when the electrical conductivity of self-standing CNF ammonia-activated webs is plotted against their BET area, a negative linear correlation is observed (Figure 24). The identification of such a correlation is useful to

select the best compromise between conductivity and BET area, which will depend on the exact electrochemical application and range of typical current densities produced by an electrode (in the order of increasing current density : batteries < fuel cells < supercapacitors). With current densities < 10 mA cm^{-2}, the reported conductivities [56] are not a limiting factor in batteries, and thus any of the ACNF webs could be selected. With current densities in the range 1-2 A cm^{-2}, fuel cells are more demanding in terms of electron conductivity in the electrodes. By comparison, the effective proton conductivity in typical active layer of PEMFC is only circa 1-2 S m^{-1}. Therefore, if the electronic conductivity through the active layer is > 20 S m^{-1} (0.2 S cm^{-1}), it should not be a factor limiting the porous electrode performance [58–61]. All present ACNF webs could therefore be applicable for self-standing electrodes in e.g. PEMFCs. Last, in electrochemical supercapacitors, the instantaneous current density can reach extremely high values of 10 A cm^{-2} due to the non-Faradaic process, and electric conductivity requirements are therefore higher. Moreover, the high electric conductivity requirement is accompanied by the high BET area requirement [62], which are shown in Figure 24 to be antagonistic.

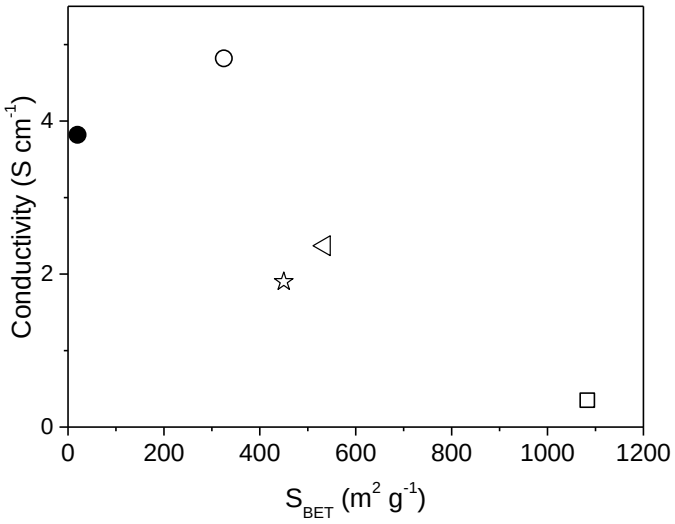

Figure 24. Electrical conductivity versus specific surface area of the ACNF fiber webs. ● - PAN_{10}-ACNF; ○ - PVP_5-PAN_{10}-ACNF; ◁ - $Nafion_2$-PAN_8-ACNF; ☆- $15kPMMA_2$-PAN_8-ACNF; □- Zn_7-PAN_{10}-ACNF.

1.5 Electrochemical properties of self-standing FeNC electrodes derived from PAN/porogen/Fe-salt

In the light of the results obtained with the different approaches for preparing porous CNFs from PAN, the porogens PVP and $ZnCl_2$ were down-selected for the preparation of FeNC electrodes. Addition of PVP leads to high electrical conductivity of ACNFs and interesting mechanical property, while $ZnCl_2$ leads to ACNF webs with highest BET area (Figure 24).

Various Fe salts were investigated (iron acetate, iron acetylacetonate, iron chloride) and in different amounts (Table 6). The synthesis procedure was identical as for the ACNF webs, except that a given amount of Fe salt was added in the initial electrospinning solution (see sub-section 1.2). The concentration of PAN in the solution was fixed at 10%.

The electrocatalytic properties of the prepared self-standing FeNC electrodes were measured with a rotating disc electrode (RDE) in oxygen saturated 0.1 M H_2SO_4 and in nitrogen saturated 0.1 M H_2SO_4. The results were then compared to the reference $Fe_{0.5}NC$ powder catalyst deposited by ink method. This catalyst was developed and investigated by previous research in our laboratory[63–65]. In this work the reference catalyst preparation was reproduced from [63]. The scalar 0.5 in the catalyst name indicates the wt% of Fe in the catalyst precursor before pyrolysis. All self-standing electrodes were die-cut to the circular surface of 0.196 cm^2 and then attached on the working electrode (glassy carbon) by depositing a drop of 5% Nafion resin solution on top of the self-standing electrodes, with the glassy carbon tip positioned below it. To better understand and to be able to compare the electrochemical activity of self-standing electrodes relative to active layers prepared via ink deposition; it is important to estimate or measure the corresponding loading of catalyst that is defined by the mass of catalyst per geometric area.

To simplify the reading of the results, the labels of the samples were simplified here, to avoid the wt% of PAN, since all the electrochemically-tested samples were prepared with 10 wt% PAN. Table 6 represents all samples that were analyzed in this subsection, as well as the theoretical quantity of Fe in the carbon fibers and the geometric loading of fibrous materials, that was measured by weighing each electrode

before addition of Nafion. The loading of $Fe_{0.5}NC$ powder was 0.8 mg cm^{-2}. The thickness of every self-standing electrode was *ca* 50-60 µm.

Table 6: Loading and composition of FeNC self-standing electrodes, derived from PAN/Porogen/Fe salt polymer solution

Sample	Fe salt concentration in solution, wt%	Fe content in precursor fibers before pyrolysis, mol%	Loading mg cm^{-2}
Zn_7-$FeAc_{0.5}$ -ACNF	0.5	0.16	0.25
Zn_7-$FeAcAc_{0.5}$ -ACNF	0.5	0.079	0.25
Zn_7-$FeCl_{3\text{-}0.5}$-ACNF	1	0.17	0.7
Zn_7-$FeAc_1$ -ACNF	1	0.32	0.25
Zn_7-$FeAcAc_1$ -ACNF	1	0.16	0.5
Zn_7-$FeCl_{3\text{-}1}$ -ACNF	1	0.34	0.7
Zn_7-$FeAc_2$ -ACNF	2	0.64	0.5
Zn_7-$FeAcAc_2$ -ACNF	2	0.32	0.5
Zn_7-$FeCl_{3\text{-}2}$ -ACNF	2	0.68	0.7
PVP_5-$FeAc_1$ -ACNF	1	0.32	1
PVP_5-$FeAcAc_1$ -ACNF	1	0.16	1
PVP_5-$FeCl_{3\text{-}1}$ -ACNF	1	0.34	1

Cyclic voltammetry was applied in N_2 –saturated solution and the results are presented in Figure 25. The CV curves of Zn_7-$FeAc_{0.5}$-ACNF and Zn_7-$FeAcAc_{0.5}$-ACNF electrodes (Figure 26a, red and black curves) showed lower electrochemical capacitance than for the reference $Fe_{0.5}NC$ layer (blue curve in Figure 26a). This corresponds to smaller accessibility of catalytic particles and, as a consequence, a much lower ORR activity is observed for those electrodes compared to the $Fe_{0.5}NC$ layer (Figure 26a). The Zn_7-$FeCl_{3\text{-}0.5}$-ACNF demonstrated significantly higher CV in N_2-saturated electrolyte compared to Zn_7-$FeAc_{0.5}$-ACNF and Zn_7-$FeAcAc_{0.5}$-ACNF electrodes (compare the green to the black and red curves in Figure 26a), and even higher than the $FeAc_{0.5}$ reference layer. This improved capacitance is correlated with a relatively high ORR activity, now quite close to that of the $Fe_{0.5}NC$ layer (Figure 26a, green curve). The reversible peak at 0.77 V/RHE

corresponds to the Fe^{2+}/Fe^{3+} redox couple (Figure 26a, green curve). Similar correlation between broad CV curve measured in nitrogen saturated electrolyte and high ORR activity is visible also for Zn_7-FeX_1-ACNF and PVP_5-FeX_1-ACNF (Figure 26 b, d and Figure 27 b,d). However, at even higher Fe content, no correlation is seen between the broad CVs in nitrogen-saturated electrolyte observed for Zn_7-FeX_2-ACNF and the ORR activity (Figure 26c). It is known in the field that excess iron before pyrolysis can lead to negative effects due to formation of Fe particles instead of atomically dispersed FeN_x sites.

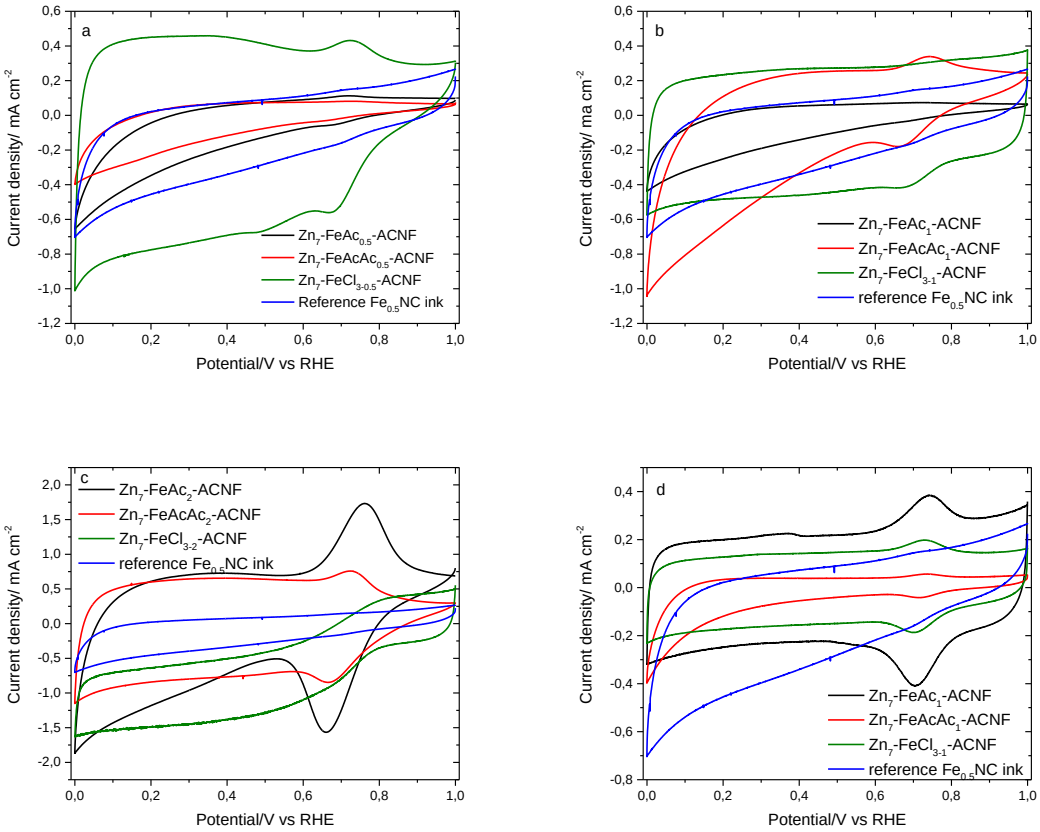

Figure 25: Cyclic voltammetry in N_2-saturated 0.1 M H_2SO_4 of FeNC self-standing electrodes measured in a RDE setup. a) 0.5%wt Fe-doped ACNF with 7%wt $ZnCl_2$ as porogen, b) 1%wt Fe-doped ACNF with 7%wt $ZnCl_2$ as porogen, c) 2%wt Fe-doped ACNF with 7%wt $ZnCl_2$ as porogen, d) 1%wt Fe-doped ACNF with 7%wt PVP as porogen.

The RDE measurements were performed for all samples described above and the results are presented in Figure 26. All self-standing electrodes showed lower activity in ORR compared to the $Fe_{0.5}$NC layer,

although Zn_7-$FeCl_{3\text{-}0.5}$-ACNF, Zn_7-$FeAc_1$-ACNF, Zn_7-$FeCl_{3\text{-}1}$-ACNF demonstrated relatively high electrocatalytic activity compared to Zn_7-$FeAc_{0.5}$-ACNF and Zn_7-$FeAcAc_{0.5}$-ACNF materials.

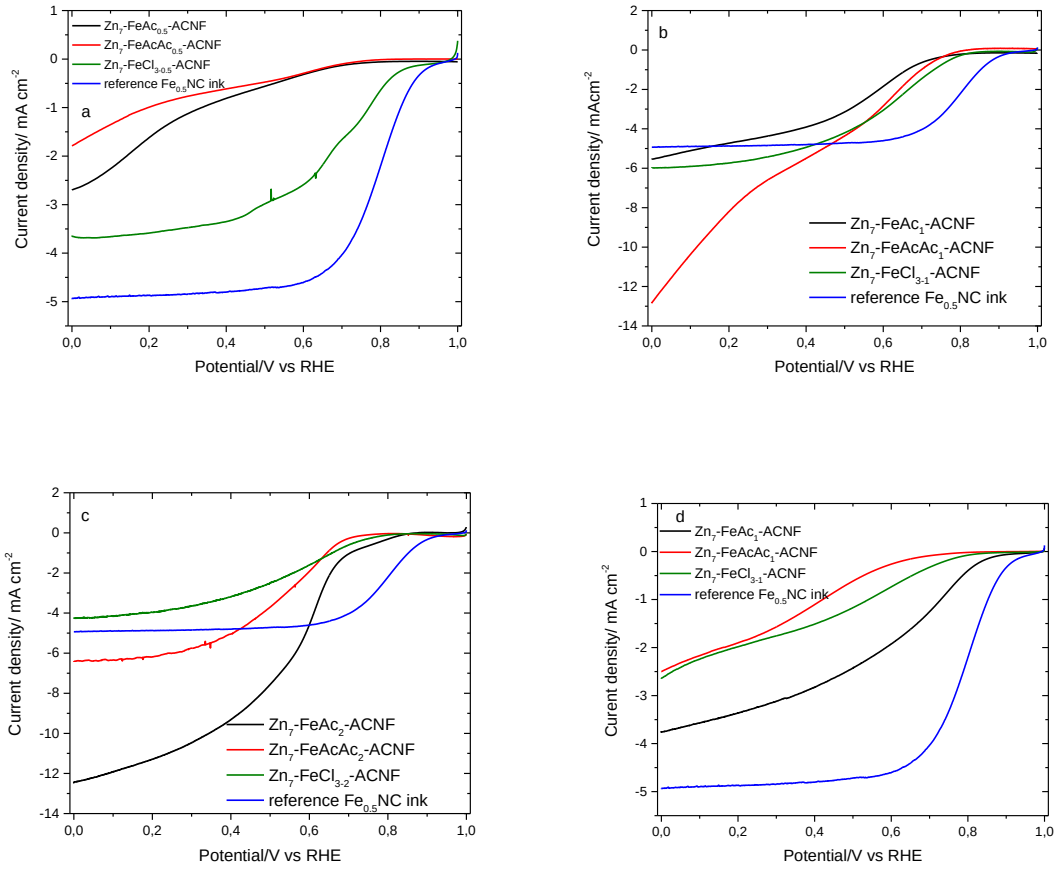

Figure 26: ORR polarization curves in O_2-saturated 0.1 M H_2SO_4 of FeNC self-standing electrodes measured in a RDE setup. a) 0.5%wt Fe-doped ACNF with 7%wt $ZnCl_2$ as porogen, b) 1%wt Fe-doped ACNF with 7%wt $ZnCl_2$ as porogen, c) 2%wt Fe-doped ACNF with 7%wt $ZnCl_2$ as porogen, d) 1%wt Fe-doped with 7%wt PVP as porogen ACNF. The curves are compared to the layer prepared from an ink of the reference $Fe_{0.5}$NC catalyst. The rotation rate was 1600 rpm.

Due to the different catalyst loadings for self-standing electrodes and the reference Fe0.5NC layer, the curves were normalized by the catalyst loading, and the ensuing mass activity measured at 0.8 V vs. RHE is presented in Figure 27 for all Zn_7-FeX_x-ACNF samples, and in Figure 28 for all PVP_5-FeX_1-ACNF

samples. The most promising materials are Zn_7-$FeCl_{3\text{-}0.5}$-ACNF, Zn_7-$FeAc_1$-ACNF, with mass activity of 0.88 A g^{-1} and 0.84 A g^{-1} respectively.

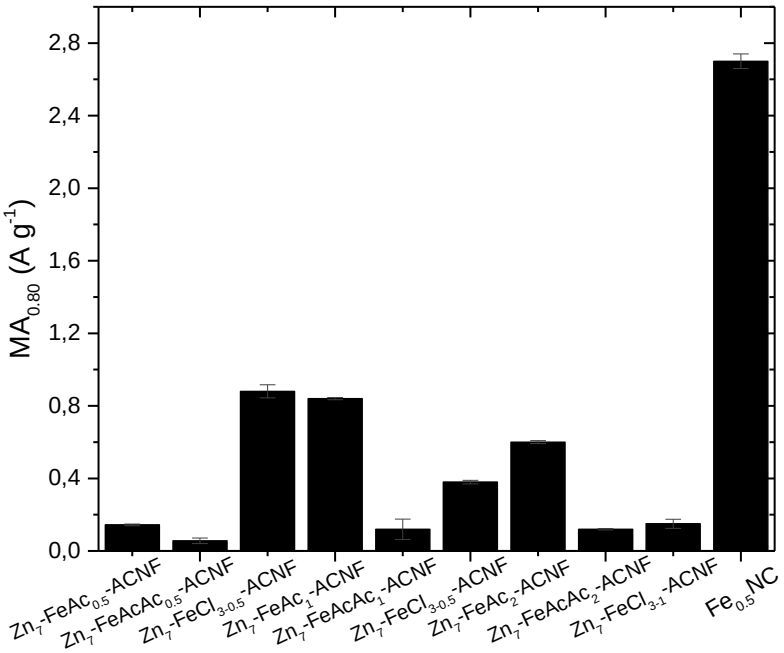

Figure 27: ORR mass activity for self-standing FeNC cathodes prepared from PAN and $ZnCl_2$, measured at 0.8 V vs RHE and comparison to the mass activity of the $Fe_{0.5}$NC powder catalyst deposited as an ink. The average activity and error bar was estimated from three independent measurements on three different layers.

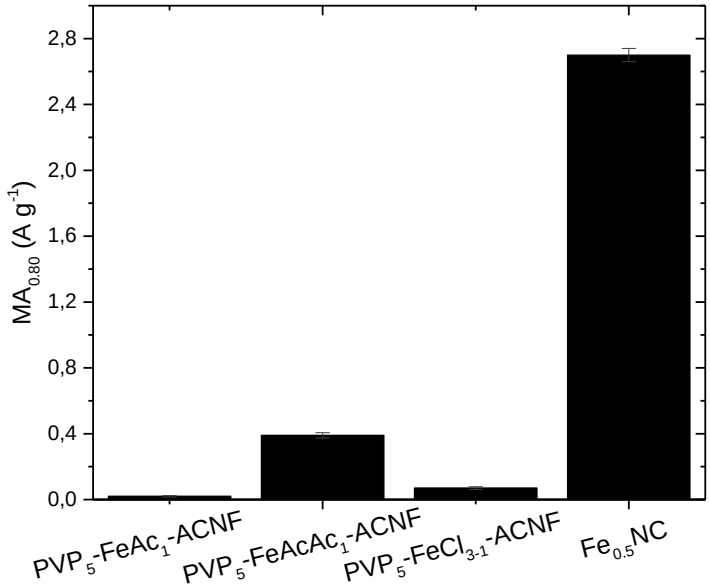

Figure 28: ORR mass activity for self-standing FeNC cathodes prepared from PAN and PVP, measured at 0.8 V vs RHE and comparison to the mass activity of the $Fe_{0.5}NC$ powder catalyst deposited as an ink. The average activtiy and error bar was estimated from three independent measurements on three different layers.

1.5.a Electrochemical properties of grinded FeNC electrodes derived from PAN/porogen/Fe-salt

To verify that RDE measurements on self-standing FeNC electrodes give an accurate value of their ORR activity and do not underestimate it (for example due to thick layers compared to active layers prepared from inks, or due to poor electric contact with the glassy carbon support), the self-standing electrodes with the highest mass activity (i.e Zn_7-$FeCl_{3\text{-}0.5}$-ACNF and Zn_7-$FeAcAc_2$-ACNF) were manually grinded in the mortar in order to obtain uniform FeNC powders. The latter still possess a fibrous structure (short fibers). Catalytic inks were then prepared as for the $Fe_{0.5}NC$ reference catalyst, and deposited on GC. The labels of these new catalyst samples are Zn_7-$FeAcAc_2$-$ACNF_g$ and Zn_7-$FeCl_{3\text{-}0.5}$-$ACNF_g$ respectively, g standing for “grinded”. The RDE results are presented in Figure 29.

The reversible peak at 0.77 V vs. RHE, related to the Fe^{2+}/Fe^{3+} redox couple, is visible in Figure 29a (CV in nitrogen saturated solution) for all ink-derived layers and self-standing electrodes, while no such peak is observed for the $Fe_{0.5}NC$ catalytic layer. Furthermore, the CV curve for the $Fe_{0.5}NC$ catalytic layer is narrow, but leads to the highest ORR activity (Figure 29b). Generally, the grinding of self-standing FeNC electrodes and deposition as catalytic layer did not improve their CV nor ORR polarization curves, compared to measurements performed on self-standing electrodes attached to the GC simply by a Nafion drop.

The mass activity of grinded FeNC electrodes at 0.8 V vs RHE is 0.18 A g^{-1} for Zn_7-$FeAcAc_2$-$ACNF_g$ and 0.28 A g^{-1} for Zn_7-$FeCl_{3\text{-}0.5}$-$ACNF_g$, respectively. There is a slight activity drop for Zn_7-$FeAcAc_2$-$ACNF_g$ compared to Zn_7-$FeAcAc_2$-ACNF (0.12 A g^{-1} vs 0.16 A/g) but a huge activity drop for Zn_7-$FeCl_{3\text{-}0.5}$-$ACNF_g$ compared to Zn_7-$FeCl_{3\text{-}0.5}$-ACNF (0.28 A g^{-1} vs 0.88 A g^{-1} , respectively). This leads to the conclusion that manual grinding does not significantly improve the activity, and that the measurements made on the self-standing electrodes are representative of the best achievable ORR activity with such electrodes. The maximum ORR activity obtained with this approach for preparing self-standing FeNC electrodes remained significantly lower than that obtained with a catalytic layer of a reference $Fe_{0.5}NC$ catalyst.

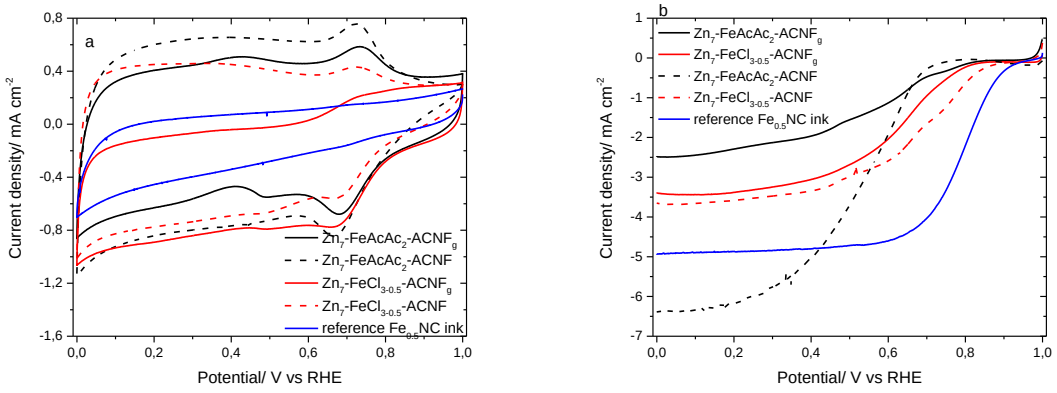

Figure 29: Electrochemical characterization with a RDE setup of self-standing FeNC electrodes (dotted curves) and grinded FeNC electrodes (solid curves) prepared from Fe salt, PAN and ZnCl2: a) CV in nitrogen saturated pH 1 solution, b) ORR polarization curves in oxygen saturated solution of 0.1 M H_2SO_4. For b), the rotation rate was 1600 rpm.

1.6 Conclusions

The approach for preparing CNFs from the co-electrospinning of PAN with a secondary polymer or inorganic porogen (PMMA, Nafion®, PVP, $ZnCl_2$) resulted in CNFs with closed porosity after carbonization in Ar. Subsequent activation in ammonia at 900 °C opened the closed porosity, resulting in high specific surface area in the range of 325-1083 m^2g^{-1}. The ammonia activation step systematically decreased the electric conductivity of the carbon fiber webs by circa a factor of two-three. However, the remaining conductivity is still sufficiently high for PEMFC application. Furthermore, a negative linear correlation between electric conductivity of ammonia-activated ACNF webs and their BET area is revealed

Self-standing FeNC electrodes were then prepared via electrospinning PAN/porogen/salt solutions (porogen = PVP or $ZnCl_2$) followed by carbonization in argon and activation in ammonia. After Fe content optimization, the highest ORR mass activity for a self-standing FeNC electrode prepared by this approach was 0.88 A g^{-1}, versus 2.71 A g^{-1} for the mass activity measured on an active layer prepared by ink formulation of the reference $Fe_{0.5}NC$ catalyst (prepared via pyrolysis in argon only). Taking into account that ammonia activation leads to enhanced activity for FeNC catalysts, but highly unstable FeN_x sites, this approach was not further pursued.

1. Liu, C.-K.; Lai, K.; Liu, W.; Yao, M.; Sun, R.-J. Preparation of carbon nanofibres through electrospinning and thermal treatment. *Polym. Int.* **2009**, *58*, 1341–1349.

2. Gopalakrishnan, A.; Sahatiya, P.; Badhulika, S. Template-Assisted Electrospinning of Bubbled Carbon Nanofibers as Binder-Free Electrodes for High-Performance Supercapacitors. *ChemElectroChem* **2018**, *5*, 531–539.

3. Nan, D.; Wang, J.-G.; Huang, Z.-H.; Wang, L.; Shen, W.; Kang, F. Highly porous carbon nanofibers from electrospun polyimide/SiO2 hybrids as an improved anode for lithium-ion batteries. *Electrochem. commun.* **2013**, *34*, 52–55.

4. Zhang, L.; Jiang, Y.; Wang, L.; Zhang, C.; Liu, S. Hierarchical porous carbon nanofibers as binder-free electrode for high-performance supercapacitor. *Electrochim. Acta* **2016**, *196*, 189–196.

5. Alothman, Z.A. A review: Fundamental aspects of silicate mesoporous materials. *Materials (Basel).* **2012**, *5*, 2874–2902.

6. Ma, C.; Cao, E.; Li, J.; Fan, Q.; Wu, L.; Song, Y.; Shi, J. Synthesis of mesoporous ribbon-shaped graphitic carbon nanofibers with superior performance as efficient supercapacitor electrodes. *Electrochim. Acta* **2018**, *292*, 364–373.

7. Chen, Y.; Lu, Z.; Zhou, L.; Mai, Y.-W.; Huang, H. In situ formation of hollow graphitic carbon nanospheres in electrospun amorphous carbon nanofibers for high-performance Li-based batteries. *Nanoscale* **2012**, *4*, 6800.

8. Xie, W.; Khan, S.; Rojas, O.J.; Parsons, G.N. Control of Micro- and Mesopores in Carbon Nanofibers and Hollow Carbon Nanofibers Derived from Cellulose Diacetate via Vapor Phase Infiltration of Diethyl Zinc. *ACS Sustain. Chem. Eng.* **2018**, *6*, 13844–13853.

9. Ma, C.; Li, Z.; Li, J.; Fan, Q.; Wu, L.; Shi, J.; Song, Y. Lignin-based hierarchical porous carbon nanofiber films with superior performance in supercapacitors. *Appl. Surf. Sci.* **2018**, *456*, 568–576.

10. Kim, C.; Ngoc, B.T.N.; Yang, K.S.; Kojima, M.; Kim, Y.A.; Kim, Y.J.; Endo, M.; Yang, S.C. Self-sustained thin Webs consisting of porous carbon nanofibers for supercapacitors via the electrospinning of polyacrylonitrile solutions containing zinc chloride. *Adv. Mater.* **2007**, *19*, 2341–2346.

11. Yin, D.; Han, C.; Bo, X.; Liu, J.; Guo, L. Prussian blue analogues derived iron-cobalt alloy embedded in nitrogen-doped porous carbon nanofibers for efficient oxygen reduction reaction in both alkaline and acidic solutions. *J. Colloid Interface Sci.* **2019**, *533*, 578–587.

12. Zhang, W.; Yao, X.; Zhou, S.; Li, X.; Li, L.; Yu, Z.; Gu, L. ZIF-8/ZIF-67-Derived Co-N $_x$ -Embedded 1D Porous Carbon Nanofibers with Graphitic Carbon-Encased Co Nanoparticles as an Efficient Bifunctional Electrocatalyst. *Small* **2018**, *14*, 1800423.

13. Yao, Y.; Liu, P.; Li, X.; Zeng, S.; Lan, T.; Huang, H.; Zeng, X.; Zou, J. Nitrogen-doped graphitic hierarchically porous carbon nanofibers obtained: Via bimetallic-coordination organic framework modification and their application in supercapacitors. *Dalt. Trans.* **2018**, *47*, 7316–7326.

14. Wang, C.; Kaneti, Y.V.; Bando, Y.; Lin, J.; Liu, C.; Li, J.; Yamauchi, Y. Metal-organic framework-derived one-dimensional porous or hollow carbon-based nanofibers for energy storage and conversion. *Mater. Horizons* **2018**, *5*, 394–407.

15. Peng, Y.; Lo, C. Electrospun porous carbon nanofibers as lithium ion battery anodes. *J. Solid State Electrochem.* **2015**, *19*, 3401–3410.

16. Cao, Y.; Lu, H.; Hong, Q.; Bai, J.; Wang, J.; Li, X. Co decorated N-doped porous carbon nanofibers as a free-standing cathode for Li-O2 battery: Emphasis on seamlessly continuously hierarchical 3D nano-architecture networks. *J. Power Sources* **2017**, *368*, 78–87.

17. Zhang, W.; Miao, W.; Liu, X.; Li, L.; Yu, Z.; Zhang, Q. High-rate and ultralong-stable potassium-ion batteries based on antimony-nanoparticles encapsulated in nitrogen and phosphorus co-doped mesoporous carbon nanofibers as an anode material. *J. Alloys Compd.* **2018**, *769*, 141–148.

18. Jeong, J.; Choun, M.; Lee, J. Tree-Bark-Shaped N-Doped Porous Carbon Anode for Hydrazine Fuel Cells. *Angew. Chemie - Int. Ed.* **2017**, *56*, 13513–13516.

19. Zhao, X.; Xiong, P.; Meng, J.; Liang, Y.; Wang, J.; Xu, Y. High rate and long cycle life porous carbon nanofiber paper anodes for potassium-ion batteries. *J. Mater. Chem. A* **2017**, *5*, 19237–19244.

20. An, G.-H.; Koo, B.-R.; Ahn, H.-J. Activated mesoporous carbon nanofibers fabricated using water etching-assisted templating for high-performance electrochemical capacitors. *Phys. Chem. Chem. Phys.* **2016**, *18*, 6587–6594.

21. He, T.; Fu, Y.; Meng, X.; Yu, X.; Wang, X. A novel strategy for the high performance supercapacitor based on polyacrylonitrile-derived porous nanofibers as electrode and separator in ionic liquid electrolyte. *Electrochim. Acta* **2018**, *282*, 97–104.

22. Yang, D.S.; Chaudhari, S.; Rajesh, K.P.; Yu, J.S. Preparation of nitrogen-doped porous carbon nanofibers and the effect of porosity, electrical conductivity, and nitrogen content on their oxygen reduction performance. *ChemCatChem* **2014**, *6*, 1236–1244.

23. Tran, C.; Kalra, V. Fabrication of porous carbon nanofibers with adjustable pore sizes as electrodes for supercapacitors. *J. Power Sources* **2013**, *235*, 289–296.

24. Wang, W.; Wang, H.; Wang, H.; Jin, X.; Li, J.; Zhu, Z. Electrospinning preparation of a large surface area, hierarchically porous, and interconnected carbon nanofibrous network using polysulfone as a sacrificial polymer for high performance supercapacitors. *RSC Adv.* **2018**, *8*, 28480–28486.

25. Liu, J.; Xiong, Z.; Wang, S.; Cai, W.; Yang, J.; Zhang, H. Structure and electrochemistry comparison of electrospun porous carbon nanofibers for capacitive deionization. *Electrochim. Acta* **2016**, *210*, 171–180.

26. Ji, L.; Zhang, X. Fabrication of porous carbon nanofibers and their application as anode materials for rechargeable lithium-ion batteries. *Nanotechnology* **2009**, *20*, 155705.

27. Zhang, H.; Xie, Z.; Wang, Y.; Shang, X.; Nie, P.; Liu, J. Electrospun polyacrylonitrile/β-cyclodextrin based porous carbon nanofiber self-supporting electrode for capacitive deionization. *RSC Adv.* **2017**, *7*, 55224–55231.

28. Le, T.H.; Tian, H.; Cheng, J.; Huang, Z.H.; Kang, F.; Yang, Y. High performance lithium-ion capacitors based on scalable surface carved multi hierarchical construction electrospun carbon fibers. *Carbon N. Y.* **2018**, *138*, 325–336.

29. Heo, Y.-J.; Lee, H.I.; Lee, J.W.; Park, M.; Rhee, K.Y.; Park, S.-J. Optimization of the pore structure of PAN-based carbon fibers for enhanced supercapacitor performances via electrospinning. *Compos.*

Part B Eng. **2019**, *161*, 10–17.

30. Lee, H.M.; Kim, H.G.; Kang, S.J.; Park, S.J.; An, K.H.; Kim, B.J. Effects of pore structures on electrochemical behaviors of polyacrylonitrile (PAN)-based activated carbon nanofibers. *J. Ind. Eng. Chem.* **2015**, *21*, 736–740.

31. Kim, C.; Yang, K.S. Electrochemical properties of carbon nanofiber web as an electrode for supercapacitor prepared by electrospinning. *Appl. Phys. Lett.* **2003**, *83*, 1216–1218.

32. Zhang, T.; Xiao, B.; Zhou, P.; Xia, L.; Wen, G.; Zhang, H. Porous-carbon-nanotube decorated carbon nanofibers with effective microwave absorption properties. *Nanotechnology* **2017**, *28*, 355708.

33. Fitzer, E.; Frohs, W.; Heine, M. Optimization of stabilization and carbonization treatment of PAN fibres and structural characterization of the resulting carbon fibres. *Carbon N. Y.* **1986**, *24*, 387–395.

34. Moon, S.; Farris, R.J. Strong electrospun nanometer-diameter polyacrylonitrile carbon fiber yarns. *Carbon N. Y.* **2009**, *47*, 2829–2839.

35. Ercolano, G.; Farina, F.; Cavaliere, S.; Jones, D.J.; Rozière, J. Towards ultrathin Pt films on nanofibres by surface-limited electrodeposition for electrocatalytic applications. *J. Mater. Chem. A* **2017**, *5*, 3974–3980.

36. Savych, I.; Bernard D'Arbigny, J.; Subianto, S.; Cavaliere, S.; Jones, D.J.; Rozière, J. On the effect of non-carbon nanostructured supports on the stability of Pt nanoparticles during voltage cycling: A study of TiO2 nanofibres. *J. Power Sources* **2014**, *257*, 147–155.

37. Peng, S.; Li, L.; Kong Yoong, J.L.; Tian, L.; Srinivasan, M.; Adams, S.; Ramakrishna, S. Electrospun carbon nanofibers and their hybrid composites as advanced materials for energy conversion and storage. *Nano Energy* **2016**.

38. Heikkilä, P.; Harlin, A. Electrospinning of polyacrylonitrile (PAN) solution: Effect of conductive additive and filler on the process. *Express Polym. Lett.* **2009**, *3*, 437–445.

39. Subianto, S.; Cornu, D.; Cavaliere, S. Fundamentals of Electrospinning. In *Electrospinning for Advanced Energy and Environmental Applications*; Cavaliere, S., Ed.; Boca Raton, 2015; pp. 1–27 ISBN 978-1-4822-1767-4.

40. Sun, J.; Zeng, L.; Jiang, H.R.; Chao, C.Y.H.; Zhao, T.S. Formation of electrodes by self-assembling porous carbon fibers into bundles for vanadium redox flow batteries. *J. Power Sources* **2018**, *405*, 106–113.

41. Zhao, X.; Xiong, P.; Meng, J.; Liang, Y.; … J.W.-J. of M.; 2017, undefined High rate and long cycle life porous carbon nanofiber paper anodes for potassium-ion batteries. *pubs.rsc.org*.

42. Karacan, I.; Erzurumluoğlu, L. The effect of carbonization temperature on the structure and properties of carbon fibers prepared from poly(m-phenylene isophthalamide) precursor. *Fibers Polym.* **2015**, *16*, 1629–1645.

43. Shi, R.; Han, C.; Xu, X.; Qin, X.; Xu, L.; Li, H.; Li, J.; Wong, C.P.; Li, B. Electrospun N-Doped Hierarchical Porous Carbon Nanofiber with Improved Degree of Graphitization for High-Performance Lithium Ion Capacitor. *Chem. - A Eur. J.* **2018**, *24*, 10460–10467.

44. Ferreira, E.H.M.; Cançado, L.G.; Kulmala, T.S.; Moutinho, M.V.O.; Capaz, R.B.; Stavale, F.; Jorio, A.;

Achete, C.A.; Ferrari, A.C.; Lombardo, A. Quantifying Defects in Graphene via Raman Spectroscopy at Different Excitation Energies. *Nano Lett.* **2011**, *11*, 3190–3196.

45. Gustavo Cançado, L.; Gomes da Silva, M.; Martins Ferreira, E.H.; Hof, F.; Kampioti, K.; Huang, K.; Pénicaud, A.; Alberto Achete, C.; Capaz, R.B.; Jorio, A. Disentangling contributions of point and line defects in the Raman spectra of graphene-related materials. *2D Mater.* **2017**, *4*, 025039.

46. Zhang, Z.; Li, X.; Wang, C.; Fu, S.; Liu, Y.; Shao, C. Polyacrylonitrile and carbon nanofibers with controllable nanoporous structures by electrospinning. *Macromol. Mater. Eng.* **2009**, *294*, 673–678.

47. Inagaki, M.; Yang, Y.; Kang, F. Carbon Nanofibers Prepared via Electrospinning. *Adv. Mater.* **2012**, *24*, 2547–2566.

48. Jaouen, F.; Serventi, A.M.; Lefèvre, M.; Dodelet, J.P.; Bertrand, P. Non-noble electrocatalysts for O2 reduction: How does heat treatment affect their activity and structure? Part II. Structural changes observed by electron microscopy, Raman, and mass spectroscopy. *J. Phys. Chem. C* **2007**, *111*, 5971–5976.

49. Jaouen, F.; Dodelet, J.P. Non-noble electrocatalysts for O2 reduction: How does heat treatment affect their activity and structure? Part I. Model for carbon black Gasification by NH3: Parametric Calibration and Electrochemical Validation. *J. Phys. Chem. C* **2007**, *111*, 5963–5970.

50. Shen, W.; Fan, W. Nitrogen-containing porous carbons: Synthesis and application. *J. Mater. Chem. A* **2013**, *1*, 999–1013.

51. Artyushkova, K.; Kiefer, B.; Halevi, B.; Knop-Gericke, A.; Schlogl, R.; Atanassov, P. Density functional theory calculations of XPS binding energy shift for nitrogen-containing graphene-like structures. *Chem. Commun.* **2013**, *49*, 2539–2541.

52. Nan, D.; Huang, Z.-H.; Lv, R.; Yang, L.; Wang, J.-G.; Shen, W.; Lin, Y.; Yu, X.; Ye, L.; Sun, H.; et al. Nitrogen-enriched electrospun porous carbon nanofiber networks as high-performance free-standing electrode materials. *J. Mater. Chem. A* **2014**, *2*, 19678–19684.

53. Subianto, S.; Cavaliere, S.; Jones, D.J.; Rozière, J. Effect of side-chain length on the electrospinning of perfluorosulfonic acid ionomers. *J. Polym. Sci. Part A Polym. Chem.* **2013**, *51*, 118–128.

54. Ballengee, J.B.; Pintauro, P.N. Morphological Control of Electrospun Nafion Nanofiber Mats. *J. Electrochem. Soc.* **2011**, *158*, B568.

55. Brunauer, S.; Emmett, P.H.; Teller, E. Adsorption of Gases in Multimolecular Layers. *J. Am. Chem. Soc.* **1938**, *60*, 309–319.

56. Fehse, M.; Cavaliere, S.; Lippens, P.E.; Savych, I.; Iadecola, A.; Monconduit, L.; Jones, D.J.; Rozière, J.; Fischer, F.; Tessier, C.; et al. Nb-doped TiO2 nanofibers for lithium ion batteries. *J. Phys. Chem. C* **2013**, *117*, 13827–13835.

57. Atamny, F.; Blöcker, J.; Dübotzky, A.; Kurt, H.; Timpe, O.; Loose, G.; Mahdi, W.; Schlögl, R. Surface chemistry of carbon: Activation of molecular oxygen. *Mol. Phys.* **1992**, *76*, 851–886.

58. Liu, Y.; Murphy, M.W.; Baker, D.R.; Gu, W.; Ji, C.; Jorne, J.; Gasteiger, H.A. Proton Conduction and Oxygen Reduction Kinetics in {PEM} Fuel Cell Cathodes: Effects of Ionomer-to-Carbon Ratio and Relative Humidity. *J. Electrochem. Soc.* **2009**, *156*, B970.

59. Liu, Y.; Ji, C.; Gu, W.; Jorne, J.; Gasteiger, H.A. Effects of Catalyst Carbon Support on Proton Conduction and Cathode Performance in {PEM} Fuel Cells. *J. Electrochem. Soc.* **2011**, *158*, B614.

60. Baghalha, M.; Stumper, J.; Harvey, D.; Eikerling, M. Modeling the Effect of Low Carbon Conductivity of the Cathode Catalyst Layer on {PEM} Fuel Cell Performance.; ECS, 2010.

61. Savych, I.; Subianto, S.; Nabil, Y.; Cavaliere, S.; Jones, D.; Rozière, J. Negligible degradation upon in situ voltage cycling of a PEMFC using an electrospun niobium-doped tin oxide supported Pt cathode. *Phys. Chem. Chem. Phys.* **2015**, *17*, 16970–16976.

62. Lu, X.; Wang, C.; Favier, F.; Pinna, N. Electrospun Nanomaterials for Supercapacitor Electrodes: Designed Architectures and Electrochemical Performance. *Adv. Energy Mater.* **2017**, *7*, 1–43.

63. Goellner, V.; Armel, V.; Zitolo, A.; Fonda, E.; Jaouen, F. Degradation by Hydrogen Peroxide of Metal-Nitrogen-Carbon Catalysts for Oxygen Reduction. *J. Electrochem. Soc.* **2015**, *162*, H403–H414.

64. Armel, V.; Hannauer, J.; Jaouen, F. Effect of ZIF-8 crystal size on the O<inf>2</inf> electro-reduction performance of pyrolyzed Fe–N–C catalysts. *Catalysts* **2015**, *5*, 1333–1351.

65. Zitolo, A.; Goellner, V.; Armel, V.; Sougrati, M.-T.; Mineva, T.; Stievano, L.; Fonda, E.; Jaouen, F. Identification of catalytic sites for oxygen reduction in iron- and nitrogen-doped graphene materials. *Nat. Mater.* **2015**, *14*, 937–942.

Chapter 2: Study of ferrocene-doped nano MOFs as precursors for active FeNC powder catalysts

Summary

2.1 Introduction

In chapter 1, a first possible route towards the preparation of FeNC self-standing electrodes was investigated. The Fe salt was introduced in the electrospinning solution comprising a polymer (PAN) as a precursor of the C and N elements, as well as an optional porogen (a second polymer or $ZnCl_2$), the Fe, N and C elements all being required for forming FeN_xC_y ORR active sites during pyrolysis. This solution was electrospun and converted via pyrolysis in Ar and then NH_3 into FeNC electrodes. The results obtained using this "one-pot" approach were not satisfactory enough, and thus other methods to fabricate fibrous self-standing FeNC cathodes were investigated.

One alternative route that can also be coined as a one-pot approach involves the use of a polymer combined with a Fe-doped metal organic frameworks (MOF) instead of simply the Fe salt as Fe precursors. MOFs, and in particular zeolitic imidazolate frameworks (ZIFs), are currently used to prepare *via* pyrolysis the state-of-art FeNC powder catalysts[1–4]. In the electrospinning approach, the Fe-doped MOF particles or crystals can thus be combined with the polymer in order to result in carbonized fibers with enhanced porosity and increased number of FeN_x sites in the carbon domains that are derived from the pyrolyzed MOFs. Compared to the synthesis of powder FeNC catalysts however, one additional requirement concerns the size of the MOF particles or crystals, which should be commensurate with the diameter of the CNFs derived from the electrospun polymer. If the MOF particles or crystals are much larger than the fiber diameters, they may not be integrated in the self-standing CNF structure.

In this approach, MOF nanoparticles or nanocrystals must first be synthesized, and then added to the electrospinning solution. The intuitively optimum approach further leans on the synthesis of Fe-doped nano-MOFs, so that Fe cations are already located on or inside the MOFs that are converted into an ORR-active FeNC domain during pyrolysis, rather than adding separately an Fe salt and nano-MOFs into the electrospinning solution.

Notably, Fe-doped ZIF-8 can first be synthesized and then introduced in the polymer solution in order to obtain FeNC 3D electrodes. This method was also investigated in the ICGM-AIME laboratory and in the frame of the CAT^{2}CAT project [5]. In summary, nanosized Fe-doped ZIF-8 was synthesized and then co-electrospun with PAN, pyrolyzed and investigated (after mild grinding) as ORR catalyst in RDE and also in PEMFC. While reasonably high ORR activity was observed both in RDE and in H_2/O_2 PEMFC measurements, structural characterization revealed that this approach resulted in a high fraction of Fe being converted to

metallic iron and iron carbide species rather than into FeN_x sites. The formation of such Fe particles was not observed when the Fe-doped nano-ZIF-8 was directly converted to an FeNC powder without using electrospinning, and it was not observed when the PAN polymer was mixed to Fe-doped nano-ZIF-8 and pyrolyzed (also without resorting to electrospinning).

It was thus concluded that the observed Fe agglomeration was intimately connected to the electrospinning process, possibly as a result of the high voltage or due to high mechanical shear-stress when the electrospun solution leaves the needle. The formation of Fe agglomerates is not only detrimental to the number of active FeN_x sites but also to the durability of FeNC electrodes, since metallic and metal-carbide particles easily leach Fe out during operation in acidic medium, polluting the Nafion ionomer and resulting in decreased proton concentration but also triggering Fenton reactions[6–8].

To overcome this challenge, another approach for the fabrication of FeNC self-standing cathodes with electrospinning technique can consist in the separate preparation of a self-standing mat of polymer fibers via electrospinning, followed by the crystalline growth of Fe-doped MOFs onto the polymer fibers. The Fe-doped MOFs can be grown or deposited onto the fiber mat, exploiting for example the possibility of Zn^{2+} to coordinate with -C≡N groups present on the surface of PAN fibers [9], or with imidazole groups present in polybenzimidazole (PBI) fibers. In this approach, the polymer nanofibrous mats are prepared via electrospinning and then immersed in a solution containing the MOF precursors (Zn^{2+} and ligand) and the Fe precursor. It is expected that this process can result in the crystalline growth of Fe-doped MOFs on the polymer webs. Such self-standing structures can then be pyrolyzed to result in self-standing FeNC cathodes with mostly FeN_x sites, since the Fe precursors will not have been subjected to the electrospinning conditions that are deleterious for the atomic dispersion of Fe.

In this chapter, the first step toward the development of self-standing electrodes via this approach was undertaken, focusing on the synthesis and optimization of Fe-doped nano-MOFs. The optimized conditions are then used for preparing Fe-doped nano-MOFs to be used via this approach (chapters 3-4).

Zeolitic Imidazolate Frameworks (ZIF) are a class of porous MOFs with extended 3D structures constructed from tetrahedral metal ions, bridged by imidazolate (dimethyl imidazole linker) and topologically isomorphic with natural zeolites[10]. They attracted significant attention due their special network structure and flexibility (e.g tunable porosity) [11] in different fields, for example, gas storage/separation [12], drug-delivery [13] or catalysis for ORR [4,11,14–16] and so on. ZIF-derived porous

carbon structures also contain a rich nitrogen source in imidazole ligands, making this class of MOFs a perfect candidate for FeNC catalysts with high ORR activity both in RDE and PEMFCs[17].

Substituted imidazolate material-1 (SIM-1) is a zeolitic imidazole framework that consists of ZnN_4 tetrahedra linked by 4,5-imidazolecarboxyaldehyde. SIM-1 was firstly synthesized by the CAT^{2}CAT project partner IRCELYON [18] and is isostructural with the Zn-based ZIF named ZIF-8. The structure of both materials is present in Figure 30. Those two materials are particularly interesting because of their cavity structure. The pore size of ZIF-8 and SIM-1 is similar of 3.4 Å and a cavity diameter is 11 Å [19].

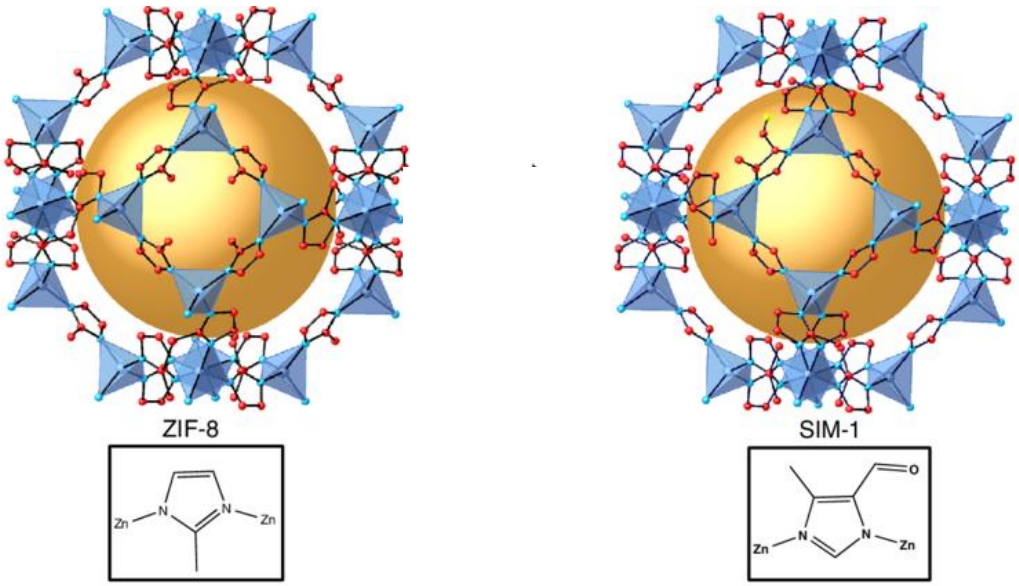

Figure 30: Cartoon representation of ZIF-8 and SIM-1. Reprinted from ref [20]

These properties allow ZIF-8 and SIM-1 to trap into its cavities Fe-based salt or even molecule, a nearly ideal precursor in order to obtain ORR-active FeNC materials after thermal treatment [21]. One of suitable Fe molecule for the encapsulation into SIM-1 or ZIF-8 cavities is ferrocene (Figure 31).

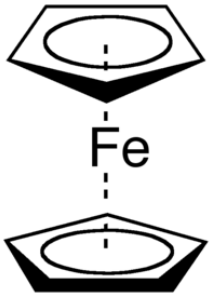

Figure 31: Structure of ferrocene

Due to its small molecular size of 6.4 Å [22], it is compatible with the target of encapsulation into the cavities of the targeted MOFs [23]. The selected ferrocene doped SIM-1 and ZIF-8 samples were investigated morphologically, texturally before and after pyrolysis, and eventually, electrochemically in order to down-select the most promising ones and apply this synthesis for their growth on electrospun polymer nanofiber webs (as described in more details in chapter 4).

2.2 Methodology

2.2.a Synthesis of Ferrocene-doped MOFs

In order to maximize the activity of Fe sites in the FeNC catalysts it is necessary to establish the optimum quantity of Fe sites in catalysts. Too large contents of Fe can lead to the formation of highly graphitized carbon structures during pyrolysis, where the quantity of FeNC sites is minimal[15,24–26]. In other hand, too small quantity of active Fe leads to insufficient ORR activity. The optimum content of Fe for FeNC catalysts before pyrolysis is studied previously and is typically below 2-3 wt%. Therefore it is important to optimize the Fe content in novel ferrocene-doped MOFs to achieve the best catalytic activity in ORR.

The precursors for growing Fe-doped SIM-1 were 4-methyl-5-imidazolecarboxaldehyde (99%, Sigma-Aldrich), ferrocene (98%, Sigma-Aldrich), zinc nitrate hexahydrate (99%, Sigma-Adrich) as adopted according to a literature report[27] .

The ligand was dissolved in 40 mL of ethanol at room temperature under magnetic stirring for few minutes. The temperature of solution was raised to 60 °C then the ferrocene and zinc nitrate were added. The molar ratio between imidazole ligand and zinc was 4:1; the quantity of doped Fe was set to 0.5; 1; 2; 5 and 10 mol % relative to Zn and the exact amount of used chemicals is presented in Table 7. The reaction leading to the growth of Fe-doped MOF was stopped after 24 hours, when the resulting solution was centrifuged at 10,000 rpm for 10 minutes and washed in ethanol. The centrifugation and washing was repeated 4 times and then the resulting powder was dried for 24h at 80 °C. The resulting materials were labelled as presented in Table 8, rows 2-6.

Table 7: Mass of each chemicals used for the synthesis of Fe-doped MOFs

	Zn/Fe at. Ratio in solution	mass 2-methylimidazole, g	mass 4-methyl-5-imidazolecarboxaldehyde, g	mass $Zn(NO_3)_2$, g	mass $FeCp_2$, mg
SIM-1	0.5	-	1	0.682	2.1
	1	-	1	0.682	4.2
	2	-	1	0.682	8.5
	5	-	1	0.682	21
	10	-	1	0.682	42
ZIF-8	0.5	2.322	-	2.1	6.7
	1	2.322	-	2.1	13.6
	2	2.322	-	2.1	27.4
	5	2.322	-	2.1	272

The precursors for growing Fe-doped ZIF-8 were 2-methylimidazole (99%, Sigma-Aldrich), ferrocene (98%, Sigma-Aldrich), zinc nitrate hexahydrate (99%, Sigma-Adrich) and N-N-dimethylformamide (DMF, 99%, Sigma-Aldrich. [28] The imidazole ligand was first dissolved in 40 mL of ethanol at room temperature using magnetic stirring for few minutes. After the heating for 140 °C, the ferrocene and zinc nitrate was added to following solution. The molar ratio between imidazole ligand and zinc was 4:1; the quantity of doped Fe was 0.5; 1; 2; and 5 mol % relative to Zn and the absolute mass that were used during synthesis are presented in Table 7.

The reaction leading to the growth of Fe-doped MOF was stopped after 24 hours, when the solution was centrifuged at 10,000 rpm for 10 minutes and washed in ethanol. The centrifugation and washing was repeated 4 times and then the resulting powder was dried for 24 h at 80 °C. The resulting materials were labelled as presented in Table 8, rows 7-10.

Table 8: Composition and labels of the prepared Fe-doped MOFs and the resulting FeNC catalysts

	Zn/Fe at. ratio in solution	Fe-doped MOFs	FeNC powder catalysts	Theoretical $(Fe/Zn)_{at}$
SIM-1	0.5	$[Fe/Zn]_{0,5}$SIM	$[Fe/Zn]_{0.5}$SIM-P	0.005
	1	$[Fe/Zn]_{1}$SIM	$[Fe/Zn]_{1}$SIM-P	0.01
	2	$[Fe/Zn]_{2}$SIM	$[Fe/Zn]_{2}$SIM-P	0.02
	5	$[Fe/Zn]_{5}$SIM	$[Fe/Zn]_{5}$SIM-P	0.05
	10	$[Fe/Zn]_{10}$SIM	$[Fe/Zn]_{10}$SIM-P	0.1
ZIF-8	0.5	$[Fe/Zn]_{0,5}$ZIF	$[Fe/Zn]_{0.5}$ZIF-P	0.005
	1	$[Fe/Zn]_{1}$ZIF	$[Fe/Zn]_{1}$ZIF-P	0.01
	2	$[Fe/Zn]_{2}$ZIF	$[Fe/Zn]_{2}$ZIF-P	0.02
	5	$[Fe/Zn]_{5}$ZIF	$[Fe/Zn]_{5}$ZIF-P	0.2

2.2.b Preparation of FeNC catalysts from ferrocene-doped MOF precursors

The catalyst precursors described in 2.1.a, were pyrolysed at 1050 °C in flowing Ar for 1 h via a ramp mode with a heating rate of 5 °C/min. After carbonization, the catalysts were manually grinded with a mortar.

2.2.c Electrochemical characterization

Electrochemical activity towards the ORR and initial performance of the catalysts was determined with a rotating disc electrode setup and in a single-cell laboratory fuel cell, respectively.

For RDE measurements, the ink was prepared by using 10 mg of grinded catalysts, 108.5 µL of Nafion perfluorinated resin solution (5 wt% in lower aliphatic alcohols and water, Sigma-Aldrich), 300 µL of ethanol (absolute, Sigma-Aldrich) and 36.5 µL ultrapure water 18MΩ. The ink was ultra-sonicated for 1h under temperature of 25 °C and then deposited on glassy carbon electrode with loading of 0.8 mg/cm^2 of catalyst and dried under air. The RDE experiment was performed in 0.1 M aqueous solution of H_2SO_4. The

working electrode was glassy carbon electrode (Pine research), rotating speed was 1600 rpm and all RDE data was measured with a BioLogic Potentiostat SP-300. Cyclic voltammetry scans were acquired between 0 and 1 V/RHE (v = 5 mV s^{-1} for nitrogen-saturated solutions and v = 2 mV s^{-1} for oxygen-saturated solutions).

2.3 Results and discussion

2.3.a Morphology of Fe-doped MOF crystals

The Fe-doped MOF crystals were grown in the organic solution of imidazole, zinc nitrate and ferrocene as described in 2.1.a and 2.1.b. The Fe/Zn ratio in solution and in the resulting ferrocene-doped MOF materials were compared, and it showed that the amount of ferrocene that can be encapsulated in ZIF-8 tends to be limited, the system reaching its saturation at the ratio of Fe/Zn of 2.5 at%. Below this ratio, the Fe/Zn ratio in solution predicts the ratio in the ferrocene doped ZIF-8, while above that ratio, the increase in ferrocene /Zn ratio in solution does not lead to a proportionaly increased Fe/Zn ratio in the Fe-doped ZIF-8 materials. For example, in order to synthesise ZIF-8 with an Fe/Zn ratio of 5 at %, it was necessary to start with a Fe/Zn ratio of 20 in solution. For even higher ferrocene content, the synthesis of ZIF-8 with an Fe/Zn ratio of 10 at % was never successful (results from ICELYON obtained in the CAT^{2}CAT project). On the contrary, with SIM-1, a 1-to-1 relation is observed between Fe/Zn ratio in solution and in the final ferrocene-doped SIM-1 materials, up to at least 10 at% Fe/Zn.

Scanning electron microscopy (SEM) was performed to investigate the morphology of the resulting MOF crystals, and their size distribution, before and after pyrolysis.

The morphology of $[Fe/Zn]_x$SIM structures prepared using different Fe/Zn ratios (see Table 8) is described in Figure 32 before and after pyrolysis. For all Fe/Zn ratios, the crystals have same shape of rhombic dodecahedra of micrometric sizes. The size of crystals of $[Fe/Zn]_{0.5}$SIM is ranging between 2 and 7 µm and this size dispersion is relatively similar for each Fe/Zn ratio, as can be seen in Figure 32.

After ramp pyrolysis at 1050 °C in Ar, the outer shape of the MOF crystals is, surprisingly, conserved for $[Fe/Zn]_x$SIM-P structures and the size of Fe-doped carbon particles remains relatively unchanged, in the range between 2 and 7 µm for $[Fe/Zn]_{0.5}$SIM-P, 3-5 µm for $[Fe/Zn]_1$SIM-P, 1-3 µm for $[Fe/Zn]_2$SIM-P, 2-4 µm for $[Fe/Zn]_5$SIM-P and 2-5 µm for $[Fe/Zn]_{10}$SIM-P (Figure 32).

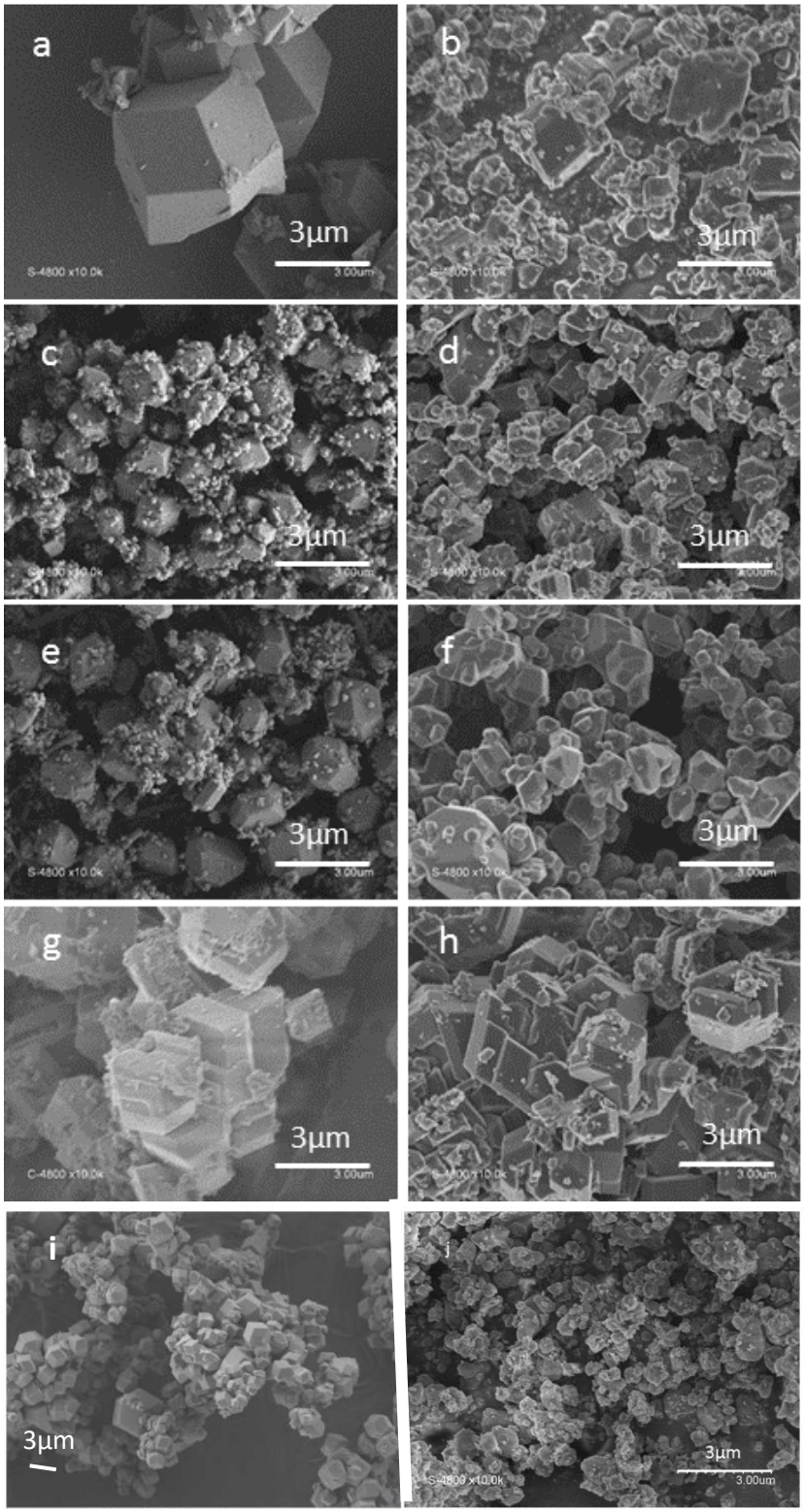

Figure 32: FE-SEM micrographs of a) $[Fe/Zn]_{0.5}$SIM, b) $[Fe/Zn]_{0.5}$SIM-P (i.e after pyrolysis at 1050° C in Ar), c) $[Fe/Zn]_{1}$SIM, d) $[Fe/Zn]_{1}$SIM-P, e) $[Fe/Zn]_{2}$SIM, f) $[Fe/Zn]_{2}$SIM-P, g) $[Fe/Zn]_{5}$SIM, h) $[Fe/Zn]_{5}$SIM-P, i) $[Fe/Zn]_{10}$SIM, j) $[Fe/Zn]_{10}$SIM

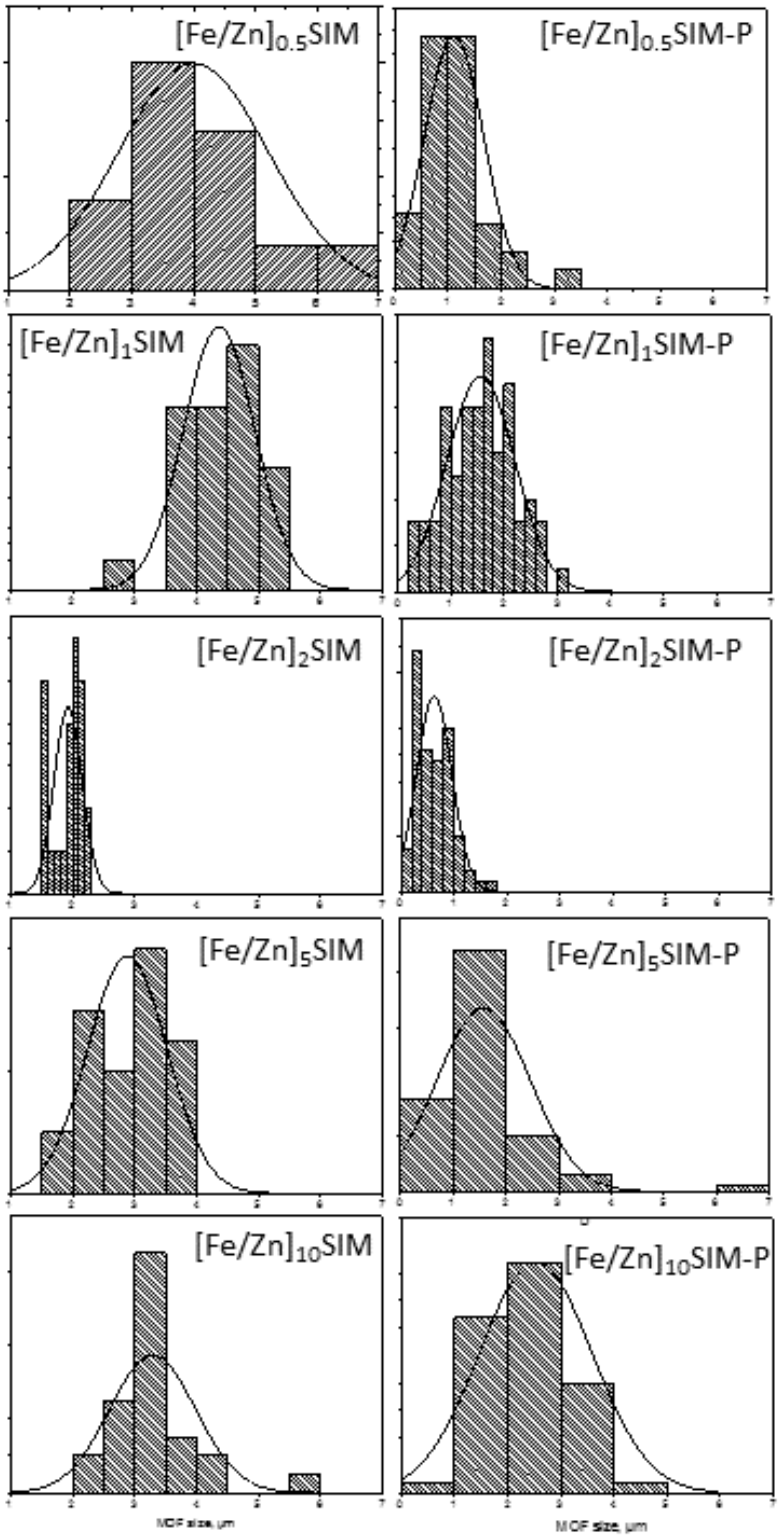

Figure 33 : MOF size distribution histogram before and after pyrolysis for SIM-1.

Figure 34 represents the FE-SEM micrographs of the $[Fe/Zn]_x$ZIF structures prepared with different Fe/Zn ratio. Compared to $[Fe/Zn]_x$SIM discussed afore, the $[Fe/Zn]_{0.5}$ZIF structures are micro-sized (ranged between 2 and 6 µm) and have a well-defined shape. The $[Fe/Zn]_1$ZIF structures are not only micro-sized (with the size between 2 and 4 µm) but also nano-sized particles can be seen (Figure 33, c). Also a bimodal size distribution of crystals can be observed for $[Fe/Zn]_2$ZIF and $[Fe/Zn]_5$ZIF, which can lead to the conclusion that ferrocene-doped ZIF-8 are represented by both micro- and nano-crystallinity.

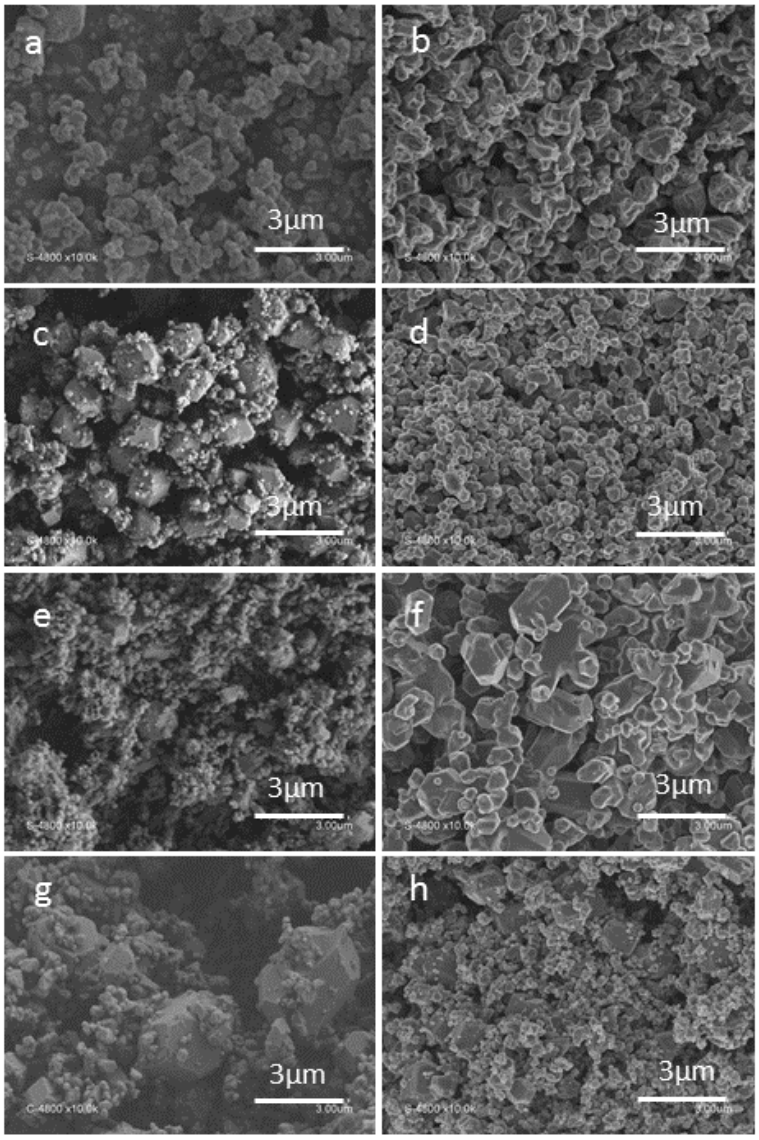

Figure 34 : FE-SEM micrographs of a) $[Fe/Zn]_{0.5}$ZIF, b) $[Fe/Zn]_{0.5}$ZIF-P (i.e after pyrolysis at 1050° C in Ar), c) $[Fe/Zn]_1$ZIF, d) $[Fe/Zn]_1$ZIF-P, e) $[Fe/Zn]_2$ZIF, f) $[Fe/Zn]_2$ZIF-P, g) $[Fe/Zn]_5$ZIF, h) $[Fe/Zn]_5$ZIF-P

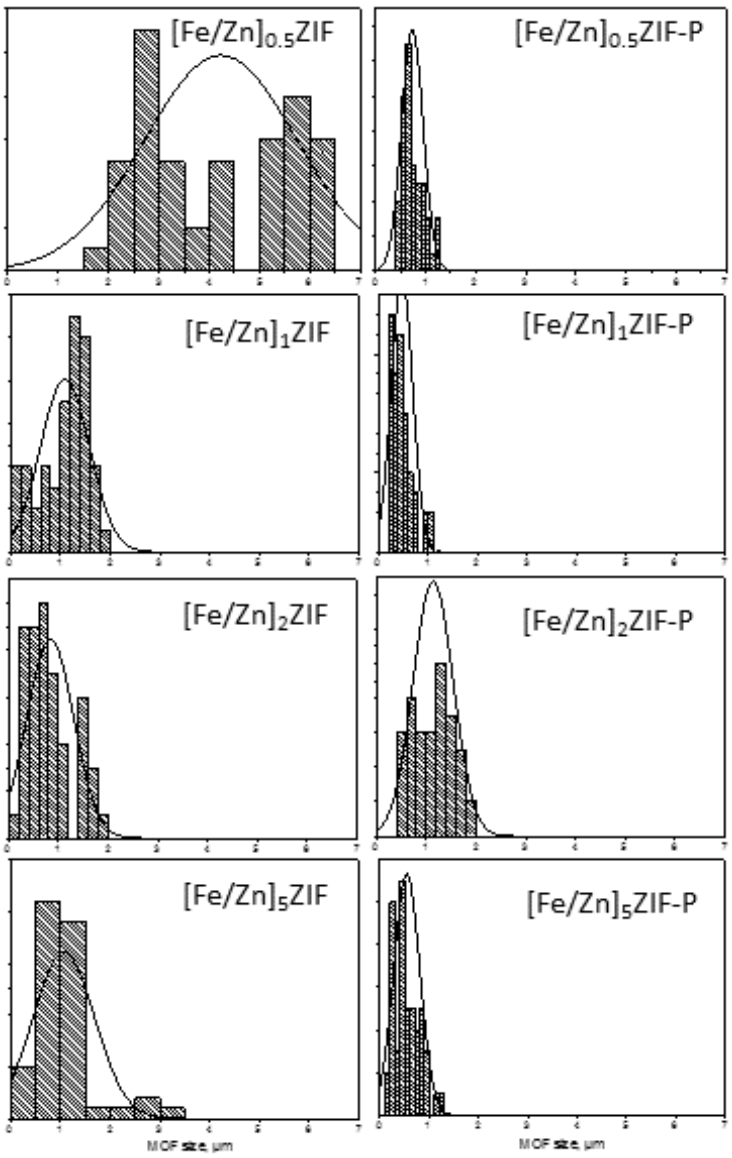

Figure 35 : MOF size distribution histogram before and after pyrolysis for ZIF-8

After pyrolysis at 1050 °C in Ar atmosphere, all $[Fe/Zn]_x$ZIF-P structures have smaller particle size (with size range of 0.5-2 µm) than the original MOFs before pyrolysis (Figure 33b-h).

The nitrogen adsorption/desorption isotherms of the investigated Fe-doped MOF crystals are shown in Figure 36 and S_{BET} values are presented in Table 9, 10. Before pyrolysis, samples $[Fe/Zn]_x$SIM demonstrated relatively high porosity. The isotherms acquired for different ferrocene contents in SIM-1 have similar forms and corresponds to type I and IV according IUPAC, which indicates overall structural microporosity (characteristic horizontal which demonstrates surface saturation) with occasional presence of mesopores (hysteresis loop). As the isotherms are corresponding mostly to microporous structure, the C_{BET} values are

expected to be higher than usual (see chapter 1.3.2). The isotherm curves corresponding to $[Fe/Zn]_1$SIM and $[Fe/Zn]_2$SIM are very similar and therefore they are superimposed on Figure 36a. The values of the S_{BET}, mesopore volume, total pore volume and pore diameter are summarized in table 9. Specific surface area of the $[Fe/Zn]_x$SIM series ranges from 406 to 614 $m^2\ g^{-1}$, with the maximum value corresponding to $[Fe/Zn]_{0.5}$SIM. For Fe/Zn ratio higher than 0.5 at%, the specific surface area decreases with increasing Fe/Zn ratio. The average pore size was calculated by α-plot method, and was found to vary between 1.4 and 1.6 nm, without any visible trend. This average pore size value comprises also the mesopores, as it was calculated as a mean between micro and mesopororous size.

Samples labelled $[Fe/Zn]_x$ZIF also demonstrated high surface porosity, but unlike $[Fe/Zn]_x$SIM, the isotherms of $[Fe/Zn]_x$ZIF correspond to the type I only, indicating the presence of a completely microporous surface. A slight decrease of horizontal isotherm for $[Fe/Zn]_1$ZIF could be explained due to device default. The specific surface area of the $[Fe/Zn]_x$ZIF series of materials was determined, ranging between 1622 and 1824 $m^2\ g^{-1}$. The maximum BET value was found for $[Fe/Zn]_5$ZIF. The specific surface area increased with increasing Fe/Zn at % in ZIF-8. This trend is opposite from the trend observed for the series of $[Fe/Zn]_x$SIM materials. The average pore size was also calculated using α-plot method and the value ranged between 1.0 and 1.2 nm, confirming uniquely microporous nature of materials.

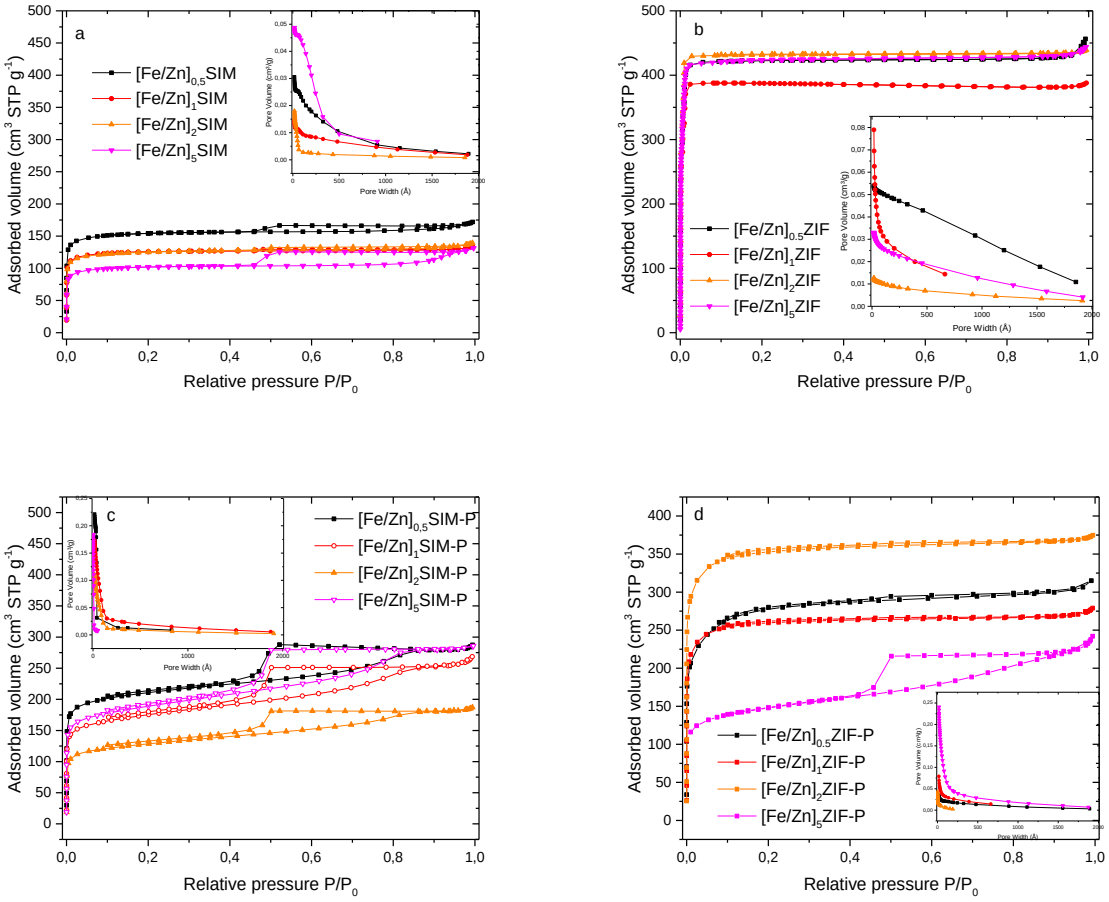

Figure 36: Selected N_2 adsorption-desorption isotherms of ferrocene-doped ZIF-8 and SIM-1 materials, before and after pyrolysis. Inset: the BJH pore size distribution curves.

After pyrolysis, samples were characterized again and the results are presented in Figure 36c, d and Table 10. Compared to $[Fe/Zn]_x$SIM, which mostly presented micropores, the $[Fe/Zn]_x$SIM-P samples demonstrated mixed micro- and mesoporosity. The isotherm curves are type I and IV according to IUPAC classification. The hysteresis loop of type H2 is observed during desorption, that could be assigned to bottle-neck type of mesopore shape.

Table 9. Textural properties of Fe-doped MOFs before pyrolysis

Sample	Theoretical $(Fe/Zn)_{at}$	EDX $(Fe/Zn)_{at}$	S_{BET} m^2 g^{-1}	V_{tot} cm^3g^{-1}	V_{mic} cm^3g^{-1}	$d_{mes+mic}$ nm	Porosity
$[Fe/Zn]_{0.5}$SIM	0.005	0.005	614	0.27	0.17	1.5	Mesopores + micropores
$[Fe/Zn]_1$SIM	0.01	0.01	504	0.28	0.17	1.6	Mesopores + micropores
$[Fe/Zn]_2$SIM	0.02	0.02	498	0.22	0.14	1.6	Mesopores + micropores
$[Fe/Zn]_5$SIM	0.05	0.05	406	0.21	0.11	1.4	Mesopores + micropores
$[Fe/Zn]_{0.5}$ZIF	0.1	0.1	1622	0.35	0.29	1.1	Micropores
$[Fe/Zn]_1$ZIF	0.005	0.007	1649	0.39	0.19	1.0	Micropores
$[Fe/Zn]_2$ZIF8	0.01	0.012	1822	0.39	0.14	1.2	Micropores
$[Fe/Zn]_5$ZIF	0.02	0.026	1824	0.38	0.27	1.1	Micropores

The specific surface area for $[Fe/Zn]_x$SIM-P catalysts is ranging between 488 and 813 m^2 g^{-1}, with the maximum value corresponding to $[Fe/Zn]_{0.5}$SIM-P. With the increase of Fe/Zn at% in the structure, the S_{BET} value decreased. This is in agreement with the trend observed for the samples before pyrolysis. For $[Fe/Zn]_5$SIM-P however, the S_{BET} increases again. The average pore size was determined by α-plot method, ranging from 2.8 nm to 3.5 nm, larger than in non-pyrolyzed samples. This could be explained by the loss of a fraction of material as volatile compounds during pyrolysis (Zn but also C, N and H), creation of mesoporous cavities and, as the consequence, growth of mean value of pore diameter.

The isotherms of the samples $[Fe/Zn]_x$ZIF-P (derived from pyrolysis of $[Fe/Zn]_x$ZIF) are presented in Figure 36d. Samples labelled $[Fe/Zn]_{0.5}$ZIF-P, $[Fe/Zn]_1$ZIF-P, $[Fe/Zn]_2$ZIF-P are mostly represented by a curve of type I according to IUPAC, meaning that the porosity remained microporous. The isotherm recorded for $[Fe/Zn]_5$ZIF-P is a mixture of curve of type I and IV, which is an indication of creation of mesopores along with remaining micropores. The specific surface area is high and ranges between 558 and 1347 m^2 g^{-1} with no particular trend with the Fe/Zn ratio (for samples $[Fe/Zn]_{0.5-2}$ZIF-P). One exception is $[Fe/Zn]_5$ZIF-P, with S_{BET} value significantly lower than that of all other samples of this series. The average pore diameter for

$[Fe/Zn]_{0.5\text{-}2}$ZIF-P ranges between 1.5 and 1.8 nm, corresponding to uniquely microporous structure. In contrast, the average pore size of $[Fe/Zn]_5$ZIF-P is 3 nm.

Table 10. Textural properties of FeNC catalysts after pyrolysis

Sample	S_{BET} m^2 g^{-1}	V_{tot} cm^3g^{-1}	V_{mic} cm^3g^{-1}	$d_{mes+mic}$ nm	Porosity
$[Fe/Zn]_{0.5}$SIM-P	813	0.23	0.19	2.8	Mesopores + micropores
$[Fe/Zn]_1$SIM-P	663	0.19	0.17	3.5	Mesopores + micropores
$[Fe/Zn]_2$SIM-P	488	0.15	0.12	3.3	Mesopores + micropores
$[Fe/Zn]_5$SIM-P	709	0.24	0.18	3.8	Mesopores + micropores
$[Fe/Zn]_{0.5}$ZIF-P	1021	0.25	0.19	1.8	only micropores
$[Fe/Zn]_1$ZIF-P	1014	-	0.25	1.5	only micropores
$[Fe/Zn]_2$ZIF-P	1347	-	0.34	1.7	only micropores
$[Fe/Zn]_5$ZIF-P	558	0.16	0.13	3	Mesopores + micropores

In order to complete the structural investigation and to confirm the presence of the desired MOF structure, XRD analysis was performed, both before and after pyrolysis of Fe-doped MOFs. Figure 37a demonstrates that the diffractograms peaks are in good agreement with those of the reference pattern of SIM-1 structure. Also for $[Fe/Zn]_x$ZIF (Figure 37b), the XRD patterns match that of pristine ZIF-8 which confirms same crystalline structure for the ferrocene-doped ZIF-8 materials. This supports that ferrocene occupies the cavities but does not change the crystalline structure.

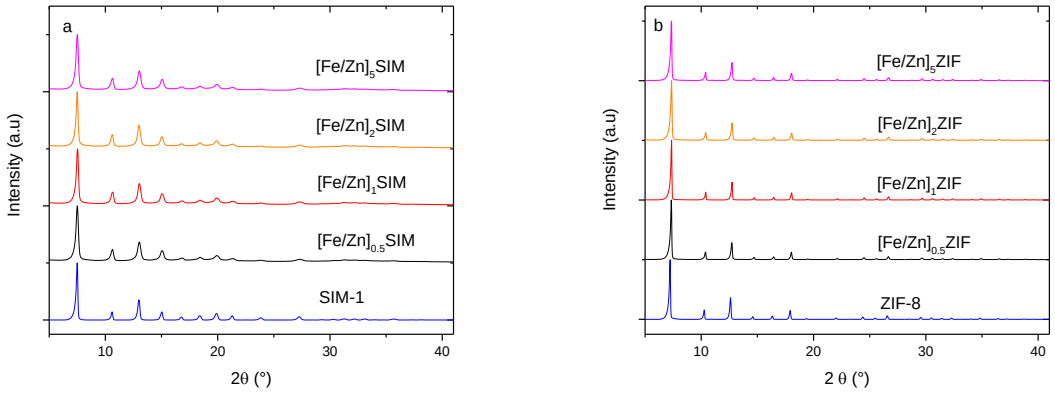

Figure 37: XRD diffractograms registered for: a) $[Fe/Zn]_xSIM$ compared to initial SIM-1 structure, b) $[Fe/Zn]_xZIF$ compared to initial ZIF-8 structure

After pyrolysis at 1050 °C in Ar atmosphere, the resulting FeNC powders were characterized, in particular in order to identify whether only FeN_x sites are formed or a mix of FeN_x sites and crystalline Fe particles. Figure 37a depicts the XRD diffractograms for $[Fe/Zn]_xSIM$-P catalysts. The large band at 26° related to the graphite (002) plane and a second band at 43° related to (100) plane corresponds to carbon of the reference JCPDS n°00-041-1487. The absence of other visible diffraction peaks can be either an indication of a) no metallic or metal-carbide Fe particles in the structure, or b) small amount of Fe particles that is too low to be detectable by XRD technique. EXAFS measurements performed for extreme Fe/Zn ratio in the MOFs are presented in Figure 39 and Figure 40, which are discussed in more detail later. The diffractograms obtained for pyrolyzed $[Fe/Zn]_xZIF$-P catalysts are presented in Figure 36. For samples $[Fe/Zn]_{0.5}ZIF$-P, $[Fe/Zn]_1ZIF$-P and $[Fe/Zn]_2ZIF$-P, one can observe only a large diffraction peak at 26° related to the graphite (002) plane and a second band at 43° related to (100) plane corresponding to the 002 plane of graphite (reference JCPDS n°00-041-1487). At highest Fe content, i.e. the $[Fe/Zn]_5ZIF$-P sample, additional intense diffraction peaks can be seen that correspond to a superposition of iron carbide and iron oxide. More, precisely, the peak at 36° corresponds to Fe_2O_3 (reference JCPDS n°1-073-0603), peaks at 29° and 43° corresponds to Fe_3O_4 (reference JCPDS n°01-074-1910), peaks at 42° and 44° corresponds to iron carbide (reference JCPDS n°00-044-1292).

The average size of the crystalline particles was determined by the Scherrer equation:

$$L_c = \frac{0.9\lambda}{\beta cos\theta}$$

Where λ is the incident X-ray radiation wavelength, β the full with at half maximum of the peak (in radian), θ the scattering angle. After calculations, the average crystalline size of Fe_2O_3 was *ca* 50 nm, size of Fe_3O_4 was *ca* 34nm and iron carbide particles was *ca* 9 nm.

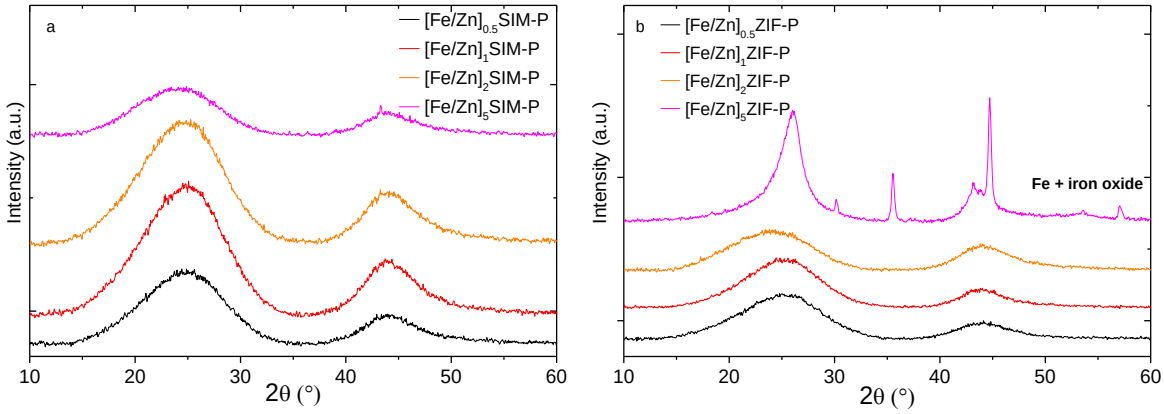

Figure 38: XRD patterns registered for FeNC catalysts series derived from pyrolysis 1050° C in Ar of ferrocene-doped MOFs: a) $[Fe/Zn]_x$SIM-P, b) $[Fe/Zn]_x$ZIF-P.

To confirm the presence of Fe particles present in at least some of the FeNC catalysts derived from MOFs, extended X-ray absorption fine structure (EXAFS) measurements were performed with synchrotron radiation on selected samples. The selected ones were $[Fe/Zn]_{0.5}$SIM-P, $[Fe/Zn]_5$SIM-P and $[Fe/Zn]_{10}$SIM-P for SIM-1 derived catalysts; $[Fe/Zn]_{0.5}$ZIF-P and $[Fe/Zn]_5$ZIF-P for ZIF-8 derived catalysts. The EXAFS spectra of these selected catalysts were compared to that of a pure metallic Fe foil and also to that of the powder reference catalyst $Fe_{0.5}$NC, known to comprise only FeN_x sites and no Fe particles (Figure 39).

The Fourier transforms of the EXAFS spectra of $[Fe/Zn]_{0.5}$SIM-P and $[Fe/Zn]_5$SIM-P show a pattern very similar to that of the model $Fe_{0.5}$NC catalyst (Figure 39a-b). In particular, the absence of characteristic peaks at 2.2 Å that corresponds to Fe-Fe interaction in metallic Fe and 2.6 Å that corresponds to Fe-C liaisons in iron carbide [29] indicate the absence of iron-based crystalline particles in the investigated materials. Also the EXAFS was performed for $[Fe/Zn]_{10}$SIM-P, and also there no signatures of iron-based particles were detected (Figure 40). The signal seen at the distance of ca 1.7 Å is assigned to Fe-N bonds from FeN_x sites[29].

For $[Fe/Zn]_{0.5}$ZIF-P, the measurements show the absence of undesired Fe-based crystalline structures (Figure 39c). In contrast, the FT-EXAFS spectrum of $[Fe/Zn]_5$ZIF-P indicates signals at 2.2 Å, 2.6 Å and 4.2 Å that leads to the conclusion that $[Fe/Zn]_5$ZIF-P sample contains a significant amount of Fe-based particles

(Figure 39d). This leads also to an apparent decrease of the signal at 1.7 Å compared to the reference powder catalyst, since not all Fe atoms form FeN_x sites but only a fraction of them for $[Fe/Zn]_5$ZIF-P.

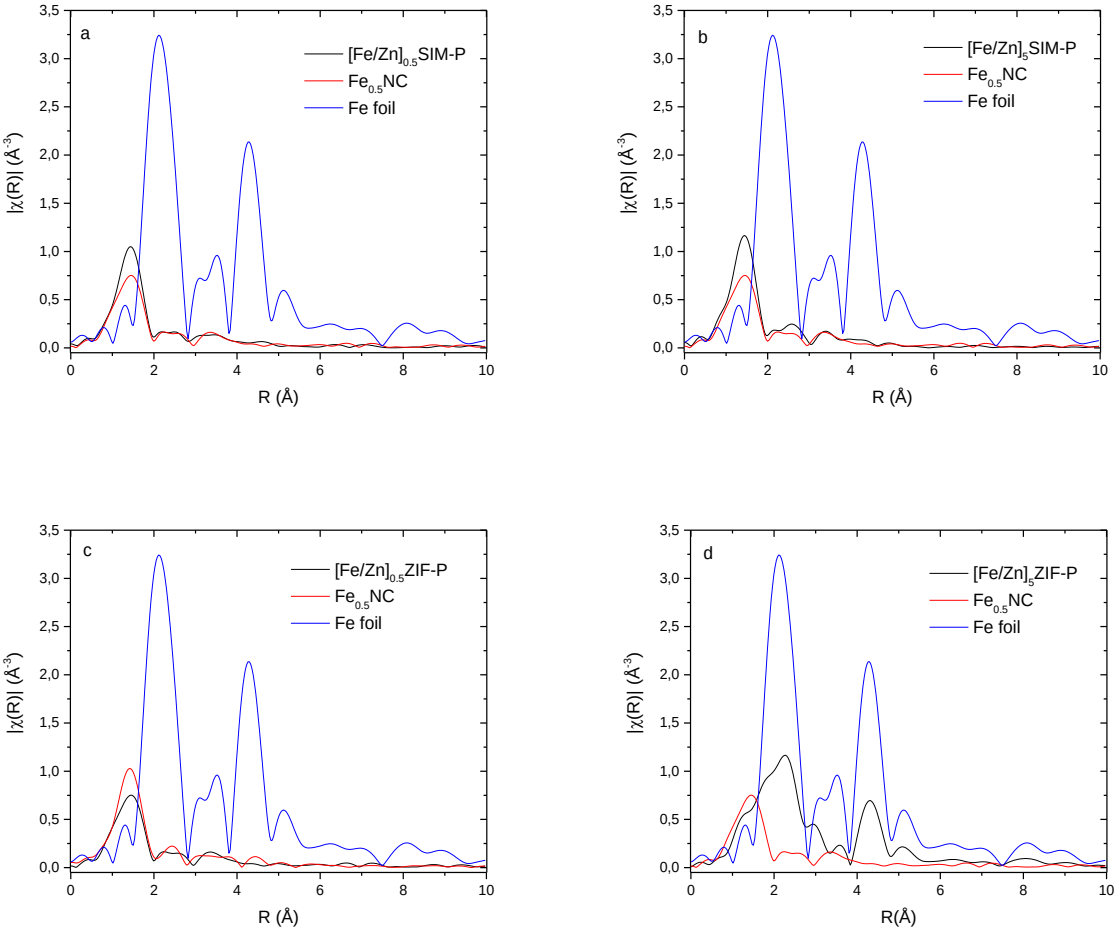

Figure 39. Fourier transforms of the experimental EXAFS spectra of $[Fe/Zn]_{0.5}$SIM-P (a), $[Fe/Zn]_{5}$SIM-P (b), $Fe/Zn]_{0.5}$ZIF-P (c), $Fe/Zn]_{0.5}$ZIF-P (d) compared to the reference $Fe_{0.5}$NC catalyst and metallic Fe foil

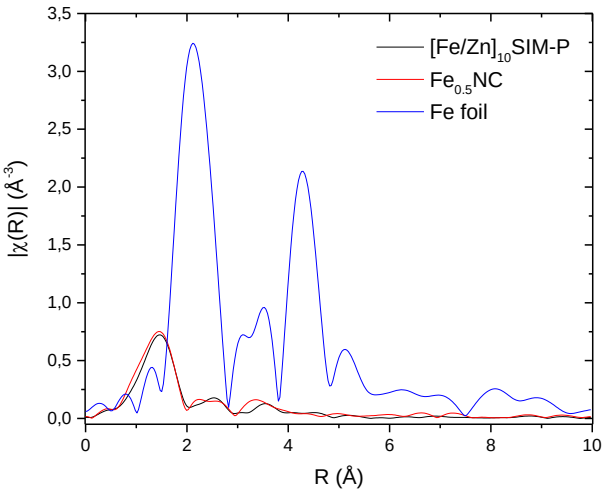

Figure 40. Fourier transforms of the experimental EXAFS spectrum of $[Fe/Zn]_{10}$SIM-P compared to the reference $Fe_{0.5}$NC catalyst and metallic Fe foil.

The FeNC catalysts obtained after pyrolysis of Fe-doped MOFs (SIM-1 and ZIF-8) were finally analyzed for their electrochemical properties towards ORR in a RDE setup, resorting to the conventional ink deposition methodology to form catalytic layers from powder catalysts. The results are presented and discussed in the following paragraph.

2.3.b Electrochemical properties of FeNC catalysts derived from ferrocene-doped MOFs

FeNC powder catalysts derived from these ferrocene-doped MOFs were characterized electrochemically by RDE to determine their ORR activity, and to compare it with the activity of the model $Fe_{0.5}$NC powder catalyst from the laboratory. Each electrode was cycled in N_2 saturated 0.1 M H_2SO_4 between 0 and 1 V vs. RHE with scan rate of 5 mV s^{-1} to assess the electrochemical capacitance and possible presence of redox peaks, and in oxygen saturated 0.1 M H_2SO_4 between 0 and 1 V vs. RHE with scan rate of 2 mV s^{-1} to evaluate the ORR activity.

Figure 41a and b presents the CV curves of the catalyst series $[Fe/Zn]_x$SIM-P and $[Fe/Zn]_x$ZIF-P, respectively. The curves of $[Fe/Zn]_{0.5}$SIM-P indicates high electrochemical capacitance, that can be connected to the high surface area measured for that sample (see section 2.2.a). Then, the $[Fe/Zn]_1$SIM-P catalyst demonstrates lower electrochemical capacitance compared to $[Fe/Zn]_{0.5}$SIM-P, while $[Fe/Zn]_2$SIM-

P shows even lower capacitance (Figure 41). Interestingly, with the augmentation of the Fe/Zn ratio in the MOFs (especially catalysts labelled $[Fe/Zn]_5$SIM-P and $[Fe/Zn]_{10}$SIM-P) their capacitance also became higher. It will be shown that this increase is also positively linked to the ORR activity of the catalysts (Figure 42). The reversible redox peak seen on Figure 41 at the potential of 0.77 V *vs.* RHE is seen only for $[Fe/Zn]_{10}$SIM-P, corresponding to Fe^{2+}/Fe^{3+} oxidation. Due to the absence of Fe-based particles in this sample, the redox peak is assigned to a high number of FeN_x sites. CV curves recorded for the $[Fe/Zn]_x$ZIF-P series of catalysts also demonstrated high capacitance for each sample (Figure 41b). The reversible peak of 0.77 V vs. RHE seen for $[Fe/Zn]_{0.5}$ZIF-P only also corresponds to Fe^{2+}/Fe^{3+} oxidation.

The ORR activity of the two series of catalysts is shown in Figure 42. The two most active materials for the SIM-1 series were $[Fe/Zn]_{0.5}$SIM-P and $[Fe/Zn]_{10}$SIM-P, that demonstrated high activity comparable to the reference $Fe_{0.5}$NC catalyst (Figure 42a). $[Fe/Zn]_1$SIM-P demonstrated intermediate activity while $[Fe/Zn]_2$SIM-P has by far the lowest activity of this series of catalysts. There is therefore no continuous trend of increasing activity with Fe/Zn ratio, but a complex dependency. Tafel plots for those samples are shown in Figure 43a and the mass activity measured at 0.8 V vs. RHE is presented in Figure 44. The most promising material is $[Fe/Zn]_{0.5}$SIM-P with a mass activity of 1.96 A g^{-1} and $[Fe/Zn]_{10}$SIM-P with a mass activity of 1.51 A g^{-1}. The existence of the two maxima of ORR activity at Fe/Zn ratio of 0.5 on one hand and 10 on the other hand, is difficult to explain, since EXAFS measurements on both materials demonstrated the absence of undesired Fe_3C or metallic Fe particles in those two samples, see Figure 39, Figure 40.

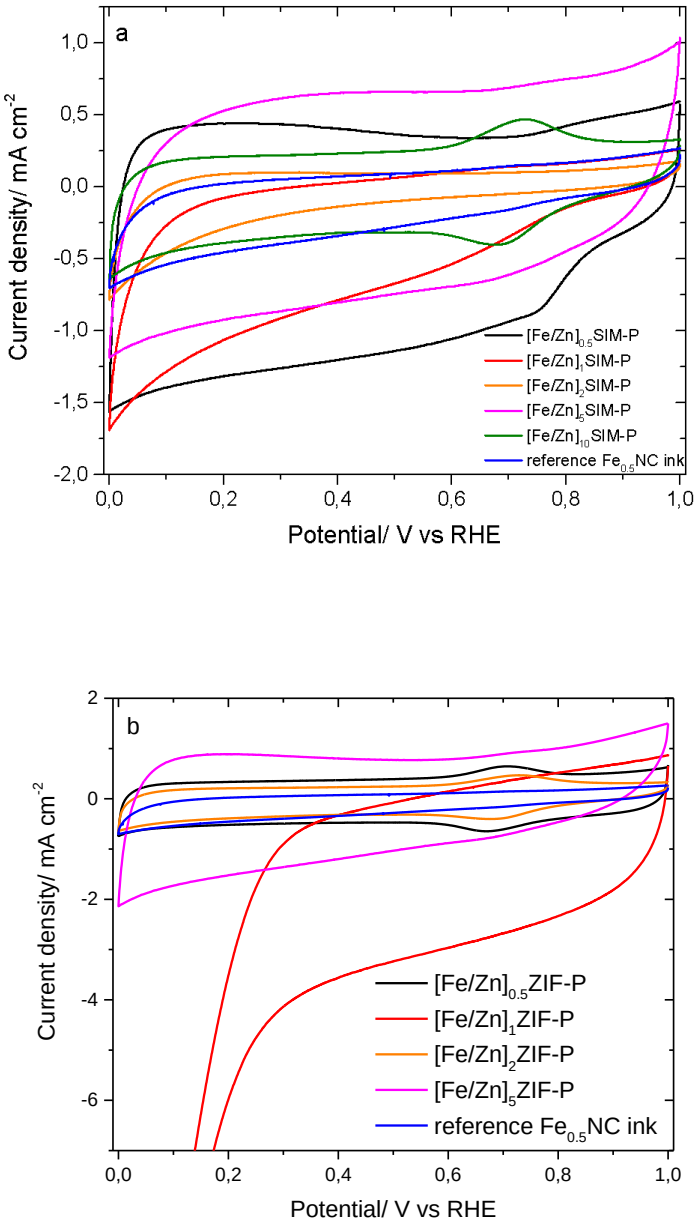

Figure 41: Electrochemical characterization in RDE of FeNC catalysts. a) CV in N_2-saturated pH 1 solution of $[Fe/Zn]_x$SIM-P (x = 0.5, 1 or 2), b) CV in N_2-saturated pH 1 solution of $[Fe/Zn]_x$ZIF-P (x = 0.5, 1 or 2), and compared to the same curves measured for the reference $Fe_{0.5}$NC active layer. The electrolyte was 0.1 M H_2SO_4, electrode rotation rate 1600 rpm and catalyst loading 1 mg cm^{-2}.

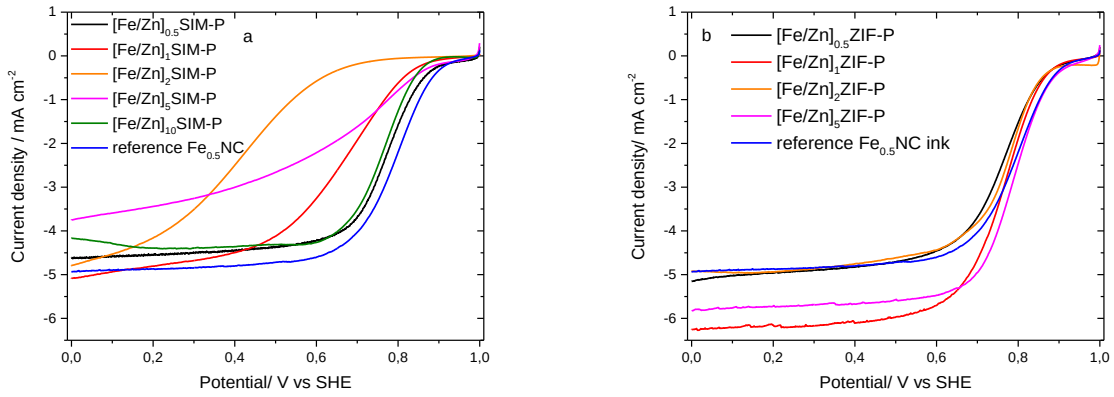

Figure 42: Electrochemical characterization in RDE of grinded FeNC electrodes. a) ORR polarization curves in O_2-saturated pH 1 solution of $[Fe/Zn]_x$SIM-P (x = 0.5, 1 or 2), b) ORR polarization curves in O_2-saturated pH 1 solution of $[Fe/Zn]_x$ZIF-P (x = 0.5, 1 or 2), and compared to the same curves measured for the reference $Fe_{0.5}$NC active layer. The electrolyte was 0.1 M H_2SO_4, electrode rotation rate 1600 rpm and catalyst loading 1 mg cm^{-2}.

The ORR activity for the series of catalysts $[Fe/Zn]_x$ZIF-P is presented in Figure 42b. All measured samples demonstrated high catalytic activity, as can also be observed in the corresponding Tafel plots in Figure 43. The most active materials of this series are $[Fe/Zn]_1$ZIF-P and $[Fe/Zn]_5$ZIF-P with the mass activity at 0.8 V vs. RHE of 2.35 A g^{-1} and 3.05 A g^{-1}, respectively. The fact that only a slightly higher activity was observed for $[Fe/Zn]_5$ZIF-P vs. $[Fe/Zn]_1$ZIF-P sample in spite of five-times more Fe can be explained by the presence of ORR-inactive or less-active metallic iron and iron carbide in $[Fe/Zn]_5$ZIF-P, as was shown by EXAFS and XRD measurements (Figures 37, 39, 40). Therefore, the Fe/Zn ratio used for preparing $[Fe/Zn]_5$ZIF-P is not ideal since Fe-based particles are known to be unstable in acid medium, and this ratio was thus not further investigated for the preparation of MOF-decorated polymer fibers (chapter 3, 4).

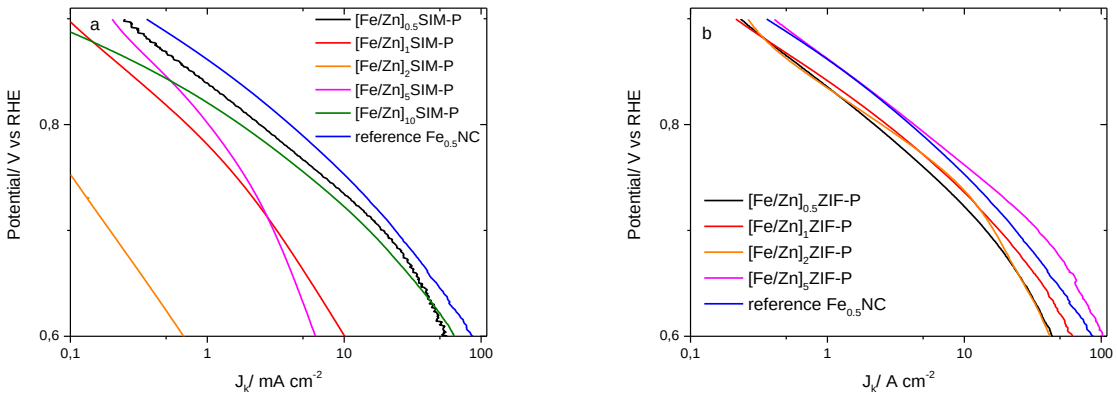

Figure 43: Tafel plots derived from RDE ORR polarization curves measured in oxygen saturated solution of 0.1M H_2SO_4 for FeNC catalysts derived from a) Ferrocene-doped SIM-1, d) Ferrocene-doped ZIF-8. The curve for the reference $Fe_{0.5}NC$ is shown as a comparison.

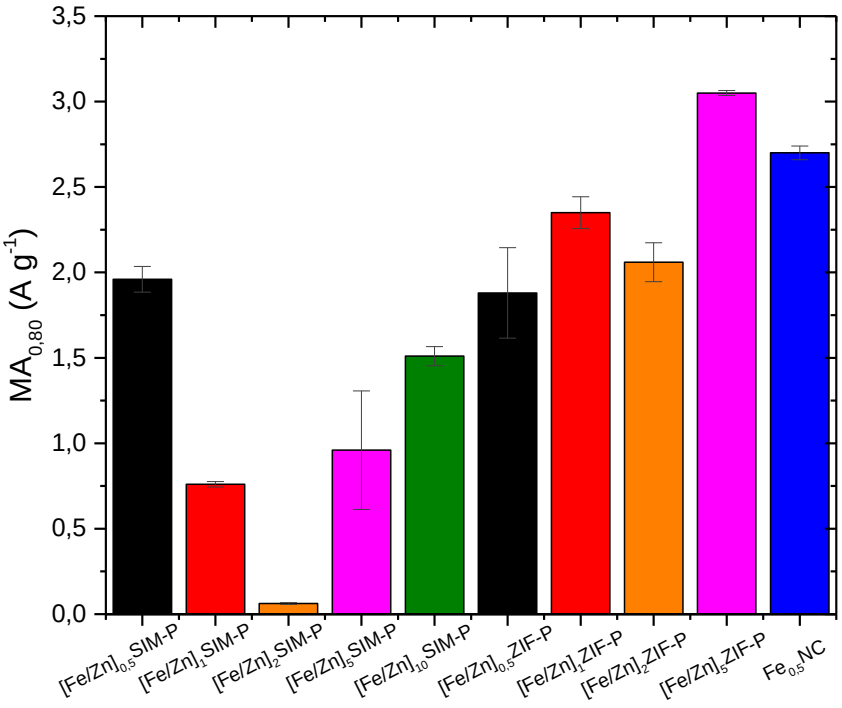

Figure 44: Mass activity for FeNC powder catalysts derived from ferrocene-doped MOFs, measured at 0.8 V vs. RHE and compared to reference $Fe_{0.5}NC$ catalyst. The average activity and error bar was estimated from three independent measurements on three different layers.

2.4 Conclusions

In this chapter, the first step for another approach of preparation of self-standing FeNC electrodes was developed, focusing on the synthesis and optimization of the ferrocene-doping of MOFs, and on the characterization of the FeNC powder catalysts obtained by the pyrolysis of ferrocene-doped MOFs. Those catalysts were characterized morphologically and electrochemically, revealing the absence of crystalline Fe-based particles, except in $[Fe/Zn]_5$ZIF, where the presence of iron oxides and carbides was detected both by XRD and EXAFS analysis.

The ORR activity measured by RDE methods revealed overall high activity for these FeNC powder materials, with the most active catalysts being $[Fe/Zn]_1$ZIF-P and $[Fe/Zn]_5$ZIF-P with the mass activity at 0.8 V vs. RHE of 2.35 and 3.05 A g^{-1}, respectively. Nevertheless, as mentioned above, the catalyst $[Fe/Zn]_5$ZIF-P contains Fe-based crystalline particles and, therefore, will not be further used in following chapters.

Based on the structural and electrochemical results obtained in this chapter, the synthesis and ferrocene/Zn ratio that were chosen for further studies of FeNC self-standing electrode fabrication in chapters 3-4 are:

- For the SIM-1 series: $[Fe/Zn]_{0.5}$SIM, $[Fe/Zn]_1$SIM, $[Fe/Zn]_2$SIM and $[Fe/Zn]_{10}$SIM
- For the ZIF-8 series: $[Fe/Zn]_{0.5}$ZIF-P, $[Fe/Zn]_1$ZIF, $[Fe/Zn]_2$ZIF

1. Santori, P.G.; Speck, F.D.; Li, J.; Zitolo, A.; Jia, Q.; Mukerjee, S.; Cherevko, S.; Jaouen, F. Effect of Pyrolysis Atmosphere and Electrolyte pH on the Oxygen Reduction Activity, Stability and Spectroscopic Signature of FeN x Moieties in Fe-N-C Catalysts . *J. Electrochem. Soc.* **2019**, *166*, F3311–F3320.

2. Mechler, A.K.; Sahraie, N.R.; Armel, V.; Zitolo, A.; Sougrati, M.T.; Schwämmlein, J.N.; Jones, D.J.; Jaouen, F. Stabilization of Iron-Based Fuel Cell Catalysts by Non-Catalytic Platinum. *J. Electrochem. Soc.* **2018**, *165*, F1084–F1091.

3. Goellner, V.; Armel, V.; Zitolo, A.; Fonda, E.; Jaouen, F. Degradation by hydrogen peroxide of metal-nitrogen-carbon catalysts for oxygen reduction. *J. Electrochem. Soc.* **2015**, *162*, H403–H414.

4. Armel, V.; Hannauer, J.; Jaouen, F. Effect of ZIF-8 crystal size on the O<inf>2</inf> electro-reduction performance of pyrolyzed Fe–N–C catalysts. *Catalysts* **2015**, *5*, 1333–1351.

5. Li, J.; Brüller, S.; Sabarirajan, D.C.; Ranjbar-Sahraie, N.; Sougrati, M.T.; Cavaliere, S.; Jones, D.; Zenyuk, I. V.; Zitolo, A.; Jaouen, F. Designing the 3D Architecture of PGM-Free Cathodes for H2/Air Proton Exchange Membrane Fuel Cells. *ACS Appl. Energy Mater.* **2019**, *2*, 7211–7222.

6. Chen, L.N.; Yu, W.S.; Wang, T.; Yang, X.D.; Yang, H.J.; Chen, Z.X.; Wang, T.; Tian, N.; Zhou, Z.Y.; Sun, S.G. Fluorescence detection of hydroxyl radical generated from oxygen reduction on Fe/N/C catalyst. *Sci. China Chem.* **2020**, *63*, 198–202.

7. Choi, C.H.; Lim, H.K.; Chung, M.W.; Chon, G.; Ranjbar Sahraie, N.; Altin, A.; Sougrati, M.T.; Stievano, L.; Oh, H.S.; Park, E.S.; et al. The Achilles' heel of iron-based catalysts during oxygen reduction in an acidic medium. *Energy Environ. Sci.* **2018**, *11*, 3176–3182.

8. Kumar, K.; Gairola, P.; Lions, M.; Ranjbar-Sahraie, N.; Mermoux, M.; Dubau, L.; Zitolo, A.; Jaouen, F.; Maillard, F. Physical and Chemical Considerations for Improving Catalytic Activity and Stability of Non-Precious-Metal Oxygen Reduction Reaction Catalysts. *ACS Catal.* **2018**, *8*, 11264–11276.

9. Wang, C.; Liu, C.; Li, J.; Sun, X.; Shen, J.; Han, W.; Wang, L. Electrospun metal-organic framework derived hierarchical carbon nanofibers with high performance for supercapacitors. *Chem. Commun.* **2017**, *53*, 1751–1754.

10. Uribe-romo, F.J.; Knobler, C.B.; Keeffe, M.O.; Yaghi, O.M. Capture Properties of Zeolitic Imidazolate Frameworks. *Acc. Chem. Res.* **2010**, *43*, 58–67.

11. Palaniselvam, T.; Biswal, B.P.; Banerjee, R.; Kurungot, S. Zeolitic imidazolate framework (ZIF)-derived, hollow-core, nitrogen-doped carbon nanostructures for oxygen-reduction reactions in PEFCs. *Chem. - A Eur. J.* **2013**, *19*, 9335–9342.

12. Ma, S.; Zhou, H.C. Gas storage in porous metal-organic frameworks for clean energy applications. *Chem. Commun.* **2010**, *46*, 44–53.

13. Horcajada, P.; Serre, C.; Maurin, G.; Ramsahye, N.A.; Balas, F.; Vallet-Regí, M.; Sebban, M.; Taulelle, F.; Férey, G. Flexible porous metal-organic frameworks for a controlled drug delivery. *J. Am. Chem. Soc.* **2008**, *130*, 6774–6780.

14. Wang, J.; Han, G.; Wang, L.; Du, L.; Chen, G.; Gao, Y.; Ma, Y.; Du, C.; Cheng, X.; Zuo, P.; et al. ZIF-8 with Ferrocene Encapsulated: A Promising Precursor to Single-Atom Fe Embedded Nitrogen-Doped Carbon as Highly Efficient Catalyst for Oxygen Electroreduction. *Small* **2018**, *14*, 1–7.

15. Lefèvre, M.; Proietti, E.; Jaouen, F.; Dodelet, J.P. Iron-Based catalysts with improved oxygen reduction activity in polymer electrolyte fuel cells. *Science (80-.).* **2009**, *324*, 71–74.

16. Yuan, Y.; Smith, J.A.; Goenaga, G.; Liu, D.J.; Luo, Z.; Liu, J. Platinum decorated aligned carbon nanotubes: Electrocatalyst for improved performance of proton exchange membrane fuel cells. *J. Power Sources* **2011**, *196*, 6160–6167.

17. Shui, J.; Chen, C.; Grabstanowicz, L.; Zhao, D.; Liu, D.J. Highly efficient nonprecious metal catalyst prepared with metal-organic framework in a continuous carbon nanofibrous network. *Proc. Natl. Acad. Sci. U. S. A.* **2015**, *112*, 10629–10634.

18. Aguado, S.; Canivet, J.; Farrusseng, D. Engineering structured MOF at nano and macroscales for catalysis and separation. *J. Mater. Chem.* **2011**, *21*, 7582–7588.

19. Ye, Y.; Cai, F.; Li, H.; Wu, H.; Wang, G.; Li, Y.; Miao, S.; Xie, S.; Si, R.; Wang, J.; et al. Surface functionalization of ZIF-8 with ammonium ferric citrate toward high exposure of Fe-N active sites for efficient oxygen and carbon dioxide electroreduction. *Nano Energy* **2017**, *38*, 281–289.

20. Marti, A.M.; Van, M.; Balkus, K.J. Tuning the crystal size and morphology of the substituted imidazole material, SIM-1. *J. Porous Mater.* **2014**, *21*, 889–902.

21. Barman, B.K.; Nanda, K.K. Prussian blue as a single precursor for synthesis of Fe/Fe3C encapsulated N-doped graphitic nanostructures as bi-functional catalysts. *Green Chem.* **2016**, *18*, 427–432.

22. Riveros, G.; Meneses, S.; Escobar, S.; Garín, C.; Chornik, B. Electron transfer rates of alkyl-ferrocene molecules forming incomplete monolayer on silicon electrodes. *J. Chil. Chem. Soc.* **2010**, *55*, 61–66.

23. Zhang, W.; Yao, X.; Zhou, S.; Li, X.; Li, L.; Yu, Z.; Gu, L. ZIF-8/ZIF-67-Derived Co-N $_x$ -Embedded 1D Porous Carbon Nanofibers with Graphitic Carbon-Encased Co Nanoparticles as an Efficient Bifunctional Electrocatalyst. *Small* **2018**, *14*, 1800423.

24. Jaouen, F.; Dodelet, J.P. Average turn-over frequency of O2 electro-reduction for Fe/N/C and Co/N/C catalysts in PEFCs. *Electrochim. Acta* **2007**, *52*, 5975–5984.

25. Ma, S.; Goenaga, G.A.; Call, A. V.; Liu, D.J. Cobalt imidazolate framework as precursor for oxygen reduction reaction electrocatalysts. *Chem. - A Eur. J.* **2011**, *17*, 2063–2067.

26. Lefevre, M.; Dodelet, J.-P. Recent Advances in Non-Precious Metal Electrocatalysts for Oxygen Reduction in {PEM} Fuel Cells. *{ECS} Trans.* **2012**, *45*, 35–44.

27. Aguado, S.; Canivet, J.; Farrusseng, D. Engineering structured MOF at nano and macroscales for catalysis and separation. *J. Mater. Chem.* **2011**, *21*, 7582–7588.

28. Banerjee, R. High-Throughput Synthesis of Zeolitic. *ReVision* **2008**, *939*, 939–944.

29. Zitolo, A.; Goellner, V.; Armel, V.; Sougrati, M.-T.; Mineva, T.; Stievano, L.; Fonda, E.; Jaouen, F. Identification of catalytic sites for oxygen reduction in iron- and nitrogen-doped graphene materials. *Nat. Mater.* **2015**, *14*, 937–942.

Chapter 3: Growth of Fe-doped MOFs on polymer fibers: effect of zinc coating

Table of content

3.1 Introduction

In chapter 2, the synthesis of ferrocene-doped MOFs as the precursors for preparing FeNC powder catalysts was investigated for two different MOFs and different ferrocene contents. The study revealed high ORR activity in RDE for most ferrocene contents, except for Fe/Zn atomic ratio of 2% with SIM-1. Moreover, all FeNC catalyst derived from SIM-1 showed the absence of undesired Fe particles after pyrolysis, even at a Fe/Zn ratio of 10 at. % in solution. The results obtained in chapter 2 are therefore promising for investigating the growth of ferrocene-doped MOFs on electrospun polymer fiber mats, as precursors for self-standing FeNC electrodes.

The possibility of using film-based metallic substrates as sites and metal-cation source for MOF germination has been firstly reported in 2008 by Allendorf et al.[1] and then followed by several researches[2,3]. For example, it was shown that it is possible to synthesize an aluminum-based MOF directly on an aluminum metallic support, without other source of Al cation than the substrate itself[4].

Another example of successful growing of supported MOF-based materials were done on PAN electrospun fibers covered by ZnO or Al_2O_3 thin layer by atomic layer deposition and then the resulting supports were put in the autoclave where different MOFs were grown under solvothermal synthesis[5]. It is also shown that it is possible to grow a MOF on grinded PAN-derived surface using a microwave irradiation[6] or on polymer brushes [7]. These earlier works inspired us for using polymer fibers as substrate for the crystalline growth of MOFs.

The aim of chapter 3 is therefore to investigate and optimize the approach of seeding and growing Fe-doped MOFs on 3D polymer fiber mats. The study was conducted in this chapter on PAN fiber mats and with ferrocene-doped SIM-1. The resulting self-standing FeNC electrodes were characterized in RDE.

For a nitrogen-containing polymer such as PAN, the N-groups may act as nucleation point for the initial adsorption of Zn cations and the further growth of ZIFs, using the ligand and Zn cations present in solution. The electrospun PAN mats were immersed in a solution containing the SIM-1 precursors (Zn(II) and 4-methyl-5-imidazolecarboxaldehyde) as well as ferrocene, with a fixed ferrocene/Zn ratio of 10 at. % that was identified as leading to high ORR activity for SIM-1 derived FeNC catalysts in chapter 2.

It may however be preferable that nucleation starts on Zn(II) surfaces, and to this end, the PAN polymer fibers were functionalized with thin layers of zinc and zinc oxide. Cathodic sputtering of metallic zinc or zinc oxide was performed on polymer fiber mats. The zinc-functionalized mats were then similarly

immersed in a solution containing the SIM-1 precursors (Zn(II) and 4-methyl-5-imidazolecarboxaldehyde) as well as ferrocene, with a fixed ferrocene/Zn ratio of 10 at. %.

These SIM-1 decorated PAN mats were characterized morphologically before pyrolysis as well as after pyrolysis with SEM, in order to assess if and how the crystallization took place. The self-standing FeNC cathodes were characterized electrochemically in RDE, revealing the effect of zinc-coating of PAN polymer fiber mats and of the stabilization steps (thermal treatment in air at 150-250°C) on the final ORR activity after pyrolysis.

3.2 Materials and methods

3.2.a Zinc functionalization of PAN fiber mats by cathodic sputtering

The polymer fiber mat was first prepared by electrospinning PAN (in DMF), as described in details in section 1.1. The raw fiber electrospun mat as well as the fiber mat after a stabilization step in air were investigated (see Table 1, column 2). The resulting fibers were cut to size of 4 x 4 x 0.005 cm, and zinc-coated by cathodic sputtering in a Q300TD (Quorum) deposition system using a metallic Zn target with a diameter of 5 cm, in argon atmosphere. The sputtering was carried out under the current of 150 mA and the deposition time was 8000 s.

3.2.b Growth of ferrocene-doped SIM-1 on Zn-coated PAN fiber mats

After Zn sputtering, a second stabilization step in air was optionally performed for some mats (Table 1, column 4, rows 2-5), after which the Zn-coated polymer fiber mats were introduced in the solution containing 1 g of 4-methyl-5-imidazolecarboxaldehyde (99%, Sigma-Aldrich), 42 mg of ferrocene (98%, Sigma-Aldrich), 0.682 g zinc nitrate hexahydrate (99%, Sigma-Aldrich) as reported in chapter 2. [8] The imidazole ligand was dissolved first in 40 mL of ethanol at room temperature under magnetic stirring for few minutes. The temperature of the solution was then raised to 60 °C, and the ferrocene and zinc nitrate were added. After few minutes needed for homogenization, the stirring was stopped and the Zn-treated PAN nanofiber mat was immersed in solution. Its thickness was *ca* 50 µm and the typical size of the piece of mat immersed in the precursor solution was 4 cm x 4 cm. The reaction was let to proceed at 60 °C for 24 h without stirring, and the nanofiber mat was then withdrawn from the solution and washed with ethanol. The resulting materials were labelled as present Table11, column 6, rows 2-5. For one mat, a stabilization step in air was performed after the growth of Fe-doped SIM-1 (Table 1, column 7, row 3).

3.2.c Growth of ferrocene-doped SIM-1 on Zn-free PAN fiber mats

As a reference free of Zn PAN fiber mats were prepared by electrospinning PAN (in DMF) and investigated as electrospun (PAN_e label), or after a stabilization step in air (PAN_f) (see Table 1, column 2, rows 6-7). These PAN fiber mats were then introduced in the solution containing Zn(II) nitrate, 4-methyl-5-imidazolecarboxaldehyde and ferrocene, as described in previous paragraph.

3.2.d Growth of ferrocene-doped SIM-1 on Zn-doped PAN fiber mats

As another reference fiber mat, the PAN fiber mat prepared by co-electrospinning PAN (in DMF) and $ZnCl_2$ was used, either as electrospun (PAN_g label), or after a stabilization step in air (PAN_g) (see Table 1, column 2, rows 8-9).

To prepare CNFs with $ZnCl_2$, 2g PAN (M_w=150,000 g mol^{-1}), 1.4 g zinc chloride ($ZnCl_2$ anhydrous, > 98 %) was first dissolved in N,N-dimethylformamide (DMF, pure) for 12 hours at 50 °C (10 wt% PAN concentration), then the solution was cooled to room temperature. The polymer fibers were then electrospun at 20 °C and collected on a rotating drum at 100 rpm (Spraybase®). The distance between the tip of the needle (22 gauge) and the collector was 10 cm, and the voltage 13 kV (Auto-Reversing High Voltage Power Supply Spellman CZE1000R) was applied to obtain a stable Taylor cone. The flow rate was kept constant at 1 mL h^{-1} (syringe pump KDS 100 Legacy Syringe Pump, KD Scientific). These PAN and $ZnCl_2$ fiber mats were then introduced in the solution containing Zn(II) nitrate, 4-methyl-5-imidazolecarboxaldehyde and ferrocene, as described in section 3.2.b.

Table 11: Composition of electrospinning solution, synthesis steps and corresponding labels for the preparation of self-standing FeNC cathodes by growing SIM-1 on PAN polymer fiber mats. The Fe/Zn at% ratio in solution was always 10 %.

Electrospinning solution composition	Stabil. (1)	Zn sputtering	Stabil.	Label	Label after growth of ferrocene doped SIM-1	Stabil.	Label, after pyrolysis
PAN 10	yes	yes	no	PAN_a	PAN_a@$[Fe/Zn]_{10}$SIM	no	PAN_a@$[Fe/Zn]_{10}$SIM-P
PAN 10	no	yes	no	PAN_b	PAN_b@$[Fe/Zn]_{10}$SIM	yes	PAN_b@$[Fe/Zn]_{10}$SIM-P
PAN 10	no	yes	yes	PAN_c	PAN_c@$[Fe/Zn]_{10}$SIM	no	PAN_c@$[Fe/Zn]_{10}$SIM-P
PAN 10	yes	yes	yes	PAN_d	PAN_d@$[Fe/Zn]_{10}$SIM	no	PAN_d@$[Fe/Zn]_{10}$SIM-P
PAN 10	no	no	no	PAN_e	PAN_e@$[Fe/Zn]_{10}$SIM	yes	PAN_e@$[Fe/Zn]_{10}$SIM-P
PAN 10	yes	no	no	PAN_f	PAN_f@$[Fe/Zn]_{10}$SIM	no	PAN_f@$[Fe/Zn]_{10}$SIM-P
PAN 10, $ZnCl_2$ 7	no	no	no	PAN_g	PAN_g@$[Fe/Zn]_{10}$SIM	yes	PAN_g@$[Fe/Zn]_{10}$SIM-P
PAN 10, $ZnCl_2$ 7	yes	no	no	PAN_h	PAN_h@$[Fe/Zn]_{10}$SIM	no	PAN_h@$[Fe/Zn]_{10}$SIM-P

(1) Stabilization step, in air, 2 h at 150 °C then 3 h at 250 °C.

3.2.e Pyrolysis and SEM characterization of FeNC electrodes derived from Zn-coated polymer fiber mats decorated with ferrocene-doped SIM-1

The electrode precursors decorated with Fe-doped SIM, as described in 3.2.b-d, were pyrolyzed at 1050 °C in flowing Ar for 1 h via a ramp mode with a heating rate of 5 °C/min. The morphology of the polymer fibers and/or CNFs was investigated by field emission-scanning electron microscopy (FE-SEM) using a Hitachi S-4800 microscope (Hitachi Europe SAS). Data analysis and fiber diameter distribution were performed using an image processing software Image J 1.48 v (U. S. National Institutes of Health).

3.2.f Electrochemical characterization of FeNC electrodes

The electrochemical activity towards the ORR was determined in the rotating disc three-electrode cell. For RDE measurements on the fibrous free-standing electrodes (FSE), the latter were cut out with a punch as disk of 0.196 cm^2, matching the size of the glassy carbon (GC) tip used for the RDE setup, with diameter of 5 mm. The FSE was then attached on GC by placing it onto the GC and using a drop of Nafion perfluorinated resin solution (5 wt% in lower aliphatic alcohols and water, Sigma-Aldrich) in between. The typical weight per geometric area of FSE electrodes for PAN_x@$[Fe/Zn]_y$SIM-P electrodes resulted in a catalyst loading of *ca* 1.2 mg/cm^2.

The RDE experiments were performed in 0.1 M aqueous solution of H_2SO_4. The working electrode was a glassy carbon electrode (Pine research), rotating speed was 1600 rpm and all RDE data was measured with a BioLogic Potentiostat SP-300. In order to remove air trapped in the large pore volume of FSE, the preliminary chronoamperometry at 0.2 V vs. RHE was applied with rotating speed of 1600 rpm, in the same solution. Cyclic voltammetry scans were acquired between 0 and 1 V vs. RHE (scan rate 5 mV s^{-1} for nitrogen-saturated solutions and 2 mV s^{-1} for oxygen-saturated solutions).

3.1 Result and discussion

3.3.a Morphology of Zn-coated PAN fiber mat

In order to investigate the effect of zinc coating on PAN fiber mats and the effect of stabilisation steps, four different possible combinations were applied for PAN-based electrospun mats, as resulting from the application or not of the stabilisation step before Zn sputtering, and after Zn sputtering (see Table 1, labels PAN_a, PAN_b, PAN_c, PAN_d). The photographs of these PAN mats after Zn sputtering and optionally

stabilisation step in air, are illustrated in Figure 45. The pale colour of PAN_b is related to the absence of stabilisation step both before and after Zn sputtering. The grey colour of PAN_a and PAN_c in contrast is related to the Zn film sputtered over a PAN film that has been stabilized only once, either before or after Zn sputtering. Last, the darker colour of PAN_d is due to the stabilisation step of PAN both before and after Zn sputtering.

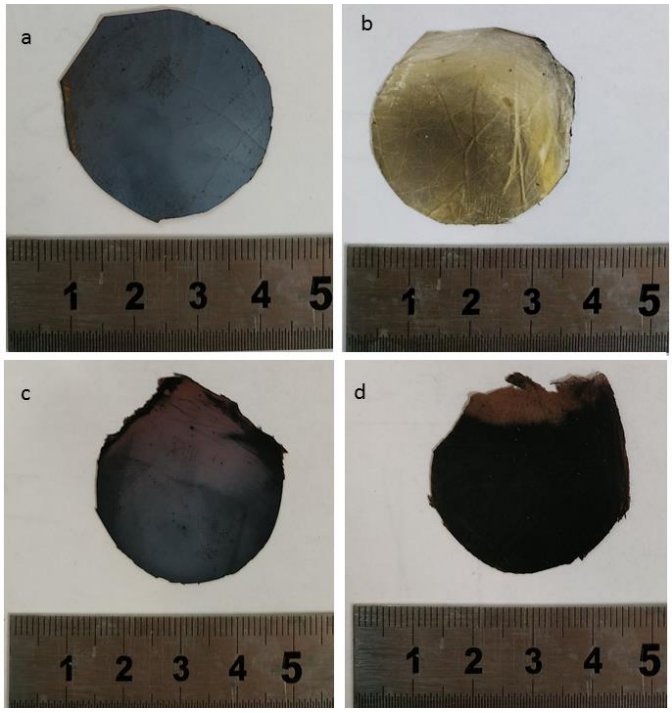

Figure 45: Picture of zinc-coated electrospun PAN fiber mats: a) PAN_a , b) PAN_b , c) PAN_c, d) PAN_d, obtained after coating with Zn, and applying a stabilization step in air before and/or after Zn sputtering (see Table 1 for explanation of PAN_a to PAN_d labels).

After Zn sputtering, the PAN fiber mats were characterized morphologically using SEM and the results are presented in Figure 46, in low magnification (a-d) and high magnification (a'-d').

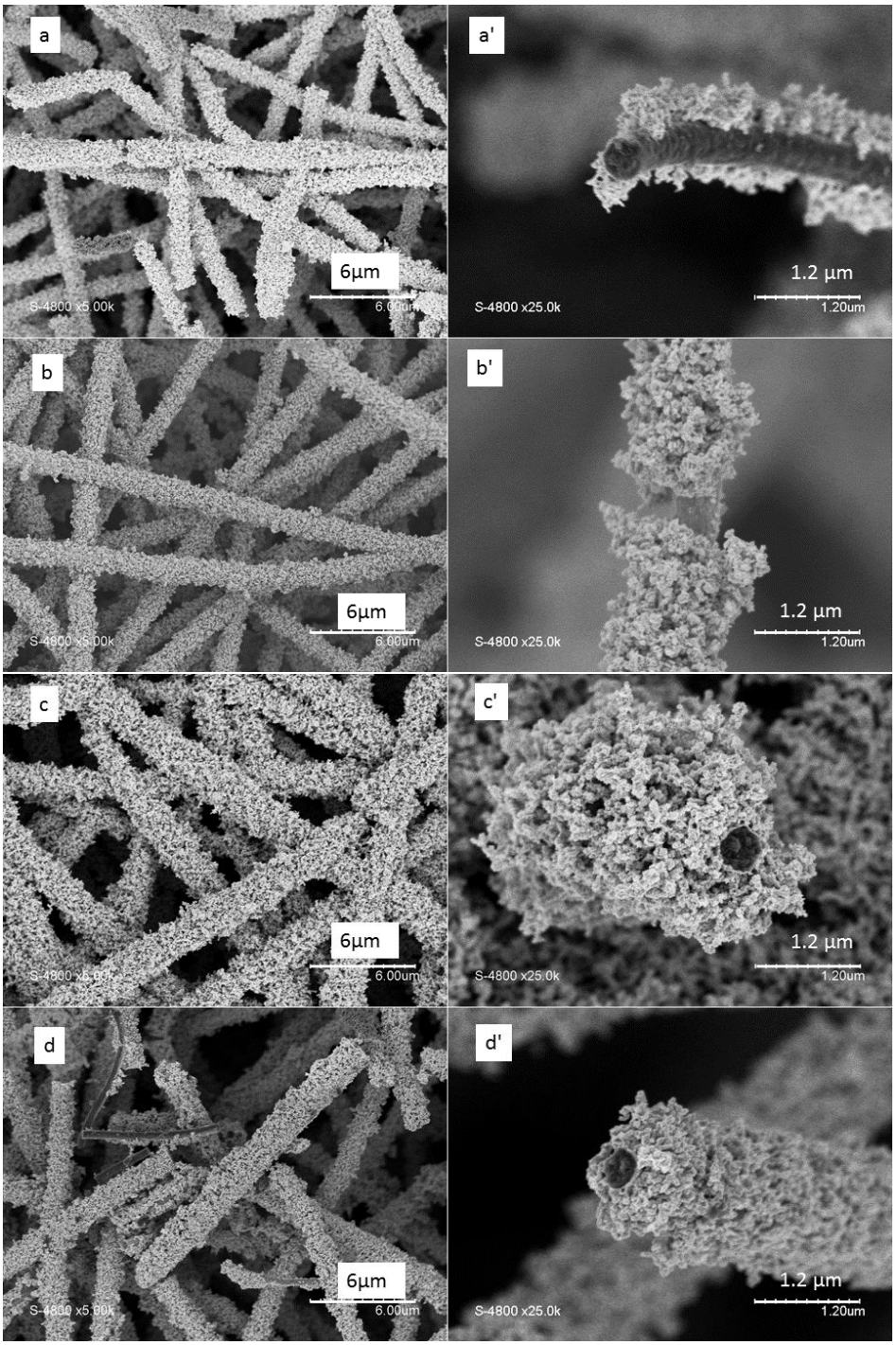

Figure 46: FE-SEM micrographs of a-a') PAN_a, b-b') PAN_b, c-c') PAN_c, d-d') PAN_d.

For the two PAN mats that were not stabilized after Zn deposition (PAN_a and PAN_b), the thickness of the Zn coating was homogeneous (Figure 46a-a', b-b'). The average diameter of the coated fibers was *ca* 1.5 µm, with average thickness of the Zn coating of *ca* 500 nm. For the fibers that were stabilized after Zn deposition (PAN_c and PAN_d), the thickness of the Zn coating was homogeneous (Figure 46 c-c', d-d'). The total diameter of the coated fibers was ca 2 µm and the thickness of the Zn coating was ca 750 nm.

To understand better the nature of the zinc-coating and to explain why the fibers were thicker after additional stabilization step after Zn-sputtering, XRD measurements were performed on the self-standing fibers. The results are represented in Figure 47. For PAN_a, PAN_c and PAN_d, one can observe diffraction peaks that can be assigned to both metallic Zn and ZnO, reference JCPDS n°96-901-1600 and JCPDS n°96-101-1259, respectively. For PAN_b one additional peak is observed at 17° corresponding to PAN, reference JCPDS n° 00-48-2119. It can be seen that for all samples the diffraction peaks, corresponding to Zn and ZnO are superimposed, however, except a peak observed at 36° it is possible to differentiate both Zn (marked as $^+$ in Figure 47) and ZnO (marked as * in Figure 47). It is seen that PAN_a and PAN_b are mostly covered by Zn, while PAN_c and PAN_d obtained after stabilization, covered by both Zn and ZnO. The oxidation of the Zn deposit is clearly due to the additional treatment under air. The average size of the crystalline particles was determined by the Scherrer equation:

$$L_c = \frac{0.9\lambda}{\beta cos\theta}$$

For PAN_a and PAN_b, the average size of Zn crystals is *ca* 29 nm while the average size for ZnO is *ca* 11 nm. For PAN_c and PAN_d, the crystal size of metallic Zn crystals changed to ca 10 nm. This decrease in average crystallite size can be assigned to the influence of the stabilization step in air, when it is performed after the Zn sputtering (case of PAN_c and PAN_d). It is noted that, macroscopically, the thickness of the Zn coating is larger for PAN_c and PAN_d vs. PAN_a and PAN_b. This may be due to the transformation from mostly metallic Zn (density 7.14 g/cm^3) to ZnO (density 5.61 g/cm^3). The dense metallic Zn coating might therefore have expanded as a result of oxidation into a lesser dense phase, ZnO.

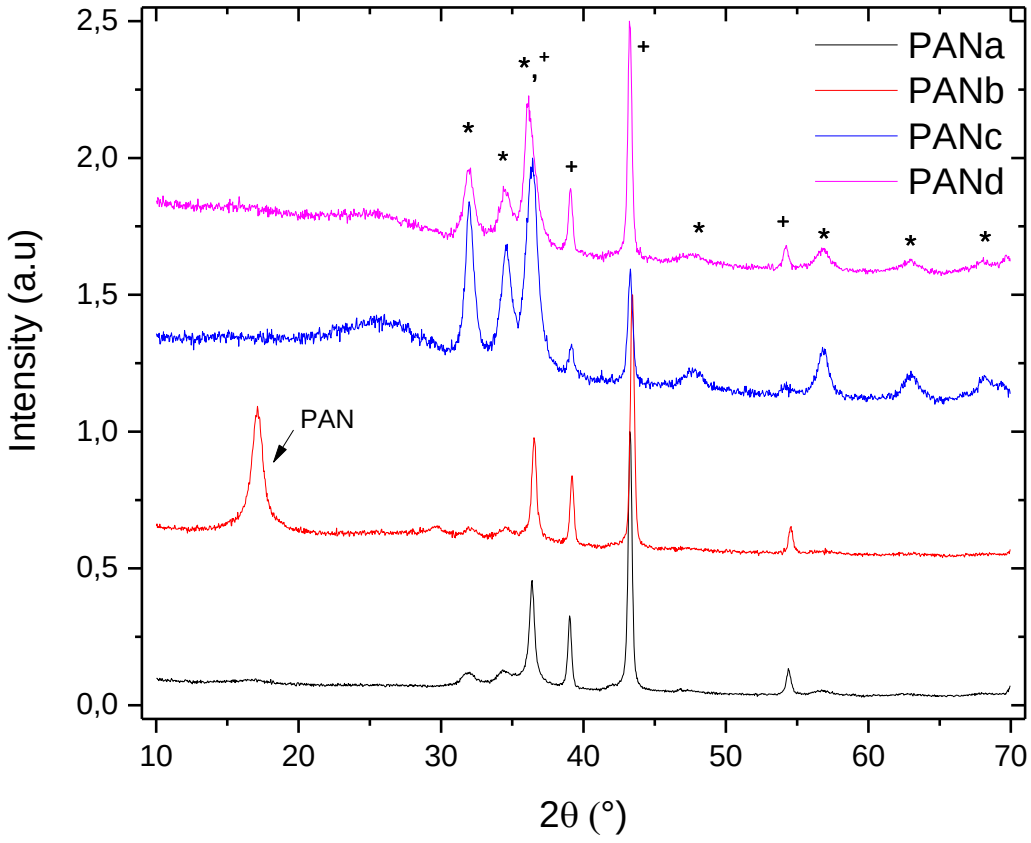

Figure 47: XRD diffractograms for a) PAN_a, b) PAN_b, c) PAN_c, d) PAN_d. * symbols correspond to ZnO peak patterns, + symbols correspond to metallic Zn peak patterns.

3.3.b Morphology of SIM-1 particles grown on the zinc-coated PAN fiber mats and derived FeNC cathodes

The Zn-coated PAN fiber supports, the fibers were immersed in solution for MOF seeding and growth. SEM images of the resulting fibers are shown in Figure 48. Sample PAN_d (stabilized in air both before and after Zn sputtering) dissolved during MOF growth and, therefore, it was impossible to further use it. SIM-1 was seeded successfully on the sample PAN_a@$[Fe/Zn]_{10}$SIM, forming crystals with average size of *ca* 600 nm (Figure 48a). The crystals were seeded and grown homogeneously on the substrate, while the porous Zn coating observed on PAN_a was no longer visible on the PAN fibers after immersion and growth of the SIM-1 crystals. SIM-1 crystals were also grown on PAN_c (PAN_c@$[Fe/Zn]_{10}$SIM) with an average size of *ca* 600 nm (Figure 48e). Compared to PAN_a@$[Fe/Zn]_{10}$SIM however, the density of SIM-1 crystals along the fibers is higher in PAN_c@$[Fe/Zn]_{10}$SIM. The latter involved no stabilization step before Zn sputtering but a stabilization step after the sputtering, which converted more Zn into ZnO. It may be hypothesized that Zn(II) on the PAN fibers is preferable for growing many small SIM-1 crystals than metallic Zn. Sample PAN_b@$[Fe/Zn]_{10}$SIM was prepared from PAN, without any stabilization step before or after Zn-sputtering. Figure 48b shows that the PAN fibers were fully covered by SIM-1 large crystals, with little porosity left between the SIM-1 covered fibers. The average crystal size was *ca* 500 nm.

The morphology of the pyrolyzed mats are now described. After pyrolysis, sample PAN_a@$[Fe/Zn]_{10}$SIM (labelled PAN_a@$[Fe/Zn]_{10}$SIM-P) resulted in an extremely shrunk electrode size (Figure 48b) and therefore no further characterization could be applied to that sample. PAN_b@$[Fe/Zn]_{10}$SIM-P shows CNFs with much smaller catalytic FeNC particles derived from SIM-1 crystals than the large SIM-1 crystals seen before pyrolysis (compare Figure 48c and d). Also a presence of nano-sized extra fibers was seen for this sample, arranged perpendicular to the main fibers. Last, PAN_c@$[Fe/Zn]_{10}$SIM-P shows smooth CNFs with sparse

catalytic particles derived from the SIM-1 crystals. It is noted that the FeNC catalytic particles derived from the pyrolysis of SIM-1 crystals are significantly smaller in size than SIM-1 crystals before pyrolysis.

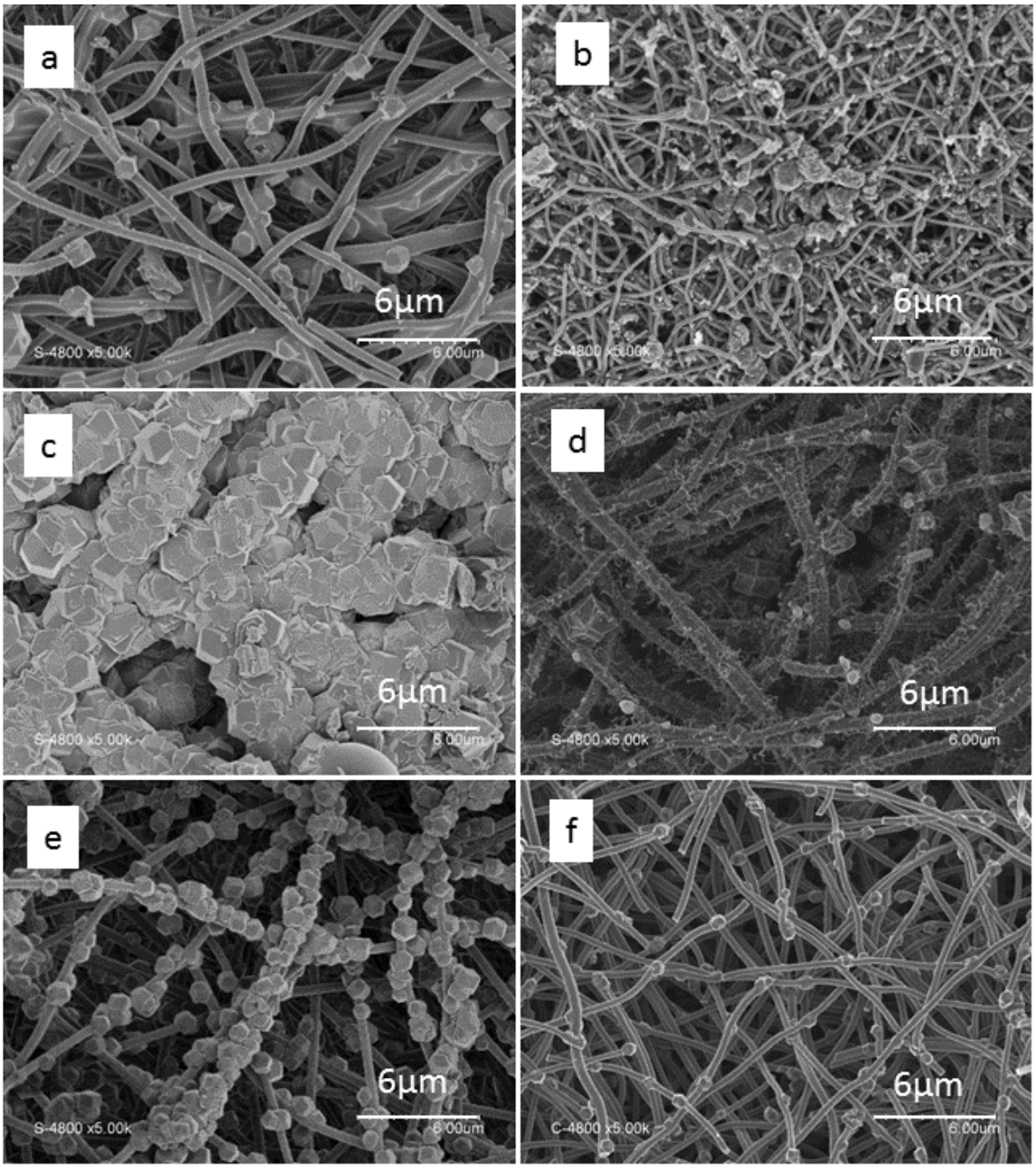

Figure 48. FE-SEM micrographs of: a) PAN_a@$[Fe/Zn]_{10}$SIM, b) PAN_a@$[Fe/Zn]_{10}$SIM-P, c) PAN_b@$[Fe/Zn]_{10}$ SIM, d) PAN_b@$[Fe/Zn]_{10}$SIM-P, e) PAN_c@$[Fe/Zn]_{10}$SIM, f) PAN_c@$[Fe/Zn]_{10}$SIM-P

3.3.c Electrochemical properties of FeNC cathodes derived from SIM-1 particles grown on zinc-coated PAN fiber mats

After successful growth of Fe-doped SIM-1 on some of the Zn-coated fibrous PAN mats and their pyrolysis, the resulting self-standing FeNC cathodes were characterized electrochemically, using the RDE technique in order to determine their ORR activity, and to compare it with that of the reference FeNC powder catalyst. Each electrode was cut and deposited on the glassy carbon electrode using Nafion resin solution. The loading of "catalyst" (mg/cm^2) was calculated by dividing the mass of the self-standing electrode (before adding Nafion) by its geometric area. This information is important to compare to the activity of the reference FeNC powder catalyst. For PAN$_b$@[Fe/Zn]$_{10}$SIM-P, the loading was 1.21 mg cm^{-2} and for PAN$_c$@[Fe/Zn]$_{10}$SIM-P, it was 1.25 mg cm^{-2}. Each sample was cycled in N_2 saturated 0.1 M H_2SO_4 in the potential range 0 and 1 V vs. RHE. The scan rate was 5 mV s^{-1}. Then every sample was cycled in O_2 saturated 0.1 M H_2SO_4 with a low scan rate of 2 mV s^{-1}. The resulting curves are presented in Figure 49.

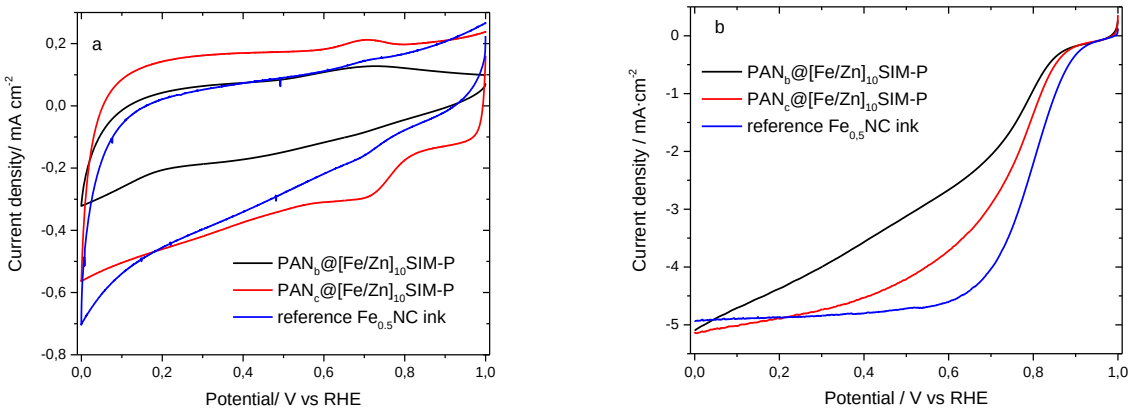

Figure 49: Electrochemical characterization in RDE of FeNC cathodes prepared by growing ferrocene-doped SIM-1 on Zn-coated PAN fiber mats, and of the reference FeNC catalyst: a) CV of in nitrogen saturated 0.1 M H_2SO_4 solution at 5 mV s^{-1}, b) ORR polarization curves in oxygen saturated solution of 0.1 M H_2SO_4. The rotation speed is 1600 rpm. The catalyst loading is 1.21-1.25 mg cm^{-2} for the self-standing FeNC cathodes and 0.8 mg cm^{-2} for $Fe_{0.5}$NC.

The CV curves of both samples (Figure 49a) indicate high electrochemical capacitance of the cathodes, in turn identifying high BET area and good wetting of the carbon surface area by the electrolyte. A reversible peak visible at *ca* 0.72 V vs. RHE is assigned to the redox transition Fe^{2+}/Fe^{3+} from the FeN_x active sites that are electrochemically accessible, as previously reported for many FeNC catalysts[121,122]. The

PAN_c@$[Fe/Zn]_{10}$SIM-P electrode shows the highest capacitive current and also the highest peak signal for Fe^{2+}/Fe^{3+}, possibly indicating a higher density of active sites than for PAN_b@$[Fe/Zn]_{10}$SIM-P.

Both electrodes show significant ORR activity, approaching that of the reference $Fe_{0.5}$NC powder catalyst (Figure 49). This activity is high, especially taking into account that a non–negligible fraction of the mass of PAN_b@$[Fe/Zn]_{10}$SIM-P and PAN_c@$[Fe/Zn]_{10}$SIM-P is made of N-doped but Fe-free CNFs whose ORR activity in acid medium is negligible. Only the carbon phase derived from the Fe-doped SIM-1 crystals significantly contributing to the overall ORR activity. In contrast, for the reference FeNC powder catalyst, all of its mass is derived from ZIF-8, with a high density of FeN_x sites. While the trend for ORR activity is qualitatively $Fe_{0.5}$NC powder > PAN_c@$[Fe/Zn]_{10}$SIM-P > PAN_b@$[Fe/Zn]_{10}$SIM-P, the shape of the ORR polarization curves also identifies additional O_2 transport limitation for PAN_b@$[Fe/Zn]_{10}$SIM-P compared to PAN_c@$[Fe/Zn]_{10}$SIM-P (Figure 49b). This is best seen in the transition region of the curves that is located between the kinetic control region (exponential shape, at high potential) and the diffusion-limited current density. PAN_b@$[Fe/Zn]_{10}$SIM-P shows an abnormal almost linear shape, while PAN_c@$[Fe/Zn]_{10}$SIM-P has a shape of the polarization curve that is more similar to that expected from theory of RDE, and more similar to that of the $Fe_{0.5}$NC powder. Increased mass-transport limitation for self-standing cathodes in RDE (the pores of the electrode being filled by liquid electrolyte) is not illogic, since such electrodes are much thicker (for a fixed catalyst loading) than an active layer prepared from a powder FeNC catalyst. In PEMFC however, the pores will not be filled by electrolyte, but by O_2 (or air), implying that a larger amount of macropores in the electrode (as expected for self-standing FeNC cathodes vs FeNC powder) may result in

improved mass-transport, while reduced mass-transport is expected for highly porous self-standing FeNC cathodes in RDE conditions.

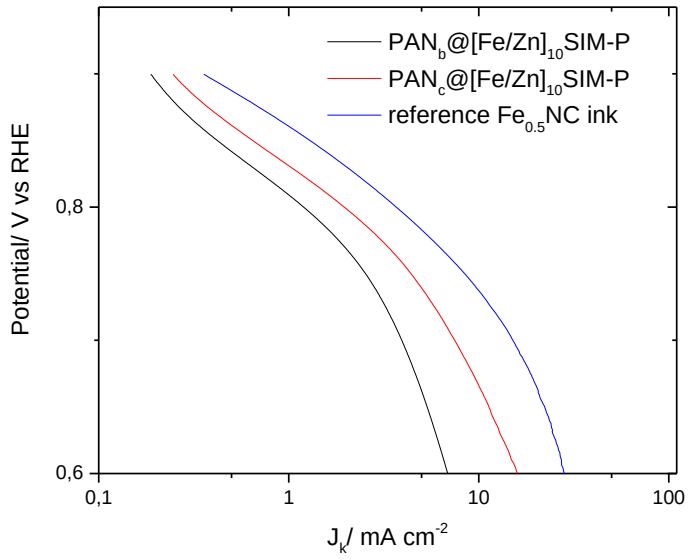

Figure 50: Tafel plots derived from RDE polarization curves for FeNC cathodes derived from Fe-doped SIM-1 grown on zinc-coated electrospun PAN support. Measured in oxygen saturated solution of 0.1 M H_2SO_4 and compared to the ink reference of $Fe_{0.5}NC$. Rotating speed is 1600 rpm.

The ORR polarization curves were corrected for O_2 diffusion limitation by the Koutecky-Levich analysis, and the mass activity at 0.8 V vs. RHE, extracted from the Tafel plots (Figure 50), are 0.77 A g^{-1} and 1.09 A g^{-1} for PAN_b@$[Fe/Zn]_{10}$SIM-P and PAN_c@$[Fe/Zn]_{10}$SIM-P, respectively (Figure 51). In summary, both self-standing FeNC electrodes demonstrate high potential for PEMFC application, and especially PAN_c@$[Fe/Zn]_{10}$SIM-P. It was obtained by sputtering Zn on the as-spun PAN fiber mat, and then applying

a stabilization step afterwards, before immersing the Zn-coated PAN mat in the solution for growing Fe-doped SIM-1.

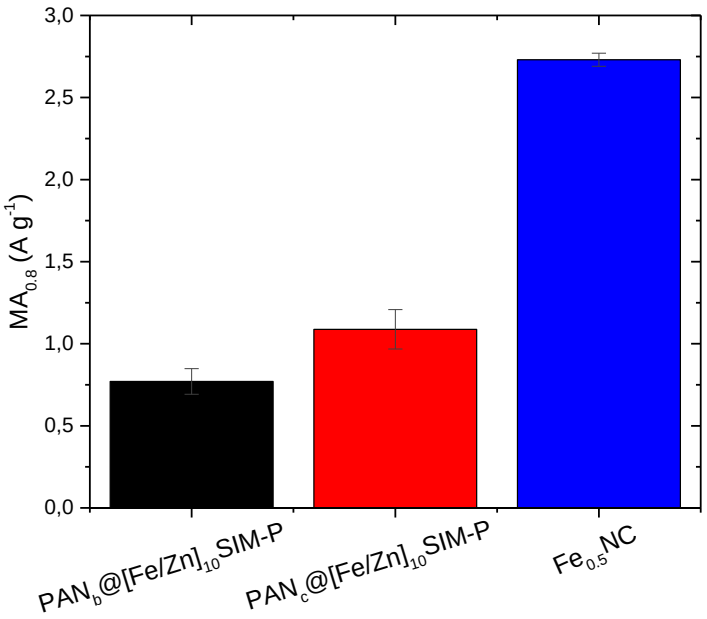

Figure 51: ORR mass activity measured at 0.8 V vs. RHE for self-standing FeNC cathodes compared to that of the reference $Fe_{0.5}NC$ catalyst deposited on GC from an ink made with a Nafion solution. The average activity and error bar was estimated from three independent measurements on three different layers.

3.3.d Properties of FeNC cathodes derived from SIM-1 particles grown on zinc-free PAN fiber mats

The ORR mass activity of FeNC cathodes derived from zinc-coated PAN fiber mats showed promising potential, as described above. However other research has also have shown the possibility of MOF seeding and growth on polymer fibrous supports, without zinc coating of the polymer fibers' surface[119,120,123–125]. Such an approach could simplify the synthesis of FeNC cathodes, without reducing the catalytic ORR activity.

To verify the validity of this approach for preparing FeNC cathodes, the growth of ferrocene-doped SIM-1 (3.2.b) was investigated on four different PAN mats (labelled PAN_e to PAN_h), whose preparation is summarized in Table 11 (rows 6-9). They differ according to whether a stabilization step was performed

or not, and whether the electrospun solution contained only PAN, or PAN and $ZnCl_2$. PAN_e and PAN_g were not stabilized, and PAN_g contained both PAN and $ZnCl_2$. Similarly, PAN_f and PAN_h were both stabilized, and PAN_h contained both PAN and $ZnCl_2$. Following the PAN mat preparation step, other steps for the cathode preparation were the same as described in part 3.2.c and 3.2.d.

The resulting materials are present in Figure 52. Ferrocene-doped SIM-1 was successfully attached to the polymer fibers and dispersed homogeneously for PAN_e@$[Fe/Zn]_{10}$SIM, PAN_f@$[Fe/Zn]_{10}$SIM and PAN_g@$[Fe/Zn]_{10}$SIM. The sample PAN_h@$[Fe/Zn]_{10}$SIM, which was grown on stabilized PAN+$ZnCl_2$ polymer mats demonstrated uneven distribution of SIM-1, and the MOF seems to agglomerate at specific places.

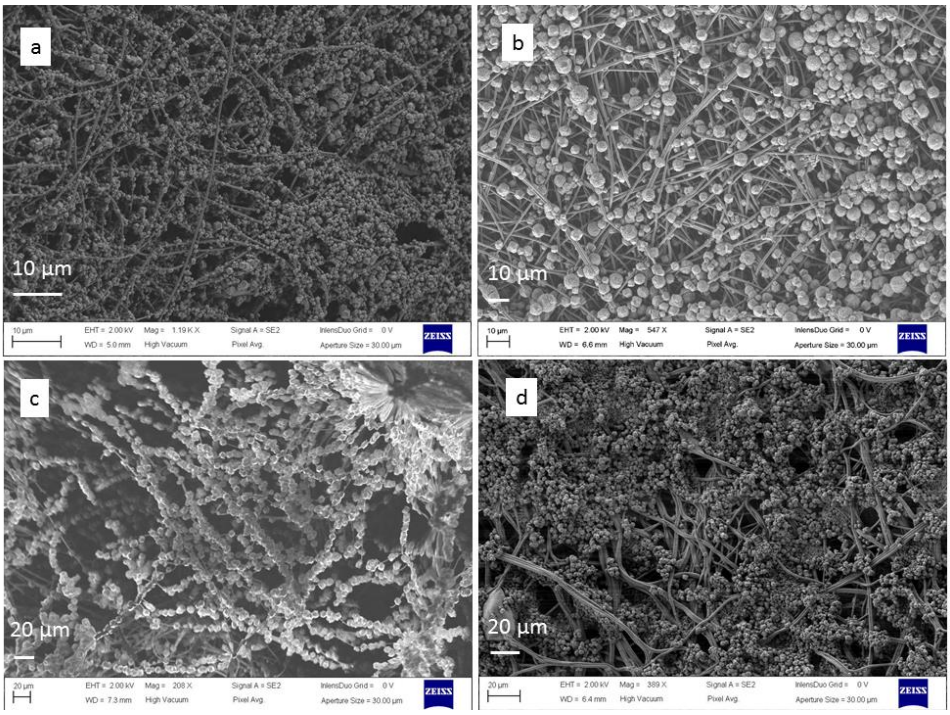

Figure 52: FE-SEM micrographs of: a) PAN_e@$[Fe/Zn]_{10}$SIM, b) PAN_f@$[Fe/Zn]_{10}$SIM, c) PAN_g@$[Fe/Zn]_{10}$SIM, d) PAN_h@$[Fe/Zn]_{10}$SIM

After successful growth of SIM-1 on the substrates and the pyrolysis, the self-standing FeNC cathodes were characterized electrochemically, using the RDE technique, as described previously. For electrode samples prepared without Zn-sputtering, the catalyst loading was *ca* 1.2 mg cm^{-2} for PAN_e@$[Fe/Zn]_{10}$SIM-

P and PAN_f@$[Fe/Zn]_{10}$SIM-P. For PAN_g@$[Fe/Zn]_{10}$SIM-P PAN_h@$[Fe/Zn]_{10}$SIM-P the loading was *ca* 1 mg cm^{-2}. The resulting ORR polarization curves are presented in Figure 53.

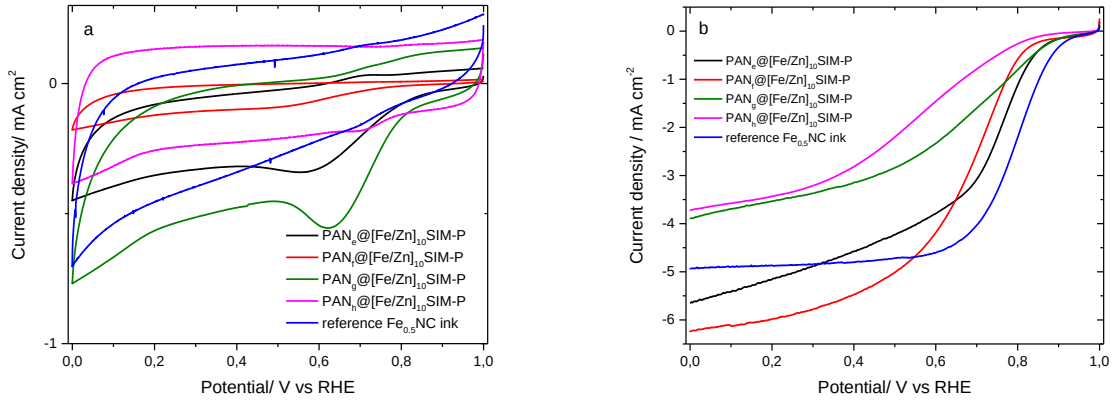

Figure 53: Electrochemical characterization in RDE of FeNC cathodes prepared by growing ferrocene-doped SIM-1 on Zn-free or $ZnCl_2$-containing PAN fiber mats, and of the reference $Fe_{0.5}$NC powder catalyst: a) CV of in nitrogen saturated 0.1 M H_2SO_4 solution at 5 mV s^{-1}, b) ORR polarization curves in oxygen saturated solution of 0.1 M H_2SO_4. Rotating speed is 1600 rpm. The catalyst loading is *ca* 1 mg cm^{-2} for the self-standing FeNC cathodes and 0.8 mg cm^{-2} for $Fe_{0.5}$NC.

The trend of activity for this series of FeNC electrodes is PAN_e@$[Fe/Zn]_{10}$SIM-P > PAN_f@$[Fe/Zn]_{10}$SIM-P on one hand, and PAN_g@$[Fe/Zn]_{10}$SIM-P > PAN_h@$[Fe/Zn]_{10}$SIM-P on the other hand, as can be seen from the high-potential region of the curves. This therefore identifies the negative effect of performing stabilization of the PAN fiber mat on the final ORR activity. The activity comparison between electrodes that involved $ZnCl_2$ in their synthesis (with label PAN_g or PAN_h) and those that did not (PAN_e and PAN_f) is more difficult, due to abnormal shape of ORR polarization curves for the former, which much lower diffusion limited current density than expected at 1600 rpm. In particular, PAN_g@$[Fe/Zn]_{10}$SIM-P shows a high onset potential for ORR but already at 0.7 V vs. RHE it results in lower current density than for PAN_e@$[Fe/Zn]_{10}$SIM-P and PAN_f@$[Fe/Zn]_{10}$SIM-P. In summary, for the most active electrode, PAN_g@$[Fe/Zn]_{10}$SIM-P, the ORR polarization curve approaches that of the $Fe_{0.5}$NC reference material within *ca* 20 mV, in the kinetic region. The curves were further analysed by correcting for O_2 diffusion limitation by Koutecky Levich analysis, leading to the Tafel plots (Figure 54). From the Tafel plots, the mass activity at 0.8 V vs. RHE were obtained by dividing by the catalyst loading measured for each electrode, and the results are presented in Figure 55. The figure confirms that PAN_e@$[Fe/Zn]_{10}$SIM-P has the highest ORR mass activity in this series, 0.77 A g^{-1}. Similar activity is seen for PAN_g@$[Fe/Zn]_{10}$SIM-P (0.71 A g^{-1}) but

the latter leads, in RDE conditions, to stronger mass transport limitation. Samples labelled PAN_f@$[Fe/Zn]_{10}$SIM-P and PAN_h@$[Fe/Zn]_{10}$SIM-P show 2x to nearly 4x smaller catalytic activity, with mass activity of 0.46 and 0.22 A g^{-1}, respectively (Figure 55).

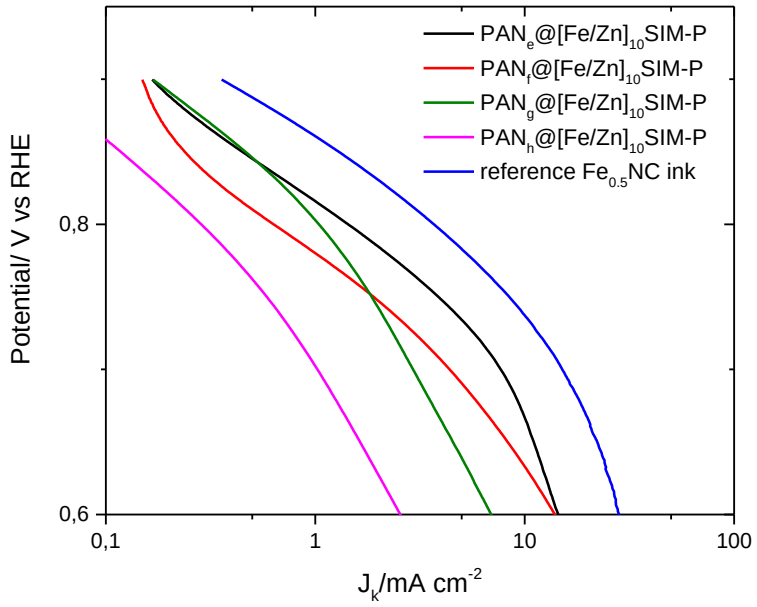

Figure 54: Tafel plots derived from RDE polarization curves for FeNC cathodes derived from Fe-doped SIM-1 grown on on Zn-free or $ZnCl_2$-containing PAN fiber mats, and of the reference $Fe_{0.5}$NC powder catalyst. Measured in oxygen saturated solution of 0.1 M H_2SO_4. Rotating speed is 1600 rpm.

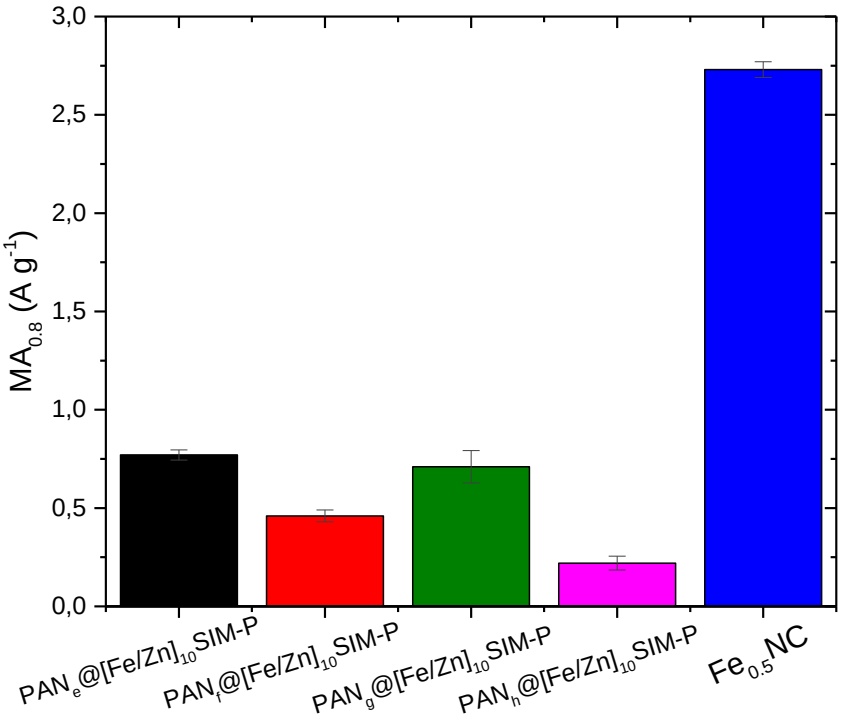

Figure 55: ORR mass activity at 0.8 V vs. RHE for self-standing FeNC cathodes and comparison to the reference $Fe_{0.5}NC$ powder catalyst. The average activity and error bar was estimated from three independent measurements on three different layers.

Conclusions

In this chapter, several series of FeNC self-standing electrodes were prepared *via* the growth of ferrocene doped SIM-1 on different PAN fiber mats, then pyrolyzed in identical condition. The electrode precursor (before pyrolysis) and electrode after pyrolysis were investigated morphologically as well as electrochemically, using an RDE setup. The effect of coating the PAN fiber mats with Zn before growing the SIM-1 crystals was studied. The results obtained with this approach were then compared to those obtained without Zn-coating the PAN fiber mat, and also compared to results obtained by doping the bulk of the PAN fibers with $ZnCl_2$.

Overall, the ORR activity results show that Zn-coating or Zn-doping of the PAN fibers does not lead to enhanced ORR activity. The FeNC electrode prepared simply by immersing a raw PAN fiber mat in a solution containing Zn(II), the SIM-1 ligand and ferrocene, followed by a stabilization step in air and then by pyrolysis, resulted in high ORR activity at 0.8 V vs RHE of 0.77 A g^{-1} (PAN_e@$[Fe/Zn]_{10}$SIM-P). This activity is comparable to the highest ORR activity obtained in this chapter (1.09 A g^{-1}), obtained with raw PAN fiber mat that was sputtered with Zn, then stabilized and then immersed in the solution for growing SIM-1 (PAN_c@$[Fe/Zn]_{10}$SIM-P).

These results show the promising approach of growing Fe-doped MOFs on PAN fibers. This approach is further investigated on ZIF-8 and with another type of polymer fibers in Chapter 4. Zn coating or functionalization was not pursued in Chapter 4, since it did not show significant benefit in terms of activity, while complexifying the preparation method.

1. Allendorf, M.D.; Houk, R.J.T.; Andruszkiewicz, L.; Talin, A.A.; Pikarsky, J.; Choudhury, A.; Gall, K.A.; Hesketh, P.J. Stress-induced chemical detection using flexible metal-organic frameworks. *J. Am. Chem. Soc.* **2008**, *130*, 14404–14405.

2. Mandemaker, L.D.B.; Rivera-Torrente, M.; Delen, G.; Hofmann, J.P.; Lorenz, M.; Belianinov, A.; Weckhuysen, B.M. Nano-Web Surface-Mounted Metal-Organic Framework Films with Tunable Amounts of Acid Sites as Tailored Catalysts. *Chem. - A Eur. J.* **2019**, 691–698.

3. Huang, Y.; Tao, C.A.; Chen, R.; Sheng, L.; Wang, J. Comparison of fabrication methods of metal-organic framework optical thin films. *Nanomaterials* **2018**, *8*, 1–10.

4. Joshi, J.N.; Moran, C.M.; Feininger, H.P.; Dow, J.M.; Walton, K.S. Household Aluminum Products as Insoluble Precursors for Directed Growth of Metal-Organic Frameworks. *Cryst. Growth Des.* **2019**, *19*, 5097–5104.

5. Bechelany, M.; Drobek, M.; Vallicari, C.; Abou Chaaya, A.; Julbe, A.; Miele, P. Highly crystalline MOF-based materials grown on electrospun nanofibers. *Nanoscale* **2015**, *7*, 5794–5802.

6. Centrone, A.; Yang, Y.; Speakman, S.; Bromberg, L.; Rutledge, G.C.; Hatton, T.A. Growth of metal-organic frameworks on polymer surfaces. *J. Am. Chem. Soc.* **2010**, *132*, 15687–15691.

7. Hou, L.; Zhou, M.; Dong, X.; Wang, L.; Xie, Z.; Dong, D.; Zhang, N. Controlled Growth of Metal-Organic Frameworks on Polymer Brushes. *Chem. - A Eur. J.* **2017**, *23*, 13337–13341.

8. Aguado, S.; Canivet, J.; Farrusseng, D. Engineering structured MOF at nano and macroscales for catalysis and separation. *J. Mater. Chem.* **2011**, *21*, 7582–7588.

9. Armel, V.; Hannauer, J.; Jaouen, F. Effect of ZIF-8 crystal size on the O<inf>2</inf> electro-reduction performance of pyrolyzed Fe–N–C catalysts. *Catalysts* **2015**, *5*, 1333–1351.

10. Zitolo, A.; Ranjbar-Sahraie, N.; Mineva, T.; Li, J.; Jia, Q.; Stamatin, S.; Harrington, G.F.; Lyth, S.M.; Krtil, P.; Mukerjee, S.; et al. Identification of catalytic sites in cobalt-nitrogen-carbon materials for the oxygen reduction reaction. *Nat. Commun.* **2017**, *8*, 1–10.

11. Jia, Q.; Ramaswamy, N.; Hafiz, H.; Tylus, U.; Strickland, K.; Wu, G.; Barbiellini, B.; Bansil, A.; Holby, E.F.; Zelenay, P.; et al. Experimental Observation of Redox-Induced Fe-N Switching Behavior as a Determinant Role for Oxygen Reduction Activity. *ACS Nano* **2015**, *9*, 12496–12505.

12. He, P.; Haw, K.G.; Ren, J.; Fang, Q.; Qiu, S.; Valtchev, V. MOF-cation exchange resin composites and their use for water decontamination. *Inorg. Chem. Front.* **2018**, *5*, 2784–2791.

13. Shangguan, J.; Bai, L.; Li, Y.; Zhang, T.; Liu, Z.; Zhao, G.; Liu, Y. Layer-by-layer decoration of MOFs on electrospun nanofibers. *RSC Adv.* **2018**, *8*, 10509–10515.

14. Liu, C.; Wu, Y.N.; Morlay, C.; Gu, Y.; Gebremariam, B.; Yuan, X.; Li, F. General Deposition of Metal-Organic Frameworks on Highly Adaptive Organic-Inorganic Hybrid Electrospun Fibrous Substrates. *ACS Appl. Mater. Interfaces* **2016**, *8*, 2552–2561.

Chapter 4: Growth of ferrocene-doped MOFs on polymer fibers: preparation of electrocatalysts and electrodes

Summary

4.1 Introduction

In chapter 3, it was found that it is possible to grow ferrocene-doped SIM-1 on electrospun PAN fibers, and this was best achieved on the non-stabilized electrospun PAN fibers. However, it was impossible to grow ferrocene-doped ZIF-8 on electrospun PAN fibers because of solvent incompatibility. The issue is that PAN is soluble in polar aprotic solvents such as DMF and DMAc, used to synthesize ferrocene-doped ZIF-8.

In this chapter, the approach for growing ferrocene-doped SIM-1 on electrospun PAN fibers was applied for different ferrocene contents. Furthermore, a different route to successfully grow ferrocene-doped ZIF-8 on polymer fibers was investigated. On the basis of the synthesis for ferrocene-doped ZIF-8 in chapter 2, carried out in DMF, we needed a polymer that is non-soluble in this solvent. Polybenzimidazole (PBI) may be an option, as upon pyrolysis it also is transformed into N-doped carbon. Furthermore it has the advantage of comprising benzimidazole, with analogous chemistry to the organic ligand in ZIF-8. However, PBI is, as PAN, soluble in DMF. To overcome this issue, we used cross-linked PBI prepared with a method previously developed in the laboratory [1]. Cross-linked PBI does not dissolve in DMF and was thus successfully used as a support to grow ferrocene-doped ZIF-8 in DMF.

The as prepared materials, labelled PAN@$[Fe/Zn]_x$SIM and PBIXL@$[Fe/Zn]_x$ZIF were characterized for their composition and morphology, then used as precursors to prepare FeNC electrode upon thermal treatments. Figure 56 is a schematic representation of the growth of MOFs onto the electrospun fiber mat (as described in section 4.1.a) and (described in section 4.1.b) the resulting formation, upon pyrolysis, of self-standing FeNC electrodes. The pyrolysis step eliminates most of the zinc present in those MOFs as volatile products and transforms the organic ligands into N-doped conductive carbon, while Fe from ferrocene is transformed into Fe-based active sites. Similar approaches were applied previously in the literature for different applications (e.g. supercapacitors or fibrous filters) [2–4]

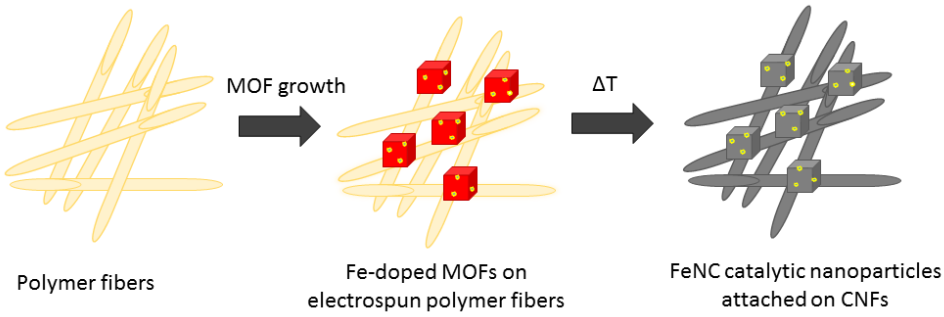

Figure 56: Scheme of the growth of ferrocene-doped MOF crystals on polymer nanofiber mats and their later conversion in FeNC self-standing cathodes.

The derived self-standing cathodes were investigated with physico-chemical and electrochemical techniques. We characterized their activity towards ORR first in RDE and then, after impregnation by Nafion, in PEMFC. In addition, the electrochemical characterization was performed also on the grinded self-standing electrodes and preparing thereafter an ink with the conventional procedure. The activity and performance is compared and discussed as a function of the preparation and morphology of the catalyst layers.

4.2 Methodology

4.2.a Synthesis of polymer fiber mats decorated with ferrocene-doped MOFs

We already reported the syntheses of ferrocene-doped ZIF-8 and SIM-1 in chapter 2. Here the aim is to grow the MOFs on the surface of polymer fibers. Thus, the synthesis takes place in the presence of the polymer fiber mat, which is dipped in the solution containing the MOF precursors. The relative ratios of the MOF ligand, the zinc salt and the ferrocene were kept the same as indicated in the syntheses in chapter 2, and the Fe/Zn mol % ratio investigated were 0.5, 1 or 2.

The precursors for growing Fe-doped SIM-1 were 4-methyl-5-imidazolecarboxaldehyde (99%, Sigma-Aldrich), ferrocene (98%, Sigma-Aldrich), zinc nitrate hexahydrate (99%, Sigma-Aldrich) as reported in chapters 2-3. [5] The imidazole ligand was dissolved first in 40 mL of ethanol at room temperature under magnetic stirring for few minutes. The temperature of the solution was then raised to 60 °C, and the ferrocene and zinc nitrate were added. The molar ratio between imidazole ligand and zinc was 4:1; the quantity of ferrocene was set to 0.5, 1 or 2 mol % relative to Zn. After few minutes needed for homogenization, the stirring was stopped and the raw PAN nanofiber mat (prepared via electrospinning as described in chapter 1) was immersed in solution and put at the bottom of the beaker. Its thickness was *ca* 50 µm and the typical size of the piece of mat immersed in solution was 4 cm x 4 cm. After introduction of the fiber mat in solution, the reaction was let to proceed at 60°C for 24 h without stirring, and the nanofiber mat was then withdrawn from the solution and washed with ethanol. To verify if some Fe-doped SIM-1 had also grown in solution, and how much, the remaining solution was centrifuged at 10,000 rpm for 10 minutes and washed in ethanol. The centrifugation and washing was repeated 4 times and then the collected powder was dried for 24 h at 80 °C.

The resulting materials were labelled as presented in Table 12, rows 2-4. For example: PAN@$[Fe/Zn]_2$SIM stands for SIM-1 doped by 2 mol% of ratio Ferrocene/Zn, grown of PAN polymer fiber, pyrolysed (capital letter P) and, optionally, grinded (lower-case letter g) afterwards.

Table 12. Investigated Zn/Fe atomic ratio in solution and labels of Fe-doped MOFs grown on polymer fibers and of the resulting FeNC catalysts

MOF	Zn/Fe at. Ratio in solution	Fe-doped MOFs grown on polymer fibers	Self-standing FeNC cathodes	Grinded self-standing FeNC cathodes
SIM-1	0.5	PAN@$[Fe/Zn]_{0.5}$SIM	PAN@$[Fe/Zn]_{0.5}$SIM-P	PAN@$[Fe/Zn]_{0.5}$SIM-P_g
	1.0	PAN@$[Fe/Zn]_{1}$SIM	PAN@$[Fe/Zn]_{1}$SIM-P	PAN@$[Fe/Zn]_{1}$SIM-P_g
	2.0	PAN@$[Fe/Zn]_{2}$SIM	PAN@$[Fe/Zn]_{2}$SIM-P	PAN@$[Fe/Zn]_{2}$SIM-P_g
ZIF-8	0.5	PBIXL@$[Fe/Zn]_{0.5}$ZIF	PBIXL@$[Fe/Zn]_{0.5}$ZIF-P	PBIXL@$[Fe/Zn]_{0.5}$ZIF-P_g
	1.0	PBIXL@$[Fe/Zn]_{1}$ZIF	PBIXL@$[Fe/Zn]_{1}$ZIF-P	PBIXL@$[Fe/Zn]_{1}$ZIF-P_g
	2.0	PBIXL@$[Fe/Zn]_{2}$ZIF	PBIXL@$[Fe/Zn]_{2}$ZIF-P	PBIXL@$[Fe/Zn]_{2}$ZIF-P_g

The precursors for growing Fe-doped ZIF-8 were 2-methylimidazole (99%, Sigma-Aldrich), ferrocene (98%, Sigma-Aldrich), zinc nitrate hexahydrate (99%, Sigma-Adrich) and N-N-dimethylformamide (DMF, 99%, Sigma-Aldrich), as reported in chapter 2. [6] The imidazole ligand was first dissolved in 40 mL of DMF at room temperature using magnetic stirring. After heating to 140 °C, ferrocene and zinc nitrate were added in the solution. The molar ratio between imidazole ligand and zinc was 4:1; the quantity of ferrocene was 0.5, 1 or 2 mol % relative to Zn. After few minutes, the stirring was stopped and the cross-linked PBI nanofiber mat was introduced in solution horizontally and was held in the solution by gravity. The preparation of this mat is separately described in the next section. The typical thickness of the PBI fiber mat was ~ 20 µm and the typical size of the piece of mat immersed in solution was 4 cm x 4 cm. After introduction of the fiber mat in solution, the reaction was let to proceed at 140°C for 24 h without stirring, and the nanofiber mat was then withdrawn from the solution and washed with ethanol. The resulting materials were labelled as presented in Table 12 rows 5-7. For example: PBIXL@$[Fe/Zn]_{2}$ZIF-P_g stands for ZIF-8 doped by 2 mol% of ratio Ferrocene/Zn, grown of cross-linked PBI polymer fiber, pyrolysed (capital letter P) and, optionally, grinded (lower-case letter g) afterwards.

4.2.b Preparation of cross-linked polybenzimidazole (PBI XL) nanofiber mats.

The polymer solution was prepared by using N-N-dimethylacetamide, DMAc (≥99%, Sigma-Aldrich), dichloroxylene DCX (98%, Sigma-Aldrich) and polybenzimidazole PBI S26 (26.2 wt% solution in DMAc, PBI Performance Products). The initial PBI solution was first diluted to 15 wt% in DMAc under mild heating (ca 50°C), and then the cross-linking agent DCX was added in the solution, under magnetic stirring. The quantity of added DCX was 200 % relative to the mass of PBI in the solution. The homogeneous solution was cooled to room temperature and then was electrospun at 20° C and collected on a drum rotating at 100 rpm (RT Advanced, Linari Engineering s.r.l). The distance between the tip of the needle (18 gauge) and the collector was 10 cm and the voltage of 20 kV was applied to obtain a stable Taylor cone. The flow rate was kept constant at 0.2 mL h^{-1}. The obtained PBI and DCX fiber mat was cross-linked in a furnace under 150° C in flowing air for 3 h in order to obtain a PBIXL fiber mat.

4.2.c Preparation of FeNC electrodes derived from polymer fiber mats decorated with ferrocene-doped MOFs

The electrode precursors described in 4.1.a, i.e. the polymer nanofiber mats (4 cm x 4 cm typically) decorated with ferrocene-doped MOFs, were pyrolysed at 1050 °C in flowing Ar for 1 h via a ramp mode with a heating rate of 5 °C/min (see scheme on the right in Figure 56). Before this pyrolysis however, the PAN@SIM-1 decorated mats were subjected to a low-temperature thermal treatment at 150° C in air for 2 hours, then 250° C in air for 3 hours, allowing the cyclisation of PAN, as described in chapter 1. This was not necessary, and therefore not performed, for the PBIXL@ZIF-8 mats[7].

For comparison, the activity of the FeNC electrodes was evaluated both in their self-standing form and in their powder form. To this end, the FSE were manually grinded and catalytic inks were then prepared as described in the next section. The typical morphology of the grinded FSE obtained is shown Figure 57. The manually grinded fibers are shorter than the CNFs seen in the FSE, with length of the fibers ranging from 0.4 to 5 µm. MOF-derived carbon particles can also be seen in this picture. They are not deviated morphologically from non-grinded fibers.

The in-plane electronic conductivity was measured using a 4 probe cell (Fumatech). The CNFs were cut into 4 cm x 1 cm strips that were attached to conducting tape. The measurement was carried out using Keithley's Series 2400 Source Measure Unit in a Fumatech MK3-L cell operated in the current range 0–100 mA at room temperature.

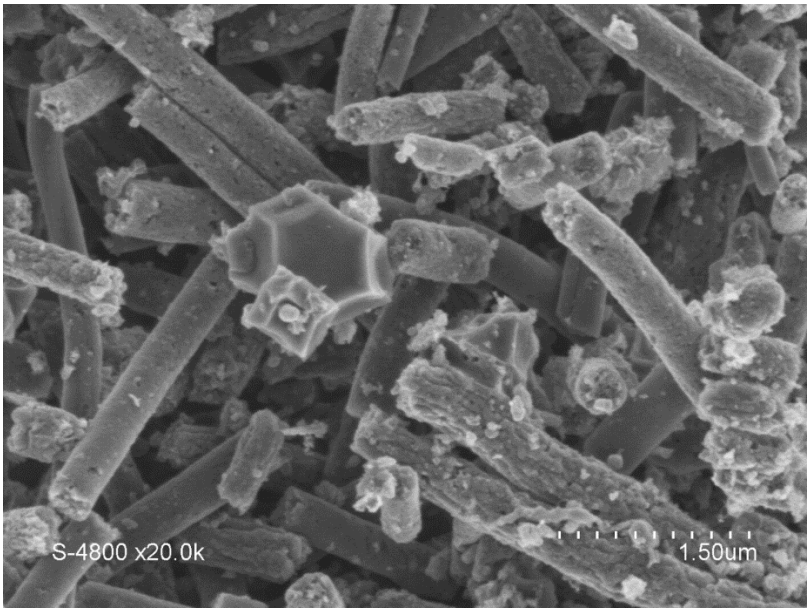

Figure 57: FE-SEM micrographs of PBIXL@$[Fe/Zn]_1$ZIF-P_g, given as an example of morphology obtained for manually grinded fiber mats.

The morphology of the polymer fibers and/or CNFs was investigated by field emission-scanning electron microscopy (FE-SEM) using a Hitachi S-4800 microscope. Data analysis and fiber diameter distribution were performed using an image processing software Image J 1.48 v (U. S. National Institutes of Health). CNFs were analyzed by transmission electron microscopy (TEM) using a JEOL 2200FS (Source: FEG) microscope operating at 200 kV equipped with a CCD camera Gatan USC (16 MP). For TEM cross-sectional analysis, a microtome was used on resin-encapsulated sample and slices were deposited on carbon-coated copper grids (Agar Scientific).

The metal content in the catalysts was measured via X-ray Fluorescence (XRF) (Axios Max from PANanalytical). Fe-doped samples were manually grinded into powder and mixed with boric acid as a binder in a ratio of 1:3 manually. Then, the mixture was pressed into pellets of a 13 mm diameter for XRF measurements. The calibration curve was performed using 0.1, 0.2, 0.5, 1.0, 1.5 and 2.0 wt. % Fe in a mixture of Fe(II) acetate and Vulcan XC72R.

4.2.d Electrochemical characterization

The electrochemical activity towards ORR was determined in RDE setup and the initial performance measured in a single-cell laboratory fuel cell.

For RDE measurements on the fibrous free-standing electrodes (FSE), the latter were cut out with a punch as circles of 0.196 cm^2, matching the size of the glassy carbon (GC) tip used for the RDE setup, with diameter of 5 mm. The FSE was then attached on GC by placing it onto the GC and adding a drop of Nafion perfluorinated resin solution (5 wt% in lower aliphatic alcohols and water, Sigma-Aldrich) on top of the FSE. The typical weight of FSE electrodes for both the PBIXL@$[Fe/Zn]_x$ZIF-P and PAN@$[Fe/Zn]_x$SIM-P electrodes resulted in a catalyst loading of *ca* 0.5 mg/cm^2. However, the electrode was thinner for PBI-derived electrodes (ca 20 µm) relative to PAN-derived electrodes (ca 50 µm).

The RDE experiment was performed in 0.1 M aqueous solution of H_2SO_4. The working electrode was glassy carbon electrode (Pine research), rotating speed was 1600 rpm and all RDE data was measured with a BioLogic Potentiostat SP-300. In order to remove air from the large pore volume of FSE the preliminary chronoamperometry at 0.2 V vs. RHE was applied with rotating speed of 1600 rpm in same solution). Cyclic voltammetry scans were acquired between 0 and 1 V vs. RHE (v = 5 mV s^{-1} for nitrogen-saturated solutions and v = 2 mV s^{-1} for oxygen-saturated solutions). The time for nitrogen or oxygen saturation of solution was 15 minutes for each measurement.

For RDE measurements on the grinded FSE, 10 mg of grinded FSE was added to 108.5 µL of Nafion perfluorinated resin solution (5 wt% in lower aliphatic alcohols and water, Sigma-Aldrich), 300 µL of ethanol (absolute, Sigma-Aldrich) and 36.5 µL ultrapure water 18 MΩ. The prepared ink was ultra-sonicated for 1 h at 25 °C and 8.8 µL were then deposited on the GC tip and dried in air, resulting in a catalyst loading of 1.0 mg cm^{-2}.

The accelerated stress tests were performed in this work with the collaboration of LEPMI, Grenoble. The load-cycling (LC) protocol was used, where the potential was stepped between 0.6 and 1.0 V vs. RHE. For each ageing test a square-wave ramp was used and each potential was held for three seconds. The electrolyte was Ar or O_2-saturated 0.1 M H_2SO_4 and the temperature was T = 25°C.

For fuel cell measurements with cathodes prepared via the conventional ink method, an ink made was prepared by using 20 mg of grinded FSE, 625 µL of Nafion perfluorinated resin solution (5 wt% in lower

aliphatic alcohols and water, Sigma-Aldrich), 300 µL of 1-propanol (99.7 % Sigma-Aldrich) and 272 µL of ultrapure water 18MΩ. The ink was ultra-sonicated for 1 h at 25 °C and then the total ink volume was deposited in 5 steps of 210 µL each, on the microporous side of a gas diffusion layer (Sigracet S10-BC, SGL Group), resulting in a catalyst loading of 4.84 mg cm^{-2}. During the ink deposition process, the gas diffusion layer was heated on a hot plate, in order to accelerate solvent evaporation, and each 210 µL aliquot of ink was introduced only after complete drying of the previous layer, in order to avoid layer cracking. The anode was a 0.5 mg_{Pt} cm^{-2} commercial layer pre-deposited on Sigracet S10-BC and S24BC. Membrane electrode assemblies (MEAs) were prepared by hot-pressing the anode and cathode with geometric areas of 4.84 cm^2 against a Nafion NRE-211 membrane at 135 °C for 2 minutes. The MEAs were installed in a single-cell PEMFC with serpentine flow fields. The fuel cell bench was an in-house bench connected to a Biologic Potentiostat with a 50 A booster. The experiments were controlled with the EC-Lab software. For all fuel cell tests reported in the present work, the cell temperature was 80 °C, the humidifier temperature was 85 °C, and the inlet gas pressures were 1 bar gauge at both the anode and the cathode. The humidified H_2 and O_2 flow rates were ca. 50–70 sccm, as controlled downstream of the fuel cell. The fuel cell polarization curves were recorded with EC lab software using cycling voltammetry experiment and scanning the cell voltage at 0.5 $mV \cdot s^{-1}$.

Last but not least, a down-selected FSE, namely PBIXL@$[Fe/Zn]_{0.5}$ZIF-P, was investigated for evaluating its performance at the cathode of a PEMFC, without grinding. The FSE was functionalized by Nafion by dipping pre-cut self-standing electrodes with geometric area of 4.96 cm^2 in the Nafion perfluorinated resin solution (5 wt% in lower aliphatic alcohols and water, Sigma-Aldrich) for 3 seconds and drying in air. The prepared thin electrode in Nafion was later assembled in MEA as described in previous paragraph. As self-standing electrodes consisted mainly out of CNFs, there was no need in the gas diffusion layer from cathode side, so several amount of CNFs (1, 4 or 7 layers) was superimposed and later hot pressed with membrane and anode. The anode and membranes were the same as described for MEA preparation with grinded FSE cathodes.

4.3 Results and discussion

4.3.a Morphology of Fe-doped MOF crystals grown on polymer fibers

The synthesis of ferrocene-doped MOFs was reported by other groups earlier [5,6] and adapted here to drive their growth from the precursor solution onto polymer nanofibers. The choice of the nature of the polymer fibrous support is however not trivial as discussed below. Moreover, the choice of the polymer also implies that some solvents may not be used for the growth of MOFs (i.e. the polymer should not dissolve).

Due to the synthesis identified in chapter 2 for preparing ferrocene-doped SIM-1, ethanol was also used as a solvent to synthesize PAN@[Fe/Zn]$_x$SIM materials. On the other hand, replicating the synthesis identified in chapter 2 for preparing ferrocene-doped ZIF-8 (in DMF solvent) was not successful due to dissolution of PAN fibers in DMF (chapter 3). For those reasons, we selected a polymer that is non-soluble in DMF, i.e. cross-linked PBI. Different tests with varying cross-linker content relative to PBI were performed, ranging from 50 to 200 % cross-linker. The results show that high cross-linker content resulted in minimized shrinking during both the MOF growth stage (Figure 58. Photograph of ferrocene-doped ZIF-8 grown on cross-linked electrospun PBI nanofibers prepared with different amount of crosslinker as indicated in % compared to their initial size before deposition in MOF precursor solution and during the pyrolysis stage (not shown). Raman spectra and electric conductivity after pyrolysis were however comparable for all PBI-XL samples (Table). Therefore, the PBIXL mat with minimized shrinking was chosen for practical reasons (200 % cross-linker, labelled simply as PBIXL thereafter).

Table 13: In-plane electrical conductivity and relative areas and intensities of D and G bands (I_D/I_G, A_D/A_G) in the Raman spectra for pyrolysed CNFs derived from cross-linked PBI

% of cross-linking agent	thickness, µm	Conductivity, S cm^{-1}	Raman I_D/I_G	Raman A_D/A_G
50	17	7.4	1.5	1.7
100	21	4.9	2.3	4.6
150	19	5.2	1.3	1.7
200	17	8.2	1.8	2.9

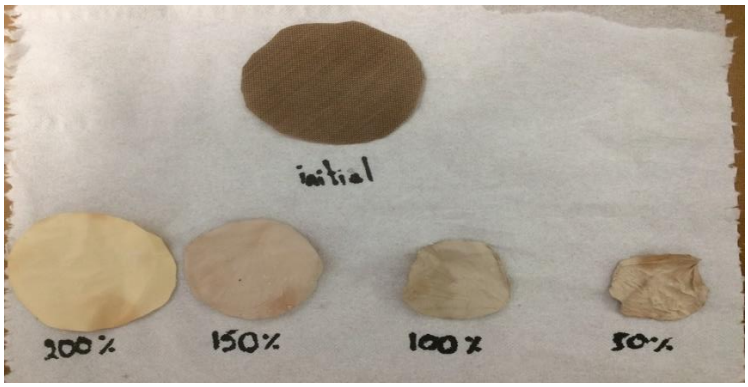

Figure 58. Photograph of ferrocene-doped ZIF-8 grown on cross-linked electrospun PBI nanofibers prepared with different amount of crosslinker as indicated in % compared to their initial size before deposition in MOF precursor solution.

The synthesis described in 4.1.a was then used to prepare the PBIXL@$[Fe/Zn]_x$ZIF mats. Interestingly, the same synthesis but with the ratio of Zn and ligand for SIM-1 did not result in PBIXL@$[Fe/Zn]_x$SIM mats. The compatibility between PAN, PBIXL, SIM-1 and ZIF-8 is summarized in Table 14.

Table 14 Possible (+) and impossible (-) combinations for growing Fe-doped MOFs onto polymer nanofiber mats.

	Polymer fibers	
MOFs	PAN	PBIXL
SIM-1	+	-
ZIF-8	-	+

XRD was performed on the polymer fiber mats decorated with Fe-doped MOFs to confirm that the targeted MOF structure was obtained. XRD was also performed on the pyrolysed mats in order to investigate whether the Fe formed large crystalline particles of metallic Fe or Fe carbide, or formed mainly atomically dispersed FeN_x sites during pyrolysis.

The XRD pattern of PAN@$[Fe/Zn]_{0.5}$SIM corresponds to the reference pattern for SIM-1, [5] and also to the pattern of ferrocene doped SIM-1 (see Figure 30 in chapter 2), confirming the presence of SIM-1 crystals (Figure 59-left). The intensity of PAN@$[Fe/Zn]_{0.5}$SIM peaks was less sharp and the width broader than for the reference SIM-1 pattern, indicating possibly than the crystal size of MOFs in

PAN@[Fe/Zn]$_{0.5}$SIM was smaller than in the reference powder. An additional peak, present at 2θ value of 17°, corresponds to PAN electrospun nanofibers.

For PBIXL@[Fe/Zn]$_{0.5}$ZIF, the diffraction peaks are matching with those for pristine ZIF-8 and Fe-doped ZIF-8 (Figure 59 - right). The relatively high intensity indicates crystal structure, except that the XRD patterns for fibrous PBIXL@[Fe/Zn]$_{0.5}$ZIF are slightly less intense and had more amorphous background (Figure 59 right). The same observations were made at the Fe/Zn ratios of 1 and 2 mol % (Figure 60).

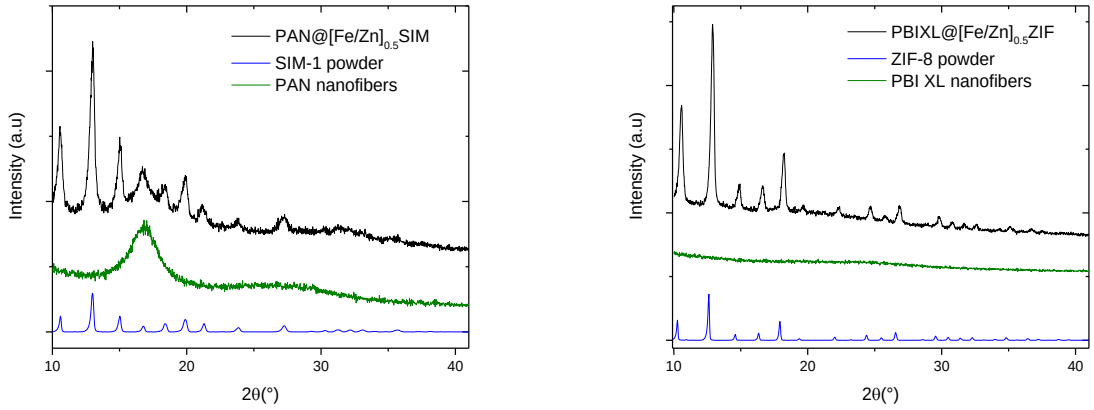

Figure 59. XRD diffractograms for PAN@[Fe/Zn]$_{0.5}$SIM (left) and PBIXL@[Fe/Zn]$_{0.5}$ZIF (right) compared to powder MOF samples.

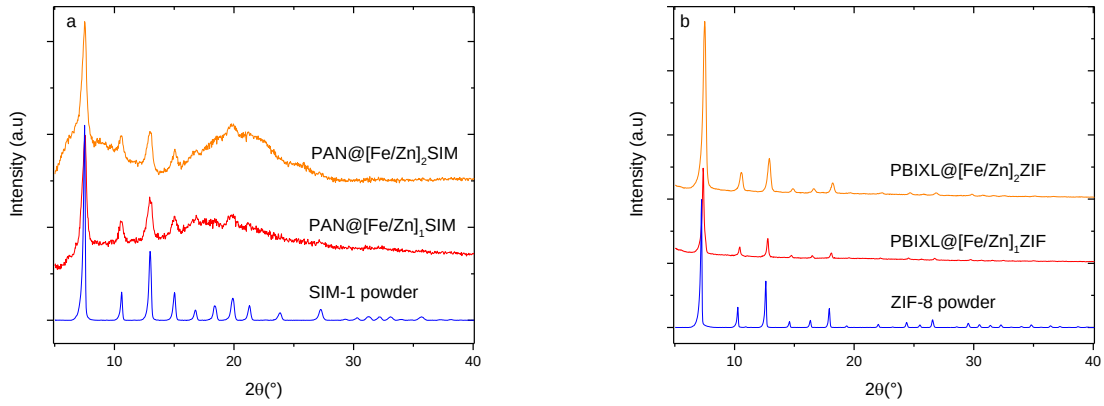

Figure 60. XRD diffractograms registered for PAN@[Fe/Zn]$_1$SIM and PAN@[Fe/Zn]$_2$SIM (a) and PBIXL@[Fe/Zn]$_1$ZIF and PBIXL@[Fe/Zn]$_2$ZIF (b) compared to powder MOF samples.

After pyrolysis, only two diffraction peaks are visible for PAN@[Fe/Zn]$_{0.5}$SIM-P, at 26° and 42°, corresponding to carbon (Figure 61a, black curve). At the higher Fe/Zn ratios of 1 and 2 mol%, only two diffraction peaks are also visible, but the position of the first peak is shifted to lower angle (red and orange curves in Figure 61a).

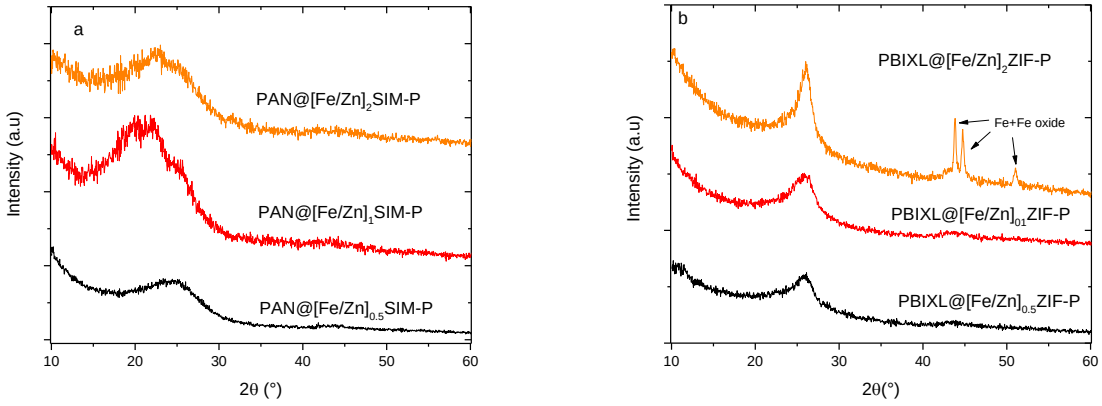

Figure 61. XRD diffractograms for PAN@[Fe/Zn]$_x$SIM-P (a) and PBIXL@[Fe/Zn]$_x$ZIF-P (b), with x = 0.5, 1 or 2.

For PBIXL@[Fe/Zn]$_{0.5}$ZIF-P and PBIXL@[Fe/Zn]$_1$ZIF-P after pyrolysis (Figure 59 right) similarly, only two broad peaks assigned to carbon are visible (at 26° and 42°, related to the graphite (002) plane and to (100) plane respectively). For PBIXL@[Fe/Zn]$_2$ZIF-P however, additional intense diffraction peaks can be seen that correspond to a superposition of iron carbide and iron oxide. More, precisely, peak at 43°, related to (400) plane corresponds to Fe_3O_4 (reference JCPDS n°01-074-1910), peaks at 42° and 44°, related to (101) plane and (110) plane respectively, corresponds to iron carbide (reference JCPDS n°00-044-1292)..

Scanning electron microscopy (SEM) characterization was then performed to investigate the size, morphology and distribution of i) the ferrocene-doped MOF crystals grown on either PAN or PBIXL mats, and ii) the same but after pyrolysis.

First, we discuss the morphology of the PAN@SIM-1 self-standing structures, before and after pyrolysis. They were prepared using three different Fe/Zn ratios (see Table 12). Figure 62 shows micrometric crystals of SIM-1 visible on PAN polymer nanofibers (Figure 62 left) and their homogeneous dispersion on the surface of polymer nanofibers. The crystalline shape is rhombic dodecahedral. The size of crystals is relatively similar for each Fe/Zn ratio, ranging between 2 and 5 µm, as shown in the inset of Figure 62. for

PAN@[Fe/Zn]$_{0.5}$SIM. Similar morphology is also observed for PAN@[Fe/Zn]$_1$SIM and PAN@[Fe/Zn]$_2$SIM (Figure 63).

One can see that, after pyrolysis at 1050 °C, the morphology of the MOF crystals was conserved (Figure 62-b,d,f), even though the XRD measurements (see Figure 61a) demonstrate complete transformation into an amorphous carbon structure. Thus, this means that the size and shape of the Fe-doped carbon particles derived from the MOF crystals are similar to those of the MOF crystals before pyrolysis. This effect has been reported previously for ZIF-8 crystals pyrolyzed in ramp heating conditions, leading to the formation of carbon particles that have the same outer morphology than the starting ZIF crystals, including the shape of the crystallographic facets[9]. This templating effect of the morphology and size of MOF crystals into FeNC or CoNC catalytic particles is important and allows tuning the size of the latter by controlling the average size of MOF crystals. In turn, a small size of FeNC (or CoNC) catalytic particles is important to facilitate O_2 and proton transport within these porous particles, important to reach the FeN_x active sites that are located in intra-particle pores.

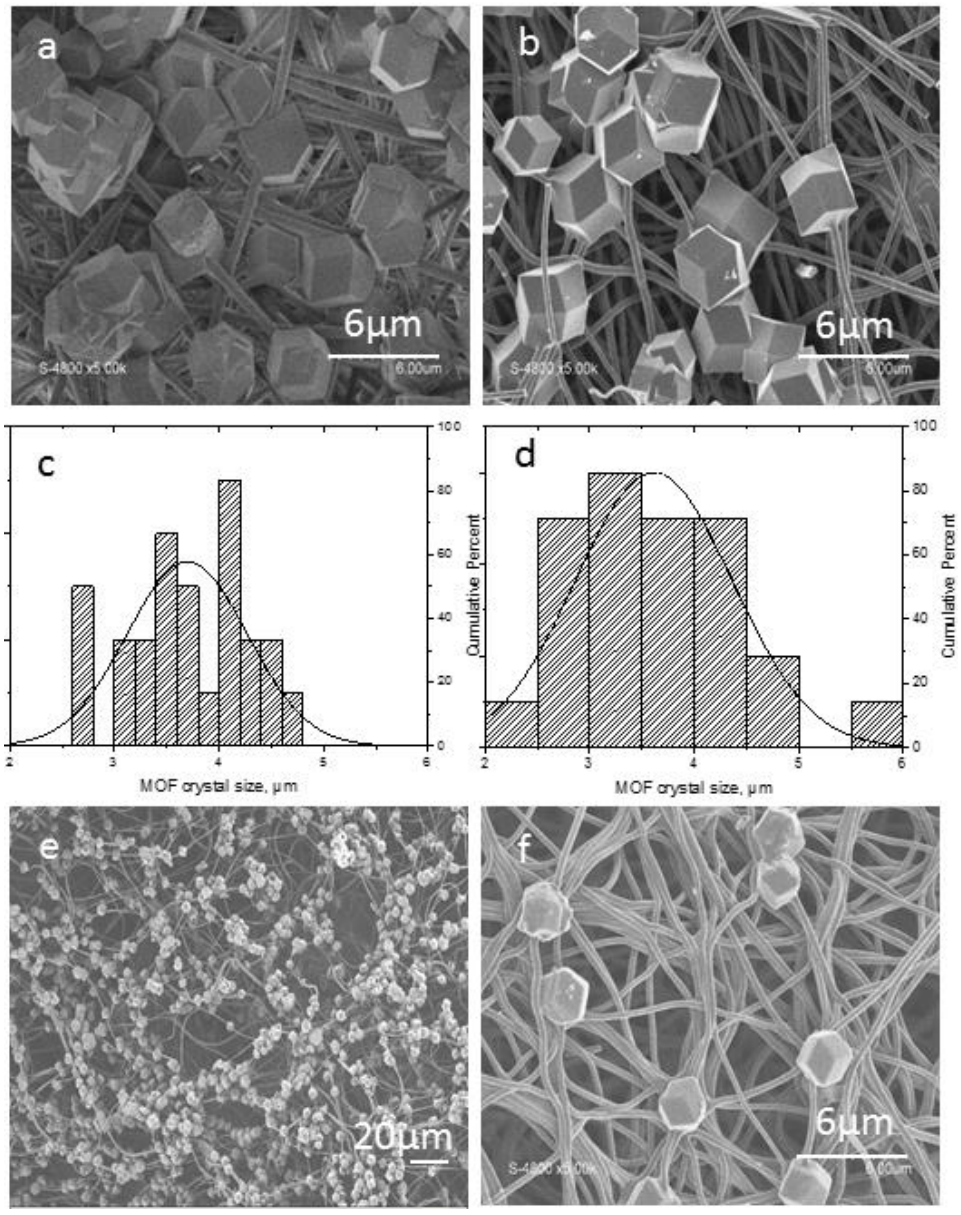

Figure 62. FE-SEM micrographs of a, e) PAN@$[Fe/Zn]_{0.5}$SIM; c) MOF size distribution histogram of PAN@$[Fe/Zn]_{0.5}$SIM; b, f) FE-SEM micrographs of PAN@$[Fe/Zn]_{0.5}$SIM-P; d) MOF size distribution histogram of PAN@$[Fe/Zn]_{0.5}$SIM-P.

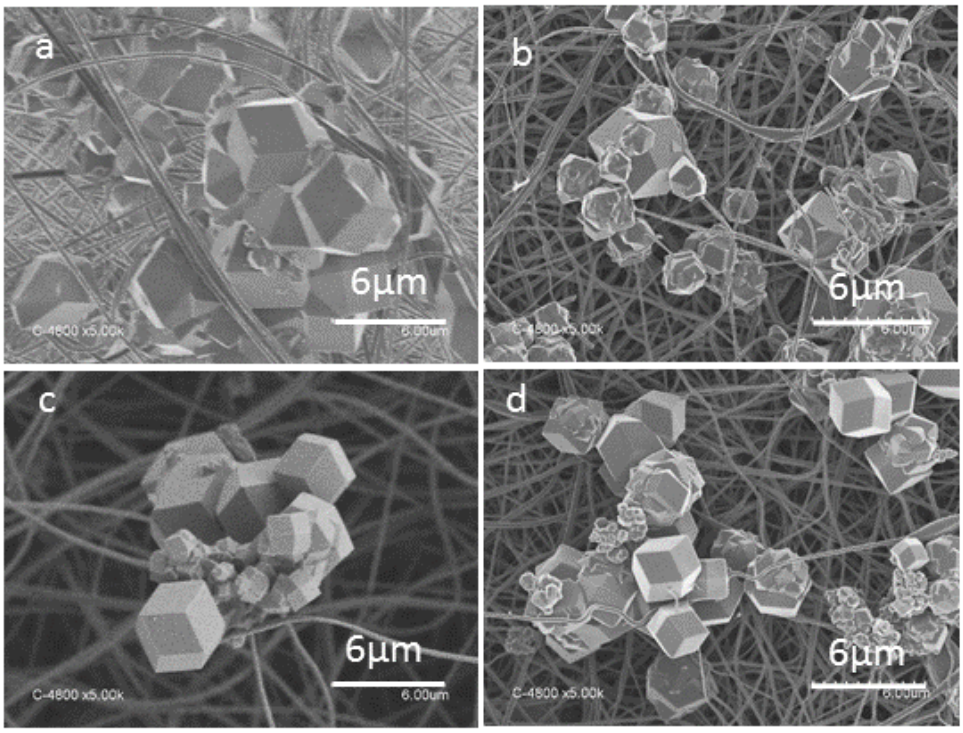

Figure 63: FE-SEM micrographs of a) PAN@$[Fe/Zn]_1$SIM, b) PAN@$[Fe/Zn]_1$SIM-P, c) PAN@$[Fe/Zn]_2$SIM, d) PAN@$[Fe/Zn]_2$SIM-P.

The SEM characterization of the PBI@ZIF-8 self-standing structures (Table 12), before and after pyrolysis are now discussed. In the SEM micrograph of PBI@ZIF-8 (Figure 64) ZIF-8 crystals with well-defined crystalline rhombic dodecahedral shape are visible on the polymer nanofibers, homogeneously distributed on the fiber. The density and amount of the large ZIF-8 crystals on PBI seems lower than the large SIM-1 crystals on PAN. The size of crystals is relatively similar for each Fe/Zn ratio, ranging between 1 and 3 µm with an average value of 2 µm, as shown in the size distribution histogram, Figure 64c-d.

After pyrolysis at 1050 °C in Ar atmosphere, the size and morphology of the FeNC particles derived from Fe-doped ZIF-8 crystals were significantly modified. This is in contrast with the results described above for PAN@$[Fe/Zn]_x$SIM. Besides the CNFs, one can only observe particles with irregular shape and broad size range from 0.1 up to 1 µm, much smaller than the size of the MOF crystals before pyrolysis. The non-conservation of MOF crystal morphology after pyrolysis was previously reported by Zhang et al, for the ZIF-8/ZIF-67 MOF backbone structure, which dissociates after decomposition at 800 °C into amorphous Fe-containing carbon particles present on CNFs [8]. It is however possible that nano-sized Fe-doped carbon particles are present and uniformly dispersed on the CNFs, but are not visible in the FE-SEM images due to limited resolution of the technique, as discussed below.

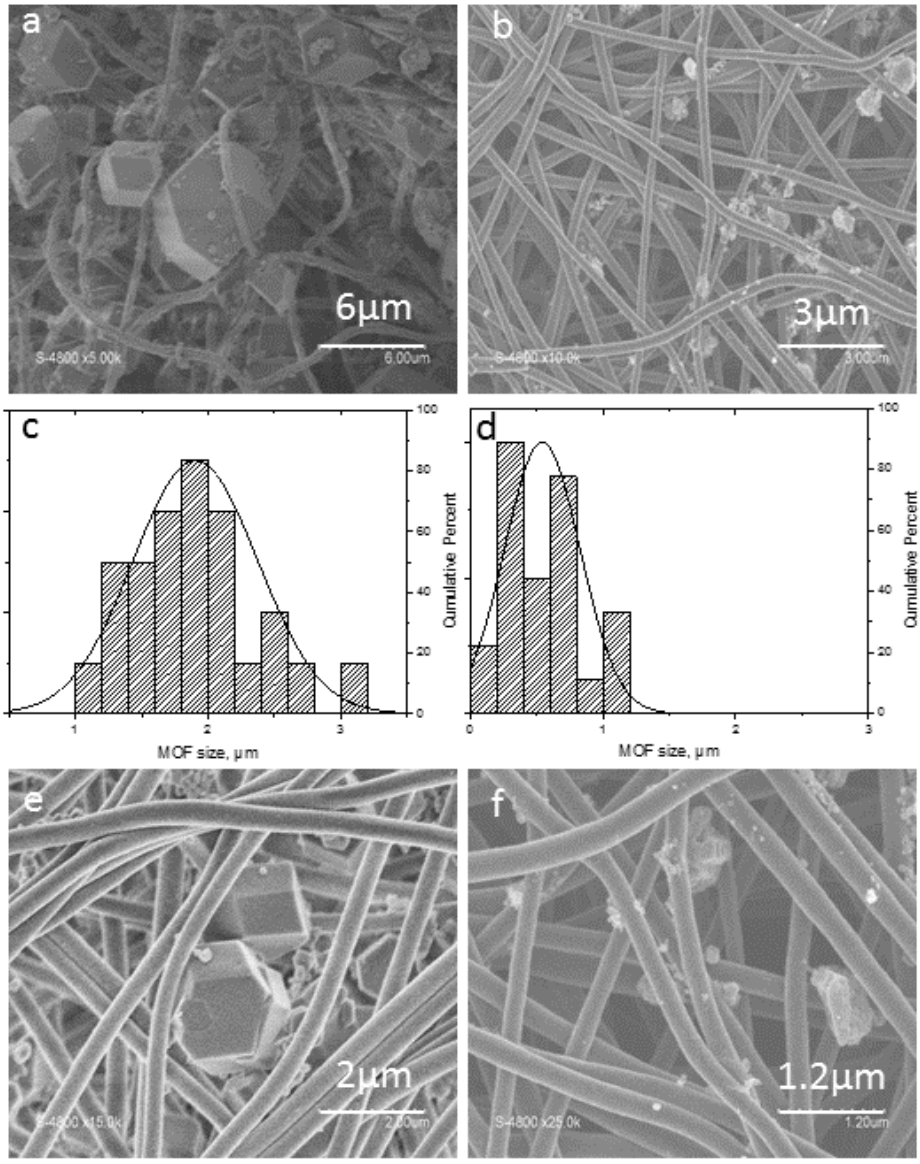

Figure 64: FE-SEM micrographs of a,e) PBIXL@$[Fe/Zn]_{0.5}$ZIF; c) MOF size distribution histogram of PBIXL@$[Fe/Zn]_{0.5}$ZIF; b,f) FE-SEM micrographs of PBIXL@$[Fe/Zn]_{0.5}$ZIF-P; d) MOF size distribution histogram of PBIXL@$[Fe/Zn]_{0.5}$ZIF-P.

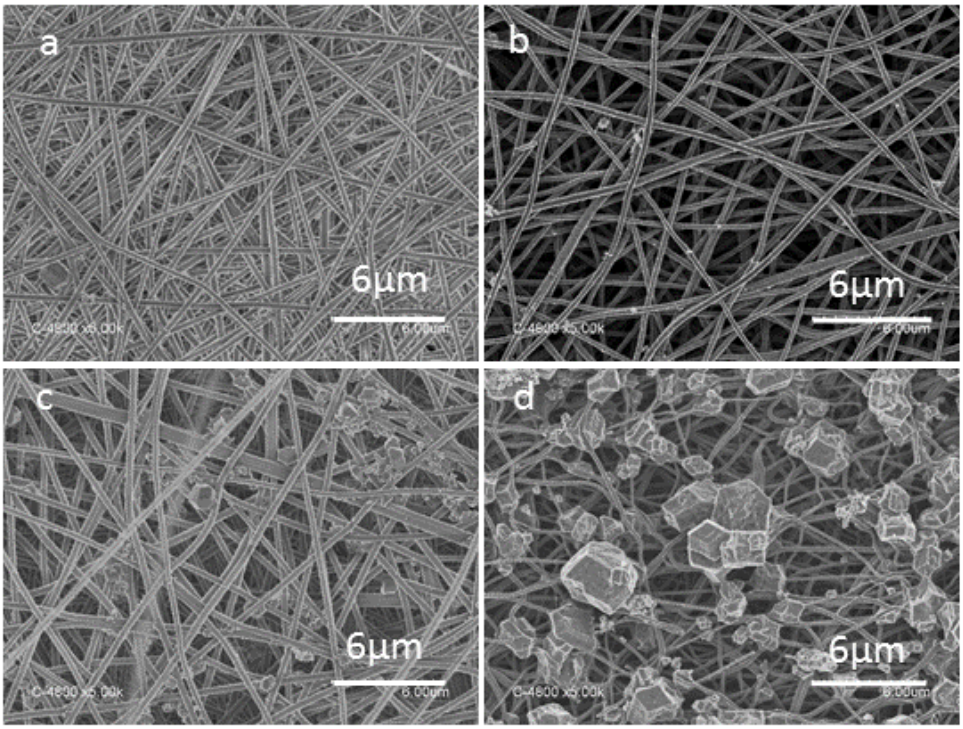

Figure 65: FE-SEM micrographs of: a) PBIXL@$[Fe/Zn]_1$ZIF before pyrolysis, b) PBIXL@$[Fe/Zn]_1$ZIF after pyrolysis 1050° C Ar, c) PBIXL@$[Fe/Zn]_2$ZIF before pyrolysis, d) PBIXL@$[Fe/Zn]_2$ZIF after pyrolysis 1050° C Ar

In order to better understand the morphological transformation of the Fe-doped MOF crystals during pyrolysis of PBIXL@$[Fe/Zn]_{0.5}$ZIF, we evaluated the elemental composition and distribution in the sample by SEM-EDX analysis. In Figure 66 is depicted the SEM-EDX mapping of the expected elements (Fe, C, N, Zn) for the PBIXL@$[Fe/Zn]_{0.5}$ZIF-P sample. One can see that Fe is homogeneously distributed on the nanofibrous structure, along with N and O. A high zinc signal is however seen in the few large particles that are derived from the large MOFs crystals. Furthermore, zinc is also homogeneously dispersed on the polymer nanofibers outside these large MOF-derived particles. The distributed background for Zn and Fe signals could possibly evidence the presence of atomically dispersed FeN_x and ZnN_x sites on the CNFs. In turn, this could imply that, before pyrolysis, nano-sized Fe-doped ZIF-8 existed, along with the micrometer sized crystals seen in the SEM images. Such nano-sized crystals cannot be detected by SEM-EDX methods because they are below the resolution limit of this technique.

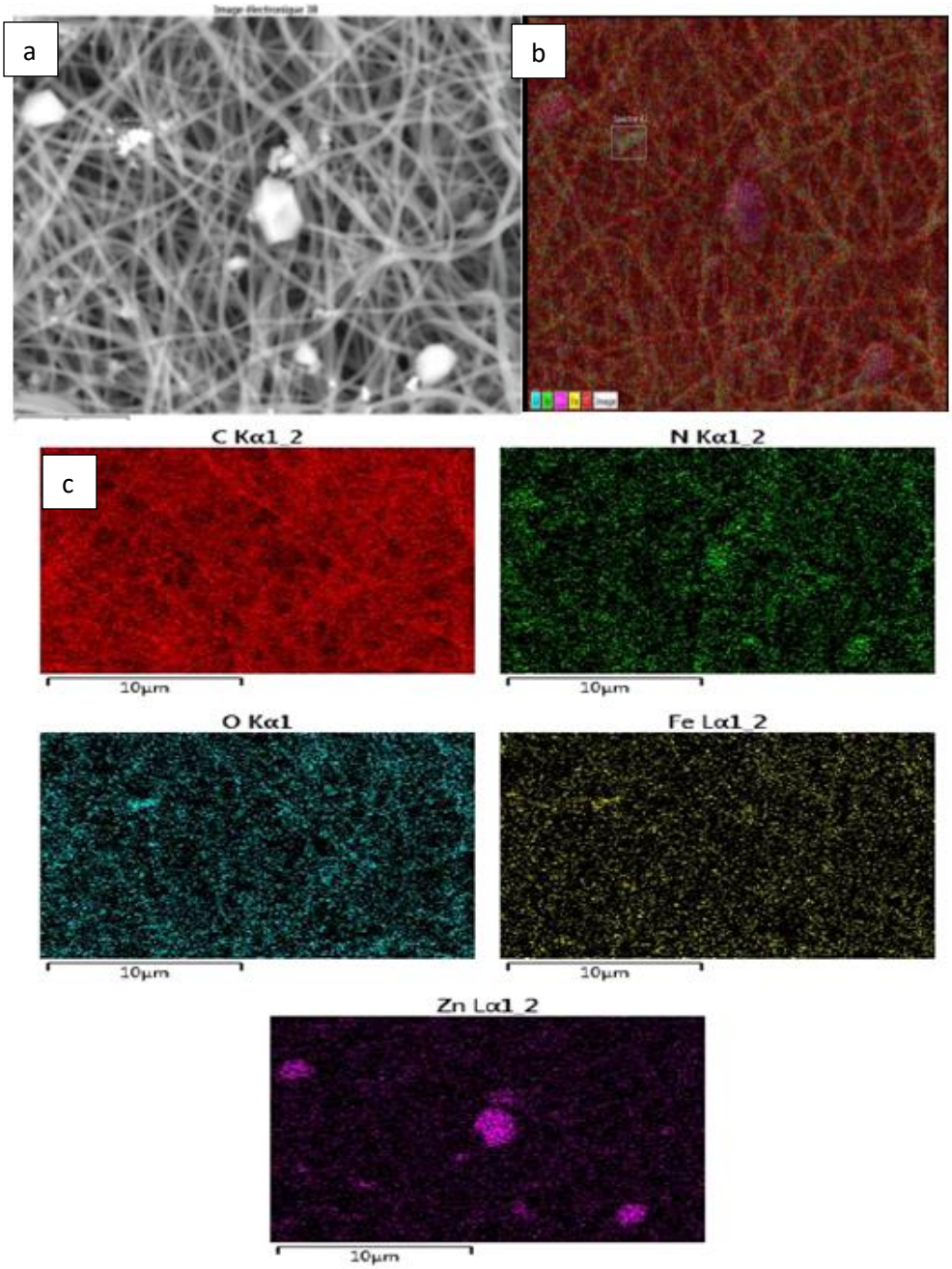

Figure 66: Elemental mapping analysis by EDX-SEM of PBIXL@$[Fe/Zn]_{0.5}$ZIF-P: a) SEM micrograph, b) elemental mapping (red for C, purple for Zn, green for N, blue for O and yellow for Fe) c) Individual elemental mapping of each element.

In order to investigate with higher resolution the dispersion of Fe over CNFs after pyrolysis, TEM coupled EDX chemical topography was performed for down-selected FSE, namely PAN@$[Fe/Zn]_{0.5}$SIM-P (Figure 67) and PBIXL@$[Fe/Zn]_{0.5}$ZIF-P (Figure 68).

The elemental mapping of C (in red) and Fe (in yellow) is shown in Figure 67 and 68. The samples were prepared by impregnation of the pores in the self-standing electrode by a resin, which appears as the red background in Figure 67 and 68. The more intense red sections, richer in carbon than the resin, represent the cross-sections of the cut CNFs in TEM while the yellow particles represent the position of Fe.

For PAN@$[Fe/Zn]_{0.5}$SIM-P, the intensity of Fe and C signal is significantly lower than as for PBIXL@$[Fe/Zn]_{0.5}$ZIF-P and they can be observed only around cut carbon nanofibers. That can be the indication of less accessible Fe sites in the SIM-1 derived carbon particles.

For PBIXL@$[Fe/Zn]_{0.5}$ZIF-P, the TEM-EDX mapping shows that Fe rich particles derived from Fe-doped MOF crystals are homogeneously dispersed around the CNFs and also it can be possible that the FeNC particles are present not only in the form of microcrystals that were visible in SEM images but also as nanometric MOF crystals.

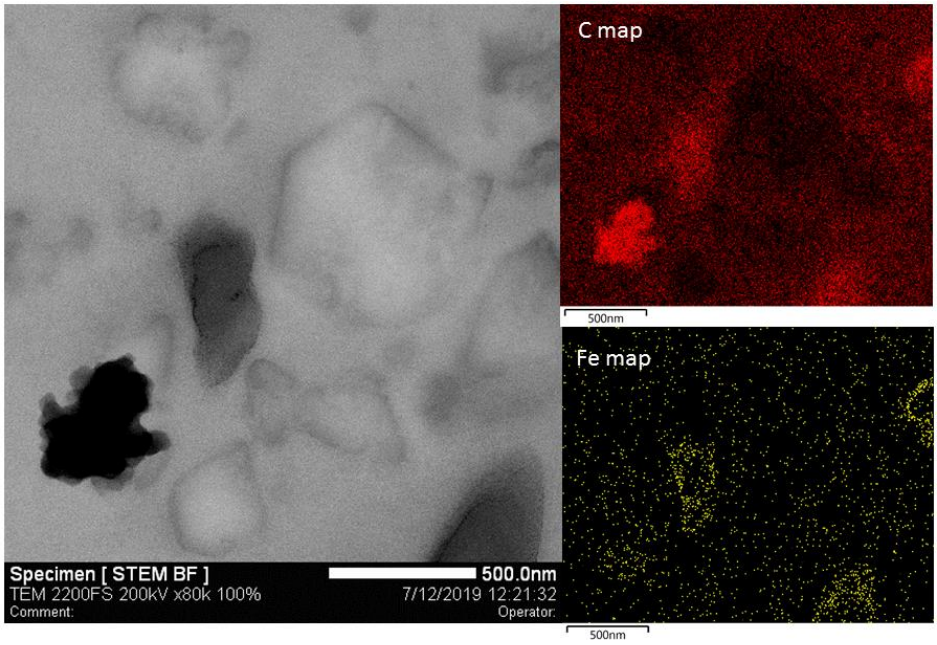

Figure 67. TEM-EDX chemical topography of PAN@$[Fe/Zn]_{0.5}$SIM-P sample.

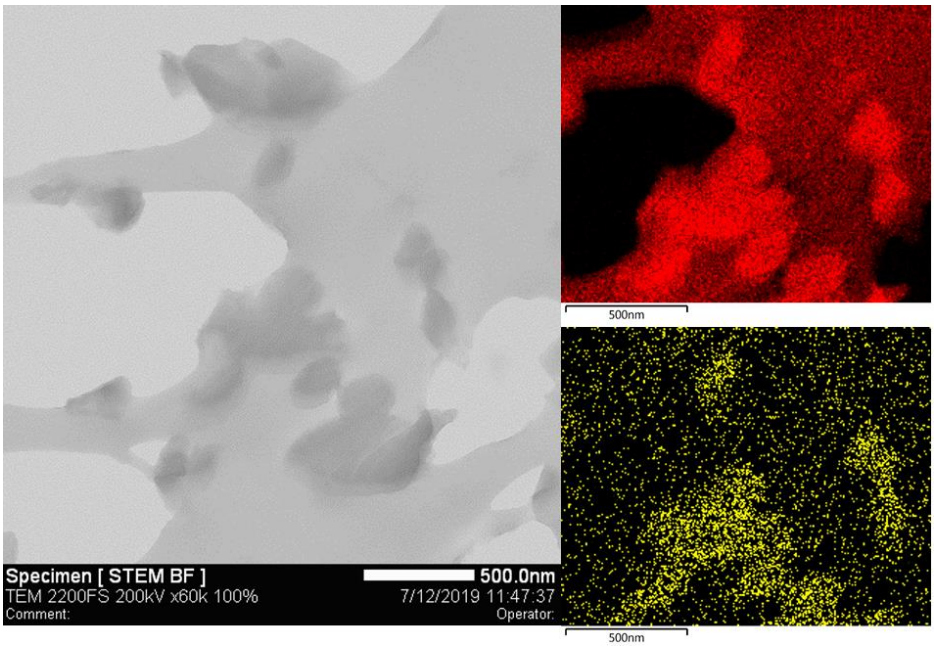

Figure 68. TEM-EDX chemical topography for PBIXL@$[Fe/Zn]_{0.5}$ZIF-P

In order to investigate the possible presence of metallic Fe particles, extended X-ray absorption fine structure (EXAFS) at the Fe K-edge was applied to characterize the electrodes with Fe/Zn extreme ratios (i.e. $[Fe/Zn]_{0.5}$ and $[Fe/Zn]_2$) to both PAN and PBIXL CNFs (Figure 69). The Fe K-edge EXAFS spectra of selected self-standing FeNC cathodes were compared to that of a pure metallic Fe foil and to that of the reference powder catalyst $Fe_{0.5}NC$ (to confirm or infirm the same FeN_4 spectroscopic signature).

The Fourier transform of the EXAFS spectra of PBIXL@$[Fe/Zn]_{0.5}$ZIF-P and PBIXL@$[Fe/Zn]_2$ZIF-P shows signals at 2.2 Å, indicating Fe-Fe interactions which leads to the conclusion that there is some metallic Fe or Fe carbide particles besides FeN_4 catalytic sites (Figure 69c-d) [9]. For PAN@$[Fe/Zn]_{0.5}$SIM-P and PAN@$[Fe/Zn]_2$SIM-P, the pattern is different, and very similar to the reference $Fe_{0.5}NC$ catalyst and the absence of signals at 2.2 Å and 2.6 Å further indicates the absence of metallic or metal carbide Fe particles (Figure 69a-b).

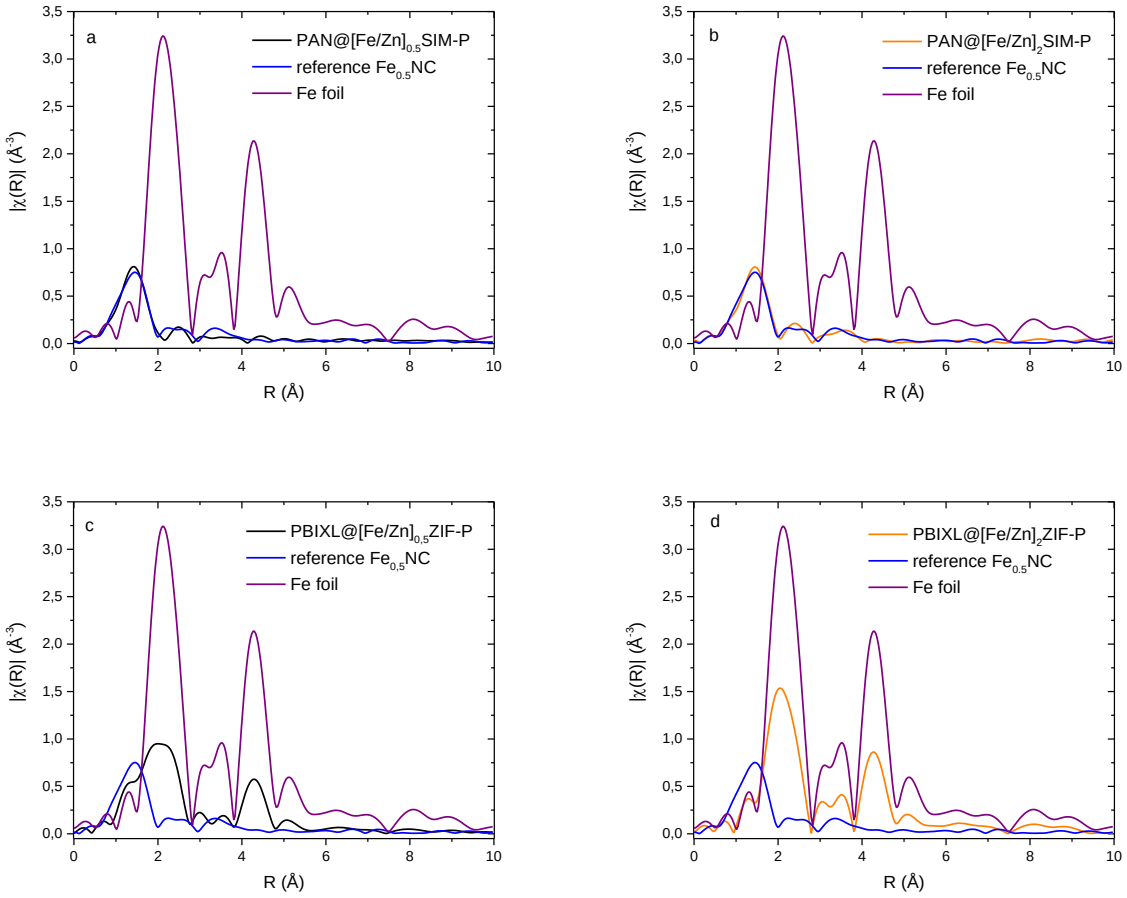

Figure 69. Fourier transforms of the experimental Fe K-edge EXAFS spectra of a) PAN@$[Fe/Zn]_{0.5}$SIM-P, b) PAN@$[Fe/Zn]_2$SIM-P, c) PBIXL@$[Fe/Zn]_{0.5}$ZIF-P, d) PBIXL@$[Fe/Zn]_{0.5}$ZIF-P and compared to the spectra for the reference $Fe_{0.5}$NC catalyst and a metallic Fe foil.

The FeNC self-standing electrodes obtained by pyrolysis of polymer fibers decorated by ferrocene-doped SIM-1 and ZIF-8 were analysed for their electrocatalytic activity towards ORR. They have been investigated as self-standing webs as well as introduced in conventional inks. The results are presented in the following paragraphs.

4.3.b Electrochemical properties of self-standing and grinded FeNC cathodes in RDE

4.3.b.1 Electrochemical properties of self-standing FeNC cathodes in RDE

The electrocatalytic properties of self-standing FeNC catalysts were first measured by a rotating disc electrode (RDE) in oxygen saturated 0.1 M H_2SO_4 and in nitrogen saturated 0.1 M H_2SO_4. The results were compared with the reference $Fe_{0.5}NC$ catalyst prepared and deposited by ink method[10] (Figure 70). It is important to take into account that the self-standing catalysts that were cut and attached to the GC electrode are thicker than the reference layer obtained by ink deposition. The thickness expected for a loading of 1 mg cm^{-2} of FeNC powder catalyst (mostly, carbon) is ca 20 µm. The lower-range thickness of self-standing FeNC cathodes that may be prepared was limited by mechanical properties. The self-standing FeNC cathode thickness was ~ 50 µm for PAN-derived cathodes and ~20 µm for PBIXL-derived cathodes, both significantly thicker that the 1 mg cm^{-2} catalytic layer deposited by ink process. The real part of the FeNC self-standing cathode involved in the ORR is not known precisely, especially for PAN-derived electrodes with a thickness higher than the diffusion layer thickness in the electrolyte at 1600 rpm.

In order to better understand differences in the activity of self-standing cathodes and ink-deposited catalyst layers, it is also important to assess the loading of catalyst (mg/cm^2) corresponding to self-standing cathodes. The latter was assessed by measuring the mass of the cut-out circular self-standing cathodes and dividing by the electrode surface (0.196 cm^2 for standard RDE glassy carbon electrode). For self-standing cathodes, the value of catalyst loading may vary by every measurement due to different thickness of the carbon webs (50-60 µm for SIM-1 and 20-30 µm for ZIF-8). However, usually for both PAN@$[Fe/Zn]_x$SIM-P and PBIXL@$[Fe/Zn]_x$ZIF-P electrodes, the value of loading was around 0.5 mg cm^{-2}. For ink-deposited catalyst powders, the catalyst loading was fixed at 1 mg cm^{-2}. To compare the electrocatalytic activity of self-standing electrodes versus ink-deposited catalytic layers, one must therefore take into account the ca double loading of the latter (1 vs. 0.5 mg cm^{-2}). In addition, one must keep in mind that the FeNC catalytic particles derived from MOFs that are present in the self-standing cathodes are diluted by the mass of carbon derived from PBI-XL or PAN. As a result, the Fe content may be lower compared to Fe0.5-NC. The absolute quantity of Fe was assessed by X-ray fluorescence spectroscopy for grinded self-standing cathodes, and results presented in Table 15.

Table 15: Bulk Fe content in the grinded self-standing FeNC cathodes

Samples	Iron, wt%
PAN@$[Fe/Zn]_{0.5}$SIM-P_g	0.112
PBIXL@$[Fe/Zn]_{0.5}$ZIF-P_g	0.460

By comparison, the bulk Fe content in $Fe_{0.5}$-NC is circa 1.5 wt%, and it is entirely present as FeN_x sites.

Firstly, the self-standing FeNC electrodes derived from PAN were characterized by RDE techniques. The cyclic voltammetry was applied in the N_2-saturated electrolyte, and the results are shown in Figure 70a. The CV curve of PAN@$[Fe/Zn]_{0.5}$SIM-P show high electrochemical capacitance that corresponds to high accessible carbon surface area (in agreement with high surface area of $[Fe/Zn]_{0.5}$SIM-P, see chapter 2) and is in correlation with its high ORR activity. The curves of PAN@$[Fe/Zn]_1$SIM-P and PAN@$[Fe/Zn]_2$SIM-P are narrower, which indicates lower electrochemical capacitance, and that can possibly be due to less accessible microporous structure inside the FeNC catalytic particles, in line with results seen in chapter 2 on the series of $[Fe/Zn]_x$SIM-P materials. The reversible peak shown at Figure 70a at the potential of 0.77 V vs. RHE corresponds to Fe^{2+}/Fe^{3+} reduction/oxidation, probably from FeN_x active sites. Now, the ORR results of PAN@$[Fe/Zn]_x$SIM-P electrodes are discussed. The ORR of PAN@$[Fe/Zn]_{0.5}$SIM-P (Figure 70c, black curve) indicates high catalytic activity that is comparable to the reference $Fe_{0.5}$NC catalytic layer. For PAN@$[Fe/Zn]_1$SIM-P and PAN@$[Fe/Zn]_2$SIM-P, they have in contrast a drastically lower activity, repetitively observed for every synthesized sample.

The CV curves of PBIXL@$[Fe/Zn]_x$ZIF-P shown in Figure 70b indicate high electrochemical capacitance of the cathodes, that is also connected to high surface area and microporous volume (in agreement with high BET area of $[Fe/Zn]_x$ZIF-P, see chapter 2). The reversible peak shown in Figure 70b at the potential of 0.77 V vs. RHE is also present for this batch of catalysts and corresponds to Fe^{2+}/Fe^{3+} reduction/oxidation. One can also see that the intensity of this peak progressively increases with increasing Fe/Zn mol %.

The ORR polarization curves of PBIXL@$[Fe/Zn]_x$ZIF-P electrodes (Figure 70) indicates high activity for all measured samples, showing almost identical curves for all three ZIF-derived electrodes. However, the activity was still lower than that of the $Fe_{0.5}$NC powder catalyst layer. The highest activity was recorded for PBIXL@$[Fe/Zn]_2$ZIF-P (Figure 70), and this is in agreement with high specific surface area (S_{BET} 1822 m^2g^{-1}) measured for the corresponding pyrolysed powder $[Fe/Zn]_2$ZIF-P (see chapter 2).

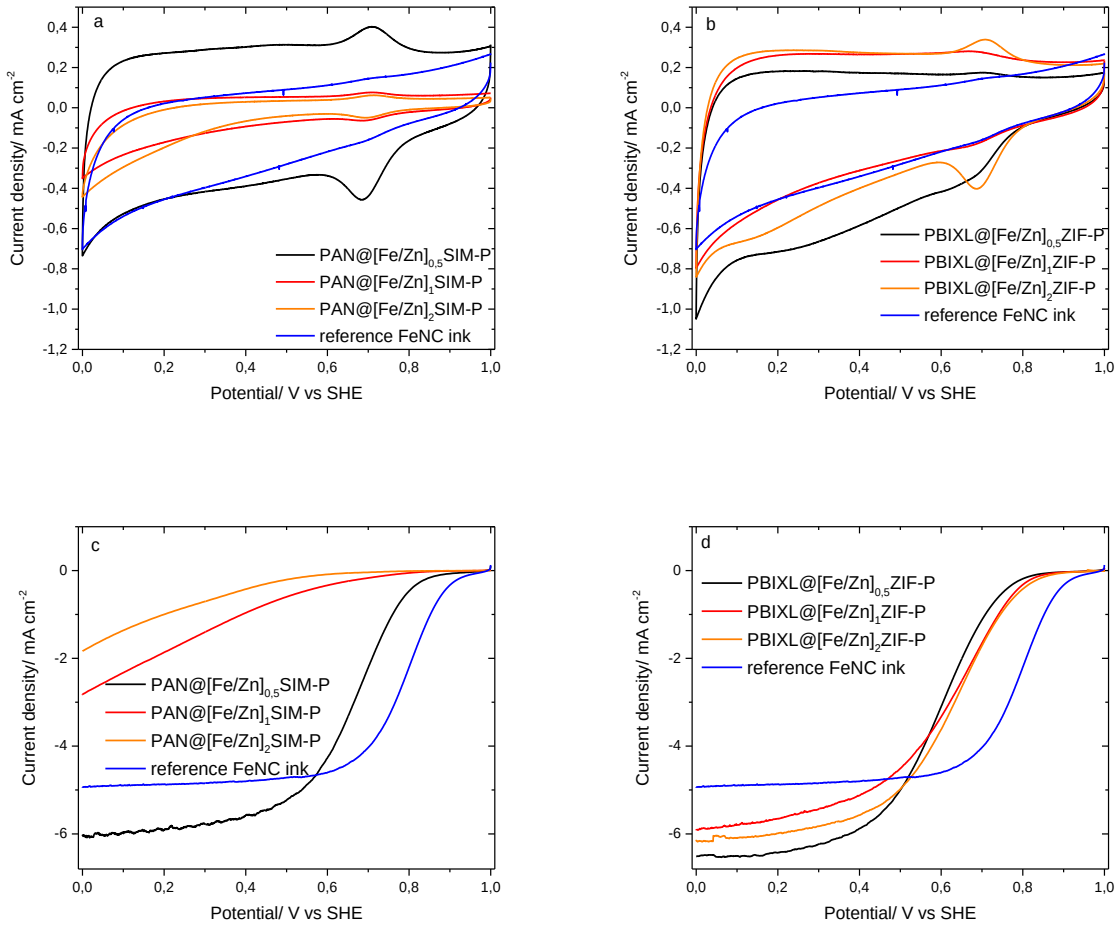

Figure 70: Electrochemical characterization in RDE of self-standing FeNC electrodes. a) CV in N_2-saturated pH 1 solution of PAN@[Fe/Zn]$_x$SIM-P (x = 0.5, 1 or 2), b) CV in N_2-saturated pH 1 solution of PBIXL@[Fe/Zn]$_x$ZIF-P (x = 0.5, 1 or 2), c) ORR polarization curves in O_2-saturated pH 1 solution of PAN@[Fe/Zn]$_x$SIM-P (x = 0.5, 1 or 2), d) ORR polarization curves in O_2-saturated pH 1 solution of PBIXL@[Fe/Zn]$_x$ZIF-P (x = 0.5, 1 or 2), and compared to the same curves measured for the reference $Fe_{0.5}$NC active layer. The electrolyte was 0.1 M H_2SO_4 and electrode rotation rate 1600 rpm.

In summary, according to the RDE measurements, the ORR catalytic activity is quite high for PAN@[Fe/Zn]$_{0.5}$SIM-P and for all three PBIXL@[Fe/Zn]$_x$ZIF-P electrodes (x=0.5, 1 or 2). The Tafel plots derived from the RDE ORR polarization curves are shown in Figure 71. The mass activity measured at 0.8 V vs. RHE for all samples is presented in Figure 72, identifying the electrodes PAN@[Fe/Zn]$_{0.5}$SIM-P and PBIXL@[Fe/Zn]$_2$ZIF-P as the most promising self-standing electrodes, with mass activity of 0.9 and 0.82 A

g^{-1}, respectively. This is however still about 3 times lower ORR activity than measured for $Fe_{0.5}$-NC, and this difference can be assigned, in part, to their lower Fe content (see Table 15).

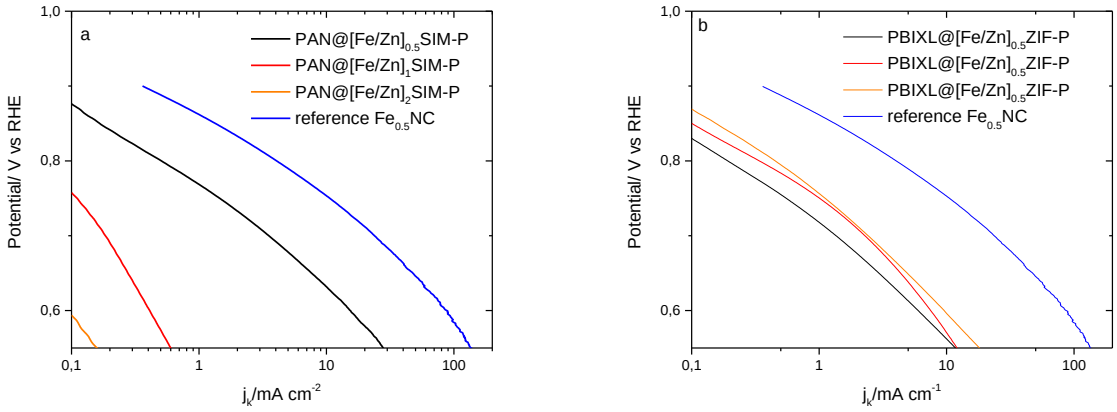

Figure 71: Tafel plots derived from RDE polarization curves measured in O_2-saturated pH 1 electrolyte for a) PAN@$[Fe/Zn]_x$SIM-P electrodes, b) PBIXL@$[Fe/Zn]_x$ZIF-P electrodes, and compared to the reference $Fe_{0.5}$NC catalytic layer

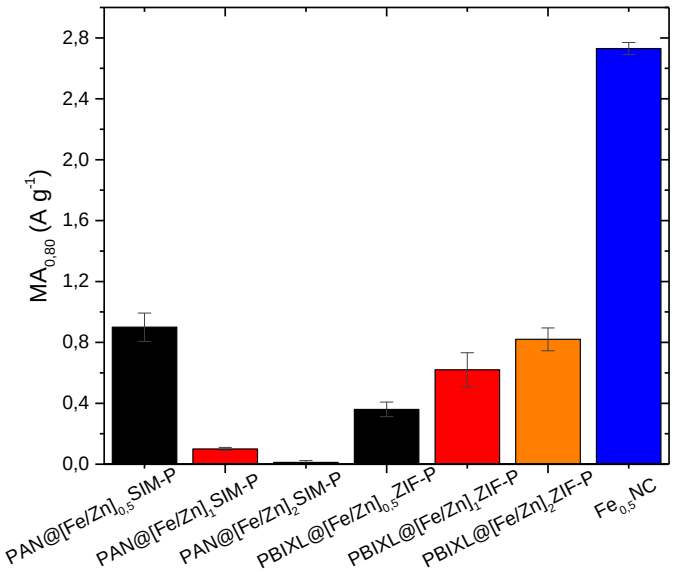

Figure 72 : Mass activity for self-standing cathodes measured at 0.8 V vs. RHE and compared to the reference $Fe_{0.5}$NC catalytic layer. The average activity and error bar was estimated from three independent measurements on three different layers.

The catalytic performance of PAN@[Fe/Zn]$_x$SIM-P and PBIXL@[Fe/Zn]$_x$ZIF-P electrodes was further characterized in fuel cell. The self-standing electrodes were used as such at the cathode, except that they needed to be impregnated with a given amount of Nafion resin solution, in order to provide some proton conductivity through the electrode. The results are reported in section 4.3.c.

The goal of the project was to improve the mass transport of FeNC electrodes by introducing self-standing electrodes that are able to provide both microporosity (to improve or maintain the ORR activity) and in particular high macroporosity (in order to improve the mass transport through the electrode).

The self-standing structures obtained here may however present a too high degree of macroporosity that leads to another extreme, with sufficient macroporosity for molecular gas iffusion but insufficient density of active sites per unit volume of electrode (leading to low volumetric ORR activity). To overcome this issue, there are several possible strategies, as for example, densification of the self-standing fiber mats. Another possible strategy is to transform the self-standing cathodes into FeNC catalyst powder but with a retained fibrous structure of the FeNC catalyst. This could lead to an optimum in terms of macroporosity inside the active layer between what may be obtained from MOF-derived FeNC catalyst powders and self-standing FeNC electrodes. As an example of this second approach, we will discuss below the effect of manual grinding of self-standing FeNC electrodes on the electrochemical properties, measured both in RDE and PEMFCs.

4.3.b.2 Electrochemical properties of grinded FeNC cathodes in RDE

The self-standing electrodes were manually grinded in order to achieve a material morphology which can be used to form a conventional catalytic ink, while still retaining the high aspect-ratio morphology of fibers. Also this method allows an easy comparison with the reference $Fe_{0.5}$-NC powder catalyst[12] that could also be beneficial in the following study. The SEM micrograph of Figure 57 depicts the typical morphology of a grinded self-standing FeNC electrode, with CNF morphology of dispersed lengths. Although the length of the fibrous carbon nano-rods cannot be precisely controlled, generally it is sohwn that this method results in anisotropic shape of FeNC catalytic domains, and the obtained nano-fibrous FeNC catalysts can be processed as an ink. The RDE measurements for grinded FeNC electrodes are shown in Figure 73.

For CV curves measured in N_2–saturated electrolyte, PAN@[Fe/Zn]$_{0.5}$SIM-P$_g$ and PAN@[Fe/Zn]$_2$SIM-P$_g$ show similar curves as before the grinding. There is a significant peak at 0.77 V vs RHE that is attributed to

Fe^{2+}/Fe^{3+} oxidation/reduction. Interestingly, the CV curve for PAN@$[Fe/Zn]_1$SIM-P_g is seemingly wider than that of PAN@$[Fe/Zn]_1$SIM-P (red curves in Figure 70), which means that during grinding some carbon surface inaccessible before the grinding became accessible after the grinding. Therefore, one expects that the grinded electrode will be more ORR active than the self-standing electrode. This expectation is confirmed in the ORR polarization curves (red curve in Figure 73c), with PAN@$[Fe/Zn]_1$SIM-P_g now identified as the most active catalyst among the series of PAN@$[Fe/Zn]_x$SIM-P_g while it was almost inactive before grinding.

The most active catalyst in the other series of materials is PBIXL@$[Fe/Zn]_{0.5}$ZIF-P_g, characterized both by highest electrochemical capacitance (black curve in Figure 73b) and highest ORR activity (black curve in Figure 73d. The other two materials of the series, PBIXL@$[Fe/Zn]_1$ZIF-P_g and PBIXL@$[Fe/Zn]_2$ZIF-P_g, have similar ORR activity in RDE, about 50 mV downshifted compared to PBIXL@$[Fe/Zn]_{0.5}$ZIF-P_g.

The Tafel plot presentations derived from the ORR polarization curves better allow the comparison of the activity of each catalyst (Figure 74), and the mass activity at 0.8 V vs. RHE are shown in Figure 75. The most active catalysts in RDE are PAN@$[Fe/Zn]_1$SIM-P_g and PBIXL@$[Fe/Zn]_{0.5}$ZIF-P_g, with electrocatalytic activity of 0.63 A g^{-1} and 0.79 A g^{-1} respectively.

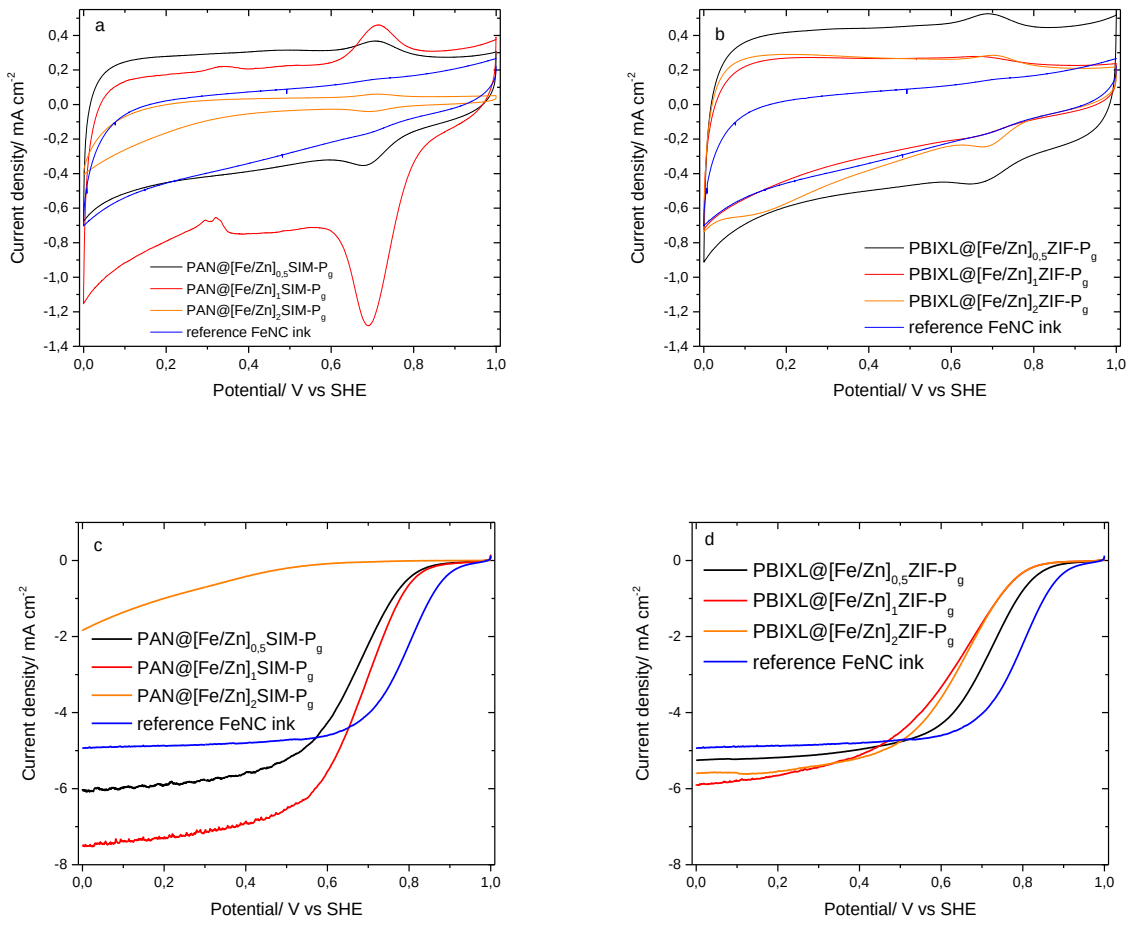

Figure 73: Electrochemical characterization in RDE of grinded FeNC electrodes. a) CV in N_2-saturated pH 1 solution of PAN@[Fe/Zn]$_x$SIM-P$_g$ (x = 0.5, 1 or 2), b) CV in N_2-saturated pH 1 solution of PBIXL@[Fe/Zn]$_x$ZIF-P$_g$ (x = 0.5, 1 or 2), c) ORR polarization curves in O_2-saturated pH 1 solution of PAN@[Fe/Zn]$_x$SIM-P$_g$ (x = 0.5, 1 or 2), d) ORR polarization curves in O_2-saturated pH 1 solution of PBIXL@[Fe/Zn]$_x$ZIF-P$_g$ (x = 0.5, 1 or 2), and compared to the same curves measured for the reference $Fe_{0.5}$NC active layer. The electrolyte was 0.1 M H_2SO_4, electrode rotation rate 1600 rpm and catalyst loading 1 mg cm^{-2}.

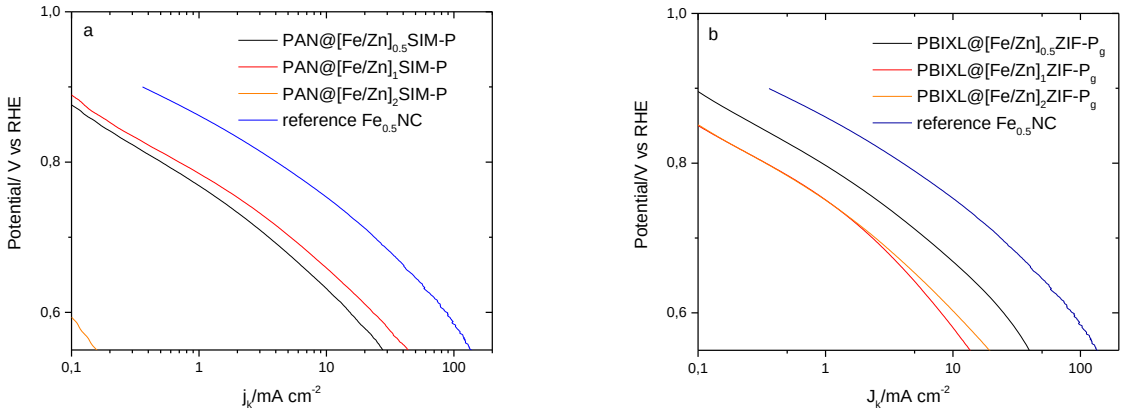

Figure 74: Tafel plots derived from RDE polarization curves measured in O_2-saturated pH 1 electrolyte for a) PAN@$[Fe/Zn]_x$SIM-P_g catalyst layers, b) PBIXL@$[Fe/Zn]_x$ZIF-P_g catalyst layers, and compared to the reference $Fe_{0.5}$NC catalytic layer.

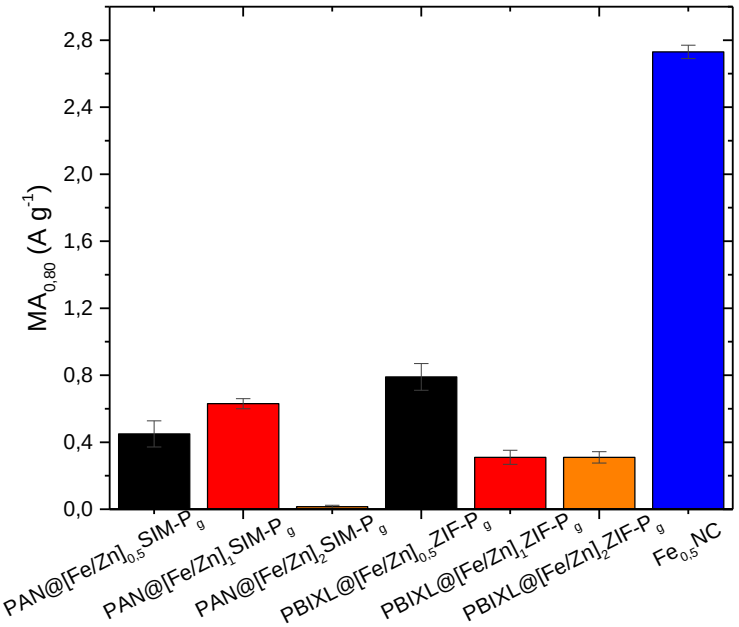

Figure 75: Mass activity for grinded FeNC electrodes, measured at 0.8 V vs. RHE and compared to the reference $Fe_{0.5}$NC powder catalyst. The average activtiy and error bar was estimated from three independent measurements on three different layers.

In summary, the grinding did not improve the ORR activity compared to what was measured for the self-standing electrodes that showed high ORR activity. One exception is seen for PAN@$[Fe/Zn]_x$SIM-P_g

with ORR activity matching that of the best grinded electrodes, while before grinding it showed almost no ORR activity. Overall, the electrochemical RDE results show that all self-standing or grinded FeNC electrodes show lower ORR mass activity than that of the reference $Fe_{0.5}$-NC material. This is mostly due to a dilution effect of the "active FeNC phase" derived from the MOFs by the inactive or less active carbon phase derived from the polymer fibers. Significant further addition of iron in the MOFs would lead to the creation of metallic iron particles (i.e. metallic iron, iron carbide or even iron nitride nanoparticles) that are not or less active for ORR than the FeN_x sites [13].

4.3.c Electrochemical properties of self-standing and grinded FeNC cathodes in PEMFC

The electrochemical performance of the MEAs prepared with different grinded FeNC cathodes with the loading of 4.84 mg cm^{-2} are shown in Figure 76.

The ORR activity of the series of PAN@$[Fe/Zn]_x$SIM-P_g fibrous catalysts is lower than that of cathodes based on $Fe_{0.5}$NC reference catalyst. The trends of ORR activity measured in aqueous conditions and in fuel cell are thus in agreement for the grinded PAN-derived electrodes, with the most active material being PAN@$[Fe/Zn]_1$SIM-P_g and the least active PAN@$[Fe/Zn]_2$SIM-P_g, respectively.

For the series of PBIXL@$[Fe/Zn]_x$ZIF-P_g fibrous catalysts, the activity trends as a function of the Fe/Zn ratio remained relatively the same in RDE and PEMFC, identifying the most promising sample as PBIXL@$[Fe/Zn]_{0.5}$ZIF-P_g. The PBIXL@$[Fe/Zn]_2$ZIF-P_g catalyst is the least active in this series, both in RDE and PEMFC data.

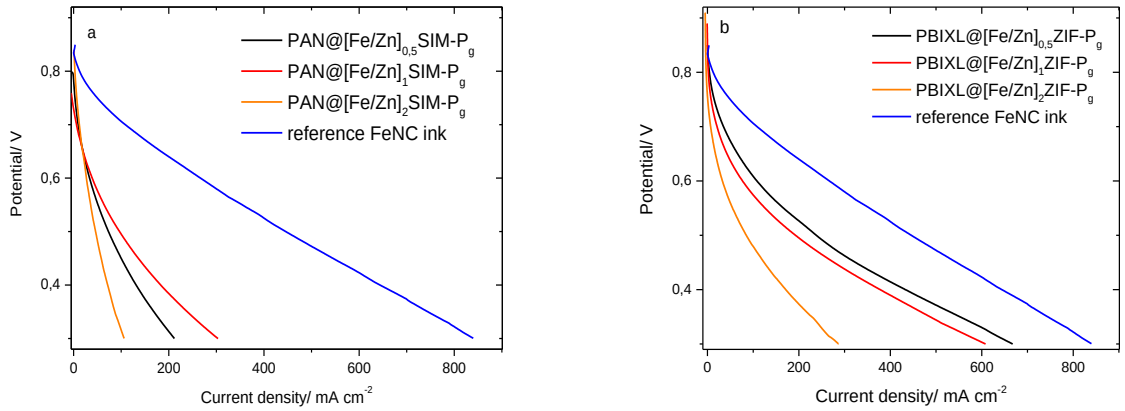

Figure 76: The polarization curves of MEAs with cathode comprising a) grinded PAN@$[Fe/Zn]_x$SIM-P_g catalysts, (x = 0.5, 1 or 2), 4 mg cm^{-2} cathode loading deposited on the microporous side of a GDL b) grinded PBIXL@$[Fe/Zn]_x$ZIF-P_g catalysts, (x = 0.5, 1 or 2), 4 mg cm^{-2} cathode loading deposited on the microporous side of a GDL. The curves are also compared to polarization curves obtained with MEAs comprising cathodes based on the $Fe_{0.5}$NC reference (4 mg cm^{-2} cathode loading, deposited on the microporous side of a GDL). Anode was GDE Sigracet 24BC with loading 0.5 $mg_{Pt\ cm\text{-}3}$. Membrane Nafion NR211. The pressure of H_2 and O_2 gases was set as 1 bar. The compression rate was *ca* 30%.

Although the activity of the fibrous FeNC catalysts remained lower than that of the $Fe_{0.5}$NC reference catalyst, we down-selected on this basis PBIXL@$[Fe/Zn]_{0.5}$ZIF-P as the most promising self-standing FeNC cathode for thorough investigation in PEMFC. Unfortunately, it was found later by EXAFS (Figure 69) that the chosen cathode PBIXL@$[Fe/Zn]_{0.5}$ZIF-P contains some metallic Fe particles. In any case, this electrode showed a decent ORR activity in both RDE and PEMFC measurements in grinded form, or in RDE as a self-standing electrode.

Since self-standing FeNC electrodes possess high macroporosity, required for gas diffusion, it is possible to prepare MEAs without GDL on the cathode side when using self-standing FeNC electrodes.

The self-standing cathode was prepared by impregnating a 20 µm layer of PBIXL@$[Fe/Zn]_{0.5}$ZIF-P in Nafion solution 5%, and successive drying in air. The resulting cathode was assembled in MEA and measured in fuel cell under pure oxygen environment (1 layer of FeNC self-standing electrode). After that, we also tested to stack 4 layers of PBIXL@$[Fe/Zn]_{0.5}$ZIF-P and even 7 layers of PBIXL@$[Fe/Zn]_{0.5}$ZIF-P. Each layer corresponds to *circa* 0.5 mg per cm^2 of FeNC catalyst. The resulting polarization curves are shown in Figure 77.

For the moment, all self-standing electrodes present a lower activity and performance than that obtained with the reference catalyst $Fe_{0.5}$-NC. Even the grinded electrode that was then deposited as an ink resulted in lower performance, for a same cathode loading of 4 mg cm^{-2} than the reference catalyst. The shape of the polarization curve indicates lower ORR activity but improved mass-transport however, compared to the polarization curve of the reference Fe0.5-NC catalyst (compare the black and blue curves).

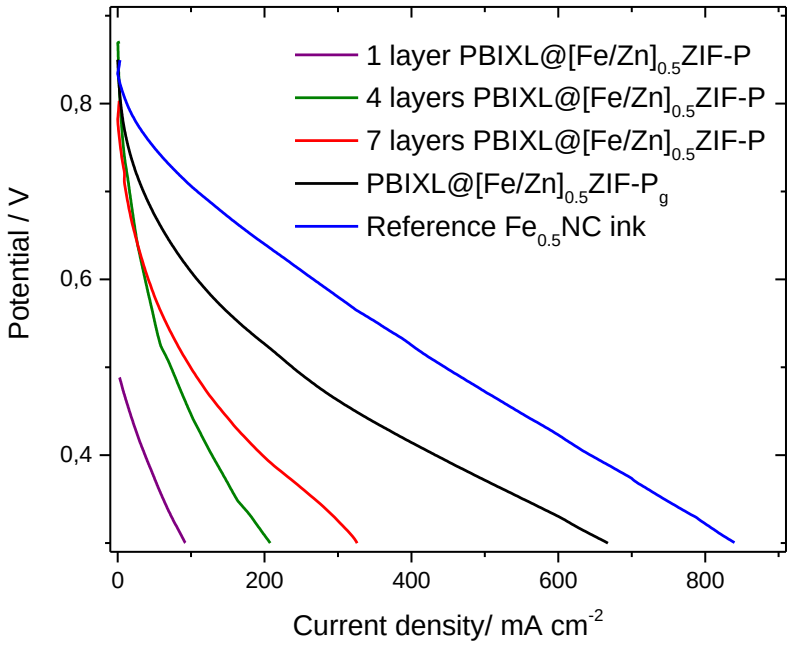

Figure 77: The polarization curves for MEAs with self-standing FeNC cathodes based on PBIXL@$[Fe/Zn]_{0.5}$ZIF-P_g (different numbers of layers of self-standing cathodes, 1, 4 or 7, loading *ca* 0.5 mg cm^{-2}, 2 mg cm^{-2} and 3.5 mg cm^{-2} respectfully) and comparison to the polarization curve obtained with PBIXL@$[Fe/Zn]_{0.5}$ZIF-P_g (4 mg cm^{-2} cathode loading) and also to that obtained with $Fe_{0.5}$NC reference catalyst (4 mg cm^{-2} cathode loading). For the self-standing FeNC cathodes, they were used as such after Nafion functionalization, and without GDL between them and the cathode endplate. Anode was GDE Sigracet 24BC with loading 0.5 mg_{Pt} cm^{-2}. Membrane Nafion NR211. The pressure of H_2 and O_2 gases was set as 1 bar. The compression rate was *ca* 30%.

4.3.d Electrochemical properties of Basolite-functionalized fibrous FeNC catalyst

The mass activity of the self-standing and/or grinded FeNC electrodes prepared by the growth of ferrocene-doped MOFs on polymer fiber mats followed by pyrolysis, has hitherto been significantly lower than that of the reference $Fe_{0.5}$NC powder material in both RDE and in PEMFC setup. This has impeded reaching higher performance in PEMFC, even if the electrode macroporosity of self-standing electrodes or layers made from grinded electrodes is higher than the macroporosity of layers made from the reference $Fe_{0.5}$NC catalyst. One of possible reasons for the lower activity is that during MOF synthesis on the polymer fibers, the quantity of Fe introduced in the self-standing polymer fiber mat is significantly lowered due to the high mass of polymer relative to the mass of MOF grown and attached on the polymer fibers. This hypothesis was confirmed by X-ray fluorescence spectroscopy on selected samples (Table 15), showing 3 to 10 times less Fe bulk content in such FeNC electrodes compared to $Fe_{0.5}$NC powder catalyst.

To increase the quantity of Fe sites in the self-standing electrodes, the synthesis procedure was modified, replacing the MOF precursor by commercial ZIF-8 (Basolite® Z1200, Sigma-Aldrich). The synthesis step for functionalizing with Basolite the polymer fiber mat was as following:

A mass of 2.32 g of Basolite® Z1200 was first dispersed in 40 mL of DMF at room temperature using magnetic stirring. After heating to 140 °C, 2.1 g of ferrocene and 6.7 g of zinc nitrate were then added in the solution. That corresponds to Zn/Fe ratio of 0.5 at %. After few minutes, the stirring was stopped and the cross-linked PBI nanofiber mat was introduced in solution and placed horizontally. The thickness of the PBI fiber mat was ~ 20 µm and the size of the piece of mat immersed in solution was 4 cm x 4 cm. After introduction of the fiber mat in solution, the reaction was let to proceed at 140°C for 24 h without stirring, and the nanofiber mat was then withdrawn from the solution and washed with ethanol.

After this step, the subsequent cathode preparation method was kept identical as before, and is described in sections 4.1.b and 4.1.c. A part of the resulting FeNC electrode was later grinded manually with a mortar in order to also obtain comparative PEMFC data for a cathode prepared by ink deposition of the grinded FeNC electrode. The self-standing FeNC electrode and grinded electrode were labelled as PBIXL@$[Fe/Zn]_{0.5}ZIF_{bas}$-P and PBIXL@$[Fe/Zn]_{0.5}ZIF_{bas}$-P_g, respectively.

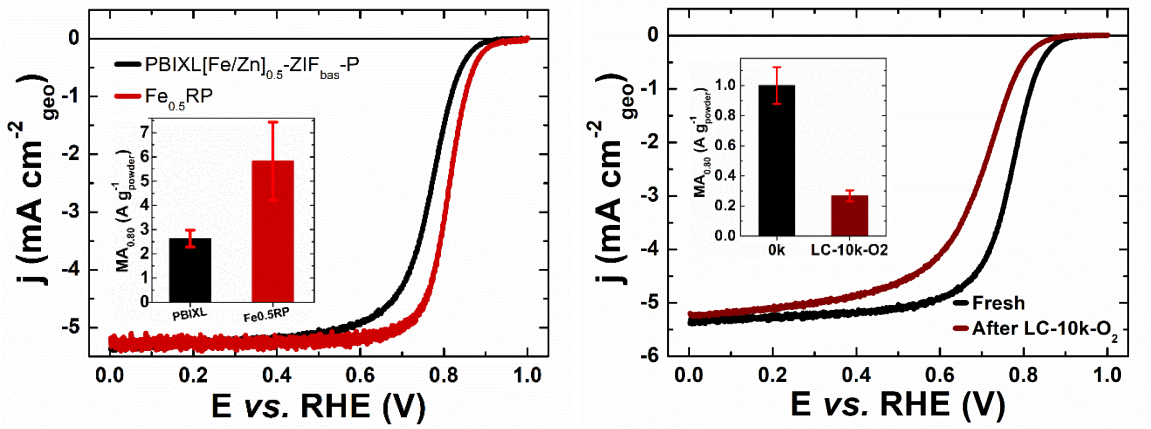

Figure 78: Electrochemical characterization in RDE of grinded PBIXL@$[Fe/Zn]_{0.5}ZIF_{bas}$-P electrode. a) ORR polarization curves in O_2-saturated pH 1 solution and compared to the same curve measured for the reference $Fe_{0.5}$NC active layer. The electrolyte was 0.1 M H_2SO_4, electrode rotation rate 1600 rpm and catalyst loading 1 mg cm^{-2}. Inset: Mass activity of grinded PBIXL@$[Fe/Zn]_{0.5}$ZIF-P electrode, measured at 0.8 V vs. RHE and compared to the reference $Fe_{0.5}$NC powder catalyst, b) ORR activity at pH 1, determined by nitrite striping method before/after, O_2-LC. Inset: Mass activity of grinded PBIXL@$[Fe/Zn]_{0.5}ZIF_{bas}$-P electrode after 10000 cycles, measured at 0.8 V vs. RHE and compared to the reference $Fe_{0.5}$NC powder catalyst. The potential was stepped between 0.6 and 1.0 V vs. RHE. Each potential was held for three seconds.

The ORR activity measured for PBIXL@$[Fe/Zn]_{0.5}ZIF_{bas}$-P and compared to $Fe_{0.5}$NC reference is present at Figure 78. For the case of basolite-based material there is clear improvement in the mass activity (Figure 78 a) compared to Figure 29 with a non-modified Fe-doped synthesis. The activity losses after AST (Figure 78 b) were compared to the reference and are in agreement with expected loses.

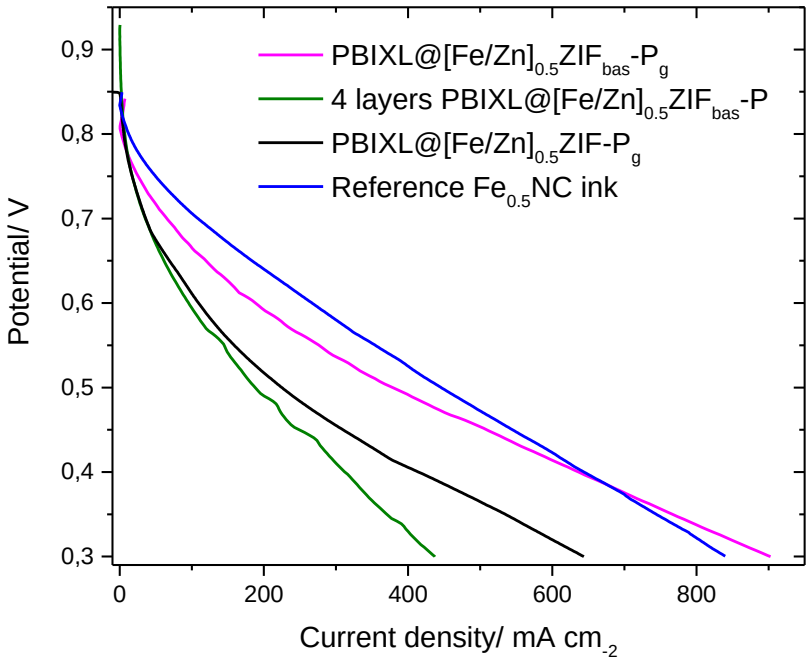

Figure 79: The polarization curves of MEAs comprising the self-standing FeNC cathode PBIXL@$[Fe/Zn]_{0.5}ZIF_{bas}$-P (4 identical layers superposed on each other, corresponding to *ca* 2 mg cm^{-2} FeNC loading) or the cathode active layer prepared by ink-deposition of PBIXL@$[Fe/Zn]_{0.5}ZIF_{bas}$-P_g (4 mg cm^{-2} cathode loading). The curves are also compared to polarization curves obtained with MEAs comprising cathodes based on a) ink-deposited PBIXL@$[Fe/Zn]_{0.5}$ZIF-P_g or b) the $Fe_{0.5}$NC reference (4 mg cm^{-2} cathode loading, deposited on the microporous side of a GDL). No GDL was used on the cathode side with the self-standing cathode. Anode was GDE Sigracet 24BC with loading 0.5 mg_{Pt} cm^{-2}. Membrane Nafion NR211. The pressure of H_2 and O_2 gases was set as 1 bar. The compression rate was *ca* 30%.

4 self-standing FeNC layers of PBIXL@$[Fe/Zn]_{0.5}ZIF_{bas}$-P were first immersed in the solution of Nafion (5wt%) and after drying they were stacked on each other and assembled in the MEA on the cathode side under hot press, labelled as "4 layers PBIXL@$[Fe/Zn]_{0.5}ZIF_{bas}$-P", in the figure. The resulting polarization curves are presented in Figure 79. The results were also compared to the most active sample obtained via MOF growth on polymer fibers, namely the grinded electrode PBIXL@$[Fe/Zn]_{0.5}$ZIF-P_g.

The PEMFC results evidence a great improvement of ORR activity at 0.8 V and overall performance at any cell voltage for the 4-layer of PBIXL@$[Fe/Zn]_{0.5}ZIF_{bas}$-P, compared to the 1-, 4- or 7-stacked layers of PBIXL@$[Fe/Zn]_{0.5}$ZIF-P (see Figure 77). It therefore seems that introducing pre-existing ZIF-8 crystals in the solution resulted in increased density of Fe active sites than when the ligand 2-methylimidazole is introduced. The initial OCP recorded for the 4-layers of PBIXL@$[Fe/Zn]_{0.5}ZIF_{bas}$-P is 0.94 V. Interestingly, this self-standing cathode is also as ORR active at 0.8 V as the catalytic layer prepared by ink deposition of PBIXL@$[Fe/Zn]_{0.5}ZIF_{bas}$-P_g (compare the green and magenta curves in Figure 79), despite of higher $Fe_{0.5}$NC loading in the latter (4 mg cm^{-2} for the PBIXL@$[Fe/Zn]_{0.5}ZIF_{bas}$-P_g cathode, versus *circa* 2 mg cm^{-2} of $Fe_{0.5}$NC expected for 4 stacked layers of self-standing FeNC electrodes). At lower cell voltage, the performance obtained with the cathode "4 mg cm^{-2} of PBIXL@$[Fe/Zn]_{0.5}ZIF_{bas}$-P_g" is however higher. Compared to the result obtained with the cathode comprising 4 mg cm^{-2} of the reference $Fe_{0.5}$NC catalyst, the latter shows higher ORR activity at e.g. 0.8 V compared to the cathode based on 4 mg cm^{-2} of PBIXL@$[Fe/Zn]_{0.5}ZIF_{bas}$-P_g. However, these two cathodes show the same performance at circa 0.4 V, and at lower cell voltage, the cathode performance becomes slightly better with the fibrous $Fe_{0.5}$NC catalyst PBIXL@$[Fe/Zn]_{0.5}ZIF_{bas}$-P_g than with the conventional Basolite-derived reference $Fe_{0.5}$NC catalyst (compare blue and magenta curves in Figure 79).

This achievement is encouraging and could lead to further studies of ZIF/polymer fiber composites for improved cathode morphology. Increasing the ratio of MOF/polymer fiber mass is important to reach sufficient ORR activity with such synthesis method, while a small amount of polymer fiber should suffice to secure a fibrous morphology of the FeNC cathode or grinded cathode, necessary for increasing the electrode or active layer macroporosity. The introduction of nano-sized ZIF-8 instead of the large crystals or particles present in the commercial Basolite Z1200 could, for example, be studied to improve the performance. In addition, PEMFC tests in air should be performed, which could further highlight the benefit of the fibrous FeNC catalysts versus the Basolite-derived reference $Fe_{0.5}$NC catalyst.

4.4 Conclusions

In this chapter, self-standing FeNC electrodes were investigated morphologically and electrochemically, using RDE and PEMFC measurements. The family of PAN@$[Fe/Zn]_x$SIM electrode precursors have well-defined MOF crystal shapes that is retained after pyrolysis. EXAFS analysis shows the absence of Fe-based crystallographic structures, implying that all Fe atoms were converted into FeN_4 active sites during pyrolysis. However, the electrochemical ORR mass activity measured in RDE and PEMFC is lower than that of the $Fe_{0.5}$NC reference catalyst.

On the other hand, the family of PBIXL@$[Fe/Zn]_x$ZIF electrode precursors comprises both nano- and micro- sized Fe-doped MOFs, homogeneously distributed on the polymer fibers. After pyrolysis, the Fe-based active sites are dispersed around the CNFs, which can explain the high activity of PBIXL@$[Fe/Zn]_x$ZIF-P electrodes in RDE and fuel cell measurements. However, EXAFS analysis also reveals the presence of Fe-based particles in this type of electrode.

Significant performance in PEMFC was obtained with stacked layers of Nafion-functionalized self-standing FeNC cathodes. The Fe content in such FeNC cathodes, and thus the active site density, seems however to strongly limit the electrode performance. In an attempt to increase the site density, the MOF ligand was exchanged by commercial ZIF-8 (Basolite Z1200) during the step of MOF growth on the polymer fibers (in this case, PBIXL polymer fibers). The resulting self-standing FeNC cathode, PBIXL@$[Fe/Zn]_{0.5}ZIF_{bas}$-P, showed much higher ORR activity and performance in PEMFC than any other self-standing cathode, reaching ca 300 mA cm^{-2} at 0.4 V. After grinding (PBIXL@$[Fe/Zn]_{0.5}ZIF_{bas}$-P_g), a cathode layer prepared by ink deposition showed further enhancement, reaching ca 640 mA cm^{-2} at 0.4 V, exactly matching the performance of the cathode layer prepared by ink deposition of the reference $Fe_{0.5}$NC catalyst. At cell voltage < 0.4 V, it even became better than the reference $Fe_{0.5}$-NC catalyst. This highlights the potential of fibrous FeNC catalysts, to tune the cathode layer morphology. Self-standing FeNC cathodes may also be optimized to a large extent in the future, for example by optimizing the Nafion content or gradient of Nafion content through the different FeNC self-standing layers.

1. Kreisz, A. Membranes PBI pour pile à combutible haute temperature., 2016.

2. Wang, C.; Kaneti, Y.V.; Bando, Y.; Lin, J.; Liu, C.; Li, J.; Yamauchi, Y. Metal-organic framework-derived one-dimensional porous or hollow carbon-based nanofibers for energy storage and conversion. *Mater. Horizons* **2018**, *5*, 394–407.

3. Yao, Y.; Liu, P.; Li, X.; Zeng, S.; Lan, T.; Huang, H.; Zeng, X.; Zou, J. Nitrogen-doped graphitic hierarchically porous carbon nanofibers obtained: Via bimetallic-coordination organic framework modification and their application in supercapacitors. *Dalt. Trans.* **2018**, *47*, 7316–7326.

4. Wang, C.; Zheng, T.; Luo, R.; Liu, C.; Zhang, M.; Li, J.; Sun, X.; Shen, J.; Han, W.; Wang, L. In Situ Growth of ZIF-8 on PAN Fibrous Filters for Highly Efficient U(VI) Removal. *ACS Appl. Mater. Interfaces* **2018**, *10*, 24164–24171.

5. Aguado, S.; Canivet, J.; Farrusseng, D. Engineering structured MOF at nano and macroscales for catalysis and separation. *J. Mater. Chem.* **2011**, *21*, 7582–7588.

6. Banerjee, R. High-Throughput Synthesis of Zeolitic. *ReVision* **2008**, *939*, 939–944.

7. Liu, C.-K.; Lai, K.; Liu, W.; Yao, M.; Sun, R.-J. Preparation of carbon nanofibres through electrospinning and thermal treatment. *Polym. Int.* **2009**, *58*, 1341–1349.

8. Zhang, W.; Yao, X.; Zhou, S.; Li, X.; Li, L.; Yu, Z.; Gu, L. ZIF-8/ZIF-67-Derived Co-N $_x$ -Embedded 1D Porous Carbon Nanofibers with Graphitic Carbon-Encased Co Nanoparticles as an Efficient Bifunctional Electrocatalyst. *Small* **2018**, *14*, 1800423.

9. Zitolo, A.; Goellner, V.; Armel, V.; Sougrati, M.-T.; Mineva, T.; Stievano, L.; Fonda, E.; Jaouen, F. Identification of catalytic sites for oxygen reduction in iron- and nitrogen-doped graphene materials. *Nat. Mater.* **2015**, *14*, 937–942.

10. Armel, V.; Hannauer, J.; Jaouen, F. Effect of ZIF-8 crystal size on the O<inf>2</inf> electro-reduction performance of pyrolyzed Fe–N–C catalysts. *Catalysts* **2015**, *5*, 1333–1351.

11. Bard, A.J.; Faulkner, L.R. *Electrochemical methods : fundamentals and applications*; John Wiley & Sons, Ltd, 2001; Vol. 1; ISBN 0-471-04372-9.

12. Goellner, V.; Armel, V.; Zitolo, A.; Fonda, E.; Jaouen, F. Degradation by hydrogen peroxide of metal-nitrogen-carbon catalysts for oxygen reduction. *J. Electrochem. Soc.* **2015**, *162*, H403–H414.

13. Sougrati, M.T.; Goellner, V.; Schuppert, A.K.; Stievano, L.; Jaouen, F. Probing active sites in iron-based catalysts for oxygen electro-reduction: A temperature-dependent 57Fe Mössbauer spectroscopy study. *Catal. Today* **2016**.

General conclusions

This thesis work was focused on the design and investigation of novel type of self-standing FeNC cathodes for PEMFC, with improved macroporosity. Those cathodes were prepared by electrospinning in order to achieve macroporosity in the fibrous web structures while microporosity, necessary for the high oxygen reduction activity and high number of Fe-based active sites in FeNC, was achieved either by forming intra-fiber micropores inside the fibers or by functionalizing the fibers with microporous MOF domains on the outside surface of the fibers.

During this work, a first approach for the preparation of CNFs with intra-fibre micropores resorted to the co-electrospinning of PAN with an added porogen agent, either a sacrificial polymer porogen (PMMA, Nafion®, PVP) or an inorganic porogen ($ZnCl_2$). The electrospun polymer fibre web was then carbonized in Ar at 1000°C and then subjected to a short ammonia activation at 900°C. Only the combination of the porogen addition during electrospinning and the ammonia activation step lead to intra-fiber open porosity, with high BET area ranging from 325 to 1083 m^2g^{-1}. Without the ammonia activation step, porosity was created in the fibers, but it was a closed porosity, as demonstrated by low BET area. Then the porogens PVP and $ZnCl_2$ were down-selected for the preparation of self-standing FeNC electrodes, prepared *via* electrospinning of a solution of PAN/porogen/Fe salt, followed by carbonization in Ar and then activation in ammonia. The highest ORR mass activity at 0.8 V vs. RHE measured in RDE for such self-standing FeNC electrodes was 0.88 A g^{-1}, versus 2.71 A g^{-1} for the mass activity of the reference catalytic layer of the Fe0.5NC reference catalyst pyrolyzed in Ar. The value of 0.88 A g^{-1} is low, especially taken into account that the self-standing FeNC cathodes were ammonia-treated, which is known to further increase the ORR mass activity of the $Fe_{0.5}$NC reference catalyst by ca a factor of x20 to x30[9].

The second approach for preparing self-standing FeNC cathodes resorted to the growth of ferrocene-doped metal organic frameworks on the 3D web of polymer nanofibers prepared by electrospinning, and then its pyrolysis in argon.

Chapter 2 described the first step toward that goal, namely the optimized synthesis of ferrocene-doped MOFs (SIM-1 and ZIF-8) to be pyrolyzed later into FeNC. These were prepared by solvothermal synthesis, optimizing the ferrocene-to-zinc molar ratio, in order to maximize the ORR activity of the resulting FeNC catalyst powders after pyrolysis in Ar. With SIM-1, it was found that the ferrocene content in the MOF is proportional to the Fe/Zn ratio in solution, while with ZIF-8 it was found that this is true only up to a maximum Fe/Zn ratio in solution, above which very little additional ferrocene could be encapsulated in

ZIF-8. The resulting FeNC powder catalysts after Ar-pyrolysis were characterized structurally and electrochemically, revealing a high microporous structure of materials (The S_{BET} was between 406 and 1824 $m^2\ g^{-1}$ before pyrolysis and between 488 and 1347 $m^2\ g^{-1}$ after pyrolysis). The highest ORR activity in RDE were obtained with $[Fe/Zn]_1$ZIF-P and $[Fe/Zn]_5$ZIF-P with the mass activity at 0.8 V vs. RHE of 2.35 A g^{-1} and 3.05 A g^{-1}, respectively. Although a high atomic ratio of Fe/Zn in ferrocene-doped ZIF-8 led to the creation of metallic Fe particles (possibly along with FeNx sites), as shown by EXAFS, the other materials were free of Fe particles, indicating the full conversion of ferrocene into atomically-dispersed FeN_x active sites during pyrolysis. Based on the results from this chapter, the following synthesis and the atomic ratio of Fe/Zn were chosen for the further preparation of self-standing FeNC electrodes: $[Fe/Zn]_{0.5}$SIM, $[Fe/Zn]_1$SIM, $[Fe/Zn]_2$SIM and $[Fe/Zn]_{10}$SIM, $[Fe/Zn]_{0.5}$ZIF-P, $[Fe/Zn]_1$ZIF, $[Fe/Zn]_2$ZIF.

This study was followed by chapter 3, where self-standing FeNC electrodes were prepared *via* the growth of ferrocene-doped SIM-1 on different PAN fibrous webs, then pyrolyzed identically as in chapter 2. The effect of coating the PAN polymer fibers with zinc was investigated and the ORR activity of the resulting self-standing FeNC electrodes were measured in RDE. Overall, the growth of ferrocene-doped SIM-1 on PAN polymer nanofibers was successful, leading to the formation of micro-sized MOFs on the surface of the polymer fibers. After pyrolysis, FeNC electrodes were characterized by RDE setup, resulting in significant ORR mass activity (0.77 A g^{-1} for SIM-1 grown on PAN fiber mat vs 1.09 A g^{-1} for SIM-1 grown on Zn-coated PAN fiber mat). However, there is no significant benefit of coating the polymer fibers with Zn, and this complexifies a lot the synthesis. Therefore, all following preparations in chapter 4 were done on pristine polymer nanofiber mats.

The last chapter was dedicated to the design and optimization of self-standing FeNC electrodes prepared by the growth of ferrocene-doped SIM-1 or ZIF-8 on different polymer fiber mats prepared by electrospinning. Another polymer fiber mat, namely cross-linked polybenzimidazole (PBIXL), was used in order to be able to grow ZIF-8 on a polymer fiber mat, since the growth of ZIF-8 on PAN fibers was unsuccessful. Resulting electrodes after Ar pyrolysis were investigated morphologically and electrochemically using RDE and PEMFC measurements. The family of PAN@$[Fe/Zn]_x$SIM-P electrodes were shown by EXAFS to comprise Fe only in the form of FeN_4 active sites. Only rather large, micrometric SIM-1 crystals were grown on the PAN polymer fibers. However the electrochemical activity in both RDE and PEMFC was lower than that of the $Fe_{0.5}$NC reference catalyst. The family of PBIXL@$[Fe/Zn]_x$ZIF-P electrodes were shown by EXAFS to comprise sometimes metallic Fe particles, depending on the Fe/Zn ratio. Both micro and nano-sized ZIF-8 crystals were formed on the surface of the PBIXL polymer fibers.

After pyrolysis self-standing FeNC electrodes were characterized by RDE setup, revealing high catalytic activity for all measured samples. PAN@$[Fe/Zn]_{0.5}$SIM-P and PBIXL@$[Fe/Zn]_2$ZIF-P were the most promising self-standing electrodes, with mass activity of 0.9 and 0.82 A g^{-1}, respectively. The self-standing electrodes were also grinded, deposited in electrode by drop-casting method and characterized in RDE setup, also revealing high catalytic activity. The most active samples were PAN@$[Fe/Zn]_1$SIM-P_g and PBIXL@$[Fe/Zn]_{0.5}$ZIF-P_g, with electrocatalytic activity of 0.63 A g^{-1} and 0.79 A g^{-1} respectively. In summary, the grinding of self-standing FeNC electrodes did not generally improve the catalytic activity, thereby validating the RDE measurement and concept of the self-standing electrodes.

The self-standing electrodes were also investigated in H_2/O_2 fuel cell. The trends of ORR activity measured in PEMFC for grinded electrodes was in agreement with the results obtained by RDE. The most promising sample was PBIXL@$[Fe/Zn]_{0.5}$ZIF-P_g, revealing decent activity, almost comparable with that of $Fe_{0.5}$NC catalyst. Several self-standing PBIXL@$[Fe/Zn]_{0.5}$ZIF-P layers were stacked on each other (1, 4 or 7 layers; corresponding to FeNC loadings of *ca* 0.5, 2 and 3.5 mg cm^{-2}, respectively) to form a complete FeNC cathode, and were installed in a single cell PEMFC without GDL between the self-standing catalyst layers and the cathode endplate. This resulted in decent ORR activity and polarization curve. While the activity and performance was lower than for the grinded version of this sample, this demonstrates the concept of self-standing FeNC cathodes in PEMFC.

Finally, the thesis work was concluded by the PEMFC investigation of cathodes prepared by the attachment of commercial ZIF-8 particles (Basolite Z1200) on PBIXL nanofibers in the presence of ferrocene. The synthesis of those cathodes was similar to previously investigated ones, but the ligand of ZIF-8 was exchanged by commercial ZIF-8 in order to increase the quantity of active sites on fibers, then pyrolyzed in Ar. The resulting self-standing FeNC cathode, PBIXL@$[Fe/Zn]_{0.5}ZIF_{bas}$-P reached ca 300 mA cm^{-2} at 0.4 V. After grinding (PBIXL@$[Fe/Zn]_{0.5}ZIF_{bas}$-P_g), a cathode layer prepared by ink deposition showed further enhancement, reaching ca 640 mA cm^{-2} at 0.4 V, exactly matching the performance of the cathode layer prepared by ink deposition of the reference $Fe_{0.5}$NC catalyst. At cell voltage < 0.4 V, it even became better than the reference $Fe_{0.5}$-NC catalyst. Therefore, this modified approach (exchanging 2-methyl-imidazole ligand for Basolite in the solution) resulted in much higher ORR activity in PEMFC, both as self-standing cathode or catalyst, compared to all other self-standing cathodes or catalysts previously studied in chapter 4.

Overall, the results obtained in this PhD thesis work highlight the potential of fibrous FeNC catalysts, to tune the cathode layer morphology.

Outlook for future studies:

The activity and power performance of self-standing FeNC cathodes could be significantly improved in the future by optimizing the following properties:

- Increased density of Fe-based actives sites per volume of electrode
- Optimized content of ionomer in the electrode
- Gradient of ionomer through the overall cathode (composed of several self-standing layers)
- Optimized content of MOFs grown or attached to the polymer fibers before pyrolysis
- Optimization of the size of MOFs
- Deposition of a microporous layer (carbon black + Teflon) on one self-standing layer, for improved water management in PEMFC operation

After optimization of such self-standing FeNC electrodes, it would also be interesting to compare the performance in fuel cell with a cathode fed with air instead of pure oxygen. Air feed is the application conditions for PEMFCs, and the expected higher porosity in self-standing electrodes vs. conventional FeNC powder catalyst layers could therefore play an important role in such conditions.

In parallel, the investigation of grinded self-standing cathodes is also promising, resulting in FeNC catalyst powders but with anisotropic, fibrous, morphology.

Also, an interesting approach could be developped by combining the self-standing electrode concept and the conventional catalyst ink process, for example by depositing optimized content of catalyst ink into self-standing FeNC electrodes.

List of acronyms

ACNF	Activated carbon nanofibers
AFC	Alkaline Fuel Cells
BET	Brunauer–Emmett–Teller theory
CNF	Carbon nanofiber
CCM	Catalyst-coated membrane
CA	Chronoamperometry
PBIXL	Cross-linked polybenzimidazole
CV	Cyclic voltammetry
DCX	α,α'-dichloro-p-xylene
DMFC	Direct Methanol Fuel Cells
EDX	Energy-dispersive X-ray spectroscopy
EXAFS	Extended X-Ray Absorption Fine Structure
FE-SEM	Field emission scanning electron microscopy
FT	Fourier transform
FSE	Free-standing electrodes
GDE	Gas diffusion electrode
GDL	Gas diffusion layer
GC	Glassy carbon
HOR	Hydrogen oxidation reaction
ICGM-AIME	Institut Charles Gerhardt Montpellier - Agrégats, Interfaces et Matériaux pour l'Energie
IRCELYON	Institut de recherches sur la catalyse et l'environnement de Lyon
FeAc	Iron acetate
FeAcAc	Iron acetylacetonate
JCPDS	Joint Committee on Powder Diffraction Standards
LEPMI	Laboratoire electrochimie et physicochimie des matériaux et des interfaces
MEA	Membrane-electrode assembly
MOF	Metal-organic framework

MCFC	Molten Carbonate Fuel Cells
MWCNT	Multiwall carbon nanotubes
DMF	N,N-dimethylformamide
ORR	Oxygen reduction reaction
PFSA	Perfluorosulfonic acid
PAFC	Phosphoric Acid Fuel Cells
PGM	Platinum Group Metal
PAA	Polyacrylic acid
PAN	Polyacrylonitrile
PBI	Polybenzimidazole
PI	Polyimide
PMMA	Polymethyl methacrylate
PVA	Polyvinylalcohol
PVDF	Polyvinylidene fluoride
PVP	Polyvinylpyrrolidone
PCFC	Proton Ceramic Fuel Cells
PEMFCs	Proton Exchange Membrane Fuel Cells
RHE	Reversible hydrogen electrode
RDE	Rotating disc electrode
SOFC	Solid Oxide Fuel Cells
SIM	Substitute imidazolate framework
TEM	Transmission electron microscopy
TPB	Triple phase boundary
USDOE	United States Department of Energy
XANES	X-ray absorption near edge structure
XRD	X-ray diffraction
XRF	X-ray fluorescence
ZIF	Zeolitic imidazolate framework

Résumé de la thèse

Français

L'objectif de ce projet de thèse était le développement de cathodes FeNC autosupportées préparées par électrofilage, pour la préparation d'électrodes à porosité hiérarchique. Une telle structure pourrait améliorer l'accessibilité des sites actifs à base de fer par l'O_2 pour la réaction de réduction de l'oxygène (ORR), et par conséquent la performance des cathodes FeNC dans la pile à combustible à membrane échangeuse de protons (PEMFC). En raison de l'activité plus faible pour l'ORR des catalyseurs FeNC par rapport au platine dispersé sur carbone, les couches actives FeNC de l'état de l'art ont une épaisseur d'environ 100 µm aujourd'hui, environ 5 à 10 fois plus épaisses que les couches Pt/C. Pour cette raison, l'optimisation de la diffusion d'O_2 dans les électrodes FeNC est cruciale pour permettre le remplacement du Pt par des catalyseurs moins chers. Différentes approches ont été étudiées pour préparer des électrodes FeNC autosupportées. Dans une première approche, un tapis 3D de nanofibres de polyacrylonitrile (PAN) comprenant également un précurseur de Fe et un porogène a été préparé par électrofilage, puis traité thermiquement sous argon et NH_3. Cela a abouti à des électrodes autosupportées à base de nanofibres de carbone microporeux avec des sites actifs à base de fer. Dans une seconde approche, des solides hybrides poreux cristallisés (MOF) dopés au fer ont été formés sur un tapis 3D de nanofibres polymères (polyacrylonitrile ou polybenzimidazole, PBI), qui a ensuite été traité thermiquement sous argon. Pour cette approche, il a d'abord été nécessaire d'établir une méthode reproductible pour la préparation de MOF dopés au fer. Ceci a été réalisé par encapsulation de ferrocène dans les cavités de deux MOF différents (SIM-1 et ZIF-8). La teneur en ferrocène et les conditions de synthèse ont été optimisées séparément pour atteindre l'activité ORR la plus élevée. La même synthèse a ensuite été appliquée pour faire croître des MOF dopés au fer sur des tapis 3D de fibres de PAN ou PBI. La croissance de ces MOFs a été étudiée soit sur les fibres polymères bruts, soit sur les fibres polymères recouvertes d'une couche mince de zinc. Les électrodes FeNC préparées par ces différentes approches ont été caractérisés vis-à-vis de leur morphologie, leur structure et type de fer par microscopie électronique à balayage, microscopie électronique à transmission, analyse dispersive en énergie, diffraction des rayons X, spectroscopie des photoélectrons X, spectroscopie Raman et spectroscopie d'absorption des rayons X. Les électrodes autosupportées et/ou les poudres de FeNC broyées ont été étudiées par voie électrochimique avec une électrode à disque tournant et en mono-cellule PEMFC. Les matériaux actifs en ORR ont été obtenus par différentes approches. La plus prometteuse d'entre elles a été la croissance cristalline de ZIF-8 dopé au ferrocène sur des fibres de PBI réticulées, puis pyrolysé sous argon. Les électrodes ont été étudiées en pile PEMFC, soit après broyage des cathodes FeNC autosupportées soit en tant que structure autosupportée. Ces dernières ont été imprégnées par le Nafion avant la caractérisation électrochimique en pile. Les cathodes broyées ont conservé leur structure fibreuse issue du filage électrostatique, et ont montré de bonnes performances en pile PEMFC. En raison de leur faible épaisseur (20 µm) plusieurs électrodes autosupportées (fonctionnalisées par le Nafion) ont été superposées pour obtenir une activité ORR suffisante. Le concept de cathode FeNC autosupportée a été validé pour la première fois, mais il est nécessaire d'optimiser encore leur fonctionnalisation par le Nafion pour démontrer tous les avantages de cette approche. De telles électrodes pourront également trouver une application dans d'autres dispositifs de conversion électrochimique de l'énergie, tel que les piles à combustible à membrane échangeuse d'anions, les supercondensateurs électrochimiques et la réduction électrochimique du CO_2.

English

The aim of this PhD thesis project was the development of self-standing FeNC cathodes prepared by electrospinning, in order to achieve hierarchical microporous and macroporous electrodes. Such a structure is desirable to improve accessibility by O_2 of the Fe-based active sites for oxygen reduction reaction (ORR), and therefore to improve the performance of FeNC cathodes in proton exchange membrane fuel cell (PEMFC). Due to the lower activity for ORR of FeNC catalysts compared to platinum on carbon, FeNC active layers of *ca* 100 µm thickness are today the state-of-art, about 5 to 10 times thicker than Pt/C layers. For this reason, the optimization of O_2 diffusion in FeNC electrodes is important to allow the replacement of Pt by less expensive catalysts. Different approaches were investigated to prepare self-standing FeNC electrodes. In a first approach, a 3D web of polyacrylonitrile (PAN) nanofibers comprising also a Fe precursor and additional porogens was first prepared by electrospinning, and then thermally treated in argon and NH_3. This resulted in self-standing electrodes based on microporous carbon nanofibers with Fe-based active sites. In a second approach, iron-doped metal-organic frameworks (MOFs) were grown on 3D web of polymer nanofibers (polyacrylonitrile or polybenzimidazole, PBI), and then thermally treated in argon. For this approach, it was first necessary to establish a reproducible method for the preparation of iron-doped MOFs, which was achieved with ferrocene encapsulation in two different MOFs (SIM-1 and ZIF-8). The ferrocene content and synthetic conditions were separately optimized to achieve the highest ORR activity. The same synthesis was then applied to grow Fe-doped MOFs on 3D webs of either PAN or PBI fibers. The growth of these MOFs was studied either on the polymer fibers, or on such fibers pre-coated with zinc. The FeNC electrodes and materials prepared by these different approaches were characterized for their morphology, structure and Fe speciation by scanning electron microscopy, transmission electron microscopy, energy-dispersive x-ray spectroscopy, x-ray diffraction, x-ray photoelectron spectroscopy, Raman spectroscopy and Fe K-edge x-ray absorption spectroscopy. The self-standing electrodes and/or grinded FeNC powders were electrochemically investigated with rotating disk electrode and single-cell PEMFC. ORR-active materials were obtained with the different approaches, but the most promising one is identified to be the crystalline growth of ferrocene-doped ZIF-8 on a web of cross-linked PBI fibers, followed by pyrolysis in argon. The electrodes were investigated in PEMFC, either after grinding the self-standing FeNC cathodes into a powder or as a self-standing structure. In the latter case, they were functionalized by Nafion before electrochemical measurement in PEMFC. Grinded FeNC cathodes are shown to retain a fibrous structure derived from the electrospinning process, leading to increased macroporosity in the electrodes and good performance in fuel cell. Due to their thickness of only *ca* 20 µm, several self-standing FeNC layers (functionalized with Nafion) were superimposed in order to reach sufficient overall ORR activity. The concept of self-standing FeNC cathode was validated for the first time, but further optimization of their functionalization by Nafion ionomer is needed to take full advantage of this approach. Future research is therefore needed to functionalize such novel electrode structures by proton-conducting ionomers to optimize the electrode activity and proton conductivity. Such electrode structure can also find application in other electrochemical energy conversion devices such as anion exchange membrane fuel cells, electrochemical supercapacitors and electrochemical CO_2 reduction.